

Morphology, Performance, and Stability
of Flexible and Transparent Electrodes
Imprinted from Gold Nanowires and -spheres

Dissertation
zur Erlangung des Grades
des Doktors der Ingenieurwissenschaften
der Naturwissenschaftlich-Technischen Fakultät
der Universität des Saarlandes

von
Lukas F. Engel
(M.Sc.)

angefertigt am
INM - Leibniz-Institut für Neue Materialien gGmbH

Saarbrücken
2024

Tag des Kolloquiums: 21.01.2025
Dekan: Univ.-Prof. Dr.-Ing. Dirk Bähre
Berichterstatter: Prof. Dr. Tobias Kraus
Priv.-Doz. Dr.-Ing. habil. Guido Falk
Vorsitz: Prof. Dr. Karen Lienkamp
Akademischer Mitarbeiter: Dr.-Ing. Andreas Tschöpe

„Das Wichtigste ist, dass man nicht aufhört zu fragen.“

— *Albert Einstein*

Abstract

Flexible transparent electrodes (FTEs) were prepared from gold nanospheres and ultra-thin gold nanowires with oleylamine ligand shell and characterised. Their colloidal inks were patterned using direct nanoimprint lithography at different particle concentrations in cyclohexane on polyethylene terephthalate substrates with a patterned polydimethylsiloxane stamp. The wire inks agglomerated upon dilution, while sphere inks did not undergo this entropy-driven mechanism. At the highest printed concentration they were still well dispersed. Plasma sintering converted the imprinted grids into conductive electrodes, but only partially removed the ligands. The sintered lines consisted of a hybrid core and a thin conductive metal shell. Wire-based shells had a coarse surface microstructure and pronounced porosity. This rendered the wire-based FTEs instable. Spheres formed smooth shells with little or no porosity, enabling a beneficial ageing process. Immediately after plasma sintering, the ratio of optical transmittance to electrical resistance for wire-based FTEs exceeded that of sphere-based FTEs. Ageing reversed this order. The instability of wire-based FTEs was overcome by PEDOT:PSS coatings.

Kurzfassung

Flexible transparente Elektroden (FTEs) wurden aus Goldnanokugeln und aus ultradünnen Goldnanodrähten mit Oleylamin-Ligandenhülle hergestellt und charakterisiert. Ihre kolloidalen Tinten wurden durch direkte Nanoprägelithographie bei verschiedenen Partikelkonzentrationen in Cyclohexan auf Polyethylenterephthalat-Substraten mit einer Prägestruktur aufweisenden Polydimethylsiloxan-Stempel strukturiert. Die drahtbasierten Tinten agglomerierten beim Verdünnen. Kugelbasierte Tinten unterlagen dem Entropie getriebenen Mechanismus nicht. Sie blieben auch bei der höchsten geprägten Konzentration dispers verteilt. Plasmasintern überführte die geprägten Gitter in leitfähige Elektroden, entfernte die Liganden dabei aber nur teilweise. Die gesinterten Linien bestanden aus einem hybriden Kern und einer dünnen leitenden Metallschale. Die Schalen auf Drahtbasis hatten eine grobe Oberflächenmikrostruktur und eine ausgeprägte Porosität. Dies machte die Draht-FTEs sehr instabil. Kugeln bildeten glatte Schalen mit wenig oder keiner Porosität. Sie sind die Basis für eine vorteilhafte Alterung. Direkt nach der Plasmabehandlung übertraf das Verhältnis von optischer Transmission zu elektrischem Widerstand bei Draht-FTEs jenes von Kugel-FTEs. Alterung kehrte diese Reihenfolge um. Die Instabilität der Draht-FTEs wurde durch eine PEDOT:PSS Beschichtung überwunden.

Publications and contributions

This cumulative dissertation comprises the following four peer-reviewed publications (one as co-author and three as first author). The author contributions according to CRediT^[1-3] (Contributor Roles Taxonomy) are as follows:

Publication 1

S. Bettscheider, B. Kuttich, L. F. Engel, L. González-García, and T. Kraus: “Bundling of Nanowires Induced by Unbound Ligand”. *J. Phys. Chem. C*, 2021, 125, 6, 3590–3598. DOI: 10.1021/acs.jpcc.0c10919.

Author contributions:

- *Simon Bettscheider*: Conceptualization; Methodology; Validation; Formal analysis; Investigation; Writing - Original Draft; Writing - Review & Editing; Visualization.
- *Björn Kuttich*: Methodology; Software; Formal analysis; Writing - Original Draft; Writing - Review & Editing; Supervision.
- *Lukas F. Engel*: Investigation; Writing - Original Draft; Writing - Review & Editing.
- *Lola González-García*: Conceptualization; Writing - Review & Editing; Supervision.
- *Tobias Kraus*: Conceptualization; Methodology; Writing - Review & Editing; Supervision; Project administration; Funding acquisition.

Publication 2

L. F. Engel, L. González-García, and T. Kraus: “Flexible and Transparent Electrodes Imprinted from Metal Nanostructures: Morphology and Opto-Electronic Performance”. *Nanoscale Adv.*, 2022, **4**, 3370-3380. DOI: 10.1039/D2NA00259K.

Author contributions:

- *Lukas F. Engel*: Conceptualization; Formal analysis; Investigation; Methodology; Software; Validation; Visualization; Writing - Original Draft; Writing - Review & Editing.
- *Lola González-García*: Conceptualization; Writing - Review & Editing; Supervision.
- *Tobias Kraus*: Conceptualization; Writing - Review & Editing; Supervision; Project administration; Funding acquisition.

Publication 3

L. F. Engel, L. González-García, and T. Kraus: “Flexible and Transparent Electrodes Imprinted from Au Nanowires: Stability and Ageing”. *Nanoscale Adv.*, 2022, **4**, 3940-3949. DOI: 10.1039/D2NA00352J.

Author contributions:

- *Lukas F. Engel*: Conceptualization; Formal analysis; Investigation; Methodology; Software; Validation; Visualization; Writing - Original Draft; Writing - Review & Editing.
- *Lola González-García*: Conceptualization; Writing - Review & Editing; Supervision.
- *Tobias Kraus*: Conceptualization; Writing - Review & Editing; Supervision; Project administration; Funding acquisition.

Publication 4

L. F. Engel, L. González-García, and T. Kraus: “Consolidation and Performance Gains in Plasma-Sintered Printed Nanoelectrodes”. *Nanoscale Adv.*, 2023, **5**, 4124-4132. DOI: 10.1039/D3NA00293D.

Author contributions:

- *Lukas F. Engel*: Conceptualization; Formal analysis; Investigation; Methodology; Software; Validation; Visualization; Writing - Original Draft; Writing - Review & Editing.
- *Lola González-García*: Conceptualization; Writing - Review & Editing; Supervision.
- *Tobias Kraus*: Conceptualization; Writing - Review & Editing; Supervision; Project administration; Funding acquisition.

Acknowledgements

“If you want to go fast, go alone. If you want to go far, go together.”

(unknown author)

First, I would like to thank my “Doktorvater”, *Prof. Dr. Tobias Kraus*, head of the Structure Formation Group at the Leibniz Institute for New Materials (INM) and head of the Chair for Colloid and Interfacial Chemistry at Saarland University. He provided me with the opportunity to contribute to the advancement of the exciting field that is printed electronics during my doctoral studies. Throughout this period, he has encouraged and facilitated my participation in seven international conferences as well as in two industrial fairs. His constructive criticism when discussing, reviewing, editing, and commenting my manuscripts was much appreciated. Admittedly, Tobias was very demanding, sometimes resulting in several iteration cycles. That felt frustrating at times. The result, however, always proved him right. But more importantly, I was able to learn a lot during that process. Last but not least, I would like to thank him for his trust and for the personal and professional development I underwent under his guidance.

Dr. Lola González-García, junior professor for electrofluids and head of the Electrofluids Group at INM, supervised me closely during my doctoral studies and had a hard time with my perfectionism. Thank you for your support, your (im)patience and for teaching me the “cutre” style.

I would also like to thank *Prof. Dr. Eduard Arzt*, former CEO and scientific director of the management board of INM, former head of the Functional Microstructures Group at INM, and former head of the Chair for New Materials at Saarland University. He provided me with the opportunity to conduct my research at such a prestigious, well-known, and -equipped research institute of international format. Also, I was allowed to use his group’s confocal laser scanning microscope (CLSM).

Additionally, I would like to thank my academic advisor, *Prof. Dr.-Ing. Ute Rabe*, adjunct professor for materials engineering at the Chair for Lightweight Systems at Saarland University and my second reviewer, *Priv.-Doz. Dr.-Ing. habil. Guido Falk*, head of the Chair for Structural

and Functional Ceramics at Saarland University as well as the other members of the examination committee.

Thank you, *Dr. Marcus Koch* and *Birgit Nothdurft*, for actively supporting me with your knowledge and expertise on cross-sectioning with a focused ion beam (FIB), on scanning electron microscopy (SEM), and on transmission electron microscopy (TEM), especially through many service measurements.

Many thanks go to *Robert Drumm*, who assisted me with his skills in thermogravimetric analysis (TGA) and conducted many service measurements.

Moreover, I would like to thank everyone who supported me with small-angle X-ray scattering (SAXS) service measurements: *Dr. David Doblás Jiménez*, *Dr. Björn Kuttich*, *Dr. Bart-Jan Niebuur*, and *Dr. Thomas Kister*.

Thank you, *Prof. Dr. Bennewitz*, *Dr. Johanna Blass*, and *Wiebke Buhrow*, for your knowledge and expertise on atomic force microscopy (AFM), and for numerous service measurements - even though I switched to CLSM in the end.

I am equally grateful for *Christian Ersfeld* and his team at the electrical workshop. They helped me equip the multiplexer cards of two multi-channel multi-meters with a total of 120 pairs of cables (2-point-probe measurement), to the ends of which miniature crocodile clamps had to be soldered.

Another thank you goes to *Herbert Beermann* with his team at the mechanical workshop. They assisted me in designing numerous custom-made parts (racks for cleaning and storage of the polyethylene terephthalate substrates, centrifuge inserts, sample holders, UV-vis masks, and further cleaning racks) to facilitate my experimental work and fabricated them.

A big thank you goes out to *Prof. Dr. Presser* whose glovebox I could use.

Thank you, *Robert Strahl* and *Anja Colbus*, for your regular engineering and lab support.

Thanks, *Mr. Krämer*, for granting me access to the Leibniz Institute for New Materials on so many weekends and for the informal conversa-

tions we had after long working days.

A big shoutout to all other not yet mentioned past and present members of the Structure Formation Group, in particular *Dr. Roman Buchheit*, *Dr. Louis Weber*, *Dr. Simon Bettscheider*, and *Dr. Alberto Escudero* as well as to all other not yet mentioned past and present employees at the INM, in particular *Jenny Kampka*, *Gabriele Koster*, *Sabine Müller*, and *Bernd Rus*. You all contributed to a productive and pleasant working atmosphere.

Last but not least, I would like to thank my parents as well as *Silviya Boyadzhieva*. Without your support I could not have made it.

At the end of the day, it's the support you get that carries you further than you ever thought.

List of abbreviations

AFM	atomic force microscopy
AR	aspect ratio: length/diameter
AuNP	Au nanosphere with a diameter of ≈ 3.7 nm
AuNW	Au nanowire with a diameter of ≈ 1.6 to 1.7 nm and a length of several μm
AZO	aluminium doped zinc oxide
c_{Au}	Au concentration in mg/mL
CLSM	confocal laser scanning microscopy
d_i	interparticle distance (surface-to-surface)
2D	two-dimensional
DNA	deoxyribonucleic acid
E	the Young's modulus of a material
EBL	electron beam lithography
e.g.	exempli gratia (Latin for "for example")
et al.	et alia (Latin for "and others")
fcc	face-centered cubic
FIB	focused ion beam
FOM	figure of merit e.g. the ratio "transmittance / sheet resistance"
FTE	flexible transparent electrode
FTO	fluorine doped tin oxide
h_{max}	average maximum height of the sintered lines
i.e.	id est (Latin for "that is")
IR	infrared
ITO	tin-doped In_2O_3
λ	wavelength
λ_{metal}^e	mean free path length of electrons in bulk metal at room temperature
LED	light-emitting diode
N	random metal nanowire network density
N_c	critical random metal nanowire network density
NIL	direct nanoimprint lithography
OAm	oleylamine

OLED	organic light-emitting diode
ω	mean width of the sintered lines
PDMS	polydimethylsiloxane
PEDOT:PSS	mixture of poly(3,4-ethylenedioxythiophene) and polystyrene sulfonate
PEN	poly(ethylene 2,6-naphthalate)
PET	polyethylene terephthalate
PVP	poly(vinyl)pyrrolidone
R	volume resistance
rf	radio frequency
rH	relative humidity
RT	room temperature
R2R	roll-to-roll
R_{sh}	sheet resistance
$R_{sh,t}$	sheet resistance after ageing time t
R_{sh,t_0}	initial sheet resistance (right after fabrication)
$\Delta R_{sh,t}$	$R_{sh,t} - R_{sh,t_0}$
SAXS	small-angle X-ray scattering
SEM	scanning electron microscopy
SEM-EDX	scanning electron microscopy with energy-dispersive X-ray spectroscopy
SI	supporting information
σ_{shell}	mean conductivity of the Au shell
t	ageing time
t_0	$t = 0$ d
TBAB	tert-butylamine-borane
TE	transparent electrode
TEM	transmission electron microscopy
T_g	glass-transition temperature
TGA	thermogravimetric analysis
TIPS	triisopropylsilane
T_λ	transmittance at a wavelength λ (in nm)
$\overline{T}_{400-800}$	average of T_λ within the visible λ -range (400 to 800 nm)
t_{shell}	average thickness of the Au shell
UV	ultraviolet

UV-vis	ultraviolet-visible spectrophotometry
XPS	X-ray photoelectron spectroscopy
vs.	versus (Latin for “compared to”)

Contents

Abstract	iii
Kurzfassung	iv
Publications and contributions	vi
Acknowledgements	x
List of abbreviations	xiv
1 Introduction	1
2 State of the Art	5
2.1 Opto-electronics and transparent electrodes (TEs)	5
2.1.1 Transparent conductive metal oxides	6
2.1.2 Metal-based flexible transparent electrodes (FTEs)	8
2.1.3 Random metal nanowire networks	10
2.1.4 Metal corrosion	15
2.1.5 Regular metal grids	16
2.2 Fabrication of nanoscale structures by direct nanoimprint lithography (NIL)	19
2.2.1 Thermal NIL of Au nanoparticle inks	21
2.2.2 Direct nanoimprinting of inks of self-assembling Au nanoparticles	22
2.3 Synthesis and self-assembly of Au nanoparticles with al- kylamine ligand shell	25
2.3.1 Au nanoparticles	25
2.3.2 Au nanowires	27
2.3.3 Ultra-thin Au nanowires - AuNWs	28
2.3.4 Properties of ultra-thin Au nanowires	30
2.3.5 Self-assembly of OAm-capped AuNWs	32
2.3.6 Au nanospheres	34

2.3.7	OAm-capped AuNPs	35
2.4	Sintering of grids made of ligand coated metal nanoparticles to form conductive electrodes	36
2.4.1	Chemical sintering	38
2.4.2	Photonic sintering	38
2.4.3	Plasma sintering	39
2.4.4	Plasma sintering depths	43
2.5	Stability of sintered TEs based on metal nanoparticle inks	45
2.5.1	Plateau-Rayleigh instability	47
2.5.2	Solid-state de-wetting	49
2.6	Opto-electronic performance of TEs	52
2.6.1	Sheet resistance	52
2.6.2	Transmittance	52
2.6.3	Figure of merit (FOM)	53
2.7	Scope and objectives of this dissertation	54
3	Results	59
3.1	Publication 1 - Bundling of Nanowires Induced by Un- bound Ligand	59
3.2	Publication 2 - Flexible and Transparent Electrodes Im- printed from Metal Nanostructures: Morphology and Opto- Electronic Performance	69
3.3	Publication 3 - Flexible and Transparent Electrodes Im- printed from Au Nanowires: Stability and Ageing	81
3.4	Publication 4 - Consolidation and Performance Gains in Plasma-Sintered Printed Nanoelectrodes	93
4	Discussion	103
4.1	Bundling mechanism of OAm-stabilized AuNWs in cyclo- hexane	104
4.2	Morphology and opto-electronic performance of printed metal grid electrodes	106
4.3	Morphology and stability of metal grid electrodes	109
5	Conclusion and Outlook	117
	Bibliography	127

Supporting Information (SI) to Publications 1-4	173
SI to Publication 1	173
SI to Publication 2	183
SI to Publication 3	193
SI to Publication 4	199

Chapter 1

Introduction

Transparent electrodes (TE) are fundamental components of opto-electronic devices that absorb or emit light while current is generated or a potential difference is applied.^[4,5] Examples of such devices are solar cells, light-emitting diodes, regular displays, and touch screens.

Only few materials offer both a high optical transmittance and a high electrical conductivity. The classic example of a transparent conductor, and at the same time the industrial benchmark, is tin-doped In_2O_3 (ITO). It has a high transmittance in the visible range ($> 80\%$) and a low sheet resistance (R_{sh}) of $< 15 \Omega_{\text{sq}}$ when sputtered thinly onto a glass substrate at elevated temperatures.^[5,6]

In modern consumer electronics, however, the trend goes towards bendable devices^[5,7] such as foldable smartphones, requiring flexible transparent electrodes (FTEs) typically applied to equally flexible and transparent polymer substrates such as low-cost polyethylene terephthalate (PET)^[8], which are usually temperature sensitive^[5,8]. This prevents the use of ITO due to its brittleness^[9,10] and high temperature processing^[11].

An alternative approach to finding a material that is electrically conductive, optically transparent, and flexible, is to look for a material that is conductive in bulk, but not necessarily transparent and flexible, and to arrange it such that the resulting system combines the three desired properties.^[12]

At room temperature, the ductile^[13] and malleable^[14] metals silver (Ag), copper (Cu), and gold (Au) exhibit the highest conductivities (descending in that order)^[15,16]. But they are opaque in bulk.^[17] Properly

structured at the nanoscale, however, the resulting structure can be both transparent and flexible, with sufficiently low sheet resistance.^[4,18] Such structures may be disordered (random) networks or regular grids. Both gain transparency from the areas where no metal is deposited (apertures)^[19] and flexibility from their geometric and material nature.

Compared to random networks, regular grids provide predictable charge transport pathways.^[20] They offer a better reproducibility and can be easily customized as their R_{sh} and optical transmittance are defined by the grid geometry and vary systematically with pattern, pitch, and conductor cross-section.^[21,22]

Various methods have been reported to fabricate metal grids with nanoscale resolution: for instance, electron beam lithography (EBL)^[23] or photolithography with subsequent metal evaporation and lift-off processes^[24], as well as direct metal deposition and patterning via focused ion beam (FIB) lithography^[25]. The lithographic processes are, however, expensive, and both EBL and FIB time-consuming^[26] and incompatible with high throughput roll-to-roll (R2R) processing.

Printing techniques have been reported to improve fabrication speed. But the lines of such grids are several microns wide^[19,27–32], necessitating large pitches to attain reasonable transparency. Such printed FTEs do not allow for ultra-high resolution displays. Other methods require multiple processing steps^[33] and may be limited to a specific grid geometry^[34].

Recently, an efficient two-step-route to grids with arbitrary geometry and line widths w down to below $1\ \mu\text{m}$ was developed, combining direct nanoimprint lithography with self-assembly.^[35–41] In the first step, metallic nanostructures (building blocks) dispersed in an organic solvent (ink) are imprinted with a patterned polymer stamp by putting it into contact with a substrate pre-wetted with the ink. The solvent of the ink, which is being confined in the stamp's cavities, permeates the stamp, causing the nanostructures to concentrate and increasingly self-assemble. This results in percolating lines being deposited onto the substrate, replicating the stamp pattern. The imprinting step can be performed under ambient conditions, e.g. on flexible polymer foils, and is R2R compatible.^[42,43]

Typically, colloidal metal nanostructures are capped with organic lig-

ands, which prevent their agglomeration but insulate them electrically. They have to be removed in a second step, e.g. via plasma sintering, which turns the imprinted grid into a conductive metal electrode while retaining the overall structure and without damaging the polymer substrate (soft plasma sintering).^[35]

Considering its high cost, limited abundance, and it being only the third most conductive element^[18], Au appears less attractive for FTE production when compared to Ag and Cu^[11]. However, the superior chemical inertness^[11], including oxidation resistance in air (even at the nanoscale)^[44–46], and its biocompatibility^[47,48] make up for its deficiencies and render Au nanostructures attractive building blocks for FTE production - in particular with regard to wearable opto-electronics^[49].

Maurer et al.^[42] and Kister et al.^[43] nanoimprinted FTEs with varying grid geometries onto PET foil using ultra-thin Au nanowires^[42] and Au nanospheres^[43] as building blocks with alkylamine (\geq C12) ligand shells and dispersed in cyclohexane. After imprinting, the grids were plasma sintered in a 5 % H₂ in 95 % Ar (H₂/Ar) atmosphere. They reached R_{sh} of 106 to 168 Ω_{sq} and transmittances in the visible range \geq 90 %. The wire-based electrodes were even shown to surpass the mechanical flexibility of commercial FTEs made of tin-doped indium oxide (ITO). Their basic functionality was demonstrated by integrating them into capacitive and resistive touch devices.

Using a simple model which assumes the grid lines as opaque rectangles of line width w such that the uncovered surface fraction corresponds to the optical transmittance, the experimentally determined transmittances could be satisfactorily approximated.^[35] This was not the case for the sheet resistances R_{sh} .^[35,42]

Kirchhoff’s circuit laws were applied to calculate theoretical resistances assuming a perfect grid, based on the resistivity of bulk gold at room temperature ($2.44 \times 10^{-8} \Omega \cdot \text{m}$) and the line geometry (w being in the range of 0.91 to 1.7 μm and maximum line heights h_{max} in the range of 60 to 76 nm). The measured resistances were 13 to 24 times above the calculated values^[42] although both h_{max} and w were well above the electron mean free path length of $\lambda_{\text{Au}}^e = 37.7 \text{ nm}$ ^[50]. This discrepancy suggests that the structure-property relationship between the morpho-

logy of metal conductors formed by nanoimprinting (including plasma sintering) and the electrodes' opto-electronic performance was not yet fully understood.

In this dissertation, I study the opto-electronic performance of such FTEs immediately after plasma sintering and after storage under ambient conditions and correlate it with the conductor morphology. I investigate the effect of geometry and concentration of the imprinted Au nanoparticles colloiddally dispersed in cyclohexane (ink), and of superstructure formation during the imprinting process on the electrode morphology and performance, both after plasma and after ageing during storage.

My results show that the wire inks used for imprinting undergo an unusual type of colloidal instability that does not exist in the sphere-based inks and which has not been observed in any other nanoparticle system so far. While the spheres were still well dispersed at the highest imprinted concentration (30 mg/mL), the majority of the wires was already bundled at the lowest concentration (1 mg/mL) used for imprinting. This dissertation also contributes to the exploration and understanding of this phenomenon.

Chapter 2

State of the Art

2.1 Opto-electronics and transparent electrodes (TEs)

The term opto-electronics refers to the combination of optical and electrical components, and comprises all devices or processes involving electrical-to-optical or optical-to-electrical transducers.^[51–53] A key element in modern opto-electronics such as flat-screen TVs, e-readers, smartphones, liquid-crystal displays, photovoltaics, smart glasses, touch screens, electronic skins, organic light-emitting diodes (OLEDs), and touch sensors are conductive transparent electrodes (TEs).^[4,6,12,18,54,55]

To convert electrical into radiation energy or vice versa, opto-electronic devices or processes make use of the photovoltaic effect:^[56] the photon-induced creation of excitons in active materials such as a Si p-n junction^[57,58] or a copper phthalocyanine/perylene tetracarboxylic derivative interface^[59], which was the first organic active material. It also works in reverse as excitons (electron-hole pairs) recombine. Examples of such opto-electronics are solar cells that convert solar power into electricity^[60], and light-emitting diodes (LEDs) where the recombination of electrons and holes produces photons^[61].

TEs ensure that light, within the spectral range of interest, can leave or reach the active material of these devices. Simultaneously, they serve to inject or extract the required charge carriers.^[5] Common is a sandwich structure:^[62–64] an active material layer between two conductive electrodes, at least one of which must be transparent.

The most important performance metric for solar cells is efficiency,

defined as the ratio of the electrical output power to the incident optical power. This efficiency is directly correlated with the performance of its transparent conductive electrode^[64] which affects the cells' core processes, namely light absorption, and charge extraction. High optical transparency (transmittance) and high electrical conductance are required to maximize the light absorption in the active material layer (to minimize optical losses) and to restrict the potential difference needed to make electricity flow.

According to Hu et al.^[4], competitive LEDs and solar cells require TEs with a transparency $\geq 90\%$ in the visible range and a sheet resistance $R_{\text{sh}} \leq 10 \Omega_{\text{sq}}$. The resistance requirements in other opto-electronic devices vary by several orders of magnitude. For example, 400 to 1000 Ω_{sq} are sufficient for voltage-driven applications^[65] such as touchscreens.^[4]

However, high conductivity and high transmittance are difficult to reconcile within the same material, as they are conflicting properties.^[12,65] Crystalline materials which are either transparent but barely conductive (semiconducting metal oxides) or highly conductive but opaque in bulk (metals), are common.^[17] The introduction (doping) of small amounts of extrinsic atoms (electron donors, n-doping, or electron acceptors, p-doping) into the crystal lattice of such metal oxides allowed to increase their conductivity and essentially retain their transparency. Thin films of such doped metal oxides are transparent conductive electrodes suitable for opto-electronic purposes.^[66]

2.1.1 Transparent conductive metal oxides

In an isolated atom, quantum mechanics only permits discrete electron energy states. In crystalline materials large numbers of energy states are allowed, and quasi-continuous energy bands form.^[67-70] The highest energy band occupied by electrons is the valence band, the next higher energy band, normally unoccupied, is the conduction band. The size of the energy gap between them renders the material a conductor, a semiconductor, or an insulator.^[67-70]

In a metal, valence and conduction bands overlap. Electrons in the conduction band are highly de-localized and lead to the reflection of visible light, which renders metals opaque in bulk.^[67-70]

Transparent crystalline semiconducting metal oxides have band gaps above 3.1 eV and typically below 6 eV.^[15,71] At room temperature, most electrons remain in the occupied valence band. Thus, they cannot appreciably reflect visible light and render the semiconductor barely conductive. Since absorption can only occur for photons with energies at least as high as the band gap (> 3.1 eV), these materials are highly transparent in the visible spectral range (≈ 400 to 800 nm, corresponding to ≈ 3.1 to 1.55 eV).

A way to change conductivity is doping which is limited by the solubility of the dopant in the host.

Indium(III) oxide (In_2O_3) is a semiconducting metal oxide with a band gap of ≈ 3.7 eV.^[6,15] It crystallizes in a cubic bixbyite lattice which can be described as face-centered cubic (fcc) In^{3+} lattice, in which O^{2-} anions occupy three fourths of the tetrahedral sites.^[6] In_2O_3 is susceptible to doping with tin(IV) oxide (SnO_2),^[72] a n-dopant,^[6] because tin has one valence electron more than indium. Sn substitutes some In in the cubic bixbyite lattice ($\text{In}_{2-x}\text{Sn}_x\text{O}_3$: ITO)^[73] without changing the lattice structure. The excess electron does not participate in bond building for the host lattice structure. It remains bound to the dopant atom and features an energy slightly lower than the edge of the conductance band.^[68]

With sufficient doping, the energy states of the dopant sites form a dopant band close to or even overlapping the host conduction band. At room temperature, thermal excitation lifts dopant electrons into the conduction band of the host lattice. These excited electrons render ITO electrically conductive and reflective in the IR range, while the band gap of the host material and thus the high transparency in the visible range remain almost unchanged.^[74-77] Doping of In_2O_3 with SnO_2 achieves charge carrier densities in ITO of up to 10^{20} cm^{-3} , keeping the plasma frequency in the IR. Therefore, ITO does not reflect visible light.^[77]

A typical ITO film of 100 nm thickness, deposited on glass, using sputter-deposition and elevated substrate temperature^[78], has a sheet resistance of 15 to 20 Ω_{sq} ^[17] and a high broadband transmittance within the whole visible wavelength range^[79] with an average visible transparency $> 85\%$ ^[17]. This meets most of the application specific optoelectronic device requirements. The extraordinary combination of optical

and electrical properties renders ITO the most widely used TE in today's industry.^[8,15,78,80] The ability to deposit thin ITO films by different methods like sputtering or chemical vapor deposition^[66,74] with controlled film thickness and controlled doping concentration on transparent glass substrates has additionally contributed to its widespread application.^[6,81]

A variety of transparent conductive n-doped metal oxides which contain less or no indium at all^[6,17], include aluminum doped zinc oxide (AZO) and fluorine doped tin oxide (FTO) as most promising materials.^[6,15] But all of them possess significantly higher resistivities than ITO.^[17] This is even more true for p-doped metal oxides due to the restricted hole mobility in the valence band of the host material.^[66,68,82]

A major common drawback of all metal oxide-based TEs is their brittleness^[83] and processing at high temperatures^[6,74]. Amorphous ITO, deposited near room temperature, exhibits a significantly reduced conductivity compared to crystalline ITO of the same thickness.^[84] This limits the compatibility with low cost, temperature sensitive transparent polymer substrates (e.g. PET) and their compatibility with the next-generation opto-electronic wearables based on organic semiconductor active material layers on flexible substrates.^[62] Such products require TEs that are mechanically flexible (FTEs), lightweight, cheap, and compatible with efficient large scale manufacturing methods (roll-to-roll processing) on temperature sensitive polymer substrates.^[17,81]

2.1.2 Metal-based flexible transparent electrodes (FTEs)

A resistivity of $10^{-4} \Omega \cdot \text{cm}$ is often quoted for optimized films of brittle ITO.^[15,85-87] The ductile,^[13] malleable,^[14] and most conductive metals silver (Ag: $1.6 \mu\Omega \cdot \text{cm}$), copper (Cu: $1.7 \mu\Omega \cdot \text{cm}$), and gold (Au: $2.4 \mu\Omega \cdot \text{cm}$), exhibit bulk resistivities in the range of 1.6 to $2.4 \mu\Omega \cdot \text{cm}$.^[15,16] This is roughly two orders of magnitude below that of ITO.

According to the Lambert-Beer law, the transmittance of a material layer, excluding any surface or interface effects, increases with decreasing layer thickness.^[62] The layer's sheet resistance R_{sh} increases concurrently.^[62] Thus one may apply these metals sufficiently thin to become transparent while still maintaining practicable R_{sh} .^[17] This could make such layers suitable transparent, conductive, and flexible electrodes for

next-generation opto-electronics.

Sheet resistances and transmittances of ultra-thin Au films were measured by Wilken et al.^[88] Au films with a thickness > 20 nm had a R_{sh} of $< 5 \Omega_{sq}$. R_{sh} increased to $> 50 \Omega_{sq}$ ($> 100 \Omega_{sq}$) for Au films with thicknesses < 10 nm (< 5 nm). For a 7 nm thick Au film, the maximum transmittance was about 70 % at a wavelength of $\lambda = 500$ nm, which decreased to < 60 % for a 12 nm thick film. The transmittance exhibited a wavelength dependence. For the 7 nm thick film it was only 50 % at $\lambda = 700$ nm. Lemasters et al.^[89] report similar results.

Xiong et al.^[90] prepared and measured ultra-thin Cu films. The films exhibited a wavelength dependent transmittance. R_{sh} increased significantly with decreasing layer thickness. For the 10 nm film the measured values were $10.2 \Omega_{sq}$ and transmittances of $T_{400} \approx 70$ %, $T_{600} \approx 84$ %, and $T_{800} \approx 75$ %. The 4 nm film exhibited a $R_{sh} > 10\,000 \Omega_{sq}$.

Zhang et al.^[91] produced ultra-thin Al doped Ag films. The 11 nm thick film had a $R_{sh} \approx 15 \Omega_{sq}$ and transmittances $T_{400} \approx 85$ %, $T_{600} \approx 65$ %, and $T_{800} \approx 50$ %. At 6 nm thickness the sheet resistance was $\approx 70 \Omega_{sq}$ and transmittances increased to $T_{400} \approx 87$ %, $T_{600} \approx 78$ %, and $T_{800} \approx 70$ %.

According to Hecht et al.^[92], metal films must be thinner than 10 nm (“ultra-thin”) to be useful as “transparent” electrodes. Films of Ag, Al, and Au, prepared with thicknesses of 10 nm and above, had sheet resistances equal to or better than ITO.^[93] Below 10 nm the metal resistivities increased steeply with decreasing thickness.^[93] In case of nickel films the resistivity increase was two orders of magnitude as the film thickness decreased from 10 nm down to 2 nm.^[92] Sondheimer^[94] reports that surface electron scattering increases resistivities of metal films significantly when their thickness becomes appreciably smaller than the mean free path of electrons: at room temperature ≈ 53 nm (Ag), 39 nm (Cu), and 38 nm (Au)^[16,50]. Grain boundary scattering,^[16] the surface morphology,^[16] and the substrate roughness^[92] further contribute to scattering of electrons and decrease the conductivity.

Metal film build-up with physical vapor deposition is often done by sputtering and thermal evaporation; pulsed laser ablation is gaining importance.^[17] According to Lemasters et al.^[89] and Zhang et al.^[91], the

deposition of continuous ultra-thin Au and Ag films is a challenge. Isolated metal island formation during film growth is common. With increasing thickness, they eventually connect to a conductive film. The critical thickness leading to conductance is defined as percolation threshold, e.g. 10 to 20 nm for Ag.^[91] The deposition of a thin and wetting auxiliary material layer before the metal deposition reduced the percolation threshold, but increased optical losses.^[91]

The transmittance in the visible range of metal (e.g., Ag, Cu, and Au) films with thicknesses ≥ 10 nm remains limiting for high performance devices.^[62] This limitation is largely due to reflection.^[16] For films with thicknesses < 10 nm, the limiting feature becomes R_{sh} . Thin silver films have the best trade-off between optical transmittance and R_{sh} .^[84,91,93] The US Company CP Films (Virginia) sells silver film products having R_{sh} between 4.5 to $8\Omega_{sq}$ with an average visible transmittance of about 75 %.^[92]

Randomly or periodically distributed holes are a promising strategy.^[12,62,79,92] A hole is 100 % transparent across the entire optical spectrum. Metal micro meshes have been achieved by properly arranging metal nanowires into random network layers.^[4,62,92]

2.1.3 Random metal nanowire networks

Suitable dispersants (capping agents) allow metal nanowires to be dispersed in water or alcohols. Percolating random nanowire networks can then be obtained by depositing such inks on a substrate and drying. Many liquid-based processing techniques such as slot-die coating, drop casting, spin coating, inkjet printing, bar coating, spray coating, Mayer rod coating, brush painting, doctor blade coating, dip-coating, screen printing or vacuum filtration have been used to fabricate films of randomly distributed and intersecting nanowires, also designated as random metal nanowire network layers.^[47,62,95,96] The majority of these processes are compatible with R2R^[47,96] and temperature sensitive polymer substrates.

Charge transport within random metal nanowire networks occurs along the wires.^[4] The electric performance of such a network thus depends on the wire dimensions and the metal, and on the wire morphology. Mono-

crystalline metal nanowires^[4,12,97], so without grain boundaries^[98], increase electrical conductivity^[99]. In general, the network conductance increases with the length L and the diameter D of its nanowires.^[62,100] A low D reduces the fraction of scattered photons^[62] and the roughness of the network films^[101]. For most opto-electronic applications, the roughness should be low to avoid shorts between top and bottom electrode,^[62] especially when thin active material layers are involved^[95].

Network conduction requires uninterrupted (continuous) conduction paths between the measuring electrodes, i.e., a network above the percolation threshold. To provide many percolating pathways, the network has to be dense enough. The network density N is defined as the number of nanowires per unit area and can be controlled by the wire concentration of the ink used for depositing the network. Increasing N improves percolation and conductance, whereas the optical transmittance of the network decreases with the areas in-between the wires. The critical network density N_c is defined as the density N at which the occurrence probability for the percolation of one-dimensional sticks amounts to 50%.^[4,95] As N_c is inversely proportional to the square of the wire length L ,^[4,95,101] N_c decreases substantially with increasing L , which increases optical transmittance. If L is doubled, the new critical network density is less than the former $N_c/2$.

The electrical resistance of nanowire networks is often high due to poor contacts between the dispersant-capped wires. Various methods have been developed to join or weld the wires at the junctions. Most of these methods involve the use of heat and/or light. Examples are annealing, electrochemical annealing, laser sintering, mechanical pressing or plasmonic nano-welding.^[4,95,102] Activated surface diffusion processes lead to local sintering at the high curvature junctions between intersecting wires. The junction resistance is key for the conductance (sheet resistance) of a well-percolating network as the intrinsic metal conductivity is usually high.^[95,102] An increasing wire length L minimizes the number of wire-to-wire junctions^[103] while the transmittance remains similar.^[100]

Wires with high aspect ratios (length/diameter = $L/D = AR$) and D above 50% of the mean free path of the electrons in bulk metal are considered advantageous^[95,103] and improve the mechanical stability of

random network films.^[6,104] The availability of synthesis protocols for defined metal nanowires is therefore a prerequisite for producing transparent electrodes made of random metal nanowire networks that exhibit the desired trade-off between sheet resistance and transmittance.^[95,103] Protocols for Ag and Cu are available,^[6,47,96,101,105,106] even for wires with monocrystalline structure^[97]. The length of the nanowires produced is in the range of 1 to 50 μm ,^[62] typical diameters range from 20 to 150 nm^[95]. Longer wires tend to break during the dispersion and deposition process.^[62]

Ag nanowires are commonly synthesized through the reduction of silver nitrate in the presence of poly(vinyl)pyrrolidone (PVP) as polymeric capping agent and hot ethylene glycol as reducing agent (the polyol process),^[4,101,107] or a salt mediated variant thereof.^[96] The dimensions of the resulting wires can be kinetically controlled by temperature, seeding conditions, and the ratio between PVP and AgNO_3 .^[96] Cu nanowires can generally be obtained in solution by reducing copper ions in the presence of an aliphatic amine as capping agent.^[47,101] The slow reduction of Cu ions (e.g., by hydrazine or glucose), together with appropriate capping ligands such as ethylenediamine or hexadecylamine, forms metal seeds which grow into nanowires.^[101,108]

Consequently, reports on flexible transparent random Ag/Cu nanowire network electrodes with a similar opto-electronic performance to ITO, but a superior mechanical stability, are common. De et al.^[54] used aqueous dispersions of silver nanowires of a length and diameter close to 6.5 μm and 85 nm to prepare thin, random network FTEs. The nanowire films exhibited no change in R_{sh} over > 1000 bending cycles. The best films on PET substrate had an optical transmittance of 85 % and a sheet resistance of $13 \Omega_{\text{sq}}$, at a film thickness of 107 nm. Lee et al.^[104] enhanced the conductance of Ag nanowire electrodes by using extra-long Ag nanowires (diameter of 100 to 150 nm) of up to 500 μm length. Wires were produced in a former stage and used as seed in a subsequent stage. They demonstrated that the opto-electronic properties of such Ag wire electrodes ($R_{\text{sh}} = 9 \Omega_{\text{sq}}$ at 90 % transmittance) were maintained despite stretching them up to 250 % elongation. Seo et al.^[109] give a review on the improved mechanical stability of silver nanowire networks compared

to ITO films. Celle et al.^[110] produced copper nanowire-based (length $\approx 33\ \mu\text{m}$ and diameter $\approx 15\ \text{nm}$) transparent electrodes on poly(ethylene 2,6-naphthalate) substrate (PEN) with $R_{\text{sh}} = 33\ \Omega_{\text{sq}}$ and a transmittance of 88%. Mayousse et al.^[111] produced Cu nanowire-based FTEs on PEN with $R_{\text{sh}} = 55\ \Omega_{\text{sq}}$ and a transmittance of 94%. The wires had diameters in the range of 50 to 400 nm and lengths up to hundreds of microns. The FTEs were used to produce transparent flexible touch sensors. Scardaci^[102] reports that the resistances of Cu nanowire networks hardly change during bending.

The fabrication of high opto-electronic performance random Au nanowire network FTEs from synthesized wires has challenges: synthesis protocols for Au nanowires with a high aspect ratio and diameters $\geq 20\ \text{nm}$ are scarce and usually result in polycrystalline^[13] wires. A synthesis procedure that allows a systematic variation of L/D does not appear available for Au nanowires.^[18,47,103]

One of the few reports on TEs based on Au nanowire networks is given by Morag et al.^[112]. A mixture of chloroauric acid and potassium thiocyanate was incubated for 24 h in a solution of water and dimethyl sulfoxide. Upon gradual evaporation of the solvent, films of Au nanowire networks were obtained. To enhance the electrical conductivity, they were plasma sintered. The wire diameter was around 300 nm and the lengths amounted up to hundreds of μm . The optical transmittance (glass substrate) was 75 to 80%, R_{sh} was $70\ \Omega_{\text{sq}}$. Another report on Au electrodes based on random nanowire networks is given by Takane et al.^[113]. The Au nanowires were synthesized by water-phase reduction of HAuCl_4 with ascorbic acid,^[114] yielding wire lengths of $\approx 17\ \mu\text{m}$ and diameters of $\approx 57\ \text{nm}$. After synthesis, the Au nanowire dispersion was vacuum filtered using a membrane filter. Subsequently, the formed network was transferred to a perylene substrate by pressing the filter to the substrate. The electrode was then used to produce a flexible organic thin film transistor. The electrode is described as mechanically flexible and stretchable, with an excellent conductance.

Protocols for the synthesis of single-crystalline ultra-thin gold nanowires with aspect ratios >1000 and diameters below 2 nm are readily available.^[115] However, the small diameters not only render the wires prone

to the Rayleigh-Plateau instability^[116], but also limit their conductivity as the diameters are well below the mean free path of electrons (≈ 38 nm at room temperature for Au^[16]). For instance, at room temperature the electrical resistivity of a monocrystalline silver nanowire with a 30 nm diameter is already 25 % higher than with a diameter of 100 nm^[117] (mean free path length of Ag at room temperature ≈ 53 nm^[16]). Moreover, these ultra-thin gold nanowires tend to bundle in organic solvents.^[35,118] Xie et al.^[119] attributed the outstanding performance of their silver nanowire networks to them being agglomeration free.

Ag and Cu FTEs based on random nanowire networks have the advantage of low R_{sh} and high optical transmittance combined with good mechanical stability as well as roll-to-roll compatibility, but involve random network specific disadvantages. The random deposition of the metal nanowires allows only for limited control of the network geometry and the resulting properties. The average network density N can be tuned, but not the deposition/position of individual wires. Fine-tuning the optoelectronic film properties for a particular application is therefore as challenging^[21] as the reproducibility^[47].

Wires are deposited where they do not contribute to performance. There are insulated wires or dangling wire parts that reduce transmittance, but do not actively participate in current transport.^[120] The irregular wire deposition also causes an inhomogeneous texture of the network film.^[20] An inhomogeneous layer can lead to thermal hot spots in a transparent heater.^[95]

The size and spacing of the nanowires in the network led to wide angle light scattering causing haze,^[92,95,121,122] which is undesirable in many display applications.^[17,101] Haze increased with the network density N and decreased with the wire diameter.^[21]

Nanowire network surfaces have a roughness of at least two times the nanowire diameter^[101], while ITO films present a smooth and continuous surface that makes them compatible with thin layers of active material. Such roughness is easily on the order of the thickness of the active material layers used for OLEDs or solar cells (typically ≈ 100 to 200 nm^[123]), often causing short-circuiting^[96,124] between top and bottom electrode.^[125] The high aspect ratio nanowires in the network are

sensitive with regard to thermal failure due to the Plateau-Rayleigh instability^[126,127], e.g., by Joule heating or elevated ambient temperature as well as electromigration-induced failure^[62,92] due to momentum transfer between electrons and the nuclei of the metal atoms caused by high density current flow through the narrow wire junctions^[17,126,128].

The disadvantages of Ag-, Cu-, and Au-based random metal nanowire network electrodes outlined above may be overcome by fabricating ordered (regular) metal grids instead. Their regular and easily adjustable apertures allow for an improved transmission of light.^[101] Since width and thickness of metallic grid lines may be larger than the diameter of individual wires (line widths below 10 μm are invisible, as they are beyond the human eye's resolution limit^[22,27]), electron scattering loses importance, so that resistivities may be closer to bulk values.^[4] Unlike random nanowire networks, regular grids do not suffer from contact resistance at wire-to-wire junctions or from high haze.^[21] One of the remaining challenges is to avoid costly and time-consuming fabrication processes which are not roll-to-roll compatible.^[21] Another persistent challenge is the susceptibility to corrosion of nanostructures of the metals silver and, in particular, copper^[17,91], as explained in the example of random nanowire networks in the next section.

2.1.4 Metal corrosion

The chemical stability of Ag- and Cu-based random nanowire networks remains a key challenge.^[17,47,65,92,95,101,102,110,126,129–132] Random nanowire networks are even more susceptible to this problem than the corresponding bulk material^[133–136] as the methods applied for network production preserve the individual high aspect ratio nanowires. These have an increased fraction of surface atoms^[137] whose “dangling” unsaturated chemical bonds^[131] give them a higher reactivity (chemical instability) compared to atoms in the bulk to reduce the surface energy.^[38,138]

Cu nanowires are susceptible to chemical degradation due to formation of less conductive oxides through reaction with atmospheric oxygen during storage or with dissolved oxygen during synthesis.^[102,110,126,131] Sunlight exposure, and especially humidity, accelerate such degradation. According to Celle et al.^[110], the decay in electrical performance of Cu-

based random nanowire network electrodes through the combination of atmospheric oxygen and humidity is so fast, even at room temperature, that it prevents any industrial use of such electrodes.

As a noble metal, Ag typically corrodes less quickly in ambient atmosphere than Cu^[101]. It has a lower affinity for oxygen than Cu.^[135,136] Therefore, the corrosion product during long term storage under ambient conditions is usually not an oxide, but the sulfide^[135] which is less conductive than Ag^[101]. It is formed through reaction with trace amounts of hydrogen sulfide (H₂S) and/or carbonyl sulfide (OCS: the most abundant sulfur species in the atmosphere^[139]) which are ubiquitous in the atmosphere^[92,140]. The presence of water, O₂, NO₂^[126,136,139] or intense light^[126,130,136] can accelerate corrosion. Another route for chemical degradation of Ag nanowires is oxidation promoted by acidic conditions.^[126,141] The outdoor corrosion products are generally more complex than their indoor counterparts and may, in addition to Ag₂S, also include oxides, chloride, carbonate, and sulfate.^[132,135] Corrosion degrades the junctions between wires,^[17] which increases R_{sh} appreciably over time,^[17,47,92] even when the Ag-wires are coated with a protective layer^[136].

Au does not suffer from chemical instability,^[11,103,129] even when miniaturized to nanowires^[47,113]. It is biocompatible^[47,113,142] and can be used in wearable skin-like devices or implantable biomedical electronics^[12,47]. As a material involving a high work function,^[143] the minimum thermodynamic work or energy needed to remove an electron from a solid to a point in the vacuum immediately outside the solid surface (Au: 5.22 eV, Cu: 4.65 eV, and Ag: 4.0 eV)^[144,145], Au is particularly well suited for flexible transparent anodes in OLEDs.^[143] According to Keast^[132], Au remains the material of choice despite being more expensive than Ag and Cu. This also applies to FTEs based on regular metal grids.

2.1.5 Regular metal grids

Compared to random metal nanowire networks, metal grids with regular unit cells and periods provide uniform charge transport pathways.^[20] Material is only placed where it is needed. The main parameters affecting the grid properties are the height or thickness and the width of the metal-

lic grid lines (i.e. the line cross-section), the pitch (a measure^[146] for the spacing between the lines), and the geometry of the unit cell (the grid pattern).^[22,146] This geometry can consist of, for example, two straight parallel lines, a regular triangle, a square, or a regular hexagon.^[22,42,146] Usually, the unit cells of metal grids are small compared to the dimensions of the grid and the line width is much smaller than the pitch.^[22,42,146] The grid's optical transmittance was found to be proportional to the percentage of the grid area not covered by grid lines which reflect the light.^[16,92] The sheet resistance of metal grids scales systematically with the grid geometry (Kirchhoff's circuit laws applied):^[147] R_{sh} is a function of line width and pitch. Increasing the line width and/or decreasing the pitch decreases the transmittance and R_{sh} . Broader and/or more lines per unit area provided more conductive material for the electron transport.

The opto-electronic trade-off for ordered grids can be partially resolved via the line height,^[143] which, if increased, lowers the resistance while keeping the transmittance largely unaffected.^[148,149] Kang et al. demonstrated that the deposition of a thicker Au grid reduced R_{sh} by a factor of three, the optical transmittance, however, by only 7%.^[22,144] The height increase did not change the opening ratio of the grid. Kang et al.^[144] also showed that the optical transmittance of Ag grids is lower than that of geometrically identical Au and Cu grids due to the optical dispersion properties of Ag. Lee et al.^[22] give an overview on the opto-electronic properties of transparent Ag/Cu grid electrodes differing in geometry and fabrication method. The parameters range from $R_{\text{sh}} = 0.3$ to $60 \Omega_{\text{sq}}$, optical transmittance $T_{550} = 71$ to > 90 %, line width = 120 nm to 132 μm , pitch = 50 to 3000 μm , and height = 40 nm to 10 μm . A disadvantage of an increased line height is a higher surface roughness.^[92] For applications that require smooth FTEs, thin conductive polymer layers such as PEDOT:PSS can be applied as overcoating.^[22,92] Alternatively, the electrodes can be embedded into a plastic substrate.^[125] This also helps to overcome fabrication problems resulting from the height increase.^[23,92] In one single case of the overview given by Lee et al.^[22], the line width was $< 1 \mu\text{m}$. Indirect metal nanoimprint lithography was used for the fabrication.^[22,143]

Next generation opto-electronic applications such as displays for vir-

tual and augmented reality use densely packed and very small (O)LEDs.^[150] To operate such LEDs, one pre-condition are transparent, squared grid electrodes having a line width equal to or smaller than the size of the LED pixel ($< 1 \mu\text{m}$)^[151] to achieve a maximum optical transmittance. A more narrow (sub- μm) width enables a smaller pitch without deteriorating optical transmittance and conductance. This ensures uniform charge injection into the active material layer of an OLED.^[143] Sub-wavelength line widths minimize light scattering.^[92]

Narrow grid lines with a small pitch are also advantageous in solar cells.^[92] In case of a too large pitch, excitons generated in the active material layer of a solar cell will not be efficiently collected from the active material which is located within the grid voids. If the diffusion pathways to the closest grid line are too long, exciton recombination losses are favored.

Therefore, there is a strong interest in efficient and economic fabrication processes for transparent metal grid electrodes with sub- μm , nano-scale line widths.^[150] Various methods have been reported for fabricating such metal grids. Metallic nanogrids can be patterned by electron beam lithography (EBL)^[23] or optical lithography with subsequent metal evaporation and lift-off processes^[24]. Direct metal deposition and patterning with focused ion beam (FIB) lithography is another approach.^[25] All these methods can lead to high resolution grids (sub- μm line width) with low R_{sh} . The lithographic processes are, however, expensive and, in the case of EBL and FIB, also particularly time-consuming.^[26]

Higher throughput printing techniques have been reported, such as electrohydrodynamic jet printing^[27], a combination of an inkjet-printed dot array as sacrificial layer and a thermal metal evaporation lift-off process^[19], a combination of electric-field-driven microscale 3D printing and hybrid hot embossing^[28], a combination of ultra-fast laser direct writing and physical metal deposition^[29], a combination of lithography and electroplating without high temperature^[30], template-less inkjet printing^[31], and screen printing of ultra-long silver wires^[32] to improve fabrication speed. The metal lines of such printed grids were several microns wide. Other methods require at least three consecutive processing steps^[33] and may be limited to a specific grid geometry^[34]. Sub- μm metal line widths

have not been achieved yet in a simple, R2R compatible process. A method to produce material structures from the micro- to the nanometer scale with high throughput is direct nanoimprint lithography.

2.2 Fabrication of nanoscale structures by direct nanoimprint lithography (NIL)

Direct nanoimprint lithography (NIL) is a method to create micro- and/or nanometer scale structures (patterns) in a material by physical deformation. This is achieved by replicating the negative surface pattern (relief features) of a prefabricated template (the stamp or mold) in the material surface. The material is deposited on a substrate (e.g., by spin coating) as a thin, soft, and deformable layer: the resist. Examples are a thermoplast above its glass-transition temperature, a melt, or a liquid of monomers. The resist is shaped by mechanical deformation through contact with the nanostructures (e.g., trenches and/or ridges in the desired dimension^[39]) on the surface of the harder mold and three-dimensional material displacement. The mold is pressed into the resist with an adequate pressure and the viscous resist flows into the cavities of the mold. The shaping is followed by the solidification (hardening) of the deformed resist. This can be caused by simple cooling (thermal NIL or hot embossing lithography) or photoinitiated polymerization (UV-NIL; a transparent mold enables UV exposure of the deformed resist). The mold is then removed from the hardened resist, revealing a positive of the mold pattern on it.^[152–157]

Often, an anisotropic etching process follows to remove any residual resist in areas where it was not fully displaced as desired during imprinting, e.g. by reactive ion etching. The hardened resist may already be the desired functional material itself or can act as an etching mask or lift-off layer for transferring the imprinted pattern into the substrate underneath or into another material.^[152–157]

NIL is a direct structure transfer. The mold is therefore required to exhibit the features to be transferred 1:1. As NIL relies on direct mechanical deformation, the ultimate resolution of a structure produced by NIL is limited by the minimum template feature size that can be fabric-

ated. Another major influence is the capability of the resist to fill the cavities of the template.^[155,158–160] All features, including defects and surface roughness, are replicated with high precision. The manufacturing of the template is usually expensive, as sophisticated fabrication techniques such as deep-UV photolithography, electron-beam lithography, and reactive ion etching are used.^[155–158]

A major advantage of NIL is the simplicity of the printing process. It requires no expensive optics, ultra-high vacuum, electron beams or excimer lasers. The template can be adapted for R2R manufacturing, thus reducing the cost of fabrication, and increasing throughput.^[161–163] Mass replication by NIL alleviates the initial capital investment for the template considerably.

Various substrates, including silicon wafers, glass plates, flexible polymer foils, and even non-planar substrates, can be used for NIL.^[164] The mold materials are classified according to their Young's modulus (E).^[165] Elastomeric molds made of materials with $E < 2$ MPa such as polydimethylsiloxane (PDMS), are referred to as soft molds. Molds made of materials like silicon, quartz, silicon nitride, or nickel with $E > \text{few GPa}$ are so called rigid molds. In general, a rigid mold ensures a better resolution. Flexible molds, on the other hand, ensure conformal contact with the substrate and are compatible with plastic substrates which may be damaged by rigid molds.

NIL allows for structures from the micron to the nanometer scale with high fidelity and throughput, at low cost, and with good reproducibility.^[166] Unfortunately, NIL is not compatible with the fabrication of metal grid-based FTEs with nanoscale line widths from metal melts. This is due to the high melting temperatures of Ag (1235 K), Au (1338 K), and Cu (1358 K),^[167] and the low thermal stability (low melting point and low glass-transition temperature T_g) of mechanically flexible, light weight, and low cost polymer substrates typically used in FTE production^[80]. T_g of PET, depending on the foil thickness f_{th} , is in the range of ≈ 45 °C at $f_{\text{th}} \approx 20$ nm to ≈ 74.5 °C at $f_{\text{th}} > 160$ nm.^[168]

Alternatively, metal nanoimprinting was carried out indirectly using a structured polymer (produced by NIL) as a mask for metal etching or metal lift-off.^[157] Kang and Guo^[143] used this approach for indirect

nanoimprinting of Cu- and Au-based transparent metal grid electrodes on glass substrates. They transferred parallel channels with rectangular cross section to a thermoplastic polymer resist on a substrate. Standard residual resist etching followed. Metal vapor deposition metallized the hardened thermoplast. The lift-off of the thermoplast from the substrate by dissolving it with an organic solvent ended the process. With a line width of 120 nm, a period of 700 nm, and a line thickness of 40 nm, the average optical transmittance (400 to 800 nm) was in both cases $\approx 76\%$, with a R_{sh} of $\approx 11.7 \Omega_{\text{sq}}$ (Au) and $\approx 14.9 \Omega_{\text{sq}}$ (Cu).^[143] The main disadvantages of indirect metal nanoimprinting are the multiple and expensive process steps, chemical demands on the polymer substrate, and temperatures and pressures exceeding the substrate capabilities.^[36,38]

2.2.1 Thermal NIL of Au nanoparticle inks

The door to the fabrication of flexible regular metal grid electrodes with ultra-high resolution through direct nanoimprinting was opened by Ko et al.^[38] They used thermal NIL for the fabrication of nanoscale electronics from an 80 °C warm Au nanoparticle ink containing α -terpineol (b.p. ≈ 218 °C^[169]) as the solvent and Au nanospheres with a diameter in the range of 1 to 3 nm and a self-assembled monolayer of hexanethiol (b.p. ≈ 153 to 154 °C^[170]) of 10 wt% Au content. An imprinting stamp made of polydimethylsiloxane^[171,172] was used as template. PDMS^[172] was chosen for its high permeability to organic solvents^[39,173,174] and their vapors^[173,175]. It also has a low surface energy and is suitable for reusable molds since other materials adhere only weakly to its surface. This enables easy material transfer to temperature- and pressure-sensitive polymer substrates.^[92] A PDMS mold's excellent conformal contact with the substrate reduces the amount of residual resist.^[38,176]

The substrate was a rigid and highly doped p-type silicon wafer with 100 nm thick SiO₂ layer. The imprinting pressure was only 5 psi (≈ 34.5 kPa). The hardening of the patterned feature was caused by evaporation/permeation of the α -terpineol through the mold during imprinting at elevated temperature, and cooling to room temperature afterwards. This prevented the imprinted structure from collapsing during the demolding step. The imprinted micro-/nanostructures were sintered for

two hours^[177] at 140 °C^[38,177] to render them conductive because metal nanoparticles show a pronounced melting temperature depression^[138,178]. Compared to the melting point of bulk Au (1063 °C),^[178] 2 to 3 nm sized Au nanospheres start already to melt at around 130 to 140 °C.^[36,38] Ko et al.^[38] fabricated a variety of micro-/nanoscale structures. The practical usefulness of high-resolution electrodes thus produced was demonstrated by using them for the fabrication of organic field effect transistors.

Park et al.^[177] report similar results for direct imprinting of a separate resist. The 3 to 7 nm diameter Ag spheres were coated with dodecylamine and dispersed in a mixture of α -terpineol and toluol. The sintering temperature was 180 °C. Park et al.^[36] repeated the NIL experiments of Ko et al.^[38], but used flexible polyimide substrates, shortened the sintering time to 10 min, and the Au particle diameter was 2 to 3 nm. They determined the resistivity ρ as an average of 53 single line conductors (width: 4 to 8 μm , length: 200 μm , height: \approx 300 nm) through $\rho = (R \cdot A)/L$, with R the resistance (measured with a micro needle probe station^[38]), A the cross-sectional area (from AFM scanning data^[38]), and L the length (AFM topography images^[38]). Despite all geometrical features being well above the mean free path of electrons (at room temperature \approx 38 nm for Au^[16]), the result $1.99 \times 10^{-7} \Omega \cdot \text{cm}$ was about 8 times higher than that of bulk Au ($2.4 \times 10^{-8} \Omega \cdot \text{cm}$ ^[36]), but still sufficiently conductive for high-performance electronics.^[36] Analysis with SEM-EDX and XPS revealed^[36] that after thermal annealing significant amounts of carbon and sulfur from hexanethiol remained in the film, which were suspected of acting as an insulating dielectric layer between Au particles.

In summary, Ko et al.^[38] and Park et al.^[36,177] have demonstrated that direct nanoimprinting of metal (e.g., Au) nanoparticle inks to metal grids has the potential for the fabrication of high performance, low cost, and large area flexible electronics: it enables low-temperature, low-pressure as well as high-resolution metal patterning on flexible substrates.

2.2.2 Direct nanoimprinting of inks of self-assembling Au nanoparticles

Kister et al.^[43] refined the approach of Park et al.^[36] and produced metal grid FTEs by direct nanoimprinting of inks of self-assembling

2.2. FABRICATION OF NANOSCALE STRUCTURES BY DIRECT NANOIMPRINT LITHOGRAPHY (NIL)

metal nanoparticles. The Au nanospheres used had a mean diameter of $3.2 \text{ nm} \pm 8.7\%$ and were thus of comparable size to those used by Park et al.^[36]. Particles $< 2 \text{ nm}$ would require an increased amount of ligand for stabilization,^[38] and particles $> 4 \text{ nm}$ likely cause cracks and pores during sintering.^[39] Furthermore, the melting temperature depression^[138,178] decreases with increasing diameter. The low-boiling (b.p.= 351.65 K ^[179]) and low-viscosity ($1029.7 \mu\text{Pa} \cdot \text{s}$ at 0.1 MPa and 290 K ^[180]) solvent cyclohexane enabled the imprinting at room temperature and the use of flexible PET substrate.^[43] PET foils are low-cost^[8] substrates with high transparency, good mechanical strength, flexibility, and resistance to many chemicals.^[181] The glass-transition temperature is below $75 \text{ }^\circ\text{C}$.^[168] PET is well renew- and recyclable.^[182,183]

The application of an alkylamine instead of an alkylthiol allowed Kister et al.^[43] for sintering at room temperature in form of a soft (gentle) low-pressure plasma (5 % hydrogen in 95 % argon: H_2/Ar) instead of thermal sintering, which is quite demanding in terms of temperature.^[36,43] The amine-Au bond is considerably weaker than the corresponding thiol-Au bond. This likely reduced the ligand shell density and facilitated the ligand removal. Sulfur atoms might remain bonded in the case of thiols even if (part of) the alkyl chain has been removed by a plasma.^[43] In contrast, O_2 -plasma had led to high resistances, probably due to oxidation of the thin lines.^[43]

Continuous (percolating) grid lines formed only when particle agglomeration was suppressed until the very end of solvent absorption during imprinting. Dodecylamine, with its not too short alkyl chain, provided sufficient stability and allowed for ligand removal without destroying the imprinted submicron lines, creating grids that were considered to be fully metallic. The Au concentration of the imprinted inks was only 0.64 %, ^[43] limiting premature particle agglomeration during imprinting,^[43] and enabling the imprinting of larger areas than in Park et al.^[36].

To demonstrate the R2R compatibility of the method, Kister et al.^[43] used a semi-continuous setup also used in this dissertation. The applied imprinting stamps ($3.5 \times 7 \text{ cm}^2$) were made of PDMS (Sylgard™ 184 from Dow Corning^[171] as in Park et al.^[36]). A stamp carried an array of square-shaped pillars with a pitch of $19.5 \mu\text{m}$, a pillar spacing of $1.8 \mu\text{m}$,

and a pillar height of 4 μm . For imprinting, a stamp was attached to a steel roller mounted on a film applicator as carrier. The linear movement of the carrier was translated into a rolling motion of the roller across the substrate onto which the ink had been dispensed. The roller speed balanced imprinting and solvent absorption by the stamp to ensure the integrity of the grid which formed via self-assembly of the ligand coated nanospheres prior to the stamp losing contact. The obtained electrodes with squared Au grids had line widths $< 1 \mu\text{m}$, transmittances (at 500 nm wavelength) $> 90 \%$, and $R_{\text{sh}} = 150 \Omega_{\text{sq}}$.^[43] The latter value is sufficient for applications such as touch sensors.^[4,43]

High aspect ratio wires percolate easier than spheres (see section 2.1.3 herein). Maurer et al.^[35,42] used colloiddally dissolved ultra-thin Au nanowires capped with an oleylamine (OAm) ligand shell^[184] as an ink. These wires had diameters of $\approx 1.6 \text{ nm}$ and aspect ratios “length/diameter” above 1000. Solvent, stamp material, basic imprinting technique, flexible substrate material, and sintering were as in Kister et al.^[43]. The imprinted patterns were of square, hexagonal, or line-like geometry. An increase in ink concentration increased width and height of the imprinted grid lines. The result for $c_{\text{Au}} = 4 \text{ mg/mL}$ at varying stamp pattern were FTEs^[42] with line widths of 0.91 to 1.7 μm , line heights of 60 to 76 nm, R_{sh} of 106 to 196 Ω_{sq} , and transmittances $> 92 \%$ over the entire visible range. Electrodes^[35] printed at $c_{\text{Au}} = 8 \text{ mg/mL}$ (4 mg/mL) had 600 nm (250 nm) width, 45 nm (15 nm) height, 29 Ω_{sq} (227 Ω_{sq}) sheet resistance, and 68 % (92 %) transmittance at 500 nm wavelength. The electrodes’ mechanical stability (determined via R_{sh} during cyclical bending) was significantly better than for a commercial ITO-coated PET foil. Building capacitive and resistive transparent touch sensors proved the electrodes’ applicability.

The experimental transmittances agreed well with the free surface fractions of the FTEs.^[35] The measured resistances differed from the values calculated for a perfect Au grid with experimentally determined FTE grid dimensions and the resistivity of bulk Au. They were about one order of magnitude larger^[35,42] and explained by imperfections in the Au lines.^[35,42] Similar discrepancies have been reported for square patterned Ag grids of similar feature size, fabricated by e-beam lithography using

vapour deposition and explained by defects, too.^[147]

In summary, the potential of the optical properties of nanoimprinted flexible metal grid electrodes appears fully realized, but electrical properties are lacking. Gaining a better understanding thereof, is an objective of this dissertation. The efficient synthesis of suitable metal nanoparticle inks is a condition sine qua non.

2.3 Synthesis and self-assembly of Au nanoparticles with alkylamine ligand shell

The term self-assembly covers any spontaneous and autonomous organization of small material sub-units (building blocks) which can move with respect to one another to form larger ordered material units without the formation of covalent chemical bonds.^[185,186] Directed self-assembly makes use of external forces such as electric and magnetic fields.^[186] There are two main kinds of self-assembly: static and dynamic.^[185] Static self-assembly is an equilibrium process. Once formed and equilibrated, the individual and the assembled units are in a thermodynamic equilibrium without dissipating any energy.^[185] In dynamic self-assemblies, however, the underlying interactions only occur if the system is dissipating energy.^[185] In the context of this dissertation, self-assembly means the static variant only.

The thermodynamics of self-assembly can be expressed in terms of the Gibbs free energy:^[187] $\Delta G_{SA} = \Delta H_{SA} - T \cdot \Delta S_{SA}$. ΔH_{SA} is the enthalpy change during self-assembly. ΔS_{SA} is the change in entropy associated with the building of the larger units, and ΔG_{SA} is the change in the Gibbs free energy. If ΔG_{SA} is negative at the respective absolute temperature T , self-assembly occurs spontaneously. Minimization of the system's Gibbs free energy is the ultimate driving force for self-assembly.

2.3.1 Au nanoparticles

The term “nanoparticle” is a combination of the Greek word “inanosí” (dwarf) and the Latin word “iparticulumi” (particle).^[188] It denotes an object having at least one of the three dimensions in the range of 1 to 100 nm.^[189]

Some scientists classify nanomaterials based on the number of their dimensions outside the nanoscale range (> 100 nm).^[190] Accordingly, a Au nanosphere is a 0D nanomaterial, whereas ultra-thin Au nanowires^[184] are 1D nanomaterials.

For the synthesis of Au nanoparticles two basic strategies are used: a) “top-down” and b) “bottom-up”.^[191,192] The top-down approach refers to synthesis methods that start from bulk material and break it down into nanoparticles.^[188,193,194] Such methods include electron beam lithographic methods, laser-based ablation, ion sputtering, UV, and IR irradiation.^[191,192] In contrast, the bottom-up approach synthesizes the Au nanoparticles from the atomic/molecular level by chemical reaction and self-assembly processes.^[185,191,193,194] Solution-phase syntheses (“wet” chemical processes) are convenient, versatile, and form nanoparticles in polar or non-polar solvents through chemical reaction.^[193,195]

A common synthesis route for the production of Au nanoparticles is the reduction of tetrachloroauric acid ($\text{H}[\text{AuCl}_4]$)^[196] with reducing agents such as borohydride, amines, triisopropylsilane^[35,42], alcohols, tert-butylamine borane^[43] and other aminoboranes^[192], formaldehyde, carboxylic acids, sugars, hydrazine, sodium citrate, or ascorbic acid in the liquid phase.^[192,196,197] Organic molecules (ligands) or polymer protective colloids are added to the system as capping agent for steric shielding to counteract the attractive Van der Waals forces between nanoparticles.^[191,196,197] Agglomeration of the metastable Au nanoparticles can thus be prevented.^[189]

Au nanoparticles typically come as a colloidal dispersion in a liquid solvent.^[198] Since hydrophobic PDMS stamps are permeable to water vapor, but not to liquid water^[172], non-polar organic solvents are often used to synthesize printable inks. Due to the ample surface energy of nanoparticles and spheres having the smallest surface-to-volume ratio of all geometric bodies, the easiest Au nanoparticle to synthesize is the sphere^[199] or quasi-sphere^[192]. In favorable cases, it is sufficient to combine the solvent, HAuCl_4 , and the capping and reducing agents (isotropic growth on Au nuclei) for the synthesis of Au nanospheres. Depending on the molar ratio of HAuCl_4 and the reducing as well as the capping agent, the sphere size can be adjusted.^[194,200–202] In case of a hydro-

phobic organic solvent, the capping agent is mostly an alkylamine (e.g., \geq C12) or an alkanethiol. The alkyl group enables the compatibility with the solvent and the functional group the attachment to the spheres' surfaces. The capping agent can simultaneously be used as a reducing agent.^[197,199,202] An example is oleylamine (OAm).^[43,202]

Other shapes are more difficult to synthesize since they require anisotropic growth on the Au nuclei.^[191] Different methods have been developed to this end. Some of the most popular ones are syntheses in hard (e.g., pores in a metal oxide layer^[203]) or soft (e.g., micelles^[192]) templates, seed-mediated growth in solution^[191,194,204], and non-seeded^[204] growth in solution.

The seed-mediated growth route uses a two-step (two-phase) process.^[191,192,204] In the first step, spherical Au seeds are synthesized which have a uniform size. In the second step, the seed acts as a template on whose surface newly reduced Au⁰ is deposited to form particles of larger size. The new capping agent can be chosen such that it promotes the anisotropic growth. The new reducing agent is relatively weak since the Au seed acts as catalyst and additional nucleation is not desired. Consequently, Au⁺³ is only reduced on seed particles and new particle nucleation does not occur. The seed-mediated growth method is favorable for the preparation of monodisperse nanospheres due to a better control of particle size.^[192,194,204] Non-seeded methods lead to the nanoparticles in a single phase.^[204]

Before using a colloidal solution created by a wet chemical process for any purpose such as nanoimprinting, the Au nanoparticles contained in it are usually separated from excess reducing and capping agents and soluble by-products of the synthesis by precipitation, sedimentation, centrifugation, filtering, and/or washing.^[42,43,184,205] The particles can be re-dispersed in different solvents, and the stabilizing ligands may be exchanged.^[197,206]

2.3.2 Au nanowires

Initial attempts to synthesize Au nanowires yielded mostly comparatively thick (> 10 nm) and polycrystalline, rigid (stiff) wires with a large surface roughness and up to tens of micrometers in length.^[203,207–212] In

many cases, the synthesis was carried out in water with hydrophilic dispersants.^[207,210,213]

For direct nanoimprinting with hydrophobic PDMS stamps that exhibit curved microscale features, however, aqueous colloidal inks of long stiff^[35], brittle^[214,215] nanowires with hydrophilic dispersants are not suitable. Colloidal inks of mechanically flexible ultra-thin Au nanowires in hydrophobic solvents are better apt in this regard.^[35,216] Mobility, flexibility, and hydrophobicity are favorable for the filling of the stamp's cavities.^[42]

2.3.3 Ultra-thin Au nanowires - AuNWs

The pioneering syntheses yielding ultra-thin Au nanowires^[211,217–220] used oleylamine (OAm) as essential component and proceeded in organic solvents. These synthesis processes were comparatively inefficient. They required reaction times of up to several days^[219,220] and partly led to low yields due to nanosphere by-production^[217]. The procedure of mixing tetrachloroauric acid in n-hexane with OAm, adding triisopropylsilane (TIPS), and then allowing to react at room temperature (RT) without stirring, developed by Feng et al.^[184], finally yielded ultra-thin Au wires within 4 to 5 h. Nouh et al.^[206] improved the efficiency of the Feng process by increasing the concentrations of each constituent in the reaction mixture by a factor of about seven and by extending the reaction time to 24 h. This procedure, including the purification by addition of ethanol for wire precipitation, accelerated sedimentation in a centrifuge, discarding the supernatant, and re-dispersion in n-hexane, was also used in this dissertation. The purification step was repeated once. The final re-dispersion occurred in cyclohexane, which swells PDMS less than n-hexane^[221]. The obtained colloidal stock solution contained ultra-thin gold nanowires (“AuNWs”) with uniform (core) diameters of ≈ 1.6 nm^[206,222] at lengths of several micrometers ($AR > 1000$)^[223], which were OAm-capped.

The mechanism underlying the formation of AuNWs has not been fully understood.^[222–224] However, considering the overall studies that have been conducted^[184,206,211,212,217–220,222,224–226], including one of the most thorough studies recently conducted by Pschunder et al.^[223], the following findings appear reliable.

2.3. SYNTHESIS AND SELF-ASSEMBLY OF AU NANOPARTICLES WITH ALKYLAMINE LIGAND SHELL

$\text{HAuCl}_4 \cdot 3\text{H}_2\text{O}$ dissolves in n-hexane at RT by the addition of oleylamine^[184,206,222–225] under formation of an orange^[223,224] colored coordination complex of presumably square planar geometry^[223]. After addition of TIPS the formation of AuNW's in the solution proceeds at RT via two successive reduction steps.^[217,218,220,223–225] OAm^[211,217–220] and TIPS^[184,206,222,225] both^[223,224] act as reducing agent. Their difference in reduction efficiency is not due to differences in reduction potentials but due to kinetic limitations (e.g., steric reasons).^[223] In the first, relatively fast^[217,220,223,224] ($\approx 3\text{ h}$ ^[223]), reduction step, primarily OAm^[223] reduces Au^{3+} to Au^+ . Au^+ forms slightly yellow-colored complexes^[223,224] in which Au^+ coordinates to one chloride ion and one OAm molecule^[223]. The linear Au(I) complexes and other constituents of the reaction mixture (e.g., n-hexane), driven by aurophilic interaction^[217], self-assemble to cylindrical structures with a diameter of 2.6 nm and a length in the range of 1 to 1.25 nm.^[223]

In the second, considerably slower ($> 10\text{ h}$ ^[223]), reduction step, mainly TIPS^[223] reduces Au^+ to Au^0 . The wire formation does not proceed via Au nanospheres as intermediate.^[223] As the reduction of Au^+ to Au^0 proceeds, the diameter of the cylindrical structures continuously shrinks to about 1.6 nm and a continuous increase in length is observed, indicating the formation of AuNWs.^[223] The AuNWs form almost in the absence of other Au by-product nanoparticles such as spheres or rods.^[118,223]

The AuNWs form self-assembled extended bundles exhibiting a regular hexagonal arrangement in which the Au cores are separated by a bilayer of OAm molecules.^[206,222,223] The OAm layer closest to the Au surface is predominantly protonated to oleylammonium due to the presence of an acid proton in the Au precursor $\text{HAuCl}_4 \cdot 3\text{H}_2\text{O}$,^[206,222,223] and the coordinating group at the Au surface is mainly the chloride anion^[206,222,223]. About 40 % of the AuNWs are embedded within the hexagonal phase and 60 % are “free” in the equilibrium state.^[222]

The co-use of TIPS not only significantly speeded up the overall reaction,^[184,222,223] but also improved the yield of wires^[223]. Diluting the reaction mixture with n-hexane improved the yield of wires, too.^[118,206,217,225]

Reiser et al.^[118] verified the relevance of n-hexane on the growth of the AuNWs by replacing it with n-octane, cyclohexane, cyclooctane, ben-

zene, and toluene. While the linear n-alkanes enhanced the growth of AuNWs, the cycloalkanes and arenes impaired (appreciable higher by-production of spheres and irregularly shaped wires), but did not prevent it entirely.^[118] A similar observation was made by Lu et al.^[217] when replacing the solvent n-hexane with chloroform. Instead of wires, only spheres were formed. Apparently, n-hexane does not only act as a solvent for the TIPS mediated AuNW synthesis, but also aids in the formation of the wire structure.

OAm is a widely used ligand in nanoparticle synthesis,^[212] whose versatility^[227] is also exploited in the AuNW synthesis. There it acts as:

- solvent for $\text{HAuCl}_4 \cdot 3\text{H}_2\text{O}$,
- coordinating ligand for Au^{3+} and Au^+ ,
- reducing agent for Au^{3+} ,
- anisotropic growth (shaping) agent for the AuNWs,
- capping agent to prevent AuNW precipitation, and
- AuNW self-assembly promoting agent.

Its high boiling point ($\approx 350^\circ\text{C}$)^[227] and liquid state at room temperature^[227] enables the removal of free OAm by applying the purification protocol of Nouh et al.^[206] to the product mixture. The binding of OAm to the Au surface is strong enough to provide long-term colloidal stability to the AuNW inks, but weak enough to allow the full removal of OAm from the AuNWs by soft (H_2/Ar) plasma sintering^[228]. The use of alkylamines for the synthesis may yield nanoparticles with different morphology and crystallinity since the characteristic feature of a $\text{C}=\text{C}$ double bond in the center is missing.^[227]

2.3.4 Properties of ultra-thin Au nanowires

The OAm-capped, highly anisotropic ultra-thin Au nanowires have core diameters below 10 nm (“ultra-thin”) and ultra-high aspect ratios AR (length/diameter) above 500.^[184,206,211,217–220,223] They exhibit a relatively smooth wire surface^[211] and are monocrystalline with a face-centered cubic (fcc) structure (111-type lattice fringes with a spacing of 0.23 nm)^[211,229].

The wire cross-section was suggested to be hexagonal.^[222,230] The high aspect ratio reduces the percolation threshold of AuNWs to lower Au concentrations.^[231] The hydrophobicity of the OAm coating of the as-made AuNWs renders them readily dispersible in non-polar organic solvents^[220] such as cyclohexane.

The diameters of AuNWs below the electron mean free path in bulk Au (≈ 38 nm^[16]) intensify surface electron scattering that increases such a wire's resistivity compared to Au in bulk.^[232] The "mirror-like", atomically smooth surface which increases the fraction of elastic electron scattering^[232], and their lack of grain boundaries^[16,98] in the monocrystalline structure, have a dampening effect^[99,230] in this regard. With a diameter of 7 nm, the resistivity of ultra-thin Au nanowires was $292.6 \Omega \cdot \text{nm}$ ^[233] compared to $24 \Omega \cdot \text{nm}$ for Au in bulk^[15,16].

In transmission electron microscopy (TEM) images, AuNWs are frequently looped or bent, just like a human hair - a clear indication that they are highly flexible.^[220,229] Bending radii down to 20 nm, without breakage of the wires, were observed.^[228] The ultra-thin Au nanowires are mechanically robust^[229] and have a tensile strength of ≈ 600 MPa^[233] which is six times that of bulk Au (≈ 100 MPa^[233]). Wu et al.^[234] related that to a reduced number of defects in the wires.

The reported core wire diameters in the range of 1.6 to 2 nm (as thin as double-stranded DNA^[235]), correspond to 6 to 7 Au atoms only. Consequently, 70 % of such a wire's atoms are on its surface.^[13] The resulting lowering of the wire melting temperature enables cold-welding close to room temperature within seconds by mechanical contact alone, and by applying relatively low pressure.^[233] Mechanically assisted, thermally activated (diffusion barrier < 1 eV^[233]) surface atom self-diffusion is likely the welding mechanism.^[233] Rubbing the OAm-capped wires against each other before welding had removed^[233] the weakly bound (binding energy of ≈ 10 kcal/mol^[218]) OAm ligand shells. Welding did not affect the monocrystal structure or the electrical or mechanical properties significantly.^[233]

2.3.5 Self-assembly of OAm-capped AuNWs

The ability of oleylamine (OAm) capped AuNWs to assemble into elongated bundles with line contact between parallel aligned wires, was noticed first when they were precipitated (Lu et al.^[217]) or dried (Feng et al.^[184]) from their colloidal solution. A SAXS analysis of the as synthesized AuNW dispersion by Loubat et al.^[222] revealed the formation of superlattices by AuNW self-assembly^[222] in the liquid phase for the first time. The peak positions in the reciprocal space indicated a regular 2D hexagonal order comprising 7 to 100 parallel wires per bundle^[236] in the plane normal to the wire bundles^[222]. From the lattice parameter (≈ 9.7 nm) and the wire diameter (≈ 1.7 nm), Loubat et al.^[222] determined an interwire distance d_i (surface-to-surface) of ≈ 8.0 nm. The large spacing was explained^[222] by a parallel assembly of AuNWs coated with an oleylammonium/OAm bilayer, since the OAm length is ≈ 2.05 nm in its fully stretched conformation.^[227,237]

Reiser et al. determined d_i for their as synthesized AuNW dispersion as ≈ 7.5 nm.^[118] An in-situ measurement during synthesis by Pschunder et al. yielded a d_i of ≈ 7.3 nm^[223]. The differences in d_i were likely due to slightly different concentrations of free OAm in the respective product dispersion.

Because OAm is used in excess during the AuNW synthesis,^[118] the addition of OAm to an as synthesized dispersion raises the concentration of free OAm whereas the addition of n-hexane reduces it. Reiser et al.^[118] found that by adding OAm to an as synthesized AuNW dispersion, d_i decreased progressively, while it increased through addition of n-hexane. Overall, the two measures allowed to vary d_i continuously in the range of ≈ 8.5 to 5.8 nm. They interpreted this finding as the result of a progressive interdigitation of the OAm molecules tethered to the surface of adjacent AuNWs, driven by the osmotic pressure of the solute free OAm molecules.

Purifying as synthesized AuNWs twice by precipitation through addition of ethanol, sedimentation by gravitation^[118] or centrifugation^[238], removal of the supernatant, re-dispersion in the solvent, and final re-dispersion in n-hexane, decreased d_i to ≈ 3.8 nm while the hexagonal arrangement of the bundling remained.^[118,238] This distance is roughly two

times the OAm length, and consistent with AuNWs coated by a single OAm ligand shell.^[238] Apparently, the purification process removes all OAm not directly bound to a wire surface.^[118] For the remaining OAm residue, X-ray photoelectron spectroscopy (XPS) revealed the presence of Cl^- ions and nitrogen in $-\text{NH}_2$ as well as $-\text{NH}^{3+}$ environment.^[238] In the absence of an excess of free solute OAm, the ligand shells of adjacent wires barely overlap.

Drying a droplet of a suspension of twice-purified AuNWs in n-hexane deposited on a silicone substrate yielded a hexagonally ordered assembly of AuNWs which exhibited a d_i of only ≈ 2.4 nm.^[206] This value is consistent with an almost full interdigitation of the relevant OAm molecules. Reiser et al.^[239] and Gao et al.^[236] both found the same tight bundles for twice purified AuNWs in poorly^[236] polar solvents such as methanol, ethanol, and n-propanol with a uniform d_i of ≈ 2.41 nm. Apparently, the (polar) solvents were completely expelled from the interface between two adjacent AuNWs, similar to the case of the evaporation of the non-polar solvent. Such super-lattice formation is enthalpy driven^[186] and caused by the direct interaction between the hydrocarbon chains of the surface-bound OAm ligand molecules of adjacent wires^[236,240].

In contrast, and contrary to intuition^[118,222], computer simulations of a suspension of twice purified AuNWs (“ex-situ” AuNWs) in n-hexane, using molecular dynamics, suggest that the observed hexagonal bundling of the OAm-capped AuNWs in suspension is entropy driven.^[236] Adjacent AuNW ligand shells do not interdigitate.^[236] The space in-between suffices to hold one layer of n-hexane molecules, as their shape is similar to the alkyl tail of OAm ligands. In the bulk solvent, n-hexane molecules are randomly oriented. They can penetrate the OAm ligand shell and align with the ordered ligand environment, normal to the wire surface. Such ordering causes a loss in entropy. If all AuNWs would remain dispersed in the solution, the solvent molecules in the immediate vicinity around each wire would be ordered, and the solution’s associated entropy loss would be proportional to the number and length of the wires present. This entropy reduction creates a driving force for the AuNWs to bundle.^[236]

By self-assembling into bundles with a hexagonal lattice, two adjacent

wires reduce the number of ordered n-hexane molecules and thus the associated loss of entropy. Aligning solvent molecules simultaneously to two ligand shells is achieved by molecules bridging the two shells over the line contact.^[236] The two shells are virtually “stapled” together through these n-hexane bridges, along a length of several microns.^[236] Thus, n-hexane serves as an auxiliary agent enabling AuNW self-assembly for the TIPS mediated AuNW synthesis.

This explains why re-dispersion of AuNWs surrounded by an OAm monolayer in n-pentane ($d_i = 3.72$ nm)^[236] and n-heptane ($d_i = 3.82$ nm)^[236] also led to hexagonal super-lattices, while re-dispersion in cyclohexane, -heptane, and -octane did not.^[118,236] n-Heptane and n-pentane can replace n-hexane almost equally, while their cyclic counterparts cannot. Cyclic alkane molecules have a more limited shape than linear alkanes due to restricted C-C bond rotations, which is not compatible with the ordered wire ligand shell.^[118] They cannot intercalate into OAm ligand layers without disturbing the order of the layers.^[118,205] Such disordered ligand shells without a preferential alignment are most likely unable to order solvent molecules in their vicinity.^[118]

Bundling of AuNWs with a single OAm shell in n-hexane is a slow process. At RT, this transformation from fully dispersed to equilibrated lasts a few hours.^[118,222] Semi-continuous direct nanoimprinting rapidly transforms a fully dispersed colloidal solution of OAm coated AuNWs in cyclohexane into a dried feature, exhibiting the Bragg peaks of crystallized hexagonal bundles of such AuNWs.^[35,42]

Based on the properties outlined in sections 2.3.3 to 2.3.5 herein, colloidal solutions of ex-situ AuNWs that bundle in cyclohexane would be appealing inks for direct nanoimprinting of FTEs.

2.3.6 Au nanospheres

Bare metal nanospheres do not form stable suspensions in apolar solvents since London dispersion forces cause attraction and thus their agglomeration.^[241,242] Metal nanospheres formed during synthesis in apolar solvents are therefore coated with dense layers of molecules having an apolar chain and a binding group with an affinity for the nanospheres’ surfaces^[242]. In case of Au, they often contain nitrogen, e.g., in alkylamines,^[43,243] or

sulfur, e.g., in alkanethiols,^[43,244] to bind to the Au.^[242]

London dispersion forces are typical short-range attractive forces. Their origin lies in induced dipole-dipole attraction which decays rapidly with increasing distance.^[198,245,246] The syntheses of metal nanospheres are therefore typically performed at low metal concentrations.^[247] They agglomerate when a certain threshold concentration c_{lim} is exceeded.

c_{lim} depends on the solvent, the ligand, and the core size.^[242,247–250] Doblas et al.^[247] demonstrated that Au nanospheres, with a core diameter of ≈ 3.4 nm and an octanethiol ligand shell, agglomerate in cyclohexane at concentrations c_{lim} which are two orders of magnitude higher than in other non-polar solvents such as heptane, nonane, decane, and toluene. Kister et al.^[43] systematically varied the alkyl chain length of alkanethiol- and of alkylamine-stabilized Au nanospheres in cyclohexane, with a core diameter of ≈ 3.2 nm, and found that c_{lim} increased with the length of the alkyl chain.

Kister et al.^[43] systematically studied the influence of the alkyl chain length of the 3.2 nm sized alkanethiol-/alkylamine-stabilized Au nanospheres in cyclohexane regarding their performance during direct nanoimprinting. They found that the imprinting quality improved with increasing c_{lim} . Disconnected agglomerates (\leq C8 alkyl) that prevented macroscopic conductivity, changed to continuous, percolating lines for dodecanethiol and -amine. The binding group had only a minor influence on c_{lim} and the imprinting quality. Continuous lines formed when agglomeration was suppressed until the very end of solvent absorption.^[43] Consequently, colloidal solutions of such gold nanospheres with OAm ligand shell in cyclohexane should be well suited as inks for direct nanoimprinting of FTEs.

2.3.7 OAm-capped AuNPs

Wu et al.^[205] observed a remarkable solvent effect on the single-phase synthesis of oleylamine (OAm) capped Au nanospheres by reducing $\text{HAuCl}_4 \cdot \text{H}_2\text{O}$ with a tert-butylamine-borane complex (TBAB) in apolar solvents. If linear alkanes such as n-hexane were used as solvent, monodisperse Au nanospheres were obtained. The size of the nanospheres could be controlled by tuning the ratio of TBAB to $\text{HAuCl}_4 \cdot \text{H}_2\text{O}$. Increasing the ratio decreased

the size and vice versa. Precipitation and washing with ethanol and subsequent re-dispersion in n-hexane to the desired concentration (typically ≈ 5 mg/mL) yielded the final colloidal solution of monodisperse OAm coated Au nanospheres with tunable size of 3 to 10 nm. Drying a droplet of the solution on a TEM grid resulted in a self-assembled, hexagonally arranged monolayer of nanospheres.^[205]

In contrast, when cyclohexane was used as solvent for the synthesis, nanospheres with a broad size distribution were obtained.^[205] Wu et al.^[205] attributed the difference in synthesis outcome to a different influence of the respective solvent on the configuration of the Au spheres' ligand shells. Together with the OAm ligands, n-hexane molecules likely form uniform hydrophobic protection layers on the Au surfaces. The cyclohexane chairs disturb the ligand layers.^[118,205] This leads to irregular gaps in the individual ligand shells, from which different growth rates and finally the polydispersity arises. A feasible route to colloidal solutions of monodisperse OAm-capped Au nanospheres in cyclohexane is the synthesis of the particles in n-hexane, and, after subsequent purification as described, their re-dispersion in cyclohexane.

Kister et al.^[43] refined the synthesis protocol of Wu et al.^[205]. Instead of n-hexane, they used n-pentane as solvent and a seed mediated two-phase process. In the first step, $\text{HAuCl}_4 \cdot \text{H}_2\text{O}$ was reduced at room temperature by OAm dissolved in n-pentane. In the second step, a solution of tert-butylamine borane-complex in a mixture of n-pentane and OAm was added. This synthesis protocol was also used in the scope of this dissertation. After purifying the synthesis product twice and then re-dispersing it in cyclohexane, a stock solution was obtained. This solution was diluted with cyclohexane to obtain nanoimprintable inks with varying contents of the OAm-capped Au nanospheres with a core size of ≈ 3.7 nm ("AuNPs").

2.4 Sintering of grids made of ligand coated metal nanoparticles to form conductive electrodes

A colloidal metal ink contains the respective metal in elemental form and solvent removal forces the suspended metal nanoparticles closer together.

2.4. SINTERING OF GRIDS MADE OF LIGAND COATED METAL NANOPARTICLES TO FORM CONDUCTIVE ELECTRODES

Nevertheless, drying such an ink usually does not render it electrically conductive.^[251,252] Insulating organic ligands remain on the surface of the particles and separate them. Good conductivity, however, requires sound metallic contacts between the particles and a percolating network throughout the printed structure, enabling electrons to move easily from one particle to another.^[252] A common way of achieving electrical conductivity is sintering: thermal energy is applied that removes the ligands from the particles' surfaces and merges the nanoparticles.^[253]

Ingham et al.^[254] investigated dried droplets of a colloidal ink containing OAm (b.p. of OAm $\approx 350^\circ\text{C}$ ^[227]) capped Au nanospheres (monodisperse, 10 nm in diameter) in toluene. They found that temperatures in the range of 150 to 165 $^\circ\text{C}$, well below the OAm desorption temperature^[254], led to conductivity, while temperatures below 150 $^\circ\text{C}$ did not. Melting ligands detached from the Au surface and acted as a quasi-liquid solvent, in which the Au spheres moved and coalesced.^[251] "Melting" of the OAm was enough to expose the particles' Au surface.^[254] Since the particles were closely packed, they quickly began interacting and aggregating, even in the presence of OAm ligands.^[254] A sintering temperature of 250 $^\circ\text{C}$ was required to achieve appreciable neck formation and eventual merging to a dense metal layer with low resistance.^[254] Volkman et al.^[255] made similar observations for dodecanethiol-stabilized Ag nanospheres (monodisperse, 3 nm in diameter). Apparently, for sintering, the lowest temperature at which printed features become conductive (the percolation temperature^[251]) is distinct from the lowest temperature required for obtaining the lowest possible resistance.^[252] Sintering in the presence of the dispersant is known from welding metal nanowires at their junctions in random metal nanowire networks, too.^[127]

The complete removal of all organic ligands through sintering generally requires temperatures well above 200 $^\circ\text{C}$.^[251,252] The conductivities reached are typically less than one tenth of the respective bulk conductivity^[36,255] (an overview is given by Maurer et al.^[35]). Only costly or barely flexible polymer substrates such as polyacrylate, poly(ether ether ketones), poly(ether sulfones), and polyimides can withstand such high sintering temperatures. Affordable and particularly flexible polymers like poly(ethylene terephthalate), poly(ethylene naphthalate), and polypro-

pylene, with glass transition temperatures below 150 °C or even less than 100 °C, cannot.^[251,252]

Many research groups tried to reduce the required sintering temperature by reducing the particle size or ligand amount or through tailoring of the ligand.^[251] Bare metal nanoparticles show a significant melting temperature depression compared to the respective bulk metal, which increases with decreasing particle size.^[138,256,257] Yet, metal nanoparticles do not fully melt at the typical sintering temperatures.^[251] Their coalescence is rather based on surface melting and diffusion of surface atoms from one particle to another. Accordingly, sintering cannot occur below the temperature at which the ligand bonds to the particle surface are broken,^[251] irrespective of any further reduction in particle size. Furthermore, the total area to be protected by ligands increases with decreasing particle size.^[251] Ligands which adsorb only weakly impair the stability of the colloidal ink during synthesis and printing,^[252] as does a lower ligand amount^[251].

2.4.1 Chemical sintering

Chemical sintering processes attempt to destabilize the particle/ligand system after printing with the aid of chemical agents,^[251,258] often at room temperature^[253]. Examples are ligand exchange, dissolution of the ligand in a solvent, and ligand modification such as neutralization of charges.^[251] The compatibility of the substrates with the agent used is an issue, as are agent residues in the printed features, and the method is often limited to specific particle/ligand/agent combinations. Fafarman et al.^[259,260] reported the exchange of long-chain OAm ligands on spherical Au nanocrystals by short NH₄SCN. They observed a clear dielectric-to-metal transition after OAm was replaced by ammonium thiocyanate in spin-coated particle layers. Attempts by Maurer et al.^[115] to apply this approach to a random network of OAm coated AuNWs were not successful.

2.4.2 Photonic sintering

Temperature-sensitive substrates may also be protected by heating the printed features only locally.^[251] Photonic sintering allows such selective

heating.^[251] It is based on the exploitation of the photothermal effect^[261] at wavelengths at which the dried ink has a high absorption and the substrate has not.^[216,251] For example, nanoparticles of the metals Ag, Au, and Cu exhibit strong surface plasmonic resonance absorption in the visible range, whereas transparent flexible polymer substrates like PET have their intense absorption bands in the UV range.^[251] Several photonic sintering processes have been developed comprising near infrared and ultraviolet light, either applied through conventional illumination or laser irradiation of the printed structures.^[262]

Since the absorption spectra of printed colloidal metal nanoparticle inks depend on their specifications such as metal type and shape, size, distribution, and ligand ligation of the particles, each ink has its own process parameter (e.g. wavelength and power density) space.^[216,251] As photonic sintering progresses, the printed feature's specification and consequently its absorption behavior continuously changes, too.^[253,261,263] This is disadvantageous as the set sintering parameters fit less and less with the feature's increasingly changing absorption characteristics. That often slows the sintering kinetics.^[216,251] Also, the generated temperatures inside the ink can dissipate into the substrate and deform the polymer foil.^[264]

2.4.3 Plasma sintering

Plasma sintering attempts to destabilize the post printing particle-ligand system at low temperature by a discharge^[265,266] plasma. It can be created by applying a breakdown voltage between two spaced electrodes in a cell filled with the discharge gas (feed gas).^[251,265,267] The plasma formed comprises reactive species such as excited atoms and molecules, electrons, ions, neutral radicals as well as UV-radiation and visible light (glow).^[253,268]

During plasma exposure of a printed sample, the organic ligands are degraded (covalent bonds are cleaved) via bombardment with the highly reactive and energetic plasma species. Their resulting low molar mass fragments are normally easier to remove from the nanoparticle surfaces, enabling direct contact of particles.^[251] Plasma species impinging on the particle surfaces cause momentum transfer involving some heating.^[269]

This and the inherent high surface energy of the small particles cause surface and grain boundary diffusion, which, together with crucial impingement driven surface sputtering^[228] finally yields a conductive material.^[216,264,270]

Paschen^[251,271] found that low temperature plasma can be generated at low and at standard pressure. The breakdown voltage^[272] and the chemical nature^[251] of the plasma - reducing, inert or oxidizing - depend on the feed gas.

Kister et al.^[43] report that low-pressure (0.3 mbar) O₂ plasma sintering of an ordered grid with sub- μm line width and nanoimprinted from dodecanethiol-capped Au nanoparticles, led to a high sheet resistance in the $k\Omega_{\text{sq}}$ range. This was attributed to the oxidation of the thin lines which induces stress and interrupts conductive pathways. Maurer et al.^[115] report on the low-pressure (0.3 mbar) plasma sintering of random network layers of OAm-capped AuNW bundles. The AuNWs were deposited from their inks in n-hexane by repeated dip-coating on silanized glass substrates (layer thickness ≈ 10 nm). They found that O₂ plasma drastically altered the morphology and attributed that to oxidation. Fuchs^[273] noticed that low-pressure oxygen plasma cleaning of Au resulted in the formation of a surface layer of Au₂O₃.

Noble gas plasma is better in this respect.^[253,270] Ar (15.76 eV) has the lower ionization potential compared with He (24.48 eV) and is readily available at a low price.^[274] According to Pappas^[267], oxygen is almost always present in plasma generation processes even when the chosen process gas is different from O₂ as most experimental systems are not fully sealed. Mixtures of Ar/H₂ (e.g., 5 % H₂) can be a preventive countermeasure^[115]. With increasing share of the low molecular weight H₂, the sputtering effect of the plasma decreases^[274]. Ar/H₂ containing 5 % H₂ was also used as plasma feed gas in the scope of this dissertation.

Wünscher et al.^[270] compared low and atmospheric pressure Ar plasma sintering on inkjet printed Ag nanosphere inks. The inks were stabilized by unspecified dispersants and varied in Ag content, sphere diameter of up to 50 nm, and solvent. There was a distinct dependency of the resulting resistivities on the nature of the individual ink used. The highest conductivity was 12 % of that of bulk Ag and was obtained at normal

pressure on a line printed with the lowest height (260 nm) from relatively large (30 nm) spheres. This delta was mainly attributed to the presumed onset of physical etching^[275] of the top metallic layers before the lower layers were fully sintered. Decomposition products of the dispersants likely remained in the sintered structure and limited conductivity, too. Electron microscopy micrographs of cross-sections of lines sintered at normal pressure consistently showed uniform sintering from top to bottom. The morphology at low pressure was not studied.

Atmospheric pressure plasma achieved conductivities in a fraction of time (a few minutes) of that required at low pressure (a few tens of minutes). This was attributed to the higher energy delivery at normal pressure per area and time. At atmospheric pressure, physical etching of the polymeric substrates was negligible due to short exposure times. At low pressures, a physical etching rate of 0.26 to 0.32 $\mu\text{m}/\text{h}$ was observed for PET substrates.

Reinhold et al.^[276] used a low pressure Ar plasma to sinter Ag nanosphere (5 to 10 nm in diameter, unspecified dispersant) tracks of unspecified height and printed with the same ink on glass and polymer substrates to reach conductivities of up to 30% of that of bulk Au. Apparently, the low pressure favored the evaporation of the low molar mass dispersant fragments. They demonstrated that plasma sintering of thicker lines, which they obtained by printing multiple tracks on top of each other, can be limited by a skin effect. Top layers of the printed feature sintered first to a conductive skin layer (a crust) whose thickness grew with plasma exposure time, but hindered fast and sufficient sintering of the material beneath. Interestingly enough, the best conductivities resulted from tracks printed on glass. This was attributed to the lower heat dissipation which caused higher substrate temperatures of 81 °C on glass versus 71 °C on the polymer foils at the end of the plasma treatment.

Ma et al.^[277] also noticed a skin effect while studying low pressure Ar plasma sintering at three different *rf* (13.56 MHz) powers (100, 500, and 900 W) on two different Ag nanosphere films of 1 μm thickness. The films were drop casted with different aqueous colloidal inks onto glass. The inks had the same metal content and protective colloidal coating, but particles differing in core size (23 nm vs. 77 nm).

The R_{sh} of all plasma sintered films decreased with increasing sintering time by more than six orders of magnitude. Prolonged plasma exposure always continued to decrease R_{sh} , but at increasingly lower rates. For any given treatment time and core size, larger power yielded lower R_{sh} . IR spectroscopy of the films' surfaces indicated the removal of the protective colloid. After 60 min of treatment time, substrate temperatures had increased by up to 125 °C, with the lower temperature for the lower plasma power. Remarkably, for a given plasma power and treatment time, smaller spheres always resulted in higher R_{sh} .

The same films were subjected to a purely thermal sintering process in Ar that followed the substrate temperature profile measured during plasma sintering. For a given treatment time, the thermal effect compared to the effect of plasma sintering was negligible. However, consistent with the expectation that smaller spheres sinter more easily,^[252,270,277] the smaller spheres now always resulted in the smaller R_{sh} . Top view and cross-sectional images of two film samples made of the differently sized spheres and treated at 900 W for 60 min revealed that only a top crust with a thickness of just under twice the sphere diameter had coalesced Ag nanospheres. The lower R_{sh} was with the thicker crust resulting from the larger spheres.

Wünscher et al.^[264] inkjet printed Ag spheres with diameters of 30 to 50 nm to lines of 360 nm height on PEN foil ($T_g = 120$ °C) and sintered them with normal pressure Ar plasma. At 25 °C substrate temperature, 15 s of plasma sintering were required to yield a resistivity of $90.6 \mu\Omega \cdot \text{cm}$ ^[264,270] and 2 min for $16.1 \mu\Omega \cdot \text{cm}$. With a substrate temperature of 110 °C (70 °C), 15 s were sufficient to reach $10.4 \mu\Omega \cdot \text{cm}$ ($35.5 \mu\Omega \cdot \text{cm}$). This corresponds to a conductivity of 15.3 % of that of bulk Ag. Thermal sintering at 110 °C for periods of 2 min had no effect. With plasma sintering, the authors found the stabilizers detaching from the particle surfaces well below their decomposition temperature of ≥ 200 °C.^[264] The relationships found at normal pressure also persisted for low-pressure Ar plasma sintering.^[264] Even moderate post-plasma substrate heating led to an additional reduction in resistivity.^[264]

Wünscher et al.^[264] related their findings to those of Volkman et al.^[255], who suggested that sintering can occur in the presence of dispersants (sta-

bilizers). Prior stabilizer removal is favorable, but not a pre-requisite. Rather, the “melting” of the stabilizer is already sufficient. However, it is more conceivable that stabilizers which have been partially fragmented by plasma exposure, exhibit a significantly lower melting off temperature and perhaps may even exert a melting off temperature lowering effect on stabilizer portions that have not yet been fragmented. Both would promote the sintering effect noticeably due to the warmed substrate and would likely improve the post-plasma homogeneity within the printed structure.

Plasma sintering has both advantages and disadvantages compared to classic sintering. Ligand decomposition promotes ligand detachment from the particle surfaces at low temperature.^[251,264] Depending on the kind of plasma, the treatment can be time consuming and cause substrate matting due to physical etching.^[270] Low pressure plasma sintering is hardly R2R compatible^[264,270], but can achieve complete ligand removal from the sintered feature^[276,277]. Due to the skin effect, the plasma sintering depth can be limited.^[276,277] Supporting substrate heating can counteract problems resulting from the skin effect.^[264] Contrary to the knowledge that small diameter particles sinter more easily due to their intrinsically better activated surface diffusion,^[252,270,277] features printed from the smaller spheres may exhibit the higher post plasma resistivities in case skin formation limits the sintering depth.^[277]

A particularly well activated surface-atom self-diffusion at RT resulting in a pronounced lowering of their melting temperature is inherent to AuNWs.^[233] However, in case of a narrowly limited sintering depth, plasma sintering for grids printed from ligand coated AuNWs would be inadequate.

The following informs on sintering depths reported in literature for low pressure plasma sintering of features based on OAm ligated AuNWs in 5 % H₂/95 % Ar atmosphere.

2.4.4 Plasma sintering depths

Maurer et al.^[115,228] and Gonzalez-Garcia et al.^[278] sintered random network layers of densely packed, hexagonal bundles of OAm-stabilized AuNWs (diameter \approx 1.6 nm) through low pressure plasma treatment

in 5 % H₂/95 % Ar atmosphere. The layers were deposited on silanized glass from their colloidal solution in n-hexane by repeated dip coating with a thickness of ≈ 10 nm. Freshly deposited layers exhibited a $R_{\text{sh}} > 40 \text{ M}\Omega_{\text{sq}}$. The average transmittance in the visible range was ≈ 70 %. Plasma exposure of 15 min was sufficient to reduce R_{sh} to $50 \Omega_{\text{sq}}$, a value similar to that of a sputtered Au layer, with a thickness of ≈ 15 nm, while essentially retaining the optical transmittance.^[115] Further plasma exposure did not yield any further significant improvement.^[115] Raman spectroscopy indicated that the OAm could be fully removed by the plasma that obviously penetrated the layer in its entire thickness.^[228]

According to Maurer et al.^[228], the H₂/Ar plasma sintering likely started by removing OAm through the plasma and the low pressure. The thin (≈ 1.6 nm) metal cores with their low surface-to-surface spacing^[115,118,206] came into direct contact. Templated by their arrangement within bundles and bundle-like superstructures formed during drying, they then fused into thicker wires^[233], retaining the overall percolation of the deposited film layer and exhibiting enhanced conductance.

Reiser et al.^[239] spun AuNWs coated with a single OAm layer from their colloidal solution in cyclohexane via controlled coagulation in ethanol (a solution spinning process) into free-standing macroscopic fibers. These could be dried and mechanically tested. The diameter of the spun fibers increased monotonously with the AuNW volume fraction in the cyclohexane solution to values above 10 μm . The authors investigated the influence of low-pressure H₂/Ar plasma treatment on the tensile strength of as spun, hanging fibers. Optical microscopy revealed that the fibers did not shrink during plasma sintering. Cross-sections of a plasma-treated fiber (diameter $\approx 10.8 \mu\text{m}$) prepared with a focused ion beam and the increased conductivity (800 S/cm; approximately 500 times below that of monocrystalline bulk Au^[239]) of the initially insulating fiber suggested that plasma sintering had penetrated ≈ 600 nm into the fiber and formed a moderately porous ≈ 600 nm thick electrically conductive Au shell by OAm removal and coalescence of the exposed nanowires. The fiber's core appeared to contain unaffected or only partially sintered Au wires with several pores. Some organics from the core flowed through the pores and accumulated at the bottom of the hanging fiber. Assuming that the core

is electrically non-conductive, the derivable conductivity of the Au shell is still roughly 100 times lower than that of bulk Au.

Kister et al.^[43] and Maurer et al.^[35,42] used low-pressure H₂/Ar plasma to prepare ordered metal grid FTEs with varying patterns and self-assembled from dodecylamine-capped Au nanospheres (3.2 nm size) or from AuNWs with a monolayer of OAm dispersed in cyclohexane by direct nanoimprinting. The thicknesses (heights) of the imprinted lines were in all cases < 100 nm (e.g., 15 nm). The line widths ranged from sub- μm (e.g., 250 nm) to 1.70 μm . Due to the plasma sintering, sheet resistances dropped to practically useful values ranging from 29 to 227 Ω_{sq} . The soft sintering step removed ligand barriers, but retained the imprinted structure. Resistivities of the sintered lines, calculated from their geometries and sheet resistances using Kirchhoff's rules,^[35,42] were about one order of magnitude above the resistivity of bulk gold.^[35,42] The scale of this deviation corresponded to that known for electrodes based on thermally sintered metal nanoparticle inks^[27,35,279–281] or based on e-beam lithography using metal vapor deposition.^[42,147] It was therefore conclusive that fully sintered lines of metallic gold were obtained, exhibiting conductivities limited by combinations of structural grid defects, grain boundary scattering, nanopores, and line width and height variations.^[35,42]

2.5 Stability of sintered TEs based on metal nanoparticle inks

Transparent electrodes based on sintered metal nanoparticle inks exhibit a strongly improved conductance immediately after sintering. However, only few authors report on whether this improvement is permanent.^[16,126,228]

To convert percolating random layers of metal (e.g., Ag) nanowires into conductive electrodes, it is sufficient to fuse the junctions locally.^[127] Complete dispersant removal is not required. Since junctions are regions of high curvature, such sintering occurs typically at temperatures^[282] at which the wires do not spheroidize^[126,127].

The stability of random silver nanowire network electrodes sintered

that way has been studied extensively.^[126,136,141,283–286] It is known that their conductance is sensitive to UV light and to chemical corrosion by sulfides, oxygen, and acids. The individual nanowires are susceptible to the thermally activated Plateau-Rayleigh instability^[283] and electromigration^[126,283]. The stability can be improved by protective coatings^[126] that hinder corrosion, slow down surface diffusion, and reduce the Plateau-Rayleigh instability.

Few studies exist on the stability of electrodes based on AuNWs covered with a monolayer of OAm ligands. Maurer et al.^[115,228] and Gonzalez-Garcia et al.^[278] prepared electrodes through low pressure H₂/Ar plasma sintering of random metal nanowire network layers dip-coated from colloidal solutions of such AuNWs in n-hexane (see section 2.4.4 herein).

According to Maurer et al.^[228], it is likely that plasma sintering (15 min) thoroughly removed the OAm (b.p. $\approx 350^\circ\text{C}$ ^[227]) to below its detection limit in a first step. The remaining gold cores fully merged^[233] into thicker polycrystalline bulk “wires” (wire-like superstructures visible in TEM) while maintaining the film layers’ overall percolation.^[228] Isolated AuNWs fragmented during plasma sintering.^[228] Bundled, ultra-thin gold nanowires in freshly prepared layers fragmented into nanospheres within few days at room temperature^[115] (Plateau-Rayleigh instability^[116]). Bundled wires of short-term (1 min) plasma sintered layers fragmented within a few hours.^[115] For 15 min plasma sintered layers were free of OAm and not only had a significantly reduced R_{sh} , but were stable and retained R_{sh} for months under ambient conditions.^[115,228] Annealing of the fully sintered layers did not cause Plateau-Rayleigh spheroidization anymore, but de-wetting and an increase in R_{sh} which accelerated with increasing temperature and decreasing film thickness.^[228]

These observations are consistent with the following hypotheses. The OAm ligands stabilize bundled AuNWs.^[115,116] Partial ligand removal after 1 min of sintering still did not allow for direct inter-wire contact and prevented the wires’ rapid subsequent fusion into more conductive and geometrically stabilized thicker structures (pinch-off faster than sintering^[287]).

Due to the observed fragmentation of solitary (unbundled) wires caused

by plasma sintering^[228], both the wires' being self-assembled into crystallized, close-packed hexagonal bundles as well as their superstructures and a fast, complete OAm removal by the plasma, appear pivotal for successfully plasma sintering AuNW-based features into stable conductors.

The findings by Maurer et al.^[115,228] should also apply similarly to AuNW-based plasma sintered FTEs from direct nanoimprinting.^[35,42] If low pressure H₂/Ar plasma sintering removes the OAm ligands through the entire depth of the imprinted lines, the FTEs' R_{sh} should be stable for months and the FTEs should neither show any signs of Plateau-Rayleigh instability nor of de-wetting when stored under ambient conditions.

2.5.1 Plateau-Rayleigh instability

Surface atoms (molecules) have fewer neighbours than bulk atoms (molecules), which lends surface atoms and molecules a higher energy.^[288] This gives condensed matter a tendency to minimize its surface area,^[288] such that, e.g. cylinder-like shapes, with a length longer than their circumference, are inherently unstable^[289]. J. A. F. Plateau used a static energy analysis to show that such a liquid cylinder fragments into a row of spherical droplets with the same total volume, but a smaller total surface area (the ratio of the sphere to cylinder radius exceeds $(3\pi/2)^{1/3}$ ^[287]) and hence, surface energy.^[288,289] J. W. S. L. Rayleigh used a dynamic stability analysis to predict the final drop size.^[289]

The Plateau-Rayleigh instability also occurs in solid materials at sufficiently small cylinder diameters.^[290] For a long wire with an isotropic surface energy, the critical diameter d_m can be approximated as $d_m = 2\sigma_S/\sigma_Y$,^[290,291] where σ_S is the surface tension, and σ_Y the yield force. Using bulk values, this results in $d_m = 14.8$ nm (Ag), 14.2 nm (Cu), and 26 nm (Au) at normal conditions.^[290,291] In solids, the yield force is orders of magnitude larger than in liquids. That explains the ubiquity of the Plateau-Rayleigh instability in liquids and its limitation in solids to small structures.^[292] The Plateau-Rayleigh instability is not restricted to nanowires with a cylindrical cross-section.^[293] It is triggered by tiny perturbations of the geometry, caused by e.g., thermal fluctuations in the material.^[294,295] The anisotropic surface energy of crystalline nanowires,^[296] the contact angle between wire and substrate,^[297]

impurities, strain, and temperature may either enhance or inhibit the instability.

F. A. Nichols and W. W. Mullins extended Rayleigh's theory to solid cylinders.^[298] Their pinch-off time scales with the cylinder radius to the fourth power,^[116,299] and shortens with increasing temperature^[116,297]. Solid cylinders with isotropic surface energy and initial radius r eventually break up into solid spheres with a diameter of $d = 3.78 \cdot r$.^[300] Ultra-thin metal nanowires are already unstable at room temperature.^[115,287,297,301] At 200 °C, OAm-capped AuNWs fragmented into small spheres within seconds^[278] by surface diffusion^[116].

Xu et al.^[302] studied the instability of bare ultra-thin gold nanowires with 5.9 nm diameter and a single crystalline structure in the [111] direction. The two wire ends were supported by a carbon film and the middle part was free standing. Heating with an electron beam to temperatures well below 100 °C (estimated from the energy-loss spectrum) through momentum transfer showed, via in situ high-resolution TEM, that the wires' evolution in shape was governed by atomic surface diffusion.

Karim et al.^[297] studied the morphological changes of bare polycrystalline Au nanowires with 25 nm diameter and several μm length during isothermal annealing for 30 min at 200 to 500 °C on SiO₂ wafer pieces in an evacuated furnace. At 200 °C, they observed no morphological changes even after annealing for several hours. At 300 °C, the wires fragmented into sections of varying length. At 400 °C, they broke into peanut-shaped fragments. Annealing at 500 °C caused spheroidization of the wires into spheres, with diameters larger than those predicted for materials with isotropic surface energy. Wires with 50 nm and 100 nm diameter remained intact after 30 min of annealing. The 100 nm wires developed axial perturbations only after annealing at 500 °C for 70 h. These results confirm the powerful interplay between pinch-off time and diameter in the Plateau-Rayleigh instability of solid cylinders predicted by F. A. Nichols and W. W. Mullins.^[116,298,299]

Bettscheider et al.^[116,287] analyzed the break-up of a nanowire, coated with an organic ligand shell, into discrete droplets due to the Plateau-Rayleigh instability. A perturbation analysis indicated that the break-up of AuNWs is delayed by an OAm ligand shell. This is consistent with the

stability observations made by Maurer et al.^[115,228] after partial removal of OAm from thin layers of AuNW bundles through plasma sintering. Bettscheider et al.^[287] investigated the impact of the self-assembly of AuNWs into crystalline hexagonal bundles on the wire Plateau-Rayleigh instability, both experimentally and theoretically. In-situ SAXS of 60 °C colloidal solutions in n-hexane/cyclooctane with ex-situ TEM of dried solution drops revealed that bundling delays the break-up. An analytical model indicated that bundle formation can render the wires geometrically stable.

Ostwald ripening may follow the Plateau-Rayleigh fragmentation of ultra-thin gold nanowires.^[115,228] It results from the dissolution of small crystals or sol particles and their re-deposition onto the surface of larger crystals or sol particles. Smaller particles have the higher specific surface energy (and hence for equal total volumes the higher Gibbs energy), giving rise to a higher solubility.^[303,304]

2.5.2 Solid-state de-wetting

Thin metal films^[305,306] that are forced^[307] onto non-wetting^[308] substrates are thermodynamically un- or metastable^[299]. This is mainly due to the resulting relatively high surface and interfacial energies.^[309] Defect energies and grain boundary energies may contribute, too. Such films tend to de-wet and transform into arrays of isolated metal islands (droplets or particles) with lower total energy^[309] when activation energy is provided, e.g., by thermal annealing, electron beam, ion beam, or laser irradiation.^[299] The driving force of the transformation^[308,309] is primarily the minimization of the total metal-substrate interface and the metal surface^[307,310]. It increases with decreasing film thickness due to the increasing surface-to-volume ratio of thinner films.^[299] The final shapes of the islands may be caps or beads^[305], exhibiting a wetting angle (contact angle) $> 0^\circ$ ^[310]. The de-wetting process can proceed even in the solid state^[299,305] and is then referred to as “solid-state de-wetting”^[309].

It is well-accepted that the dominating mass transport mechanism of solid-state de-wetting in metal films is atomic surface self-diffusion.^[311,312] However, grain boundary and interfacial diffusion can also play a crucial role.^[311,312] Typically, all of them accelerate exponentially with temperat-

ure.^[299] Grids with sub-micron line width, imprinted from dodecanethiol coated Au nanospheres (3.2 nm in diameter), de-wetted during thermal sintering at 200 °C and lost conductivity within minutes.^[43]

The nucleation mechanism of solid-state de-wetting is still under debate.^[309] Contrary to a thin metal cylinder, where small amplitude fluctuations in the diameter cause the cylinder to evolve into a row of beads (Plateau-Rayleigh instability)^[291,297,300,305], a plane metal surface does not exhibit inherent instability.^[305] Small fluctuations in the planar surface of an infinite, defect-free, and zero-stress film with isotropic surface energy will not grow, regardless of their wavelength.^[299,305,313] The process of de-wetting either occurs at pre-existing holes that fully protrude through the film's thickness (voids), at film edges, or requires the formation of such new holes.^[299] Thus, very thin, porous films are particularly prone to solid-state de-wetting.

In void-less films, a sufficient stage in the initiation of solid-state de-wetting is the formation of a pinhole. Such hole formation is usually discussed in terms of random heterogeneous nucleation at defect sites and around impurities, at grain boundaries of polycrystalline films, or at pre-existing pores at the film-substrate interface.^[299,307,309] An example are film thickness fluctuations large enough to penetrate the film, which can occur at grain boundaries and finally result in hole formation.^[305] Once the hole reaches the super-critical size, its further growth becomes energetically favorable.^[309] Grown voids tend to have complicated shapes (e.g., can have the appearance of a snowflake^[310]).^[305] The film becomes discontinuous when voids impinge and islands of material form.^[307] These evolve into their stable shapes (spherical caps, beads),^[305] exhibiting a wetting angle of $> 0^\circ$. During this transition, finger-like features can form.^[299] No appreciable exchange of mass is observed for islands that are disconnected from any other remaining film area.^[311] A suitable measure for suppressing solid-state de-wetting is the hindrance of surface diffusion either with an adsorbate layer or with a capping layer.^[299] The references listed below confirm and illustrate the relevance of the relationships outlined above for thermally activated gold films of varying thinness.

In the work of Magnozzi et al.^[314], the temperature-induced solid-state de-wetting of thin Au layers on Si wafers, covered by a native oxide

layer, were investigated (layer thickness 20 nm: sample 1, 11 nm: sample 2, and 8 nm: sample 3) in a vacuum chamber. The samples were heated at a rate of 5 °C/min up to 350 °C and thereby annealed. No de-wetting was observed for the 20 nm sample. In case of sample 2, the Au film de-wetted only partly, exposing 15 % of the substrate surface. For the 8 nm sample, complete de-wetting was achieved. Formation of isolated gold particles with different shapes (typical size around 100 nm) occurred. In case of samples 2 and 3, a de-wetting threshold temperature could be established at about 200 °C.

Kwon et al.^[310] studied the de-wetting behavior of Au films with a thickness of 5 nm, deposited on thermally grown SiO₂ by dc magnetron sputtering. Annealing of the films at 300 °C for 15 min in a hydrogen environment achieved complete de-wetting. The average size of the Au islands was about 110 nm. The particle density was $\approx 30/\mu\text{m}^2$. Increasing the annealing time did not alter the results significantly. Further coalescence was too slow at 300 °C.

Gadkari et al.^[307] studied the thermal stability and de-wetting behavior of Au films with thicknesses in the range of 10 to 100 nm, deposited on a thermally grown and 100 nm thick SiO₂ layer on a Si substrate, using ultra-high vacuum dc magnetron sputtering. The films were annealed in a 3 % H₂ in Ar gas mixture at 1 atm and temperatures in the range of 100 to 1000 °C for 30 min. The evaluation criterion was the lowest temperature required for layers to turn non-conductive end to end due to islanding. For a film thickness of 10 nm, that occurred at 150 °C, in the case of 20 nm at 350 °C, and for 50 nm (100 nm) at 540 °C (790 °C). The thicker films required the higher annealing temperature to achieve the same extent of agglomeration within the same time. The agglomeration for all films followed the two-step process of void nucleation and void growth. Voids in all films were typically observed to grow in a branched manner, described as fractals. An encapsulation layer on 20 nm and 50 nm thick Au layer samples of 3 nm and 10 nm thick SiO₂ slowed the void nucleation kinetics. The thicker overlayer had the stronger effect. Otherwise, void growth progressed similarly to that of the bare films. This result hinted at a mechanical hindrance of void initiation at the film surface rather than a surface chemistry effect that modifies the mass

transport on the film top surface.

In summary, the de-wetting studies indicate that smooth gold films with a thickness ≥ 5 nm are likely stable at room temperature. It was shown that encapsulation layers can be effective means to stabilize thin gold films from de-wetting.

2.6 Opto-electronic performance of TEs

The opto-electronic performance of transparent electrodes can be assessed through their two main functional properties: sheet resistance R_{sh} and transmittance T in the visible range (400 to 800 nm). It is desirable to have a low R_{sh} with a high T , but R_{sh} and T can typically not be adjusted independently of each other, resulting in a trade-off: a lower R_{sh} leads to a lower T and vice versa.^[6,148,315]

2.6.1 Sheet resistance

A transparent electrode can be formed from a metal grid on a transparent substrate. The TEs' resistance R is measured between two opposite, parallel contacts of equal length, running perpendicular to the current flow and depends on the dimensions of the TE size. The sheet resistance R_{sh} characterizes the TE's resistance opposing the current flow independent of size. R_{sh} can be calculated as the product of R and the ratio of the TE width W (perpendicular to the current direction) to the TE length L (parallel to the current direction): $R_{\text{sh}} = R \cdot W/L$.^[316] The sheet resistance can be measured on representative square areas of the TE. For rectangular areas, the resistance measurement has to be corrected based on width and length of the rectangle. R_{sh} is measured in ohms (Ω). To avoid confusion with volume resistances, R_{sh} is expressed in "ohms per square" (Ω_{sq} , or Ω/sq , or Ω_{\square} , or Ω/\square). This reflects that R_{sh} corresponds to the resistance R of any representative square TE surface section.^[317,318]

2.6.2 Transmittance

Light can be transmitted, reflected, and absorbed by the TE. The extent of each process is quantified by transmittance T , reflectance R , and

absorbance A . These numbers refer to the respective ratio of the transmitted (P_T), reflected (P_R) or absorbed (P_A) radiant power (radiant energy per time) to the incident radiant power (radiant flux) P_0 . Due to energy conservation, $T + R + A = 1$. If there is a wavelength (λ) dependence, the adjective “spectral” is added (e.g., the spectral transmittance $T(\lambda)$).^[319] The percentage transmittance (T in %) is obtained as $T(\%) = (P_T/P_0) \cdot 100\%$.

If the incident and exiting light are rays of parallel light, the material exhibits regular transmittance (T_{reg}).^[320] If the transmittance results from forward scattering of such incident flux as it travels through the material, the transmittance is referred to as diffuse (T_{diff}).^[320] Snellius’ law^[321] then no longer applies, and the unidirectional incident beam is deflected into many directions. Often both types of transmittances occur simultaneously such that the complete or total transmittance T consists of two parts: $T = T_{\text{reg}} + T_{\text{diff}}$.

Haze (H) is defined as the ratio of T_{diff}^H to the total transmittance T , with T_{diff}^H being defined as the T_{diff} deviating more than 2.5° from the flux undergoing regular transmittance.^[101,322] TEs with high haze values can cause blurriness if used as transparent electrode in displays.^[121,323] The haze of touch screens should thus be less than 1%.^[101] TEs with higher haze can be advantageous for the performance of solar cells: scattering of incoming photons increases their optical path lengths in the active material layer and thus the probability for absorption.^[101,323,324]

Spectral transmittances $T(\lambda)$ of the FTEs in this dissertation were determined as the ratio of the radiant power $P_T(\lambda)$, received at the detector of the spectrophotometer with an FTE sample in the beam path, to the radiant power $P_0(\lambda)$, received without a sample in the beam path.^[325] Baselines of the bare substrates were recorded as reference. A mask with a circular aperture with a diameter of 5 mm ensured that a defined and representative part of the FTE was measured.

2.6.3 Figure of merit (FOM)

A figure of merit (FOM) is a useful indicator of a TE’s opto-electronic performance and allows for a direct comparison with other TEs.^[317]

Fraser and Cook^[326] were the first to use the ratio of T_{500} (%) to

$R_{\text{sh}}(\Omega_{\text{sq}})$ as a figure of merit, with 500 standing for a wavelength λ of 500 nm: $FOM = T_{500}(\%)/R_{\text{sh}}(\Omega_{\text{sq}})$. Later, T_{550} was often used in literature instead of T_{500} , since the human eye has its highest sensitivity at a wavelength $\lambda = 550$ nm.^[6,22,317,323] The *FOM* according to Fraser and Cook^[326] is particularly apt when comparing electrodes of the same design. That is the case, for example, in metal nanogrid electrodes which have the same pattern, but different line dimensions and morphologies. For commercial applications, a TE is typically required to exhibit at least $T > 90\%$ and $R_{\text{sh}} < 100 \Omega_{\text{sq}}$.^[22] That corresponds to a minimum *FOM* of $0.9\%/\Omega_{\text{sq}}$.

Sometimes, the limitation to a single wavelength does not meet the need for high transmittance across a certain range of λ .^[6,317] In such a case, an averaged value (e.g., $\bar{T}_{400-800}$) over the respective wavelength range (e.g., the visible range of 400 to 800 nm) may be used for the calculation of the *FOM*.^[16] This is particularly useful when the TE's dispersion $T(\lambda)$ in that range is not pronounced. Examples for such a case in the visible range are FTEs obtained by direct nanoimprinting of colloidal gold inks.^[35,42,43]

2.7 Scope and objectives of this dissertation

The understanding of the electric performance of transparent (regular) metal grid electrodes which are based on sintered colloidal metal inks is still deficient. Unpatterned (plain) metal film electrodes require low thicknesses (< 10 nm) to achieve reasonable transmittances.^[4] This comes at the price of a significant increase in R_{sh} due to strong electron scattering.^[4] Unlike plain metal films, metal grid electrodes ensure high transmittances through their voids. Thus, the dimensions of their grid lines can be above the mean free path of electrons in bulk metal (λ_{metal}^e) without suffering a significant loss in transmittance.^[4] For Au, λ_{Au}^e is ≈ 38 nm at RT.^[16] Consequently, such “highly transmissive” metal grid electrodes should allow resistivities/conductivities close to those of the bulk counterpart.

The potential of transparent metal grid electrodes, based on sintered metal nanoparticles, has not been fully exploited yet.^[35,36,38] This also ap-

plies for the readily percolating grids imprinted from AuNWs capped with OAm monolayers and dispersed in cyclohexane solvent, even if sintered in low pressure H₂/Ar plasma rather than thermally.^[35,42] Experimental transmittances could be modeled sufficiently well when assuming the grid lines as opaque rectangles. In contrast, R_{sh} , calculated based on Kirchhoff's circuit laws, the determined grid line geometries, and the resistivity of bulk gold, were up to above an order of magnitude smaller than what was measured, despite all dimensions of the grid lines being well-above $\lambda_{\text{Au}}^{\text{e}}$.^[35,42]

This discrepancy indicates that the structure-property relationship governing the electric performance of nanoimprinted and plasma sintered metal conductors is not yet well understood. That is, however, a major piece of the puzzle to change the fabrication of metal grid FTEs via direct nanoimprinting of colloidal gold nanoparticle inks such that they maintain their high transmittance while improving their R_{sh} . Gaining this understanding is the first objective of this dissertation.

To that end, FTEs were nanoimprinted as grids of straight, parallel lines from OAm-stabilized AuNWs/AuNPs dispersed in cyclohexane, using the same PDMS stamp. The inks were systematically varied in their gold concentration c_{Au} . Printed grids were converted into metal lines by low pressure H₂/Ar plasma sintering. Due to different concentrations c_{Au} and/or particle geometry, the sintered lines varied in width w and maximum height h_{max} at a pitch p . The FTEs' opto-electronic performance was quantified by measuring $\bar{T}_{400-800}$, R_{sh} , and calculating their ratio (FOM). Small-angle X-ray scattering (SAXS) revealed the structural arrangement of the Au nanoparticles within the pre-plasma lines right after imprinting as well as the colloidal state of order and the size of the Au nanoparticles in the inks. Additional pre- and post-plasma top-view scanning electron microscopy (SEM) images of the imprinted grids, transmission electron microscopy (TEM) images of dried ink droplets and of cross-sections of pre- and post-plasma lines as well as the electrodes' surface topographies and conductor geometries in the sintered state, obtained via confocal laser scanning microscopy (CLSM), revealed the grid morphology. The comparison of morphology with performance, both as a function of nanoparticle shape and c_{Au} , led to the desired understanding.

The stability of nanoimprinted, plasma sintered TEs is another knowledge gap in the state of the art. In case of such pure gold electrodes, with all dimensions of their grid lines $> \lambda_{\text{Au}}^e$, the morphology and thus the performance was expected to be stable, at least during storage under ambient conditions. The clarification of the stability issue was the second objective of this dissertation. The strategy followed here was to use the same kind of FTEs imprinted as described above to unravel structure-property relationships. Monitoring their relevant opto-electronic performance parameters during storage at $\approx 22^\circ\text{C}$ and $\approx 55\%$ rH in the dark and observing the grid morphology by SEM and TEM, revealed changes that could then be correlated. In the event of unforeseen instability, overcoming it was an additional objective. The strategy was to slow down the kinetics of the underlying mechanism. Of particular interest was whether the difference in particle geometry (spheres versus ultra-thin, high aspect ratio wires) is noticeable in the opto-electronic performance and ageing behavior of the imprinted FTEs.

A further knowledge gap concerns the bundling of AuNWs coated by a single OAm ligand shell. Such bundling is known to occur in n-alkanes like n-hexane and is well understood,^[118,236] but has not been observed yet in cycloalkanes such as cyclohexane^[118,236]. The concentration-dependent agglomeration of such AuNWs in the solvent cyclohexane, leading to the formation of crystalline hexagonal wire bundles at low Au concentrations only, was first observed during the course of this dissertation.

Kister et al.^[43] found that longer-chain alkylamine ligands allow Au nanospheres (3.2 nm in diameter) in cyclohexane to agglomerate only at high Au concentrations. This proved essential for the formation of continuous lines when nanoimprinting from such colloidal solutions. Similarly, Doblus et al.^[247] found that the agglomeration concentration c_{lim} of gold nanospheres (size 3.4 nm) with an octanethiol ligand shell is two orders of magnitude higher when dispersed in cyclohexane than in n-heptane. Maurer et al.^[42] assumed that cyclohexane keeps AuNWs with OAm ligand shell similarly dispersed.

The third objective of this dissertation is thus to understand the peculiar behavior of the above colloidal solutions of AuNWs in cyclohexane: what differentiates the solvent n-hexane from cyclohexane, and

the spheres capped with longer-chain alkylamine ligands from OAm-capped AuNWs? This matters since the tendency of nanoparticles to self-assemble within colloidal inks can significantly affect the imprinting of transparent electrodes from such inks.^[35,42,43] Two characterization methods are of importance in that regard: thermogravimetry (TGA) of dried AuNW/AuNP inks which allows to measure the amount of OAm ligand in the ink, and SAXS which can be used to determine the colloidal state of order of the dispersed AuNWs/AuNPs.

Chapter 3

Results

3.1 Publication 1

Reprinted with permission from

S. Bettscheider, B. Kuttich, [L. F. Engel](#), L. González-García, and T. Kraus: “Bundling of Nanowires Induced by Unbound Ligand”.
J. Phys. Chem. C, 2021, 125, 6, 3590–3598.
DOI: [10.1021/acs.jpcc.0c10919](https://doi.org/10.1021/acs.jpcc.0c10919).

Copyright 2021 American Chemical Society.

Bundling of Nanowires Induced by Unbound Ligand

Simon Bettscheider, Björn Kuttich, Lukas F. Engel, Lola González-García, and Tobias Kraus*

Cite This: *J. Phys. Chem. C* 2021, 125, 3590–3598

Read Online

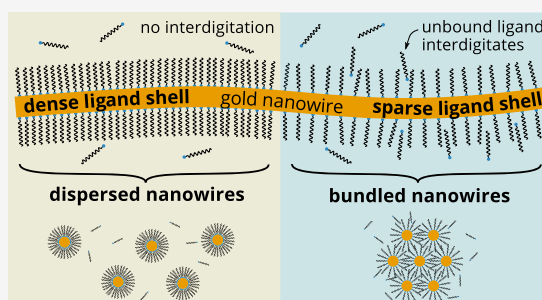
ACCESS |

Metrics & More

Article Recommendations

Supporting Information

ABSTRACT: We report on the dilution-induced agglomeration of ultrathin gold nanowires (AuNWs) into regular bundles. Wires with a metal core diameter of 1.6–1.7 nm surrounded by a ligand shell of oleylamine formed stable colloids in *n*-hexane and cyclohexane. Dilution with pure solvent induced the self-assembly into bundles with a regular, hexagonal cross-section. Small-angle X-ray scattering and thermogravimetric analysis indicated that bundles formed only if the ligand shell was sufficiently sparse. Dilution with pure solvent shifts the chemical equilibrium and reduces the ligand density, thus enabling agglomeration. We show that agglomeration is driven not by van der Waals forces but by the depletion forces of linearly shaped molecules. Linear solvent molecules or small amounts of unbound ligand align normal to the nanowire if the ligand shell is sparse. The resulting reduction in entropy creates a driving force for the AuNWs to bundle such that the low-entropy domains overlap and the overall entropy is increased. Dilution-induced nanowire bundling is thus explained as a combined effect of ligand desorption and destabilization by depletion.



INTRODUCTION

Ultrathin nanowires are chemically synthesized, solid objects that form colloidal dispersions in suitable solvents. Such wires can be several micrometers long but a few nanometers in diameter, mechanically flexible, and mobile enough to align laterally. Attractive forces that act along the length of two adjacent wires can lead to unusual colloidal properties. Even weak attractive forces accumulate and lend the wires a strong tendency to assemble into elongated bundles. The colloidal stability of ultrathin nanowires thus differs from that of spheres with similar molecular structures and diameters.

Here, we discuss an unusual agglomeration mechanism of ultrathin gold nanowires (AuNWs) in alkanes. The wires agglomerate and form bundles upon dilution, a type of colloidal instability that has not yet been observed in other nanoparticle systems. For example, spherical nanoparticles with nonpolar ligand shells agglomerate at increasing particle concentrations with a solubility that depends on the solvent.¹ Apparently, the colloidal stability of AuNWs cannot be understood in similar terms.

We link the dilution-induced destabilization of AuNWs to the depletion of unbound ligand molecules. Such unbound (also called “free” or “solvated”) ligands are in a dynamic equilibrium with adsorbed (“coordinated” or “bound”) ligands.^{2,3} The number ratio between unbound and adsorbed ligands depends on the adsorption energy of the ligand, among other factors. Their role in the colloidal stability of ultrathin nanowires has not yet been discussed.

Ultrathin gold nanowires can be synthesized by reducing chloroauric acid in the presence of the ligand oleylamine. This

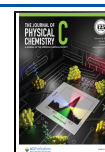
route was pioneered by Halder and Ravishanker in 2007⁴ and advanced by several research groups in 2008.^{5–8} The resulting nanowires consist of a gold core of diameter of 1.6 to 1.7 nm (corresponding to 6 to 7 gold atoms along the diameter) surrounded by an organic ligand shell of oleylammonium chloride of similar thickness. The wires reach typical lengths of 4 μm ,^{5,6} although up to 6.4 μm long wires have been observed.⁹

Large aspect ratios above 1:10³ and their electrically conductive cores make AuNWs appealing as nanoscale building blocks. For example, Gong et al.¹⁰ created monolayers of AuNWs on polydimethylsiloxane in order to create flexible electrodes for supercapacitors. Porter et al.¹¹ used striped phases of phospholipids to precisely align individual wires over micrometer-wide areas. Roy et al.¹² demonstrated that AuNWs are suitable as chemical sensors to detect CO, CH₃NH₂, and CH₃CHO. Reiser et al.¹³ spun AuNWs into free-standing macroscopic fibers with a mechanical strength that could be tuned by varying the alignment of the AuNWs. Many applications require control over nanowire bundling. For example, our group reported that the printing of AuNW meshes for flexible and transparent conductive electrodes

Received: December 7, 2020

Revised: January 25, 2021

Published: February 3, 2021



requires that the wires bundle inside the structuring stamp and not earlier.¹⁴

The formation of AuNW bundles has already been reported in the first synthesis papers,^{6,15} and some of its mechanisms are well understood. As-synthesized AuNWs carry a double layer of oleylammonium chloride/oleylamine and arrange into bundles with two-dimensional hexagonal packing cross-section at a center-to-center interwire distance of 9.5 nm.^{16,17} Purification decreased the interwire distance to 5.5 nm for AuNWs in *n*-hexane.¹⁷ No bundles were observed for AuNWs redispersed in cyclohexane.¹⁷ Tighter bundles form in polar solvents such as ethanol in order to reduce the AuNW–solvent interfacial area.¹⁸ The lattice constant of bundles has been tuned by modifying the ligand shell. For example, Nouh et al. reduced the center-to-center distance from 5.5 to 3.8 nm by replacing oleylamine with the shorter trioctylphosphine. Molecular dynamics simulations showed that the driving force for bundling in linear alkanes such as *n*-hexane is entropic:¹⁸ solvent molecules close to the ligand shell align normal to the nanowire surface and lose entropy. Bundling excludes (“depletes”) solvent molecules from the ligand shells and decreases the loss in entropy.

In the following, we focus on the unexpected bundling of nonpolar AuNWs upon dilution. We find that AuNWs remain dispersed in nonpolar solvents at large nanowire concentrations but form bundles at smaller concentrations, whereas most colloidal systems become more stable at lower concentrations. Small-angle X-ray scattering and thermogravimetric analysis were used to assess the role of the amount of ligand present in the system. Our results indicate that a combination of ligand desorption and the depletion of unbound ligand can initiate bundling.

METHODS

Synthesis of Ultrathin Gold Nanowires. Materials. Hydrogen tetrachloroaurate trihydrate (HAuCl₄·3H₂O) was synthesized following Schubert et al.²⁰ and was dried for at least 30 min on a Schlenk line (<1 mbar). Oleylamine (OAm), 80–90% C18, was purchased from Acros Organics and filtered with a syringe filter (Millex, 0.45 μm, hydrophobic PTFE). All other chemicals were used as received. Triisopropylsilane (TIPS), 98%, and *n*-hexane, ≥99%, were obtained from abcr. Absolute ethanol (EtOH), ≥ 99.8%, was provided by Fisher Scientific. Cyclohexane, ≥99.9%, was received from Carl Roth.

Synthesis. AuNWs were synthesized under ambient conditions using the protocols of Feng et al.¹⁵ and Nouh et al.¹⁹ For a typical synthesis, 60 mg of the dry precursor HAuCl₄·3H₂O was quickly weighed into a 50 mL glass snap-on vial preflushed with Ar, and the sample was immediately covered with 9.9 mL of the solvent *n*-hexane. Then 2.04 mL of the ligand OAm was added, and the resulting mixture was thoroughly vortexed for 5 min (both under Ar) to achieve complete dissolution of the precursor. Subsequently, 3.06 mL of the reducing agent TIPS was added, and the obtained mixture was vortexed for 30 s (both under Ar). The solution was then kept still under Ar at 25 °C for 24 h without stirring. As the reaction progressed, the solution's color evolved during the first hours from orange to bright yellow to pitch black as the precursor was being reduced, the AuNWs grew and consequently the light scattering changed.

Purification. Three different purification protocols were used (see main text), differing in the number of carried out cycles and whether precipitation was accelerated by

centrifugation. Each purification cycle consisted of adding two volumes of ethanol, precipitating the AuNWs either by sedimenting for 10 min or by centrifuging at 100 rcf for 1 min, followed by removal of the supernatant and resuspension in the desired solvent.

Transmission Electron Microscopy. Samples for observation in transmission electron microscopy were prepared by diluting the dispersion of AuNWs to a concentration of approximately 0.05 mg/mL and drying an amount of 3 μL on a carbon-coated copper grid (Plano, Germany). The samples were observed at an acceleration voltage of 200 kV in the JEM 2010 microscope (JEOL).

Thermogravimetric Analysis. Samples for thermogravimetric analysis were prepared by drying an amount of 1 mL of a dispersion of AuNWs at 2 mg/mL in a crucible made from aluminum oxide. To remove any moisture, the samples were dried in a vacuum oven overnight before being placed in the analyzer (Netsch STA 449 F3 Jupiter). The samples were heated from room temperature to 1000 °C at a rate of 10 °C/min under argon followed by an isothermal stage of 10 min under oxygen while the mass of the samples was continuously recorded.

The ratio of ligand molecules to gold atoms and the grafting density were determined assuming that the residual mass was pure gold and the loss pure oleylammonium chloride. We assumed an AuNW core diameter of 1.65 nm, consistent without our SAXS measurements and literature.^{5,7,16}

Small-Angle X-ray Scattering. The colloidal state of AuNWs was observed by small-angle X-ray scattering (SAXS). Samples were let rest at least 16 h before being filled into glass capillaries with an inner diameter of 1.5 mm for the SAXS measurement. The scattering setup (XEUSS 2.0, XENOCs,) used a Cu Kα source, and the scattered beam was captured by a detector (PILATUS3 R 1 M DECTRIS) at a distance of approx. 550 mm from the sample. The exact sample-to-detector distance was calibrated with a standard of silver behenate prior to each measurement. If not noted otherwise, each sample was measured for a total duration of 25 min. The two-dimensional scattering images were azimuthally integrated with the software Foxtrott (Synchrotron Soleil) to obtain scattering curves. To correct for the background, the respective solvent was subtracted from all scattering curves.

The (center-to-center) interwire distance *d* in bundled AuNWs was determined following Förster et al.²¹ using

$$q_{hk} = \frac{4\pi}{\sqrt{3}d} \sqrt{h^2 + hk + k^2} \quad (1)$$

where q_{hk} is the value of the *q*-vector of the Bragg scattering peak of two-dimensional hexagonal lattice with the Miller indices *h* and *k*.²¹

Analysis of the Ratio of Bundled and Dispersed Nanowires. The ratio of bundled and dispersed nanowires was obtained from small-angle X-ray scattering data using a scattering model. The scattering of single, well-dispersed nanowires can be approximated by the form factor of a cylinder with a variable diameter. Polydispersity is taken into account by convolution with a Schulz–Zimm distribution. The length of the cylinder is too large to be resolved by our SAXS instrument and will be assumed to be infinity, resulting in a power-law decay of intensity at the lowest measured scattering vectors *q* which is proportional to q^{-1} .^{16,22,23} Scattering from bundled nanowires was modeled by multiplying the cylindrical form factor with the structure factor of a 2D hexagonal lattice,

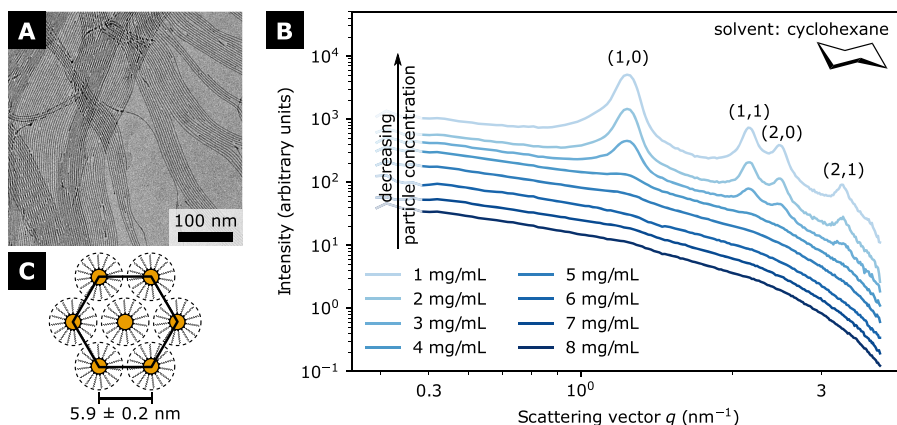


Figure 1. (A) Transmission electron micrograph (TEM) of ultrathin gold nanowires. (B) Radially integrated small-angle X-ray scattering (SAXS) curves of ultrathin gold nanowires in cyclohexane at different concentrations. The tuples indicate a two-dimensional hexagonal lattice; curves were shifted vertically for visibility. (C) Schematic of the hexagonal packing and center-to-center distances with mean and standard deviations of 82 samples.

which is the sum of Lorentzian functions at the respective positions of the Bragg-peaks. Disorder of the lattice due to thermal fluctuations for example was taken into account by a Debye–Waller factor.^{16,22,23} Concurrent scattering from both dispersed and bundled nanowires was modeled by a weighted sum in scattered intensity of both dispersed and bundled contributions, with the weighting factor allowing to determine the dispersed/bundled ratio.

RESULTS

Ultrathin gold nanowires with uniform core diameters and oleylamine (OAm) shells were prepared using a well-established synthesis in *n*-hexane, purified, and redispersed in cyclohexane.^{15,19} The resulting wires had diameters in the range of 1.6–1.7 nm and lengths exceeding 427 nm according to transmission electron microscopy (TEM); see Figure 1A. Small-angle X-ray scattering (SAXS) indicated full dispersion in cyclohexane (Figure 1B), without signs of bundling at large gold concentrations of $[\text{Au}] \gtrsim 5 \text{ mg/mL}$ (2.5 times above that during synthesis). Dilution of the dispersion with pure cyclohexane to concentrations $\lesssim 4 \text{ mg/mL}$ led to scattering peaks with a hexagonal arrangement (see Figure 1C) that have been reported for bundled AuNWs previously.^{13,16,17,19} Here, the center-to-center distance was $5.9 \pm 0.2 \text{ nm}$.

Dilution reduces the concentration of both wires and OAm in the dispersion. Since a dynamic equilibrium exists between adsorbed and unbound OAm,^{2,3} diluting will affect the ratio of adsorbed and unbound ligand and will decrease the ligand shell density (see illustration in Figure 2A). Oleylamine-coated gold nanowires are colloidal stabilized by the interactions between solvents and OAm shells.¹⁷ Changing the ligand density can therefore affect their stability, too. A rigorous analysis of the destabilizing mechanism of dilution requires the analysis of both OAm concentration in the solvent and ligand shell density.

The amount of OAm in freshly prepared AuNW dispersions depends on the purification protocol. The literature contains different approaches to remove the excess OAm after synthesis; they involve precipitation by ethanol (sometimes with the aid of centrifugation), removal of the supernatant, and resuspension. We used three different protocols to purify AuNWs after synthesis (Figure 2B): one cycle of centrifugation

at 100 rcf for 1 min (sample 1), two cycles of sedimentation for 10 min (sample 2), and two cycles of centrifugation at 100 rcf for 1 min (sample 3). Appropriate dilution ensured that the AuNW concentration remained constant for all three samples. The three resulting dispersions were then dried and analyzed for their organic content.

Thermogravimetric analyses in Figure 2C and Table 1 indicated distinct, but quantitatively different mass losses between 140 and 470 °C in argon and after oxygen introduction for all samples. The greatest loss of $52.2 \pm 5.2 \text{ wt\%}$ was observed for sample 1 (Figure 2B). It is reasonable to assume that all losses were due to the decomposition of OAm, which implies a ratio of 0.708 ± 0.148 ligands per gold atom, far below the 40 ligands per gold atom used in synthesis.^{15,16,24} This corresponds to a nominal ligand density of $17.3 \pm 3.6 \text{ ligands/nm}^2$, far above the values around 4–6 ligands/nm² that are often reported for gold nanoparticles.²³ Thus, sample 1 must have contained considerable amounts of unbound ligand. Sample 2 contained 0.216 ± 0.013 ligands per gold atom corresponding to an intermediate nominal density of $5.3 \pm 0.3 \text{ ligands/nm}^2$, while sample 3 only contained 0.183 ± 0.002 ligands per gold atom, corresponding to $4.5 \pm 0.1 \text{ ligands/nm}^2$ (Figure 2B). It is not possible at this stage to differentiate unbound from adsorbed OAm. It is clear, however, that samples 1–3 contained different total [OAm] values, and it is very likely that both the ligand density and the unbound OAm concentration were different for each sample.

We split and diluted the three samples 1–3 to observe the effects on colloidal nanowire stability. Each sample was split in eight aliquots, and pure cyclohexane was added to create series with gold concentrations [Au] in the range of 1 to 8 mg/mL. We let the samples equilibrate for at least 16 h and then used SAXS to detect bundling for the full series (Figure 2D–F). Clear scattering peaks from the diluted samples with the smallest $[\text{OAm}]/[\text{Au}] = 0.18$ (Figure 2D) indicated considerable bundling of up to 75% of AuNWs, while the samples with the greatest $[\text{OAm}]/[\text{Au}] = 0.71$ had no bundling visible in SAXS; see Figure 2F (we estimate the limit of detection for bundles at approximately 5%). Bundling in the sample with intermediate $[\text{OAm}]/[\text{Au}] = 0.22$ began at

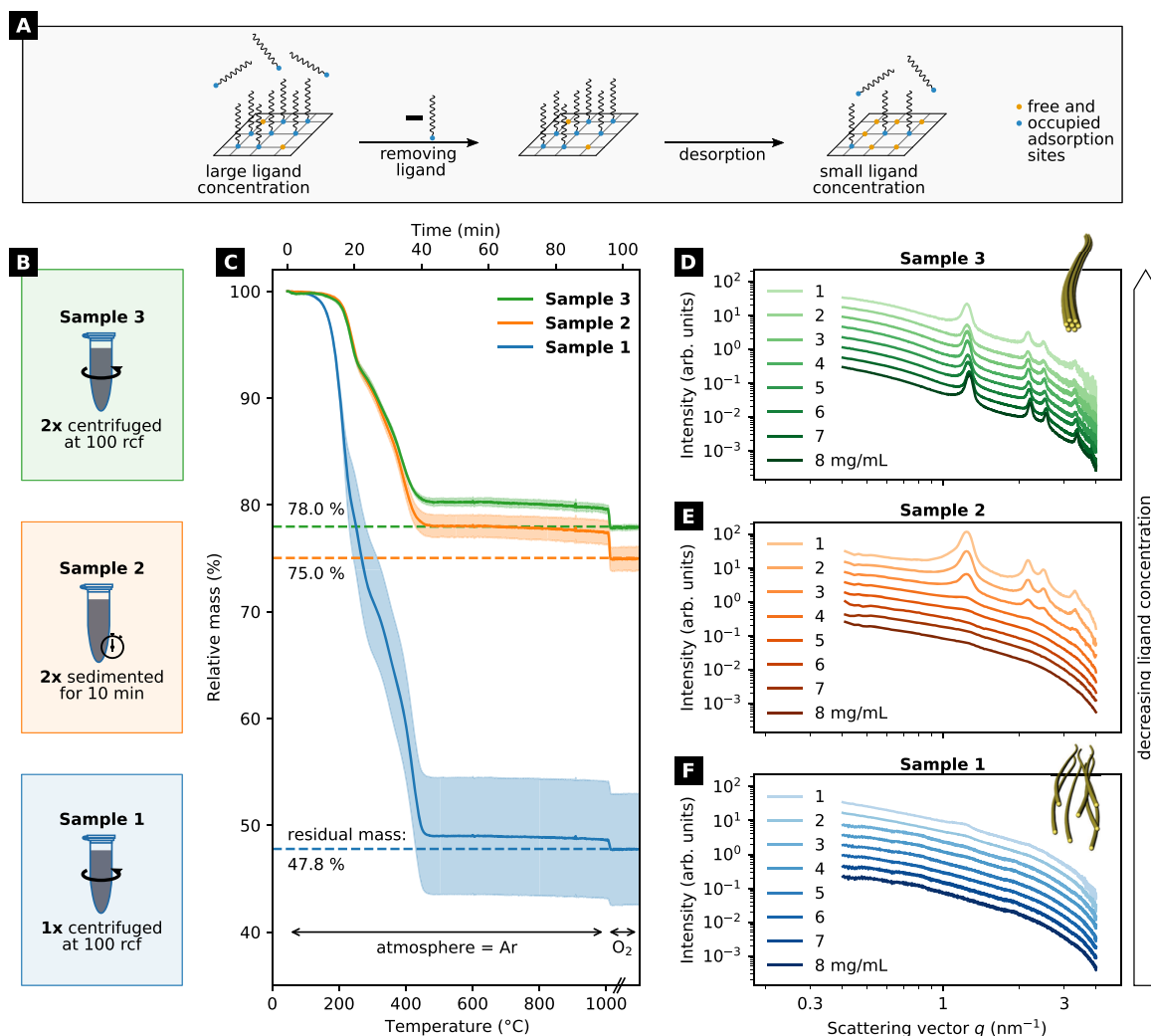


Figure 2. (A) Dilution and purification of AuNW dispersions shifts the adsorption equilibrium between free and adsorbed ligands to fewer adsorbed ligands and “removes” ligands from the particles into the solvent. The extent of removal depends on the exact protocol. (B) Purification of the as-synthesized samples involved precipitation by ethanol, removal of the supernatant, and resuspension. We tested three purification protocols that differed in the number of purification cycles and use of centrifugation. (C) Thermogravimetric analysis (TGA) of dried AuNWs prepared with different purification protocols indicated differences in organic content. The shaded areas indicate ± 1 standard deviation of three independently prepared samples. (D–F) Strong peaks in SAXS of sample 3 indicate that the AuNWs with the smallest OAm content agglomerated into hexagonal bundles (see inset) at all concentrations. Sample 2 did not exhibit such peaks until diluted to approximately 4 mg/mL. Sample 1, with the highest OAm content, did not agglomerate even upon maximal dilution. (The SAXS curves are shifted vertically for better visualization.)

Table 1. Amount of Ligand in the Three Different Samples as Obtained from the Thermogravimetric Analysis

sample name	purification protocol	residual mass (wt %)	amount of ligand ([OAm]/[Au])	nominal density (ligands/nm ²)
sample 1	centrifuged once	47.8 \pm 5.2	0.708 \pm 0.148	17.3 \pm 3.6
sample 2	sedimented twice	75.0 \pm 1.1	0.216 \pm 0.013	5.3 \pm 0.3
sample 3	centrifuged twice	78.0 \pm 0.2	0.183 \pm 0.002	4.5 \pm 0.1

a dilution of $[Au] \approx 4$ mg/mL and increased upon further dilution.

These results indicate a stabilizing effect of OAm that is reduced by dilution. We further investigated this correlation by adding pure OAm to the dispersions. Sample 2 was enriched with 1 mol of OAm for every mole of gold in order to reach $[OAm]/[Au] = 1.2$ at $[Au] = 6$ mg/mL. This did not initiate any bundling visible in SAXS (see Figure S3 in the Supporting

Information). Sample 3 was diluted to 2 mg/mL with pure cyclohexane, which initiated bundling. Subsequent addition of 0.031 to 2.0 mol OAm per mol gold led to deagglomeration of the AuNWs according to SAXS (Figure 3B).

We quantified the stabilizing effect of OAm using a SAXS scattering model (Figure 3B).^{16,22,23} The model fits provide the ratio of bundled and dispersed AuNWs (Figure 3C), the diameter of the bundles' cross sections (Figure 3D), and the

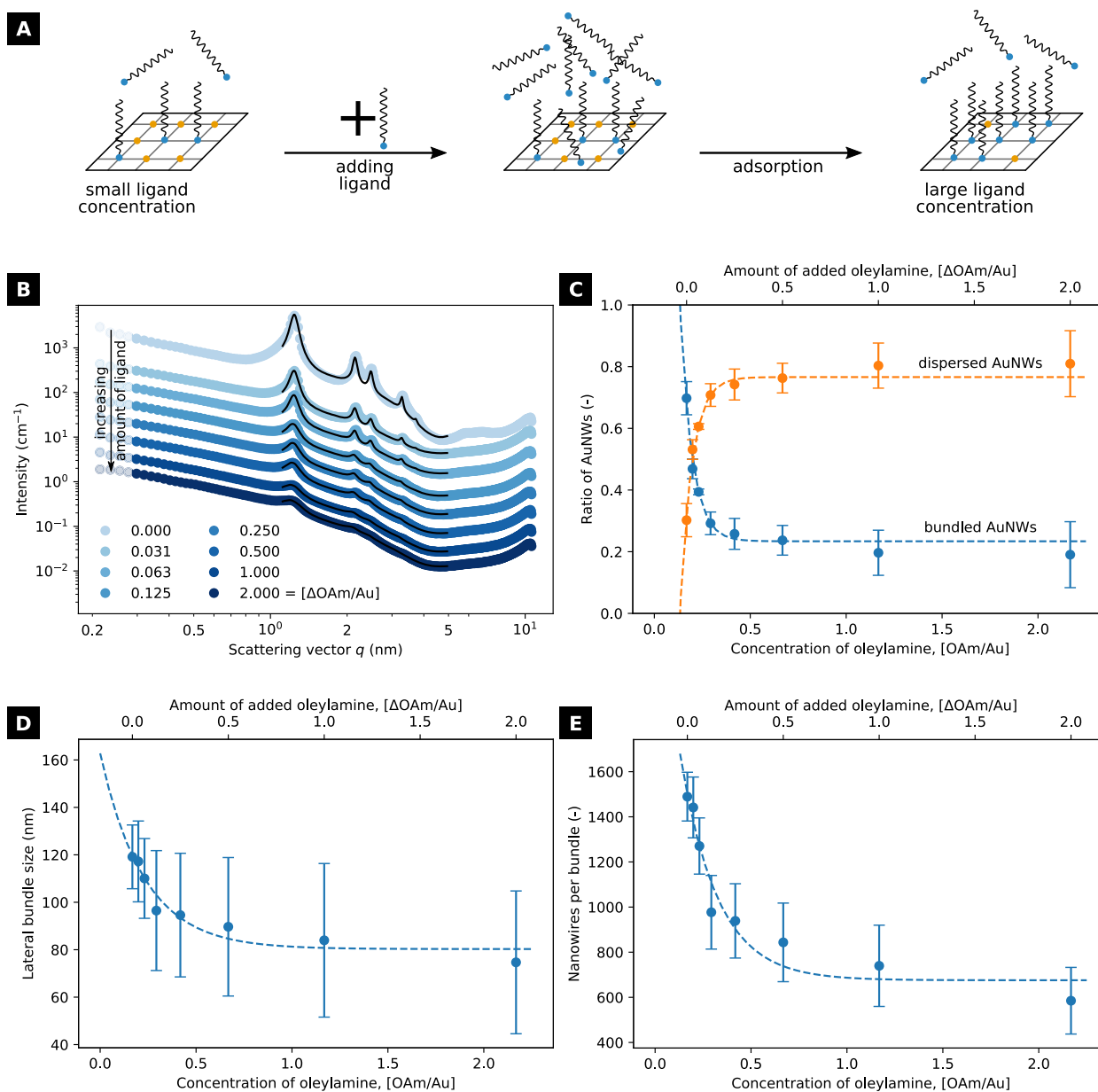


Figure 3. (A) Adding pure OAm ligand to AuNW dispersion shifts the equilibrium and leads to denser ligand shells. (B) Degree of bundling in sample 3 at a gold concentration of 2 mg/mL decreased upon addition of pure OAm. The black solid lines show fits based on a scattering model for bundled cylinders.^{16,22,23} The scattering curves (with the exception of that for $[\Delta\text{OAm}/\text{Au}] = 2.0$) are shifted for better visualization. (C) Ratios of bundled and dispersed AuNWs as obtained by the fits in part B. Error bars equal ± 1 standard deviation from three independent experiments. (D) Average lateral sizes of AuNW bundles and (E) average number of AuNWs per bundle as a function of $[\text{OAm}]$. The dashed lines are exponential fits.

number of nanowires per bundle (Figure 3E) as a function of $[\text{OAm}]/[\text{Au}]$. Small changes in $[\text{OAm}]$ strongly affected bundling: increasing $[\text{OAm}]/[\text{Au}]$ from 0.168 to 0.231 reduced the fraction of bundled AuNW from 0.7 to 0.39.

The exchange between adsorbed and unbound oleylamine is fast (on the millisecond time scale) so that AuNW dispersions rapidly reach an equilibrium.^{26,27} The maximum ligand shell density of AuNW and the change of shell density with $[\text{OAm}]$ is presently unknown. The following considerations provide useful estimates. We purified as-synthesized AuNWs three

times by centrifugation and determined $[\text{OAm}]/[\text{Au}]$ for each purification cycle. The ratio dropped from 40 ligands per gold atom to 0.708 ± 0.148 ligands per gold atom in the first purification cycle, then to 0.183 ± 0.002 , and, finally, to 0.178 ± 0.008 ligands per gold atom (see Figure S1 in the Supporting Information), which corresponds to 4.5 ligands/nm². This provides an upper limit for the ligand shell density of the AuNWs. A dense alkanethiol monolayer on a flat gold surface has been reported to contain 4 ligands/nm².²⁸ Thermodynamic data indicates a free energy of adsorption

for OAm on Au of $\Delta G_{\text{ads}} = -8.1$ kJ/mol (see details in the Supporting Information).^{19,28–34} Assuming equilibrium between unbound and adsorbed OAm and using the above numbers suggest that agglomeration was induced at a grafting density of about 90% corresponding to 4.1 ligands/nm².

Dilution-induced agglomeration of AuNWs apparently requires an incomplete ligand shell. The sparse shell induces enthalpic and/or entropic attraction between the wires. Temperature-dependent stability data can help in distinguishing enthalpic from entropic mechanisms. We diluted sample 2 to $[\text{Au}] = 4$ mg/mL and observed bundling with SAXS at temperatures between 25 to 65 °C. Each temperature was held for 15 min to ensure thermal equilibration. The fraction of bundles at 25 °C was minute; it increased to 45% when increasing the temperature to 65 °C. The center-to-center distance slightly increased from 5.9 to 6.1 nm. Given that Brownian motion increases with temperature, this result clearly suggests an entropic origin of dilution-induced AuNW agglomeration.

Finally, we tested whether bundle formation upon dilution is unique to cyclohexane or occurs in other solvents, too. To this end, AuNWs were synthesized and purified as for samples 1 and 3 but were redispersed in *n*-hexane instead of cyclohexane. We diluted the new samples with *n*-hexane and detected bundling via SAXS as shown in Figure S4 in the Supporting Information. The results were qualitatively similar to the situation in cyclohexane: scattering peaks indicative of bundles were only present at small $[\text{OAm}]$. The transition occurred at $[\text{OAm}] \approx 14.2$ mmol/L, which was far above that for cyclohexane (≈ 3.2 mmol/L).

DISCUSSION

The aim of the following discussion is to identify the most likely mechanism of dilution-induced bundling in AuNWs. First, we discuss and rule out well-known agglomeration mechanisms. An entropic model based on the depletion of unbound ligand is then introduced and shown to be consistent with the experimental results.

Solid particles in nonpolar dispersions attract each other due to dispersive van der Waals (vdW) forces. Stability requires opposing them with repulsive interactions; these are often entropic or “steric” forces caused by the overlap of ligand shells.^{35–37} The magnitude of such repulsive forces depends on the length of the ligands and their grafting density. Shorter ligands and smaller grafting densities reduce repulsion.^{38–41}

Reducing the grafting density of ligands on AuNWs by dilution could induce bundling by reducing steric repulsion so that vdW forces become dominant. However, several experimental observations are inconsistent with this idea. First, bundling driven by vdW forces should lead to compressed ligand shells. The measured interwire distance (center-to-center) in cyclohexane was 5.9 ± 0.2 nm, above the distance of 5.5 nm reported for neighboring nanowires whose ligand shells no longer touch.¹⁸ Second, the vdW interaction energy between two parallel gold cylinders with a diameter of 1.7 nm at a distance of 5.9 ± 0.2 nm in alkanes is very likely too small to cause agglomeration. An estimate using standard expressions (eq S2 in the Supporting Information; see, for example, Parsegian⁴²) indicates an interaction energy of approximately $1.245 \times 10^{-3} k_{\text{B}}T/\text{nm}$ of wire contact, below the thermal energy even if two AuNWs formed contact over several hundred nanometers. Third, raising the temperature increased bundling, which indicates an entropic rather than an

enthalpic mechanism (see Figure 4). Note that increasing temperature may affect the ligand shell density by shifting the

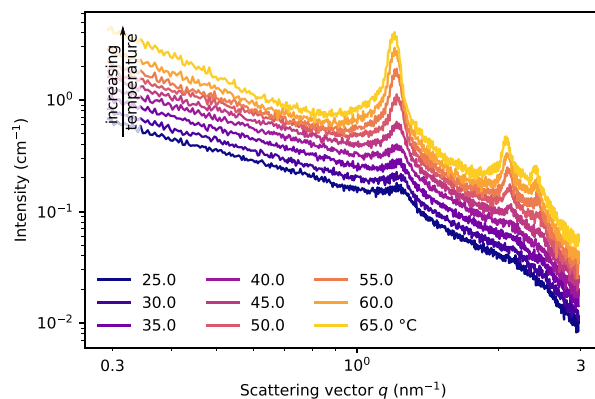


Figure 4. Temperature-dependent SAXS on sample 2 at $[\text{Au}] = 4$ mg/mL. Increasing temperatures led to additional bundling as visible in the growing structure peaks.

adsorption equilibrium. However, we found that AuNW spacing increased with temperature and conclude that an entropic destabilization mechanism is at play.

The bundling of AuNWs in linear alkanes has recently been explained with the depletion of ordered solvent molecules in the direct vicinity of the ligand shell.¹⁸ Dense wire packing reduces the loss in rotational entropy of solvent molecules, because the bundled wires share domains of ordered solvent. The resulting entropic force is attractive (on the order of $0.2 k_{\text{B}}T/\text{nm}$ of wire contact) and leads to bundling. Our experiments show that this mechanism can be induced by dilution, because it requires sufficiently sparse ligand shells (Figure S4 in the Supporting Information). Could this entropic mechanism explain the effect of dilution-induced bundling in cyclic alkanes, too?

The entropic mechanism requires solvent molecules that align in the ligand shell. The structure of cyclohexane makes it difficult for the molecule to align in a way that markedly reduces entropy. The linear ligand molecule OAm, in contrast, readily aligns and is known to interdigitate into the ligand shell.⁴³ It is very likely that unbound OAm plays the role of *n*-alkanes in entropic bundling¹⁸ for the case of dilution-induced bundling in cyclohexane. Unbound OAm that interdigitates in the shell of bound OAm loses entropy (upper part of Figure 5B). When AuNWs bundle, they can share ordered OAm molecules so that the low-entropy domains overlap and some of the entropic losses are avoided (lower part of Figure 5B). Dense ligand shells prevent preferential alignment of unbound OAm and remove the driving force for bundling (Figure 5A).

It is instructive to compare this mechanism to the action of the well-known “depletion forces” that can initiate agglomeration of colloidal particles. Depletion forces can occur if a colloid contains smaller particles or molecules (the “depletants”) that cannot enter the liquid volumes in the immediate vicinity of the larger particles. The resulting gradients in depletant concentration give rise to an osmotic pressure that pushes the larger particles together.^{36,37,44} The concentration gradient can be due to steric limitations or (for anisotropic depletants) entropic constraints. For example, rod-shaped depletants that orient parallel to the surface of the larger particles lose rotational entropy and thus form a concentration

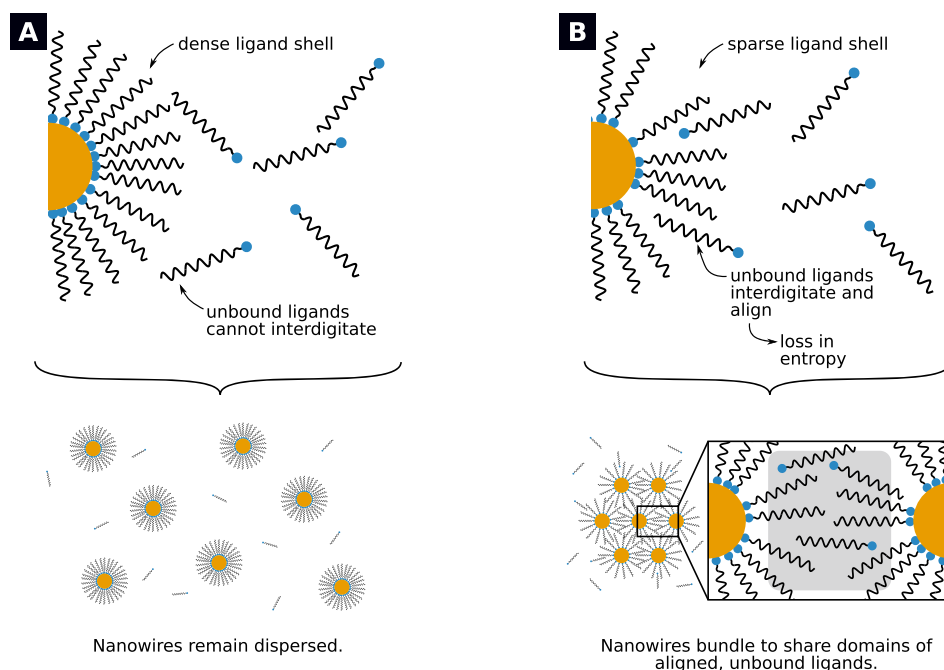


Figure 5. Illustration of the proposed mechanism. (A) Dense ligand shells preclude interdigitation of unbound ligand into the shell. (B) Sparse ligand shells provide gaps where unbound ligand can interdigitate and orient. The associated decrease in entropy is minimized if nanowires form bundles to share domains of ordered ligands (shaded area). The drawings are approximately to scale and show the cross sections of a 1 nm-long wire segment with a shell denser (4.5 ligands/nm^2) (A) and sparser (3.6 ligands/nm^2) (B) than the measured threshold for bundling (4.1 ligands/nm^2).

gradient.^{45–51} One may argue that the mechanism above involves a depletion force that is caused by alignment of the depletant OAm normal to the AuNW surface in the sparse ligand shell.

The role of unbound molecules in nonpolar dispersions has recently attracted interest more broadly. Current reports indicate that the formation of nanoparticle superlattices from nonpolar solvents can be tuned by adding unbound oleic acid or oleylamine to the dispersion, where they act as depletants.^{43,52–55} Winslow et al.⁴³ used molecular dynamics simulations to show that free oleic acid preferably interdigitates into ligand shells and associated this ligand shell swelling with a change in the crystal structure from bcc to fcc. Baranov et al.⁵² assembled semiconductor nanorods covered by phosphonate and trioctylphosphine oxide into hexagonal arrays by adding oleic acid and other macromolecules. These reports highlight the role of unbound ligands and similar molecules as destabilizing agents.

CONCLUSIONS

We studied the agglomeration of AuNWs into crystalline bundles upon dilution. Only AuNWs with sufficiently sparse ligand shells exhibit this unusual type of self-assembly. We show evidence for an entropy-driven self-assembly mechanism based on the depletion of linear molecules. Linear solvent or unbound ligand molecules initiate bundling when they interdigitate into the ligand shell and lose some of their rotational entropy.

Note that unbound ligands are in a dynamic equilibrium with the adsorbed ligands on the particles. It is thus impossible to completely remove the destabilizing agent. Few cases of agglomeration by unbound ligand have been reported in

literature, possibly because it is often difficult to conclusively identify the depletant that causes entropic attraction. Note that the mechanism described here is not unique to ultrathin gold nanowires and likely to operate in other nanowires or nanoparticle dispersions with ligands of linear shape.

Our findings have several implications. First, bundling can be turned on and off by controlling the number of adsorbed and excess ligands in the system. This could be of interest for processes that require switching between dispersed and assembled AuNWs such as stamp imprinting AuNWs into transparent conductive electrodes.¹⁴ Second, the ligand grafting density is of importance to colloidal systems beyond the “simple” task of stabilizing a colloid against the van der Waals attraction. Molecular dynamics simulations by Gao et al.¹⁸ indicate that the interaction energies caused by the proposed mechanism are small (on the order of 0.1 to $1 k_B T/\text{nm}$) and can induce bundling only because the attraction accumulates along an elongated contact line of several 10 to $100 \mu\text{m}$. Equally large contact areas might be formed between assembled nanosheets or nanoplatelets^{56–58} and between larger spherical nanoparticles. In such systems, future research may have to pay more attention to grafting densities and the chemical equilibria between adsorbed and unbound ligand.

ASSOCIATED CONTENT

Supporting Information

The Supporting Information is available free of charge at <https://pubs.acs.org/doi/10.1021/acs.jpcc.0c10919>.

Additional figures on the grafting density and AuNW dispersions with added oleylamine and in *n*-hexane and additional data and rationale on the adsorption energy,

as well as calculations on the van der Waals interaction energy (PDF)

AUTHOR INFORMATION

Corresponding Author

Tobias Kraus – INM–Leibniz Institute for New Materials, 66123 Saarbrücken, Germany; Colloid and Interface Chemistry, Saarland University, 66123 Saarbrücken, Germany; orcid.org/0000-0003-2951-1704; Email: tobias.kraus@leibniz-inm.de

Authors

Simon Bettscheider – INM–Leibniz Institute for New Materials, 66123 Saarbrücken, Germany; Colloid and Interface Chemistry, Saarland University, 66123 Saarbrücken, Germany; orcid.org/0000-0001-6068-246X

Björn Kuttich – INM–Leibniz Institute for New Materials, 66123 Saarbrücken, Germany; Colloid and Interface Chemistry, Saarland University, 66123 Saarbrücken, Germany

Lukas F. Engel – INM–Leibniz Institute for New Materials, 66123 Saarbrücken, Germany; Colloid and Interface Chemistry, Saarland University, 66123 Saarbrücken, Germany

Lola González-García – INM–Leibniz Institute for New Materials, 66123 Saarbrücken, Germany; Colloid and Interface Chemistry, Saarland University, 66123 Saarbrücken, Germany

Complete contact information is available at: <https://pubs.acs.org/10.1021/acs.jpcc.0c10919>

Notes

The authors declare no competing financial interest.

ACKNOWLEDGMENTS

The authors thank Robert Drumm for performing TGA measurements, and Eduard Arzt for his continuing support of the project. S.B. thanks the Foundation of German Business for his Ph.D. scholarship.

REFERENCES

- (1) Doblas, D.; Kister, T.; Cano-Bonilla, M.; González-García, L.; Kraus, T. Colloidal Solubility and Agglomeration of Apolar Nanoparticles in Different Solvents. *Nano Lett.* **2019**, *19*, 5246–5252.
- (2) Langmuir, I. The Adsorption of Gases on Plane Surfaces of Glass, Mica and Platinum. *J. Am. Chem. Soc.* **1918**, *40*, 1361–1403.
- (3) Adamson, A. W.; Gast, A. P. *Physical Chemistry of Surfaces*; Wiley: New York, 1997.
- (4) Halder, A.; Ravishankar, N. Ultrafine Single-Crystalline Gold Nanowire Arrays by Oriented Attachment. *Adv. Mater.* **2007**, *19*, 1854–1858.
- (5) Huo, Z.; Tsung, C.-k.; Huang, W.; Zhang, X.; Yang, P. Sub-Two Nanometer Single Crystal Au Nanowires. *Nano Lett.* **2008**, *8*, 2041–2044.
- (6) Lu, X.; Yavuz, M. S.; Tuan, H.-y.; Korgel, B. A.; Xia, Y. Ultrathin Gold Nanowires Can Be Obtained by Reducing Polymeric Strands of Oleylamine-AuCl Complexes Formed via Aurophilic Interaction. *J. Am. Chem. Soc.* **2008**, *130*, 8900–8901.
- (7) Pazos-Pérez, N.; Baranov, D.; Irsen, S.; Hilgendorff, M.; Liz-Marzán, L. M.; Giersig, M. Synthesis of Flexible, Ultrathin Gold Nanowires in Organic Media. *Langmuir* **2008**, *24*, 9855–9860.
- (8) Wang, C.; Hu, Y.; Lieber, C. M.; Sun, S. Ultrathin Au Nanowires and Their Transport Properties. *J. Am. Chem. Soc.* **2008**, *130*, 8902–8903.
- (9) Saitoh, M.; Kashiwagi, Y.; Chigane, M. Structural Analysis of Micrometer-Long Gold Nanowires Using a Wormlike Chain Model and Their Rheological Properties. *Soft Matter* **2017**, *13*, 3927–3935.
- (10) Gong, S.; Zhao, Y.; Shi, Q.; Wang, Y.; Yap, L. W.; Cheng, W. Self-assembled Ultrathin Gold Nanowires as Highly Transparent, Conductive and Stretchable Supercapacitor. *Electroanalysis* **2016**, *28*, 1298–1304.
- (11) Porter, A. G.; Ouyang, T.; Hayes, T. R.; Biechele-Speziale, J.; Russell, S. R.; Claridge, S. A. 1-nm-Wide Hydrated Dipole Arrays Regulate AuNW Assembly on Striped Monolayers in Nonpolar Solvent. *Chem.* **2019**, *5*, 2264–2275.
- (12) Roy, A.; Pandey, T.; Ravishankar, N.; Singh, A. K. Semiconductor-like Sensitivity in Metallic Ultrathin Gold Nanowire-Based Sensors. *J. Phys. Chem. C* **2014**, *118*, 18676–18682.
- (13) Reiser, B.; Gerstner, D.; Gonzalez-Garcia, L.; Maurer, J. H. M.; Kanelidis, I.; Kraus, T. Spinning Hierarchical Gold Nanowire Microfibers by Shear Alignment and Intermolecular Self-Assembly. *ACS Nano* **2017**, *11*, 4934–4942.
- (14) Maurer, J. H. M.; González-García, L.; Reiser, B.; Kanelidis, I.; Kraus, T. Templated Self-Assembly of Ultrathin Gold Nanowires by Nanoimprinting for Transparent Flexible Electronics. *Nano Lett.* **2016**, *16*, 2921–2925.
- (15) Feng, H.; Yang, Y.; You, Y.; Li, G.; Guo, J.; Yu, T.; Shen, Z.; Wu, T.; Xing, B. Simple and Rapid Synthesis of Ultrathin Gold Nanowires, their Self-Assembly and Application in Surface-Enhanced Raman Scattering. *Chem. Commun.* **2009**, *0*, 1984.
- (16) Loubat, A.; Impéror-Clerc, M.; Pansu, B.; Meneau, F.; Raquet, B.; Viau, G.; Lacroix, L.-M. Growth and Self-Assembly of Ultrathin Au Nanowires into Expanded Hexagonal Superlattice Studied by in Situ SAXS. *Langmuir* **2014**, *30*, 4005–4012.
- (17) Reiser, B.; Gerstner, D.; Gonzalez-Garcia, L.; Maurer, J. H. M.; Kanelidis, I.; Kraus, T. Multivalent Bonds in Self-Assembled Bundles of Ultrathin Gold Nanowires. *Phys. Chem. Chem. Phys.* **2016**, *18*, 27165–27169.
- (18) Gao, H.; Bettscheider, S.; Kraus, T.; Müser, M. H. Entropy Can Bundle Nanowires in Good Solvents. *Nano Lett.* **2019**, *19*, 6993–6999.
- (19) Nouh, E. S. A.; Baquero, E. A.; Lacroix, L.-M.; Delpéch, F.; Poteau, R.; Viau, G. Surface-Engineering of Ultrathin Gold Nanowires: Tailored Self-Assembly and Enhanced Stability. *Langmuir* **2017**, *33*, 5456–5463.
- (20) Schubert, U.; Hüsing, N.; Laine, R. M., Eds. *Materials Syntheses*; Springer Vienna: Vienna, 2008; DOI: 10.1007/978-3-211-75125-1.
- (21) Förster, S.; Timmann, A.; Konrad, M.; Schellbach, C.; Meyer, A.; Funari, S. S.; Mulvaney, P.; Knott, R. Scattering Curves of Ordered Mesoscopic materials. *J. Phys. Chem. B* **2005**, *109*, 1347–1360.
- (22) Sundblom, A.; Oliveira, C. L. P.; Palmqvist, A. E. C.; Pedersen, J. S. Modeling in Situ Small-Angle X-ray Scattering Measurements Following the Formation of Mesostructured Silica. *J. Phys. Chem. C* **2009**, *113*, 7706–7713.
- (23) Manet, S.; Schmitt, J.; Impéror-Clerc, M.; Zholobenko, V.; Durand, D.; Oliveira, C. L. P.; Pedersen, J. S.; Gervais, C.; Baccile, N.; Babonneau, F.; et al. Kinetics of the Formation of 2D-Hexagonal Silica Nanostructured Materials by Nonionic Block Copolymer Templating in Solution. *J. Phys. Chem. B* **2011**, *115*, 11330–11344.
- (24) Loubat, A.; Lacroix, L.-M.; Robert, A.; Impéror-Clerc, M.; Poteau, R.; Maron, L.; Arenal, R.; Pansu, B.; Viau, G. Ultrathin Gold Nanowires: Soft-Templating versus Liquid Phase Synthesis, a Quantitative Study. *J. Phys. Chem. C* **2015**, *119*, 4422–4430.
- (25) Smith, A. M.; Johnston, K. A.; Crawford, S. E.; Marbella, L. E.; Millstone, J. E. Ligand Density Quantification on Colloidal Inorganic Nanoparticles. *Analyst* **2017**, *142*, 11–29.
- (26) Thomson, J. W.; Cademartiri, L.; MacDonald, M.; Petrov, S.; Calestani, G.; Zhang, P.; Ozin, G. A. Ultrathin Bi₂S₃ Nanowires: Surface and Core Structure at the Cluster-Nanocrystal Transition. *J. Am. Chem. Soc.* **2010**, *132*, 9058–9068.

- (27) Moreels, I.; Justo, Y.; De Geyter, B.; Haustraete, K.; Martins, J. C.; Hens, Z. Size-Tunable, Bright, and Stable PbS Quantum Dots: A Surface Chemistry Study. *ACS Nano* **2011**, *5*, 2004–2012.
- (28) Vericat, C.; Vela, M. E.; Benitez, G.; Carro, P.; Salvarezza, R. C. Self-Assembled Monolayers of Thiols and Dithiols on Gold: New Challenges for a Well-Known System. *Chem. Soc. Rev.* **2010**, *39*, 1805.
- (29) Karpovich, D. S.; Blanchard, G. J. Direct Measurement of the Adsorption Kinetics of Alkanethiolate Self-Assembled Monolayers on a Microcrystalline Gold Surface. *Langmuir* **1994**, *10*, 3315–3322.
- (30) Schessler, H. M.; Karpovich, D. S.; Blanchard, G. J. Quantitating the Balance between Enthalpic and Entropic Forces in Alkanethiol/Gold Monolayer Self Assembly. *J. Am. Chem. Soc.* **1996**, *118*, 9645–9651.
- (31) Peiretti, L. F.; Quaino, P.; Tielens, F. Competition between Two High-Density Assemblies of Poly(phenyl)thiols on Au(111). *J. Phys. Chem. C* **2016**, *120*, 25462–25472.
- (32) Grönbeck, H.; Curioni, A.; Andreoni, W. Thiols and Disulfides on the Au(111) Surface: The Headgroup-Gold Interaction. *J. Am. Chem. Soc.* **2000**, *122*, 3839–3842.
- (33) Fajin, J. L. C.; Teixeira, F.; Gomes, J. R. B.; Cordeiro, M. N. D. S. Effect of van der Waals Interactions in the DFT Description of Self-Assembled Monolayers of Thiols on Gold. *Theor. Chem. Acc.* **2015**, *134*, 67.
- (34) Mete, E.; Yortanli, M.; Danisman, M. F. A van der Waals DFT Study of Chain Length Dependence of Alkanethiol Adsorption on Au(111): Physisorption vs. Chemisorption. *Phys. Chem. Chem. Phys.* **2017**, *19*, 13756–13766.
- (35) Goubet, N.; Richardi, J.; Albouy, P. A.; Pileni, M. P. How to Predict the Growth Mechanism of Supracrystals from Gold Nanocrystals. *J. Phys. Chem. Lett.* **2011**, *2*, 417–422.
- (36) Evans, D. F.; Wennerström, H. *The Colloidal Domain: Where Physics, Chemistry, Biology, and Technology Meet*, 2nd ed.; Wiley-VCH: New York, 1999.
- (37) Israelachvili, J. N. *Intermolecular and Surface Forces*, 3rd ed.; Academic Press: Boston, MA, 2011.
- (38) Marla, K. T.; Meredith, J. C. Simulation of Interaction Forces between Nanoparticles: End-Grafted Polymer Modifiers. *J. Chem. Theory Comput.* **2006**, *2*, 1624–1631.
- (39) Khan, S. J.; Pierce, F.; Sorensen, C. M.; Chakrabarti, A. Self-Assembly of Ligated Gold Nanoparticles: Phenomenological Modeling and Computer Simulations †. *Langmuir* **2009**, *25*, 13861–13868.
- (40) Martin, T. B.; Jayaraman, A. Identifying the Ideal Characteristics of the Grafted Polymer Chain Length Distribution for Maximizing Dispersion of Polymer Grafted Nanoparticles in a Polymer Matrix. *Macromolecules* **2013**, *46*, 9144–9150.
- (41) Monego, D.; Kister, T.; Kirkwood, N.; Mulvaney, P.; Widmer-Cooper, A.; Kraus, T. Colloidal Stability of Apolar Nanoparticles: Role of Ligand Length. *Langmuir* **2018**, *34*, 12982–12989.
- (42) Parsegian, V. A. *Van der Waals Forces*; Cambridge University Press: Cambridge, U.K., 2006; DOI: 10.2277/0521839068.
- (43) Winslow, S. W.; Swan, J. W.; Tisdale, W. A. The Importance of Unbound Ligand in Nanocrystal Superlattice Formation. *J. Am. Chem. Soc.* **2020**, *142*, 9675–9685.
- (44) Lekkerkerker, H. N.; Tuinier, R. *Colloids and the Depletion Interaction*; Lecture Notes in Physics; Springer Netherlands: Dordrecht, 2011; Vol. 833; DOI: 10.1007/978-94-007-1223-2.
- (45) Auvray, L. Solutions de macromolécules rigides: effets de paroi, de confinement et d'orientation par un écoulement. *J. Phys. (Paris)* **1981**, *42*, 79–95.
- (46) Mao, Y.; Cates, M.; Lekkerkerker, H. Depletion Force in Colloidal Systems. *Phys. A* **1995**, *222*, 10–24.
- (47) Mao, Y.; Cates, M. E.; Lekkerkerker, H. N. W. Depletion Stabilization by Semidilute Rods. *Phys. Rev. Lett.* **1995**, *75*, 4548–4551.
- (48) Mao, Y.; Cates, M. E.; Lekkerkerker, H. N. W. Theory of the Depletion Force due to Rodlike Polymers. *J. Chem. Phys.* **1997**, *106*, 3721–3729.
- (49) Lin, K.-h.; Crocker, J. C.; Zeri, A. C.; Yodh, A. G. Colloidal Interactions in Suspensions of Rods. *Phys. Rev. Lett.* **2001**, *87*, No. 088301.
- (50) Helden, L.; Roth, R.; Koenderink, G. H.; Leiderer, P.; Bechinger, C. Direct Measurement of Entropic Forces Induced by Rigid Rods. *Phys. Rev. Lett.* **2003**, *90*, No. 048301.
- (51) Guu, D.; Dhont, J. K. G.; Vliegthart, G. A.; Lettinga, M. P. Depletion Induced Clustering in Mixtures of Colloidal Spheres and fd-Virus. *J. Phys.: Condens. Matter* **2012**, *24*, 464101.
- (52) Baranov, D.; Fiore, A.; van Huis, M.; Giannini, C.; Falqui, A.; Lafont, U.; Zandbergen, H.; Zanella, M.; Cingolani, R.; Manna, L. Assembly of Colloidal Semiconductor Nanorods in Solution by Depletion Attraction. *Nano Lett.* **2010**, *10*, 743–749.
- (53) Lau, C. Y.; Duan, H.; Wang, F.; He, C. B.; Low, H. Y.; Yang, J. K. W. Enhanced Ordering in Gold Nanoparticles Self-Assembly Through Excess Free Ligands. *Langmuir* **2011**, *27*, 3355–3360.
- (54) Brown, S. L.; Shah, V. D.; Morrell, M. V.; Zubich, M.; Wagner, A.; Denton, A. R.; Hobbie, E. K. Superlattice Formation in Colloidal Nanocrystal Suspensions: Hard-Sphere Freezing and Depletion Effects. *Phys. Rev. E: Stat. Phys., Plasmas, Fluids, Relat. Interdiscip. Top.* **2018**, *98*, No. 062616.
- (55) Kim, D.; Bae, W. K.; Kim, S.-H.; Lee, D. C. Depletion-Mediated Interfacial Assembly of Semiconductor Nanorods. *Nano Lett.* **2019**, *19*, 963–970.
- (56) Ithurria, S.; Tessier, M. D.; Mahler, B.; Lobo, R. P. S. M.; Dubertret, B.; Efron, A. L. Colloidal Nanoplatelets with Two-Dimensional Electronic Structure. *Nat. Mater.* **2011**, *10*, 936–941.
- (57) Sichert, J. A.; Tong, Y.; Mutz, N.; Vollmer, M.; Fischer, S.; Milowska, K. Z.; García Cortadella, R.; Nickel, B.; Cardenas-Daw, C.; Stolarczyk, J. K.; et al. Quantum Size Effect in Organometal Halide Perovskite Nanoplatelets. *Nano Lett.* **2015**, *15*, 6521–6527.
- (58) Nasilowski, M.; Mahler, B.; Lhuillier, E.; Ithurria, S.; Dubertret, B. Two-Dimensional Colloidal Nanocrystals. *Chem. Rev.* **2016**, *116*, 10934–10982.

3.2 Publication 2

Reproduced from

L. F. Engel, L. González-García, and T. Kraus: “Flexible and Transparent Electrodes Imprinted from Metal Nanostructures: Morphology and Opto-Electronic Performance”. *Nanoscale Adv.*, 2022, **4**, 3370-3380. DOI: 10.1039/D2NA00259K.

with permission from the Royal Society of Chemistry.



Flexible and transparent electrodes imprinted from metal nanostructures: morphology and opto-electronic performance†

Lukas F. Engel, ^b Lola González-García ^{*b} and Tobias Kraus ^{*ab}

We directed the self-assembly of nanoscale colloids *via* direct nanoimprint lithography to create flexible transparent electrodes (FTEs) with metal line widths below 3 μm in a roll-to-roll-compatible process. Gold nanowires and nanospheres with oleylamine shells were imprinted with soft silicone stamps, arranged into grids of parallel lines, and converted into metal lines in a plasma process. We studied the hierarchical structure and opto-electronic performance of the resulting grids as a function of particle geometry and concentration. The performance in terms of optical transmittance was dominated by the line width. Analysis of cross-sections indicated that plasma sintering only partially removed the insulating ligands and formed lines with thin conductive shells and a non-conductive core. We provide evidence that the self-assembly of high-aspect nanowires can compensate for defects of the stamp and substrate irregularities during imprinting, while spheres cannot. The wire-based electrodes thus outperformed the sphere-based electrodes at ratios of optical transmittance to sheet resistance of up to $\approx 0.9\% \Omega_{\text{sq}}^{-1}$, while spheres only reached $\approx 0.55\% \Omega_{\text{sq}}^{-1}$.

Received 27th April 2022
Accepted 2nd July 2022

DOI: 10.1039/d2na00259k

rsc.li/nanoscale-advances

1 Introduction

Solar cells, light-emitting diodes, and other devices that convert between photons and excitons require transparent conductive electrodes. They are often based on thin films of noble metals, indium tin oxide, semiconductor polymers or hybrids, networks of graphene or carbon nanotubes, metal nanowires, or metal grids.^{1,2} All of them can be used to create flexible transparent electrodes (FTEs) on thin, flexible and transparent polymer substrates, with performances that depend on the material and the layer morphology.

Metal grids are particularly cost-effective transparent electrodes that can be customized:³ their sheet resistance and optical transmittance are defined by the chosen grid geometry and vary with pattern, pitch, conductor width, and conductor thickness.⁴ Foldable high resolution displays, for instance, require FTEs with a large density of separate, parallel conductors to control the individual pixels. This can be realized with a dense grid of very narrow lines that provide high optical transmittances. The thickness of the lines can be tuned to achieve a conductive cross section that yields an acceptable

sheet resistance. Both requires a process that can pattern dense, narrow lines.

E-beam lithography offers the necessary resolution but has a low throughput.⁵ Printing techniques have been reported to improve fabrication speed. Many are limited to line widths above several micrometers, requiring large pitches to attain transparency. Zhu *et al.*⁶ combined an electric-field-driven microscale 3D printing technique with a hybrid hot-embossing process to fabricate Ag-based square grid FTEs with sheet resistances of $0.75 \Omega_{\text{sq}}$ and optical transmittances of $T_{500} \approx 85.79\%$ at a line width of 10 μm and a pitch of 1000 μm . Wang *et al.*⁷ report sheet resistances of $0.86 \Omega_{\text{sq}}$ and optical transmittances of $T_{500} \approx 91.26\%$ at a line width of 18 μm and a pitch of 800 μm for their Ag-based square grid FTEs fabricated *via* ultra-fast laser direct writing. Le Zhao *et al.*⁸ demonstrate FTEs based on Cu/Ni square grids, fabricated using lithography and electroplating. They achieved sheet resistances of $0.13 \Omega_{\text{sq}}$ and optical transmittances of $T_{500} \approx 86\%$ at a line width of 8 μm and a pitch of 170 μm . Zhou *et al.*⁹ inkjet printed Ag-based square grid FTEs with sheet resistances of $9.56 \Omega_{\text{sq}}$ and optical transmittances of $T_{500} \approx 64.05\%$ at a line width of 46.2 μm and a pitch of 200 μm . Li *et al.*¹⁰ screen printed Ag-based honeycomb FTEs with sheet resistances of $27 \Omega_{\text{sq}}$ and optical transmittances of $T_{500} \approx 67\%$ at a line width of 200 μm and a pitch of 1040 μm . Scraping is an alternative 5-step process where the electrode material is spread across a previously prepared substrate pre-patterned with recesses and can yield 3 μm wide lines, for example.¹¹

^aColloid and Interface Chemistry, Saarland University, Campus D2 2, 66123 Saarbrücken, Germany. Tel: +49 (0)681-9300-389

^bINM – Leibniz Institute for New Materials, Campus D2 2, 66123 Saarbrücken, Germany. E-mail: tobias.kraus@leibniz-inm.de; lola.garcia@leibniz-inm.de; Tel: +49 (0)681-9300-269

† Electronic supplementary information (ESI) available. See <https://doi.org/10.1039/d2na00259k>

Nanoimprinting combined with self-assembly provides an efficient 2-step route to grids of sub-micron metal lines.^{12–18} Dispersions of metallic nanocolloids (colloidal inks) can be imprinted under ambient conditions in a roll-to-roll compatible process with a patterned polymer stamp that is being rolled over the substrate.^{19,20} The colloidal ink is confined in the stamps' cavities and the solvent permeates through the polymer. The dispersed particles self-assemble into features defined by the stamp. Particle geometry and concentration can be tuned to affect self-assembly and the resulting structures.²⁰ Metallic nanocolloids often carry organic ligand shells that prevent agglomeration and have to be removed after imprinting, for example in a plasma.²¹

Maurer *et al.*¹⁹ nanoimprinted self-assembling Au nanowires with a core diameter of 1.6 nm, an aspect ratio on the order of 10^3 , and an oleylamine ligand shell. The wires self-assembled into bundles inside the square grid defined by the stamp. The resulting grid was sintered using a low-pressure, room temperature plasma treatment that retained the overall geometry and did not damage the thin polymer substrate. The resulting FTEs had sheet resistances of $128 \Omega_{\text{sq}}/196 \Omega_{\text{sq}}$ (in printing direction/perpendicular) and optical transmittances of $T_{500} \approx 86\%$ at line widths of $1.41 \mu\text{m}/0.91 \mu\text{m}$ and a pitch of $19.5 \mu\text{m}$.¹⁹ Kister *et al.* imprinted Au nanospheres with a core diameter of 3.2 nm and C4-, C8- or C12-thiols or amines. Both reports used the same printing method that we study here, but different process parameters and particle ligands. The best-performing FTEs formed from particles with dodecylamine ligand shells and had sheet resistances of $150 \Omega_{\text{sq}}$ and optical transmittances of $T_{500} \approx 91\%$ at line widths $< 1 \mu\text{m}$ and a pitch of $19.5 \mu\text{m}$.²⁰ The basic functionality of such nanoimprinted electrodes was demonstrated by integrating them into capacitive and resistive touch devices.¹⁹ Other examples for the integration of nanoimprinted electrodes into functional devices include organic field effect transistors,^{13,15} nanobatteries²² and flexible organic light-emitting devices.²³

The structure–property relations between the morphology of metal conductors formed during nanoimprinting and the optoelectronic electrode performance are not fully understood. There are, however, some studies on spin-coated, inkjet-printed and drop-casted nanoparticle assemblies and the effect of plasma sintering on their morphology and/or sheet resistance. Shaw *et al.*²⁴ investigated crack formation in spin-coated assemblies of ligand-capped colloids (varying in composition, shape, size and ligand as well as the used solvent) on Si substrate during drying, O_2 plasma-induced ligand removal, and thermal sintering. They found that close-packed and ordered particle packing always led to cracking, while disordered particle films with thicknesses up to 440 nm remained crack-free. Reinhold *et al.*²⁵ studied the effect of Ar plasma sintering on the morphology and resistivity of inkjet printed tracks (Ag nanoparticles with a diameter of 5 to 10 nm in tetradecane) on polymer substrates. They report the formation of a conductive Ag skin layer and a non-conductive core. The skin layer thickness was independent of the printed layer thickness and increased with plasma treatment time before saturating. Ma *et al.*²⁶ investigated the effect of Ar plasma sintering on the

morphology of drop-casted layers of Ag nanoparticles (gum arabicum capped, 23 nm and 77 nm in diameter, dispersed in DI water) on glass and the resulting sheet resistance. Plasma sintering converted discrete particles to a more continuous film with time, and increasing RF power accelerated this transition. A simple parallel circuit model was formulated based on a fully sintered skin layer and a less or non-conductive core. Assuming a non-conductive core, the calculated skin layer resistivities matched the morphological development with increasing plasma sintering time and increasing RF power well.

Here, we study the effects of particle shape and superstructure formation on the conductor morphology and optoelectronic performance. Au nanowires (wires) and Au nanospheres (spheres) were imprinted as grids of parallel lines with a width of about $1.6 \mu\text{m}$ and a pitch of $19.5 \mu\text{m}$ at different Au concentrations c_{Au} on polyethylene terephthalate (PET) foil. The lines underwent H_2/Ar plasma sintering. We quantified the performances of the resulting transparent electrodes using a figure of merit (FOM) and compared them to the electrode morphologies before and after plasma sintering. We found that wires form lines with a coarse surface microstructure and pronounced bleeding, while spheres form smooth lines with less bleeding. The plasma formed a conductive shell and a non-conductive core for both particle types, with the thicker shell in case of the spheres. Electrode performance was dominated by defect densities, where wires outperformed spheres because they better bridged stamp and substrate irregularities during imprinting. The FOM always increased with increasing c_{Au} , but the FOM with wires was at least 3.4 times higher at any given c_{Au} .

2 Materials and methods

2.1 Synthesis of Au nanowires/-spheres

2.1.1 Chemicals. Tetrachloroauric(III) acid trihydrate ($\text{HAuCl}_4 \cdot 3\text{H}_2\text{O}$) was synthesized according to Schubert *et al.*,²⁷ oleylamine (Acros Organics, C18 content of about 80–90%) was purchased from Fisher Scientific GmbH (Schwerte, Germany) and filtered with a $0.45 \mu\text{m}$ Rotilabo-PTFE syringe filter from Carl Roth GmbH + Co. KG (Karlsruhe, Germany) prior to each usage to remove any oxidized residues, triisopropylsilane (95%) and *n*-hexane (at least 99% p.a.) were obtained from abcr GmbH (Karlsruhe, Germany), pentane (Sigma Aldrich, for HPLC, $\geq 99\%$) and borane *tert*-butylamine complex (Sigma Aldrich, 97%) were obtained from Merck KGaA (Darmstadt, Germany), cyclohexane (ROTISOLV $\geq 99.9\%$, GC Ultra Grade) was bought from Carl Roth GmbH + Co. KG (Karlsruhe, Germany) and absolute ethanol (99.8%, analytical reagent grade) was procured from Fisher Scientific GmbH (Schwerte, Germany). All chemicals were used without further purification unless explicitly mentioned.

2.1.2 Syntheses. Ultrathin nanowires (AuNW) with a gold (Au) core and an oleylamine (OAm) ligand shell were synthesised according to Nough *et al.*,²⁸ a route based on the original research by Feng *et al.*²⁹ Nanospheres (AuNP) with Au cores and OAm ligand shells were synthesised according to Kister *et al.*,²⁰ a route based on the original research by Wu *et al.*³⁰

In a typical AuNW synthesis, 60 mg of $\text{HAuCl}_4 \cdot 3\text{H}_2\text{O}$ (10 mM) were weighed into a disposable 50 mL glass snap-on vial from Carl Roth GmbH + Co. KG (Karlsruhe, Germany). Then, 9.9 mL of *n*-hexane and 2.04 mL of oleylamine (400 mM) were added. The mixture was vortexed for 1 min to fully dissolve the Au acid. Then, 3.06 mL (1 M) of triisopropylsilane (TIPS) were added as reducing agent. The solution was vortexed for 30 s and kept in an oven at 25 °C for 24 h without any mechanical agitation.

The highly hygroscopic $\text{HAuCl}_4 \cdot 3\text{H}_2\text{O}$ was weighed in dry in a glove box from SylaTech GmbH (Walzbachtal, Germany) because the presence of water results in shorter wires.³¹ The reaction vessel was filled with dry Ar. OAm acts both as ligand and as reducing agent, albeit weaker than TIPS. OAm and TIPS were added in that order using a 5 mL pipette. The interval between injections was minimized to avoid reduction in the absence of TIPS.

In a typical AuNP synthesis, 200 mg of $\text{HAuCl}_4 \cdot 3\text{H}_2\text{O}$ were weighed into a disposable 100 mL glass snap-on vial from Carl Roth GmbH + Co. KG (Karlsruhe, Germany) under ambient conditions because the synthesis is less water sensitive. Then, 16 mL of pentane and 16 mL of OAm were added. The mixture was stirred at 500 rad min^{-1} and room temperature for 45 min (solution A). In the meantime, 80 mg of tert-butylamine borane were dissolved in a mixture of 4 mL pentane and 4 mL OAm (solution B). After precisely 45 min (the waiting time determines the sphere diameter), solution B was added to solution A and the color turned immediately dark brown. Then the mixture was stirred for another 60 min with a loose lid.

2.1.3 Purification, dilution, and storage. After synthesis, AuNW were purified by adding twice the reaction volume of absolute ethanol and shaking the snap-on vial. Sedimentation occurred in a Rotanta 460 RS centrifuge from Andreas Hettich GmbH & Co. KG (Tuttlingen, Germany) with a swing-out rotor at 110 rcf for 2 min and the slowest possible deceleration. The supernatant was discarded and the wires were re-dispersed in an amount of *n*-hexane corresponding to the original reaction volume. The purification procedure was repeated before re-dispersing the wires in cyclohexane to obtain a stock dispersion of $c_{\text{Au}} \approx 10 \text{ mg mL}^{-1}$ (estimated based on $\text{HAuCl}_4 \cdot 3\text{H}_2\text{O}$ weighed in and 100% yield).

The purification of AuNP was similar, but with centrifugation at 3435 rcf and 5 min for the first and 3435 rcf and 60 min for the second step. The AuNP were re-dispersed to $c_{\text{Au}} \approx 30 \text{ mg mL}^{-1}$.

Other ink concentrations were produced through dilution of the respective stock dispersion. AuNW inks were stored in a fridge at 5 °C, AuNP inks were stored at room temperature for 16 h before usage.

2.2 Small-angle X-ray scattering (SAXS)

Sphere diameter and dispersion state were characterized *via* SAXS. The dispersion was transferred to glass mark-tubes from Hilgenberg GmbH (Malfeld, Germany) with an inner diameter of 1.5 mm. The tubes were sealed with a fast-curing two-component epoxy from R&G Faserverbundwerkstoff GmbH (Waldenbuch, Germany) to prevent solvent evaporation.

The scattering setup, a Xeuss 2.0 HR SAXS/WAXS instrument from Xenocs SAS (Grenoble, France) used a Cu K α source and a detector PILATUS3 R 1 M from DECTRIS AG (Baden, Switzerland) at a distance of about 550 mm from the samples. The distance was calibrated with a Ag behenate sample before each measurement. Each sample was measured for a total of 30 min. The two-dimensional scattering images were azimuthally integrated with the software Foxtrot from Synchrotron SOLEIL (Saint-Aubin, France) to obtain the scattering curves. The solvent background was measured separately and subtracted. To determine the average sphere diameter, fitting of the scattering curves was performed with the software SASfit from the Laboratory for Neutron Scattering at Paul Scherrer Institute (Villigen, Switzerland).

2.3 Nanoimprinting

2.3.1 Substrate cleaning. PET substrates of type Melinex 401 CW from DuPont Teijin Films UK Ltd (Redcar, United Kingdom) with a thickness of 0.75 μm were cleaned using an ultrasonic bath in a custom-made cleaning rack using the following sequence of solvents: 5 min acetone, 5 min ethanol, and 5 min Milli-Q ultrapure water. The substrates dried for 30 min at 60 °C, just below their glass transition temperature of 70–80 °C. Acetone removed any grease residues, ethanol and the ultrapure water removed acetone and increased polarity, the ultrapure water dried without residues.

2.3.2 Polydimethylsiloxane (PDMS) imprinting stamp fabrication. PDMS imprinting stamps were fabricated in a two-step-moulding process. First, a PDMS master was moulded off a silanized silicon master from AMO GmbH (Aachen, Germany) with a pattern of parallel line channels (patterned area $A \approx 7 \text{ cm} \times 7 \text{ cm}$, pitch $p \approx 19.5 \mu\text{m}$, channel width $w_c \approx 1.6 \mu\text{m}$ and channel depth $d_c \approx 4.2 \mu\text{m}$). The imprinting stamp was moulded off the silanized master stamp.

Silanization was performed directly on the silicon master and after plasma activation of the PDMS master for 1.5 min using an oxygen plasma at 0.3 mbar in a low pressure plasma reactor of type Pico from Diener electronic GmbH & Co. KG (Ebhausen, Germany). Silanization took place inside a conventional glass desiccator with a snap-on vial cap containing 30 μL of (tridecafluoro-1,1,2,2-tetrahydrooctyl)trichlorosilane from abcr GmbH (Karlsruhe, Germany). The vial was shielded from the masters to increase uniformity. The desiccator was flushed with Ar, evacuated to 3 mbar, and disconnected from the vacuum pump. After 30 min, the desiccator was slowly ventilated with air.

PDMS base and curing agent, Sylgard 184 from Dow Inc. (Midland, USA), were mixed in a 10 : 1 (w/w) ratio and degassed in a Speedmixer DAC 600.2 VAC-P from Hauschild GmbH & Co. KG (Hamm, Germany) at a speed of 2350 rpm and a pressure of 1 mbar for 3 min. The mixture was poured onto the respective master with a Teflon spacer ring (2 mm thick) and a glass plate as top sealing. The PDMS was fully cured at 80 °C for 3 h and the replica were carefully peeled off along the stamp channels.

Imprinting stamps were cut into two parts with an area of 3.5 cm \times 8 cm of which 3.5 cm \times 7 cm were patterned. Larger

areas can be printed using the complete imprinting stamp.¹⁹ The flat 3.5 cm × 0.5 cm at either end of the stamp served as run-in and run-out areas during imprinting.

2.3.3 Nanoimprinting. Nanoimprinting was carried out using a modified TQC Sheen automatic film applicator from Industrial Physics Inks & Coatings GmbH (Hilden, Germany), equipped with a custom-made 3 kg steel cylinder (8 cm in diameter and height) that was moved at a constant speed of 4 mm s⁻¹. The PDMS stamps were attached to the steel cylinder using a double-sided tape from tesa SE (Norderstedt, Germany). Immediately before imprinting, 60 μL of ink were injected directly into the gap between the PDMS imprinting stamp and the PET substrate using a pipette. Continuous processing is possible *e.g.* using a syringe pump for the ink. After imprinting, ink residues on the PDMS stamp were removed using Scotch Magic Tape from 3 M Deutschland GmbH (Kleinostheim, Germany). There was no degradation of the stamps apparent from the geometry of the prints after using the same stamp for 60 prints. A detailed, illustrated description of the nanoimprinting process is included in Section 1 of the ESI.† Note that nanoimprinting is sensitive to humidity and has to be carried out well above the dew point to avoid capillary condensation. We typically imprinted at 22 °C and 55% *rH* at a dew point of 12.5 °C.

2.4 Plasma sintering

Plasma sintering was performed in a low pressure 13.56 MHz RF plasma reactor of type Pico from Diener electronic GmbH & Co. KG (Ebhausen, Germany) immediately after nanoimprinting. Ar/H₂ (95% Ar and 5% H₂) was used as process gas. The procedure was carried out at room temperature and ≈ 0.3 mbar for 20 min with 100 W RF power.

2.5 Sheet resistance measurements

Sheet resistances were determined in a 2-point-probe configuration using a multi-channel multi-meter (DAQ6510 data acquisition logging multi-meter system) equipped with multiplexer cards (7702 40-channel differential multiplexer module with screw terminals) from Keithley Instruments GmbH (Germaring, Germany). The electrodes were contacted using a fast drying Ag paste ACHESON Ag DAG 1415 from Plano GmbH (Wetzlar, Germany) and AGF 1 miniature crocodile clamps from SKS Kontakttechnik GmbH (Niederdorf, Germany). Ag paste was applied in two parallel lines, each 1.5 cm long and spaced 1.5 cm apart, resulting in a square measurement field. The determined resistances corresponded directly to the desired sheet resistances.

2.6 UV-vis spectroscopy

The optical transmittance of the electrodes was determined with a Cary 5000 UV-vis-NIR spectrophotometer from Agilent Technologies Deutschland GmbH (Waldbronn, Germany) with a tungsten halogen light source for the visible range and a deuterium arc light source for the UV range. The samples were mounted behind blackened metal masks with circular apertures (5 mm in diameter). Measurements were performed in

double-beam mode against air at scan rates of 600 nm min⁻¹. The samples were placed such that the blank sides were in contact with the mask to prevent any damage to the electrodes on the other side. Baselines of bare PET substrates were recorded as references.

2.7 Confocal laser scanning microscopy (CLSM)

The electrodes' surface topographies were characterized using a MarSurf CM explorer from Mahr AG (Thalwil, Switzerland) at 100-fold magnification, which corresponded to a measuring field of about 161 μm by 161 μm. The vertical resolution was 2 nm, the lateral resolution 320 nm, effectively allowing for data points every ≈ 130 nm. For a single topography map, 1240 equidistant height traces across eight parallel conductor segments were acquired. Data analysis was performed with Python (Anaconda distribution) as described below. Note that CLSM overestimates the height of the material at the edge of the lines, blurring the edge. We thus detected the edge with a slope-based (*m*) termination criterion (absolute values of *m*: $|m_{\text{wires}}| \leq 0.03$ and $|m_{\text{spheres}}| \leq 0.06$) for both S-shaped sides of the Gaussian conductor profile.

2.8 Cross-sectioning *via* focused ion beam (FIB)

The conductor cross sections were prepared using a FEI Versa 3D DualBeam from Thermo Fisher Scientific GmbH (Schwerte, Germany). The conductors were protected by subsequently deposited layers of Pt using the electron beam first, then the ion beam.

2.9 Transmission electron microscopy (TEM)

Dry particle samples were prepared by diluting AuNW and AuNP dispersions to concentrations of approximately 0.1 mg mL⁻¹ and drop-casting 3 μL on a carbon-coated copper grid from Plano GmbH (Wetzlar, Germany). All samples were characterized at an acceleration voltage of 200 kV in a JEM 2010 from JEOL GmbH (Freising, Germany).

2.10 Scanning electron microscopy (SEM)

Scanning electron micrographs were recorded using either a FEI Quanta 400 ESEM or a FEI Versa 3D DualBeam from Thermo Fisher Scientific GmbH (Schwerte, Germany) with secondary electron detectors. The electrodes for SEM were imprinted onto polished, p-type silicon wafers from Siebert Wafer GmbH (Aachen, Germany).

3 Results and discussion

Fig. 1 illustrates the trade-off between electrical resistance *R* and optical transmittance *T* of metal grid-based FTEs. We prepared grids of parallel lines using gold nanosphere (AuNP) and gold nanowire (AuNW) colloids with increasing concentration *c*_{Au} (three samples per concentration), plasma-sintered them, and compared their average transmittances $\bar{T}_{400-800}$ in the visible range (from 400 nm to 800 nm) to their sheet resistances *R*_{sh}. It

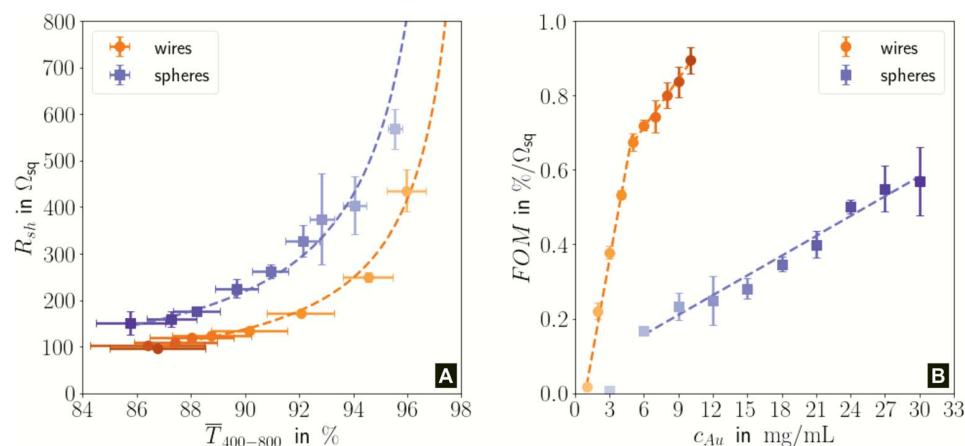


Fig. 1 (A): Sheet resistances R_{sh} and optical transmittances $\bar{T}_{400-800}$ for wire- and sphere-based electrodes directly after plasma sintering. Data for electrodes with R_{sh} that exceeded the scale are not included (Section 2 of the ESI† has the complete data set). (B): Dependence of $FOM = \bar{T}_{400-800} \cdot R_{sh}^{-1}$ with concentration c_{Au} . All graphs show average values from three measurements, the standard deviation, and a fit (dashed lines). Light colours represent the lowest and dark colours the highest Au concentrations in the printed colloids.

is convenient to express the overall performances using the Figure of Merit developed by Fraser and Cook,³²

$$FOM = \bar{T}_{400-800} \cdot R_{sh}^{-1}, \quad (1)$$

that compares the ratio of the mean optical transmittance $\bar{T}_{400-800}$ and the sheet resistance R_{sh} .

The concentrations of the colloids were varied in the range of 1–10 mg mL⁻¹ for the wires and 3–30 mg mL⁻¹ for the spheres. The lower limit was set by percolation; the upper limit was set by requiring a minimum optical transmission of 85%. Darker colors in the plots indicate larger concentrations.

Sheet resistance and optical transmittance decreased with increasing c_{Au} for both wires and spheres, but wires always had lower $\bar{T}_{400-800}$ and R_{sh} for a given concentration. Functional electrodes could be made from both wires and spheres in the range $c_{Au} \in 3$ to 10 mg mL⁻¹. The FOM for wire-based electrodes in this range was at least 3.4 times larger than that of sphere-based electrodes. Resistances were more sensitive to c_{Au} than transmittances, and the FOM increased with c_{Au} for both nanocolloids. FTEs with the same optical transmittance always had lower R_{sh} when made from wires. Interestingly, $\delta FOM/\delta c_{Au}$ for wire-based electrodes abruptly decreased at $c_{Au} \approx 5$ mg mL⁻¹ to 75%. The highest FOM $\approx 0.9\% \Omega_{sq}^{-1}$ of all FTEs in this study was for AuNW at $c_{Au} = 10$ mg mL⁻¹.

In the following, we analyze the effect of particle shape on grid morphology, starting with nanowires. The wires (Fig. 2A) had a core diameter d_w of 1.7 nm²⁸ and lengths l_w between 2 μ m³³ and 6.4 μ m³⁴ (aspect ratio on the order of 10³). Previous studies have shown that 70% of the wires at the concentrations used here are part of dispersed bundles.³⁵

Fig. 2 shows top-view electron micrographs of grids imprinted from wire dispersions with $c_{Au} = 6$ mg mL⁻¹ on doped Si before (B) and after (C) plasma sintering. Approximately 90% of the wires were concentrated and aligned in lines of width w_c , the rest exceeded the boundaries (bleeding) and was only partially aligned. A sharp ridge formed in the center of

the line. Plasma sintering partially removed the oleylamine and blunted the ridge. The wires in particularly thinly covered areas of the bled part fragmented, rendering them non-conductive. Fig. 2D shows the profile of a plasma-sintered line on PET foil obtained from CLSM. The wires formed a flat, Gaussian profile that was wider than the stamp feature, probably because the material flowed when the stamp was removed.

Bundling wires form extended networks.^{12,19,36} We propose that they are gel-like and cannot be easily displaced by the stamp, which causes further bleeding (Fig. 2B and C). Defects in the conformal stamp-substrate contact due to edge imperfections and reduced contact pressure around the channel edges aggravate the effect.³⁷

Fig. 2E is a transmission electron micrograph of a plasma-treated line on a silicon substrate. The change of the cross-sectional profile during plasma sintering was minor. Only the outermost part of the conductor was fully sintered, resulting in a structure with a metallic Au shell (average thickness $t_{shell} = 5.7 \pm 1.1$ nm) and a hybrid, probably less conductive core. The plasma did not fully penetrate the deposited material, probably because shell formation is self-limiting. This explains why extended plasma sintering barely lowered R_{sh} . The cross section confirms that material beyond w_c contributes to conductivity and suggests that CLSM overestimates the height of the non-conductive areas next to the conductor. The shell of the center part was porous as marked in Fig. 2E, probably due to the AuNW bundle superstructure.

Compare, now, the wire-derived lines to samples formed from spheres. We imprinted Au cores with diameters d_{sp} of about 3.7 nm that were coated with a dense shell of OAm (shell thickness approximately 2 nm) as seen in Fig. 3A. They were fully dispersed according to Small Angle X-ray Scattering (Fig. S3 of the ESI†). Fig. 3 shows top-view electron micrographs of imprinted grids formed at $c_{Au} = 30$ mg mL⁻¹ on doped silicon before (B) and after (C) plasma sintering. The lines were sharply delineated with little bleeding and a homogeneous surface

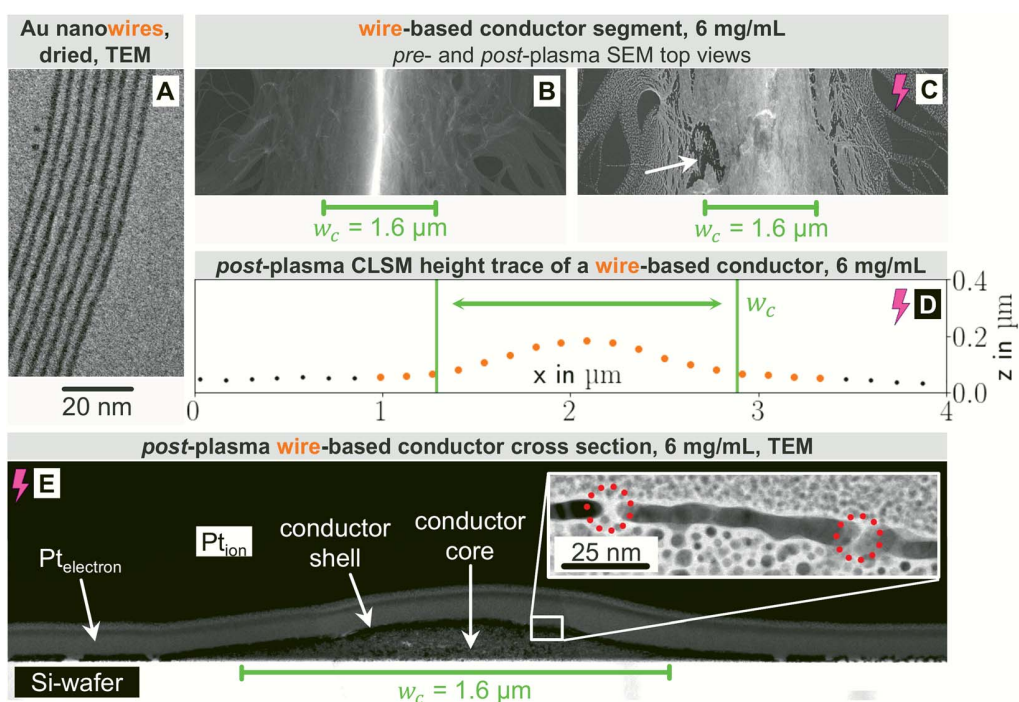


Fig. 2 Typical morphological features of lines printed from AuNW at $c_{Au} = 6 \text{ mg mL}^{-1}$ before and (purple flash) after plasma. (A): TEM image of dried and self-assembled wires. (B): SEM image (top-view) of a printed line. (C): SEM image (top-view) of a printed, plasma-sintered line; the white arrow indicates one of the typical crack-like defects which start forming at 6 mg mL^{-1} in the bled parts. (D): Height trace of a printed, plasma-sintered line. (E): TEM image of a cross-section of a printed, plasma-sintered line. Inset: A shell formed by the plasma. The red dashed circles indicate gaps within the shell.

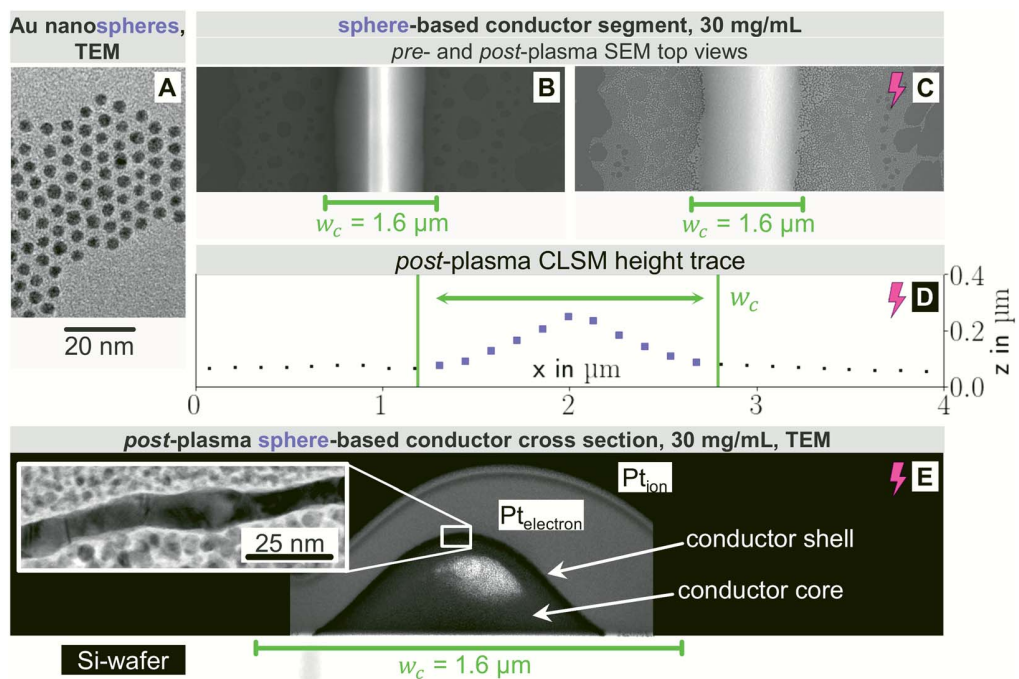


Fig. 3 Typical morphological features of lines printed from AuNP at $c_{Au} = 30 \text{ mg mL}^{-1}$ before and (purple flash) after plasma. (A): TEM image of dried and self-assembled spheres. (B): SEM image (top-view) of a printed line. (C): SEM image (top-view) of a printed, plasma-sintered line. (D): Height trace of a printed, plasma-sintered line. (E): TEM image of a cross-section of a printed, plasma-sintered line. Inset: A shell formed by the plasma.

microstructure. The difference to wires is probably due to the spheres' excellent dispersion state even at high c_{Au} towards the end of the printing process. A ridge formed along the centre that was blunted by the plasma sintering and is no longer visible after plasma sintering. The center line microstructure remained homogeneous after plasma; coalescence and island formation beyond the defined feature did not contribute to conductivity.

Fig. 3D shows the CLSM profile of a plasma-sintered line on PET with a similar Gaussian profile as for nanowires above. Fig. 3E depicts the core-shell structure with a shell thickness $t_{\text{shell}} = 8.1 \pm 1.4$ nm, slightly above that for wires, and a non-porous structure. Lines printed at $c_{\text{Au}} = 12$ mg mL⁻¹ had similar features. At lower concentrations, closer to the percolation threshold, pores and disconnected segments formed (Fig. S7 in the ESI†).

In the following, we analyze the effect of particle concentration on the geometry of the printed, plasma-sintered grids. Confocal metrology provided a total of twenty height profiles measured on PET – one at each of the respective ten c_{Au} for both wires and spheres. Fig. 4A and B show topography maps of selected conductor segments, Fig. S4 and S5 of the ESI† show larger areas for the lowest and highest c_{Au} . We detected the edges of printed lines using a slope-based termination criterion (see Materials & Methods Section on CLSM). The cross sections of the shells were calculated by multiplying the average t_{shell}

(Section S6 in the ESI†) with the outer contour length. The mean values of w , h_{max} and A_{shell} as a function of gold concentration are shown in Fig. 4C, D and E.

The width and height of wire-derived imprinted lines increased with c_{Au} (Fig. 4A). The height of sphere-derived imprinted lines increased with c_{Au} , while their width was maximal at the lowest concentration and minimal at 12 mg mL⁻¹. The difference between wires and spheres is likely due to the different agglomeration mechanisms. A considerable fraction of wires at $c_{\text{Au}} = 1$ mg mL⁻¹ is bundled,³⁵ while spheres are still well dispersed at 30 mg mL⁻¹ (Fig. S3 in the ESI†).

The variation of $\delta w/\delta c_{\text{Au}}$ for spheres is likely connected to ink viscosity and agglomeration. Low-concentration inks tend to have low viscosities, low contact angles, and longer drying times. They can easily migrate beyond w_c before complete solvent evaporation. Higher concentrations increase the viscosity and agglomeration rate, reducing w to below w_c . A small fraction of the ink still bleeds, and the highest concentration leads to a perceptible amount of metal deposited beyond w_c .

For wires, $\delta h_{\text{max}}/\delta c_{\text{Au}}$ showed an increase at 3 mg mL⁻¹ which roughly coincided with w reaching w_c . This suggests that at lower concentrations, particles can freely assemble into increasingly wide lines. When w reaches w_c , additional particles add to the thickness or cause bleeding, and w/h_{max} drops

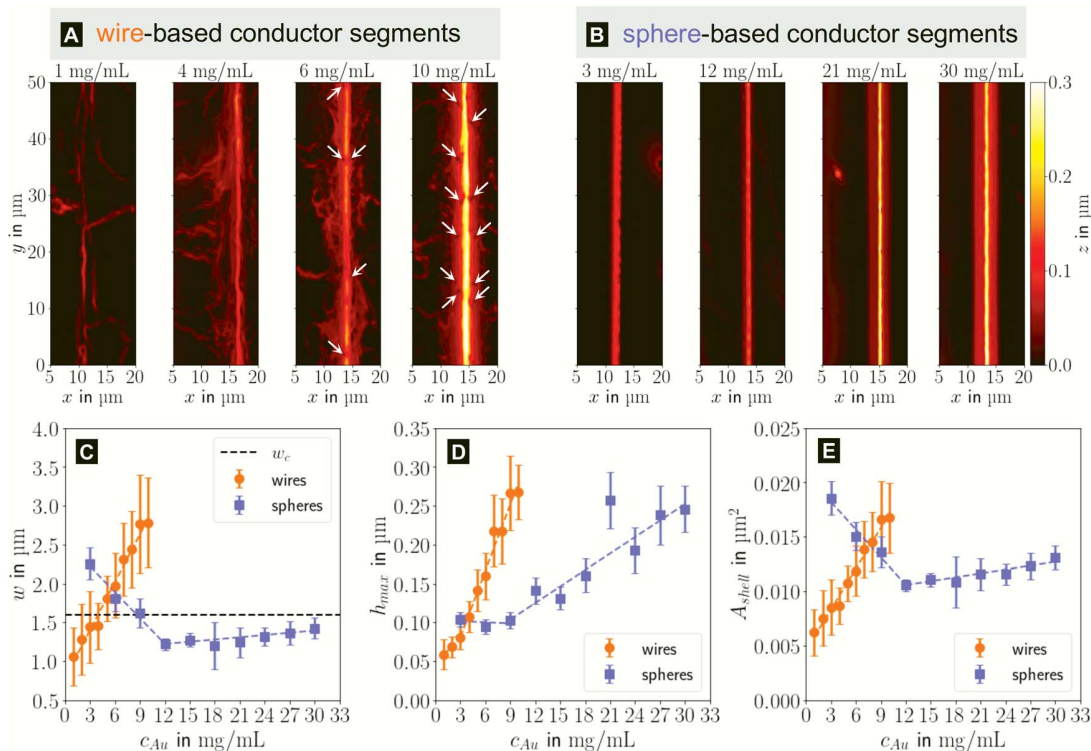


Fig. 4 Topography maps of (A) wire- and (B) sphere-based printed lines after plasma sintering. White arrows indicate defects similar to those in Fig. 2C. (C) Average conductor width w , (D) maximum conductor height h_{max} and (E) cross-sectional area A_{shell} as a function of gold concentration c_{Au} . Standard deviations are indicated as error bars, the dashed lines are fits by linear regression to better illustrate the (piece-wise) linear behaviour.

steadily at 4 mg mL^{-1} and above (Fig. S9 in the ESI†). A similar change of $\delta h_{\text{max}}/\delta c_{\text{Au}}$ for spheres at 9 mg mL^{-1} coincided with the $w = w_c$, too, suggesting the same mechanism.

The cross-sectional area A_{shell} was almost proportional to w for both wires and spheres (Fig. 4E). This is because t_{shell} is set by the plasma process and practically independent of c_{Au} . The conductor width $w \gg h_{\text{max}}$ dominates the product $t_{\text{shell}} \cdot w$.

For wires, percolation and electrical conductivity occurred at 2 mg mL^{-1} ; crack-like defects appeared at 6 mg mL^{-1} (white arrows in Fig. 4A), and became denser with increasing c_{Au} . They did not affect w and A_{shell} but affected the conductivity σ_{shell} , which changed sign and slope at 6 mg mL^{-1} (Fig. 5C).

With CLSM, the sphere-derived lines appeared mostly defect-free (due to the limited resolution and field of vision) as shown in Fig. 4B. A detailed analysis indicated, however, that lines formed at low concentrations (3 to 9 mg mL^{-1}) contained large discontinuous segments and exhibited numerous pores (Fig. S7 of the ESI†). Additionally, we found imprinting defects (Fig. S8 in the ESI†) due to tapered or clogged stamp channels and stamp irregularities. They appear less frequently than the cracks in wire-based lines but reduce σ_{shell} more drastically because they often affect the entire width of the line and render it non-conductive. We propose that small, dispersed spheres are more susceptible to such defects because their superstructures are more easily disrupted than network-forming, bundling wires. Increasing c_{Au} increases the probability that irregularities are bridged by a thicker particle layer.

The measured macroscopic sheet resistance R_{sh} of the transparent electrodes is due to the parallel conductivity of 750 parallel printed lines of length $l = 1.5 \text{ cm}$. If we assume that only their shells with cross-sectional areas A_{shell} conduct, the overall sheet resistance is

$$R_{\text{sh}}^{-1} = R^{-1} = G = \sigma_{\text{shell}} \cdot \frac{750 \cdot A_{\text{shell}}}{l} \Rightarrow \sigma_{\text{shell}} = G \cdot \frac{l}{750 \cdot A_{\text{shell}}}, \quad (2)$$

and we can calculate conductivities of the shell material σ_{shell} as shown in Fig. 5C. We test this assumption below.

The shell conductivities σ_{shell} universally increased with increasing c_{Au} . They remained below one third that of bulk Au

($\sigma_{\text{Au}} \approx 4.52 \times 10^7 \text{ S m}^{-1}$).³⁸ The most conductive shells had $1.39 \times 10^7 \text{ S m}^{-1}$ for wire-based and $1.02 \times 10^7 \text{ S m}^{-1}$ for sphere-based line arrays, in the range reported for ultra-thin polycrystalline Au films with thicknesses of 5.5 to 8.0 nm,³⁹ below the electron mean free path of $\lambda_{\text{Au}} \approx 37.7 \text{ nm}$.⁴⁰ This is consistent with a shell-dominated conductivity.

The change of $\delta\sigma_{\text{shell}}/\delta c_{\text{Au}}$ at 5 mg mL^{-1} for wire-based lines is due to the line width w that exceeds w_c (Fig. 4C), accompanied by an increasing number of crack-like defects in the shell as discussed above (Fig. 4A).

The wire-based lines outperformed the sphere-based lines at every c_{Au} despite a thinner (5.66 nm vs. 8.07 nm), porous shell. A possible explanation is the increased defect density in sphere-based lines. It does not affect w , h_{max} and A_{shell} , but can render entire lines non-conductive so that they contribute nothing to σ_{shell} . A second difference are grain boundary densities in the shells. The wires are micrometer-long single crystals²⁹ and largely oriented in imprinting direction. Their crystallinity may be at least partly retained during plasma sintering,⁴¹ while spheres are likely to create small grains. Thirdly, the likelihood that the only partially sintered line core also contributes to conduction, is higher in case of the high aspect ratio wires than in case of the spheres ($l_w \gg d_{\text{sp}}$).

In summary, the electrical properties of both electrode types were dominated by the core/shell structure of its conductors. Defects within the conductor shell and concentration independent shell thicknesses below λ_{Au} prevented σ_{shell} from reaching bulk Au conductivity. The wires' ability to self-assemble into percolating superstructures even at the lowest concentration used is the basis for the superior performance of wire-derived electrodes.

The printed lines reduce the optical transmittance mainly by masking parts of the substrate. The change in optical transmittance $\delta T_{400-800}/\delta c_{\text{Au}}$ was always negative for both wires and spheres (Fig. 6A and B). The value was constant for spheres; it changed at 6 mg mL^{-1} for wires, close to where w exceeded w_c (Fig. 4C). Wire-based electrodes had lower optical transmittances; all were above $\approx 85\%$ and thus practically useful.

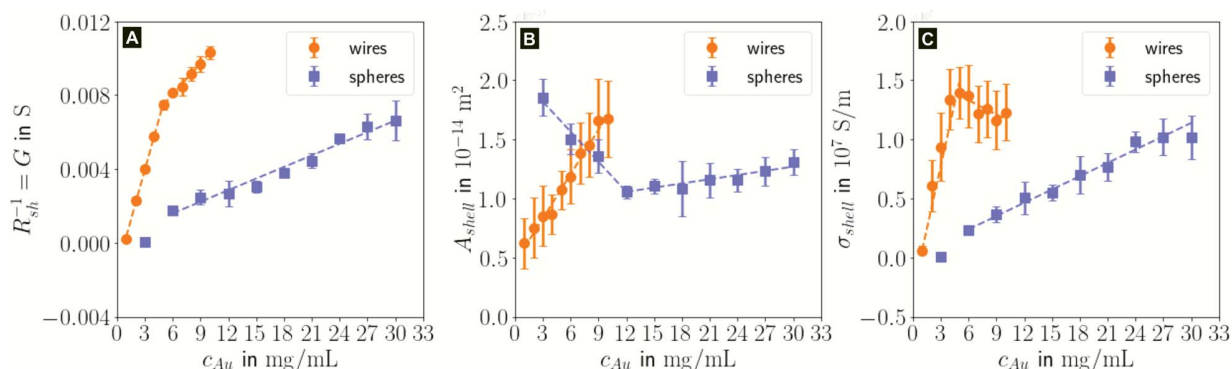


Fig. 5 Effect of particle concentration c_{Au} on (A) the conductance G of a representative square electrode sub-section, (B) the cross-sectional area A_{shell} and (C), the shell conductivity σ_{shell} . Standard deviations are indicated as error bars, the dashed lines are fits by linear regression to better illustrate the piece-wise linear relations.

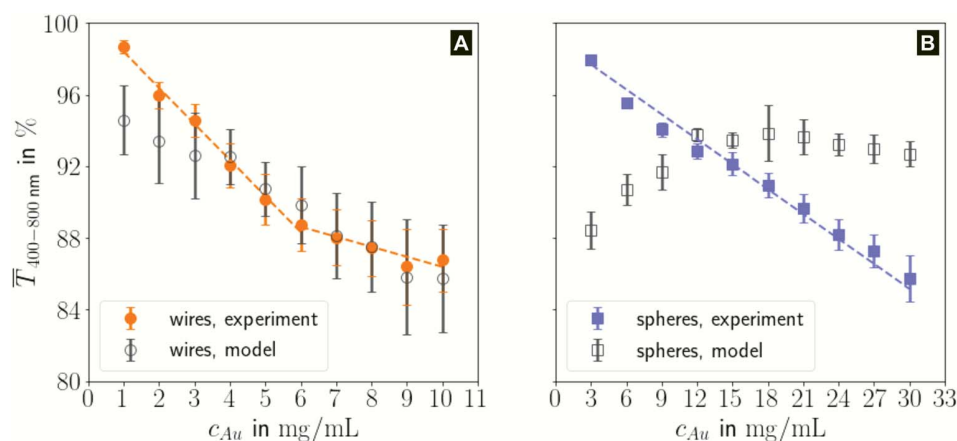


Fig. 6 Development of the optical transmittance $\bar{T}_{400-800}$ for (A) wire- and (B) sphere-based electrodes (experiment and model) with concentration c_{Au} , the belonging standard deviation and a data fit (dashed lines).

We approximated the metal lines as rectangles of width w at pitch p using data from CLSM measurements (the stamp pitch was $p = 19.5 \mu\text{m}$). The PET substrate was taken to be transparent and the rectangular lines as opaque. This yields a model transmittance T_{model} (Fig. S10 of the ESI[†]) of

$$T_{\text{model}} = \left(1 - \frac{w}{p}\right) \cdot 100\% \quad (3)$$

The experimental $\bar{T}_{400-800}$ for wire-based lines were above T_{model} (Fig. 6A) up to $c_{Au} = 3 \text{ mg mL}^{-1}$. The lines at such low concentrations were narrow but thin (Fig. 4C and D) and likely not fully opaque over the entire width. The lines formed above 4 mg mL^{-1} had $w > w_c$ (Fig. 4C) and became increasingly thicker (Fig. 4D and S9 in the ESI[†]). This increased their opacity and improved the match between model and experiment in the range 4 to 10 mg mL^{-1} .

The experimental $\bar{T}_{400-800}$ for sphere-based lines exceeded T_{model} for 3 to 9 mg mL^{-1} . The lines were broad (Fig. 4C) and thin in this range, only growing in thickness at 9 mg mL^{-1} and above (Fig. 4D and S9 in the ESI[†]). In contrast to wires, we found that $T_{\text{model}} - \bar{T}_{400-800} > 0$ above 12 mg mL^{-1} , probably because the metal that was deposited beyond w (Fig. 3C) caused strong diffuse scattering.

In summary, sphere-based outperformed wire-based electrodes in optical transmittance. Lines formed from spheres at low concentrations were more transparent; lines formed at higher concentrations were narrower. This is likely a direct consequence of the bundling wires' lower percolation threshold that enabled significant material deposition beyond w_c , which more than compensated for the increasing bleeding of spheres at high concentrations.

Considering both optical and electrical properties, c_{Au} affected optical transmittance much less than R_{sh} for both wires and spheres (Fig. 5A). The overall FOM was dominated by the sheet resistance, which explains the better performance of wire-based electrodes (Fig. 1).

4 Conclusion

Flexible transparent electrodes were imprinted from AuNP or AuNW at different concentrations and treated with plasma that partially removed the oleylamine ligand. We found strong correlations between the geometry of the nanocolloid, the concentration used for imprinting, the resulting post-plasma grid morphology, and the opto-electronic performances.

Plasma sintering led to a conductor structure with an outer gold shell that covered a hybrid core. The imprinted lines' average conductivity σ_{shell} depended on the density of defects in the shell that changed depending on concentration and particle type and rendered some lines discontinuous. Wire-based inks were less prone to such discontinuities and thus outperformed the sphere-based inks. The wires' aspect ratios of above 1000 facilitated their self-assembly into percolating superstructures that bridged stamp and substrate irregularities. This result is interesting for industrial processes that require a robust printing of lines. At concentrations $\geq 6 \text{ mg mL}^{-1}$, an increasing number of crack-like defects occurred within the bled parts of wire-based conductors and impaired σ_{shell} .

The optical transmittance of wire-based electrodes made with concentrated inks followed a simple model that assumes opaque lines. $\bar{T}_{400-800}$ of sphere-based electrodes made with concentrated inks was more strongly affected by bleeding that led to areas of partial transmittance. Nevertheless, sphere-based outperformed wire-based electrodes due to a better definition of geometry at high concentrations ($7-10 \text{ mg mL}^{-1}$) and due to more transparent lines at lower concentrations ($3-6 \text{ mg mL}^{-1}$).

For both wires and spheres, concentration affected $\bar{T}_{400-800}$ much less than R_{sh} . The FOM was thus dominated by R_{sh} , and wire-based electrodes that reached significantly lower R_{sh} at the same Au content performed better than sphere-based electrodes.

Both wire- and sphere-based electrodes had relatively large non-conductive parts. Their fraction may be reduced by tuning the ligand chemistry and the plasma process. It should be

possible to deposit lines that are thin enough to be entirely converted into metal, for example, if the plasma step is optimized such that it does not degrade their continuity.

An important aspect that has not been covered here is the stability of printed conductors. Thin metal films are prone to slow de-wetting⁴² and electromigration.⁴³ Wire-based electrodes with their pores and large, crack-like defects at higher concentrations are particularly vulnerable to such mechanism. Their relevance will be discussed in a forthcoming manuscript.

Author contributions

L. F. Engel designed the studies, performed the experiments himself or supervised them, implemented Python code for data analysis and visualization, analysed and visualized all acquired data and wrote the original draft. L. González-García and T. Kraus conceptualized the overarching research goals, acquired funding, administered, and supervised the project. They reviewed, edited and commented on the manuscript drafts.

Conflicts of interest

There are no conflicts to declare.

Acknowledgements

The authors thank Birgit Nothdurft for recording transmission electron micrographs of conductor cross-sections after preparation *via* FIB and for additional SEM microscopy, Marcus Koch for TEM images of the conductor cross-sections, Louis Weber for TEM images of dried AuNW and AuNP, Bart-Jan Niebuur for SAXS measurements, and Eduard Arzt for his continuing support of the project.

Notes and references

- 1 A. I. Hofmann, E. Cloutet and G. Hadziioannou, *Adv. Electron. Mater.*, 2018, **4**, 1700412.
- 2 T. Wang, K. Lu, Z. Xu, Z. Lin, H. Ning, T. Qiu, Z. Yang, H. Zheng, R. Yao and J. Peng, *Crystals*, 2021, **11**, 511.
- 3 H. B. Lee, W.-Y. Jin, M. M. Ovhall, N. Kumar and J.-W. Kang, *J. Mater. Chem. C*, 2019, **7**, 1087–1110.
- 4 X. Lu, Y. Zhang and Z. Zheng, *Adv. Electron. Mater.*, 2021, **7**, 2001121.
- 5 *Nanolithography: The Art of Fabricating Nanoelectronic and Nanophotonic Devices and Systems*, ed. M. Feldman, WP Woodhead Publ, Oxford, 2014, vol. 42.
- 6 X. Zhu, M. Liu, X. Qi, H. Li, Y.-F. Zhang, Z. Li, Z. Peng, J. Yang, L. Qian, Q. Xu, N. Gou, J. He, D. Li and H. Lan, *Adv. Mater.*, 2021, **33**, e2007772.
- 7 Y.-l. Wang, B.-j. Li, S.-s. Li, L.-j. Huang, Y.-y. Wang and N.-f. Ren, *Opt. Laser Technol.*, 2021, **138**, 106867.
- 8 Le Zhao, S. Yu, J. Li, M. Wu, L. Li and X. Wang, *Opt. Mater.*, 2021, **120**, 111427.
- 9 L. Zhou, X. Chen, W. Su, Z. Cui and W.-Y. Lai, *Adv. Mater. Interfaces*, 2022, 2102548.
- 10 D. Li, X. Liu, X. Chen, W.-Y. Lai and W. Huang, *Adv. Mater. Technol.*, 2019, **4**, 1900196.
- 11 L. Zhou, H.-Y. Xiang, S. Shen, Y.-Q. Li, J.-D. Chen, H.-J. Xie, I. A. Goldthorpe, L.-S. Chen, S.-T. Lee and J.-X. Tang, *ACS Nano*, 2014, **8**, 12796–12805.
- 12 J. H. M. Maurer, L. González-García, B. Reiser, I. Kanelidis and T. Kraus, *Nano Lett.*, 2016, **16**, 2921–2925.
- 13 I. Park, S. H. Ko, H. Pan, C. P. Grigoropoulos, A. P. Pisano, J. M. J. Fréchet, E.-S. Lee and J.-H. Jeong, *Adv. Mater.*, 2008, **20**, 489–496.
- 14 F. McGrath, J. Qian, K. Gwynne, C. Kumah, D. Daly, C. Hrelescu, X. Zhang, D. M. O'Carroll and A. Louise Bradley, *Appl. Surf. Sci.*, 2021, **537**, 147892.
- 15 S. H. Ko, I. Park, H. Pan, C. P. Grigoropoulos, A. P. Pisano, C. K. Luscombe and J. M. J. Fréchet, *Nano Lett.*, 2007, **7**, 1869–1877.
- 16 H. Agrawal and E. C. Garnett, *ACS Nano*, 2020, **14**, 11009–11016.
- 17 X. Yu, J. T. Pham, C. Subramani, B. Creran, Y.-C. Yeh, K. Du, D. Patra, O. R. Miranda, A. J. Crosby and V. M. Rotello, *Adv. Mater.*, 2012, **24**, 6330–6334.
- 18 Y. Kim, G. Kim and J. Lee, *Microelectron. Eng.*, 2010, **87**, 839–842.
- 19 J. H. M. Maurer, L. González-García, I. K. Backes, B. Reiser, S. M. Schlossberg and T. Kraus, *Adv. Mater. Technol.*, 2017, **2**, 1700034.
- 20 T. Kister, J. H. M. Maurer, L. González-García and T. Kraus, *ACS Appl. Mater. Interfaces*, 2018, **10**, 6079–6083.
- 21 J. H. M. Maurer, L. González-García, B. Reiser, I. Kanelidis and T. Kraus, *Phys. Status Solidi A*, 2016, **213**, 2336–2340.
- 22 W. Li, Y. Zhou, I. R. Howell, Y. Gai, A. R. Naik, S. Li, K. R. Carter and J. J. Watkins, *ACS Appl. Mater. Interfaces*, 2018, **10**, 5447–5454.
- 23 Y. S. Oh, H. Choi, J. Lee, H. Lee, D. Y. Choi, S.-U. Lee, K.-S. Yun, S. Yoo, T.-S. Kim, I. Park and H. J. Sung, *Sci. Rep.*, 2017, **7**, 11220.
- 24 S. Shaw, B. Yuan, X. Tian, K. J. Miller, B. M. Cote, J. L. Colaux, A. Migliori, M. G. Panthani and L. Cademartiri, *Adv. Mater.*, 2016, **28**, 8892–8899.
- 25 I. Reinhold, C. E. Hendriks, R. Eckardt, J. M. Kranenburg, J. Perelaer, R. R. Baumann and U. S. Schubert, *J. Mater. Chem.*, 2009, **19**, 3384.
- 26 S. Ma, V. Bromberg, L. Liu, F. D. Egitto, P. R. Chiarot and T. J. Singler, *Appl. Surf. Sci.*, 2014, **293**, 207–215.
- 27 U. Schubert, N. Hüsing and R. M. Laine, *Materials Syntheses: A Practical Guide*, Springer, Wien, 2008.
- 28 E. S. A. Nouh, E. A. Baquero, L.-M. Lacroix, F. Delpech, R. Poteau and G. Viau, *Langmuir*, 2017, **33**, 5456–5463.
- 29 H. Feng, Y. Yang, Y. You, G. Li, J. Guo, T. Yu, Z. Shen, T. Wu and B. Xing, *Chem. Commun.*, 2009, 1984–1986.
- 30 B.-H. Wu, H.-Y. Yang, H.-Q. Huang, G.-X. Chen and N.-F. Zheng, *Chin. Chem. Lett.*, 2013, **24**, 457–462.
- 31 Y. Chen, Y. Wang, J. Peng, Q. Xu, J. Weng and J. Xu, *ACS Nano*, 2017, **11**, 2756–2763.
- 32 D. B. Fraser and H. D. Cook, *J. Electrochem. Soc.*, 1972, **119**, 1368.

- 33 X. Lu, M. S. Yavuz, H.-Y. Tuan, B. A. Korgel and Y. Xia, *J. Am. Chem. Soc.*, 2008, **130**, 8900–8901.
- 34 M. Saitoh, Y. Kashiwagi and M. Chigane, *Soft Matter*, 2017, **13**, 3927–3935.
- 35 S. Bettscheider, B. Kuttich, L. F. Engel, L. González-García and T. Kraus, *J. Phys. Chem. C*, 2021, **125**, 3590–3598.
- 36 B. Reiser, D. Gerstner, L. González-García, J. H. M. Maurer, I. Kanelidis and T. Kraus, *Phys. Chem. Chem. Phys.*, 2016, **18**, 27165–27169.
- 37 M. Yin, H. Sun and H. Wang, *Micro Nano Lett.*, 2018, **13**, 887–891.
- 38 *CRC Handbook of Chemistry and Physics: A Ready-Reference Book of Chemical and Physical Data*, ed. W. M. Haynes, CRC Press, Boca Raton and London and New York, 97th edn, 2017.
- 39 M. C. Salvadori, A. R. Vaz, R. J. C. Farias and M. Cattani, *Surf. Rev. Lett.*, 2004, **11**, 223–227.
- 40 D. Gall, *J. Appl. Phys.*, 2016, **119**, 085101.
- 41 S. Bettscheider, T. Kraus and N. A. Fleck, *Acta Mater.*, 2022, **231**, 117799.
- 42 C. V. Thompson, *Annu. Rev. Mater. Res.*, 2012, **42**, 399–434.
- 43 D. G. Pierce and P. G. Brusius, *Microelectron. Reliab.*, 1997, **37**, 1053–1072.

3.3 Publication 3



Reproduced from

L. F. Engel, L. González-García, and T. Kraus: “Flexible and Transparent Electrodes Imprinted from Au Nanowires: Stability and Ageing”. *Nanoscale Adv.*, 2022, 4, 3940-3949.
DOI: 10.1039/D2NA00352J.

with permission from the Royal Society of Chemistry.



Flexible and transparent electrodes imprinted from Au nanowires: stability and ageing†

Lukas F. Engel, ^a Lola González-García ^{*a} and Tobias Kraus ^{*ab}

We study the stability of flexible transparent electrodes (FTEs) that were self-assembled from ultra-thin gold nanowires (AuNW) by direct nanoimprinting of inks with different particle concentrations (1 to 10 mg mL⁻¹). The resulting lines were less than 3 μm wide and contained bundles of AuNW with oleylamine (OAm) ligand shells. Small-angle X-ray scattering confirmed a concentration-independent bundle structure. Plasma sintering converted the wire assemblies into lines with a thin metal shell that contributes most to electrical conductivity and covers a hybrid core. We studied the relative change in sheet resistance and the morphology of the FTEs with time. The sheet resistance increased at all concentrations, but at different rates. The metal shell aged by de-wetting and pore formation. The hybrid core de-mixed and densified, which led to a partial collapse of the shell. Residual organics migrated through the shell *via* its pores. Lines formed at low concentration ($c_{\text{Au}} = 2$ to 3 mg mL⁻¹) contained less residual organics and aged slower than those formed at high $c_{\text{Au}} \geq 5$ mg mL⁻¹. We passivated the conductive shell with thin, adsorbed layers of PEDOT:PSS and found that it decelerated degradation by slowing surface diffusion and hindering further rupture of the shell. Thick capping layers prevented degradation entirely and stopped pore formation.

Received 3rd June 2022
Accepted 26th July 2022DOI: 10.1039/d2na00352j
rsc.li/nanoscale-advances

1 Introduction

Ultra-thin gold nanowires (AuNW) have core diameters $d_w \approx 1.7$ nm,¹ a shell of oleylamine (OAm), and lengths around $l_w \approx 3$ to 6 μm.^{2,3} They are suitable as building blocks of flexible and transparent electrodes (FTEs).^{4,5} The wires form in a simple one-pot synthesis,⁶ and have a conductive⁷ and chemically inert⁸ Au core and a low percolation threshold⁹ due to their high aspect ratio $l_w : d_w > 10^3$. Purification and re-dispersion of the AuNW in cyclohexane provides colloidal inks of varying Au concentration c_{Au} (AuNW inks) in which >70% of the wires self-assemble into bundles even at low $c_{\text{Au}} = 1$ mg mL⁻¹.¹⁰ Maurer *et al.*⁵ showed that direct nanoimprinting of AuNW inks leads to the self-assembly of AuNW bundles on flexible, transparent polyethylene terephthalate (PET) foils.

Transparent electrodes are key components¹¹ in opto-electronic devices¹² to collect charges from layers, *e.g.* in solar cells, or to supply layers with charge carriers, *e.g.* in light-emitting diode displays.¹³ Transparent electrodes for light and flexible devices¹⁴ should provide low sheet resistance, high optical transmittance, good mechanical flexibility, and long

term stability. Thin metal grids have the potential to combine these characteristics.

Grids with arbitrary geometry and sub-micron line width are attainable under ambient conditions in an efficient roll-to-roll compatible process using a soft silicone elastomer stamp as described by Maurer *et al.*⁵ The ink is confined in the stamp's cavities and the solvent (cyclohexane) permeates through the silicone. Ligand-dominated supra-molecular interactions cause the wires to bundle into hierarchical, percolating superstructures in the stamp's features. A soft plasma sintering step in a 5% H₂ in Ar (H₂/Ar) atmosphere removes insulating OAm ligands while retaining the overall imprinted structure and turns the grid into a conductive electrode. Maurer *et al.*⁵ nanoimprinted FTEs with square, hexagonal, and line-like features on PET and found optical transmittances $\geq 90\%$ over the entire visible range and sheet resistances R_{sh} ranging from 106 to 168 Ω_{sq} with better mechanical flexibility than commercial electrodes based on tin-doped indium oxide (ITO).

In our previous work,¹⁵ we studied the effect of the grid line morphology of AuNW-derived FTEs on their opto-electronic performance as a function of gold concentration c_{Au} and found that plasma sintering removed the insulating OAm ligands only partially. The plasma-sintered lines have thin conductive Au shells covering an insulating hybrid core. The thickness t_{shell} of the porous shell is virtually independent of c_{Au} ($t_{\text{shell}} = 5.66 \pm 1.06$ nm). Thin, porous metal films are prone to de-wetting,¹⁶ and AuNW are prone to the Rayleigh-Plateau

^aINM – Leibniz Institute for New Materials, Campus D2 2, 66123 Saarbrücken, Germany. E-mail: tobias.kraus@leibniz-inm.de; lola.gonzalez-garcia@leibniz-inm.de; Tel: +49 (0)681-9300-269, +49 (0)681-9300-389

^bColloid and Interface Chemistry, Saarland University, Campus D2 2, 66123 Saarbrücken, Germany

† Electronic supplementary information (ESI) available. See <https://doi.org/10.1039/d2na00352j>

instability,^{17–19} which raises the question of stability for electrodes imprinted from AuNWs.

The stability of random silver nanowire (AgNW) network electrodes has been studied extensively.^{13,20–25} They were found to be sensitive to UV light, chemical corrosion by sulfides, oxygen, and acids; the wires undergo thermally activated spheroidization due to the Rayleigh–Plateau instability and can fail through electromigration. Stability was improved by coatings that protect the metal surface from corrosion or reduce its diffusivity.

Few studies exist on the stability of AuNW based electrodes. Maurer *et al.*²⁶ prepared ≈ 10 nm thick, disordered layers of AuNW on glass *via* dip-coating at $c_{\text{Au}} \approx 2$ mg mL⁻¹, subjected them to plasma sintering in O₂ or H₂/Ar for different periods, and investigated their stability under ambient conditions. Untreated AuNW layers were non-conductive and fragmented within one week. Plasma sintering for 1 min led to conductive layers whose R_{sh} exceeded the measurable range after 4 h. The AuNW fragmented into spheres with diameters above those expected for the Rayleigh–Plateau instability, suggesting subsequent Ostwald ripening. Plasma sintering for 5 min or 15 min led to conductive layers that were stable for at least 4 months. Maurer *et al.*²⁶ concluded that OAm slows wire fragmentation, whereas partial OAm removal accelerates it.

In a different study, Maurer *et al.*²⁷ prepared ≈ 3 nm and ≈ 9 nm thick disordered AuNW layers on glass by dip-coating at $c_{\text{Au}} \approx 3$ mg mL⁻¹ and investigated their stability at 120 °C, 180 °C, and 250 °C with and without plasma sintering in H₂/Ar. Unsintered AuNW fragmented within 30 min of annealing, followed by a ripening process. Annealing of sintered layers caused de-wetting that accelerated with increasing temperature and decreasing film thickness. We are not aware of any studies on the stability of structured AuNW layers.

Here, we report on the stability of grid-like FTEs imprinted from AuNW. Arrays of about 1.6 μm wide, parallel lines with a pitch of 19.5 μm and heights of up to ≈ 275 nm were imprinted with inks of different c_{Au} on PET foils as in Engel *et al.*,¹⁵ analyzed with small-angle X-ray scattering (SAXS), and sintered in H₂/Ar plasma. Their R_{sh} was monitored during storage under ambient conditions in the dark and correlated with the grid morphology from scanning (SEM) and transmission electron microscopy (TEM). The sheet resistance R_{sh} increased at all c_{Au} , but the rates depended on c_{Au} and the line height. The decisive factor was the fraction of residual organics in the partially sintered cores. We adsorbed thin layers of PEDOT:PSS and found that it slowed electrode degradation. A thick capping layer of PEDOT:PSS prevented degradation and resulted in a slow decrease of R_{sh} during ≈ 3.5 months.

2 Materials and methods

2.1 Synthesis of Au nanowires

2.1.1 Chemicals. Tetrachloroauric(III) acid trihydrate (HAuCl₄·3H₂O) was synthesized according to Schubert *et al.*,²⁸ oleylamine (Acros Organics, C18 content of about 80–90%) was purchased from Fisher Scientific GmbH (Schwerte, Germany) and filtered with a 0.45 μm Rotilabo-PTFE syringe filter from

Carl Roth GmbH + Co. KG (Karlsruhe, Germany) directly before use, triisopropylsilane (95%) and *n*-hexane (at least 99% p.a.) were obtained from abcr GmbH (Karlsruhe, Germany), cyclohexane (ROTISOLV $\geq 99.9\%$, GC Ultra Grade) was bought from Carl Roth GmbH + Co. KG (Karlsruhe, Germany), and absolute ethanol ($\geq 99.8\%$, analytical reagent grade) was procured from Fisher Scientific GmbH (Schwerte, Germany). All chemicals were used without further purification unless explicitly mentioned.

2.1.2 Synthesis. Synthesis of the ultrathin nanowires (AuNW) having a gold (Au) core and being capped with an oleylamine (OAm) ligand shell followed a protocol of Nouh *et al.*,¹ which was based on the original research by Feng *et al.*⁶

For a typical synthesis, 60 mg of HAuCl₄·3H₂O (10 mM) were placed in a disposable 50 mL glass snap-on vial from Carl Roth GmbH + Co. KG (Karlsruhe, Germany), followed by 9.9 mL of *n*-hexane and 2.04 mL of oleylamine (400 mM). The resulting mixture was vortexed for 1 min to obtain a solution. To the solution, 3.06 mL (1 M) of triisopropylsilane (TIPS) were added as reducing agent. The mixture was vortexed for 30 s and then left to itself in an oven at 25 °C for 24 h.

The weighing of the very hygroscopic HAuCl₄·3H₂O was carried out in a glove box from SylaTech GmbH (Walzbachtal, Germany) since the presence of water causes shorter wires.²⁹ The glass snap-on vial was pre-flushed with dry Ar. OAm and TIPS were added with a 5 mL pipette in the given order and immediate succession.

2.1.3 Purification, dilution and storage. After synthesis, the AuNW were precipitated by adding twice the reaction volume of absolute ethanol and gently shaking the snap-on vial. Sedimentation was accelerated in a Rotanta 460 RS centrifuge from Andreas Hettich GmbH & Co. KG (Tuttlingen, Germany) with a swing-out rotor at 110 rcf for 2 min and the slowest possible deceleration. The supernatant was removed and the wires were re-dispersed in an amount of *n*-hexane corresponding to the initial reaction volume. This washing step was repeated once before re-dispersing the wires in cyclohexane to obtain a stock dispersion of $c_{\text{Au}} \approx 10$ mg mL⁻¹ (estimated based on HAuCl₄·3H₂O weighed in and 100% yield). By diluting the stock dispersion, the other concentrations of the AuNW inks applied were prepared. After synthesis and dilution, all dispersions were stored in a fridge at 5 °C for 16 h before use. Note that the storage time of the ink can affect the wire bundling as reported by Gong *et al.*³⁰ and Reiser *et al.*³¹ for AuNW dispersed in *n*-hexane as well as by Bettscheider *et al.*¹⁰ for AuNW dispersed in cyclohexane, and is thus an important parameter.

2.2 Nanoimprinting

2.2.1 Substrate cleaning. The PET substrates were of type Melinex 401 CW from DuPont Teijin Films UK Ltd (Redcar, United Kingdom) and had a thickness of 0.75 μm . They were pre-cleaned in ultrasonic baths using a custom rack and according to the following sequence: 5 min acetone, 5 min ethanol, and 5 min Milli-Q ultrapure water. Then the substrates,

which have a glass transition temperature of 70–80 °C, were dried at 60 °C for 30 min.

2.2.2 Polydimethylsiloxane (PDMS) imprinting stamp fabrication. The PDMS imprinting stamps were manufactured in a two-step process. In the first step, a PDMS master was moulded off a silanized silicon master from Amo GmbH (Aachen, Germany) carrying a pattern of parallel line channels (patterned area $A \approx 7 \text{ cm} \times 7 \text{ cm}$, pitch $p \approx 19.5 \text{ }\mu\text{m}$, channel width $w_c \approx 1.6 \text{ }\mu\text{m}$ and channel depth $d_c \approx 4.2 \text{ }\mu\text{m}$). In the second step, the PDMS imprinting stamp was moulded off the silanized PDMS master.

Silanization of the silicon master was directly performed, while silanization of the PDMS master was performed after its plasma activation for 1.5 min using an oxygen plasma at 0.3 mbar in a low pressure plasma reactor of type Pico from Diener electronic GmbH & Co. KG (Ebhausen, Germany). Silanization of each master was performed by vapour phase deposition inside a conventional glass desiccator with a snap-on vial cap containing 30 μL of (tridecafluoro-1,1,2,2-tetrahydrooctyl)trichlorosilane from aber GmbH (Karlsruhe, Germany). The snap-on vial cap was shielded from the masters to achieve uniform silanization. The desiccator was flushed with Ar, evacuated to 3 mbar, and disconnected from the vacuum pump. After 30 min, the desiccator was slowly ventilated with air.

The pre-polymer and the cross-linker of a PDMS kit, Sylgard 184 from Dow Inc. (Midland, USA), were mixed in a 10 : 1 (w/w) ratio and degassed in a Speedmixer DAC 600.2 VAC-P from Hauschild GmbH & Co. KG (Hamm, Germany) at a speed of 2350 rpm and a pressure of 1 mbar for 3 min so that no air bubbles remained. This mixture was poured onto the respective master. A Teflon ring (2 mm thick) which was sealed at the edges with add-i-gum light N from DE Healthcare Products (Gillingham, UK) and on top with a glass plate, was used as a spacer to ensure uniform thickness. Before carefully peeling off the replicate along the stamp channels, the PDMS was cured at 80 °C for 3 h.

The replicates of the PDMS masters were cut into two halves, each constituting an imprinting stamp. Both had an area of 3.5 cm \times 8 cm of which 3.5 cm \times 7 cm were patterned and 3.5 cm \times 0.5 cm at either end were not. The latter were run-in and run-out areas during imprinting.

2.2.3 Nanoimprinting. Nanoimprinting was performed using a modified TQC Sheen automatic film applicator from Industrial Physics Inks & Coatings GmbH (Hilden, Germany). It was equipped with a custom-made 3 kg steel cylinder (8 cm in diameter and height) onto which a single PDMS stamp was attached using a double-sided tape from tesa SE (Norderstedt, Germany). Such an equipped steel cylinder was moved at 4 mm s^{-1} during imprinting. 60 μL of ink were injected directly in-between imprinting stamp and PET substrate using a pipette, right before imprinting. Ink residues adhering to the PDMS stamp after imprinting were removed using Scotch Magic Tape from 3 M Deutschland GmbH (Kleinstheim, Germany) before re-use. A comprehensive description of the imprinting process is given in Maurer *et al.*⁵ The process is sensitive to humidity and must be performed above the dew point to prevent capillary

condensation. Imprinting was typically carried out at 22 °C and 55% rH (dew point of 12.5 °C).

2.3 Plasma sintering

Plasma sintering was performed in a low pressure 13.56 MHz RF plasma reactor of type Pico from Diener electronic GmbH & Co. KG (Ebhausen, Germany) right after imprinting. A mixture of 5% H_2 in Ar was used as process gas. The sintering conditions were: room temperature and ≈ 0.3 mbar for 20 min with 100 W RF power.

2.4 Small-Angle X-Ray Scattering (SAXS)

The structural arrangement of the wires within the pre-plasma lines was studied in transmission *via* SAXS on PET right after imprinting. Any influence of applied vacuum was avoided by performing the measurements in air at room temperature. Background scattering due to the substrate was measured separately as reference. The scattering instrument was a Xeuss 2.0 HR SAXS/WAXS instrument from Xenocs SAS (Grenoble, France) with a Cu $K\alpha$ source. The detector was a PILATUS3 R 1 M from DECTRIS AG (Baden, Switzerland) which was set up at a distance of ≈ 550 mm from the samples. The distance was precisely calibrated with a Ag behenate sample prior to each measurement. Samples were measured for a total of 2 h each. The 2D scattering images were azimuthally integrated over an angular sector at 90° and an aperture angle of 10° (to take the anisotropy due to the alignment of wires in imprinting direction into account) with the software Foxtrot from Synchrotron SOL-EIL (Saint-Aubin, France) to obtain the scattering curves.

2.5 Sheet resistance measurements

Electrical resistances were measured in 2-point-probe configuration using a multi-channel multi-meter (DAQ6510 data acquisition logging multi-meter system) equipped with multiplexer cards (7702 40-channel differential multiplexer module with screw terminals) from Keithley Instruments GmbH (Germaring, Germany). Electrodes were contacted by applying a fast drying Ag paste ACHESON Ag DAG 1415 from Plano GmbH (Wetzlar, Germany) and AGF 1 miniature crocodile clamps from SKS Kontakttechnik GmbH (Niederdorf, Germany). The Ag paste was deposited in two parallel lines, each 1.5 cm long and spaced 1.5 cm apart, yielding a square measurement field. This caused the measured resistances being equal to the desired sheet resistances. Measurements were automatically recorded every 10 min during storage under controlled ambient conditions ($T \approx 22 \text{ }^\circ\text{C}$, $\text{rH} \approx 55\%$) in the dark. Light was excluded to avoid *e.g.* radiation heating.

2.6 Dip coating

Electrodes were dip coated in an aqueous PEDOT:PSS dispersion of type Clevios™ P from Heraeus Deutschland GmbH & Co. KG (Hanau, Germany) right after plasma treatment (taking advantage of the plasma's hydrophilising effect) and the subsequent preparation for contacting. For contacting purposes, a fast drying Ag paste ACHESON Ag DAG 1415 from

Plano GmbH (Wetzlar, Germany) was applied as described in the section above. The contacted electrodes were slowly dipped into the dispersion and were then immediately pulled out again slowly. Excess PEDOT:PSS was either allowed to drip off (capping layer) or was washed off (adsorbate layer) in deionised water by carefully moving the electrode up and down until no more PEDOT:PSS residues were visible (PEDOT:PSS is deep blue) and presumably only a thin layer of chemisorbed PEDOT:PSS remained (Au–S bond). Such coated electrodes were then dried for 15 min in a drying oven at 50 mbar and room temperature. Afterwards, for the electrodes from which the excess PEDOT:PSS only dripped off, the Ag paste contacting was gently freed from the PEDOT:PSS capping layer using mini head clean room polyester swabs moistened with deionised water.

2.7 Cross-sectioning *via* Focused Ion Beam (FIB)

Cross-sections of printed and of sintered lines were prepared using a FEI Versa 3D DualBeam from Thermo Fisher Scientific GmbH (Schwerte, Germany). The surfaces of the lines were protected by Pt-layers first deposited by an electron beam, then with an ion beam.

2.8 Transmission Electron Microscopy (TEM)

All TEM lamellae from FIB cross-sectioning were imaged at an acceleration voltage of 200 kV in a JEM 2010 from JEOL GmbH (Freising, Germany).

2.9 Scanning Electron Microscopy (SEM)

Scanning electron micrographs were taken with a FEI Quanta 400 ESEM or a FEI Versa 3D DualBeam from Thermo Fisher Scientific GmbH (Schwerte, Germany) using the secondary electron detectors. For better imaging, the grids were imprinted onto polished, p-type Si wafers from Siegert Wafer GmbH (Aachen, Germany).

3 Results and discussion

We prepared inks from oleylamine-covered gold nanowires and printed grids at different nanowire concentrations on flexible polyethylene terephthalate (PET) foils using the same stamp. All grids underwent plasma sintering to obtain electrically conductive FTEs. We monitored the change in their sheet resistance R_{sh} over a storage period of 14 days at a constant temperature $T \approx 22^\circ\text{C}$ and a humidity of $rH \approx 55\%$ in the dark. Fig. 1 shows the change in R_{sh} as a function of the ink concentration. The lowest concentration of $c_{Au} = 2\text{ mg mL}^{-1}$ was the minimum to achieve sufficient percolation and reasonable conductivities. The highest $c_{Au} = 6\text{ mg mL}^{-1}$ marks the concentration from which on ageing became concentration-independent.

The sheet resistances of all electrodes increased with time. The rate of increase was much larger for electrodes imprinted at 5 mg mL^{-1} than at 3 mg mL^{-1} . The resistance of electrodes imprinted at 3 mg mL^{-1} increased by $\approx 30\%$ within 14 days of ageing; electrodes imprinted at 5 mg mL^{-1} became non-conductive within 8 h.

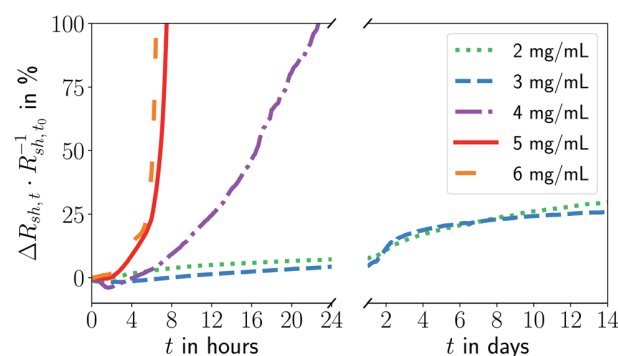


Fig. 1 Relative change in sheet resistance $(R_{sh,t} - R_{sh,t_0})R_{sh,t_0}^{-1} = \Delta R_{sh,t}R_{sh,t_0}^{-1}$ after time t for electrodes imprinted at different ink concentrations c_{Au} . The results of repeated experiments and additional concentrations are shown in Fig. S1 in the ESI.†

Fig. 2 and 3 show electron micrographs of the surfaces and cross-sections of relatively stable grid lines imprinted at 2 mg mL^{-1} (“low c_{Au} ”) and highly unstable lines imprinted at 6 mg mL^{-1} (“high c_{Au} ”), respectively. Images were taken directly after imprinting, after plasma sintering, and after 24 h of storage under ambient conditions ($T \approx 22^\circ\text{C}$, $rH \approx 55\%$) in the dark. Plasma sintering led to a structure with a thin shell, a coarsened core, and a loss in height (compare panel A with C and B with D). Height loss continued during ageing with the core further densifying (compare panel C with E and D with F). At high c_{Au} , ageing also caused de-mixing inside the core (Fig. 3F) and rupture of the shell (Fig. 3E). This is consistent with the illustrations in panels G–I, which illustrate the associated change in the line structure: orange depicts gold wires or shells, with the wires arranged in hexagonal bundles (dotted black lines); green indicates oleylamine ligand molecules and their fragments (residual organics).

We first consider lines printed at low c_{Au} in more detail (Fig. 2). The pre-plasma lines (Fig. 2A) contained AuNW in hexagonally packed bundles. They are visible in the TEM cross-section in Fig. 2B and caused peaks in SAXS (Fig. S2 in the ESI†). The bundle packing was noticeably denser than inside the ink, with a center-to-center distance $a_{c-c} = 4.22 \pm 0.04\text{ nm}$ versus $a_{c-c}^{\text{ink}} = 5.9 \pm 0.02\text{ nm}$ in liquid.¹⁰ The surface-to-surface distance of the gold cores was $a_{s-s} \approx 2.52\text{ nm}$. a_{s-s} is only $\approx 23\%$ above the length of an OAm molecule ($l_{OAm} \approx 2.05\text{ nm}$ (ref. 32)), probably due to a zipper-like interdigitation of the OAm shells.³¹

Most of the wires were well aligned in lines that were narrower than the channel width of the imprinting stamp. Some wires bled beyond the channel width; these were only partially aligned in imprinting direction (Fig. 2J). The surface of the freshly printed lines exhibited a ridge that is visible as a bright area in Fig. 2J. Fig. 2G shows an illustration of the rough surface of the lines before plasma sintering that is caused by the bundled wires.

Plasma sintering formed a thin metal shell around a hybrid core (Fig. 2C and D). The surface of the sintered line appears coarse, the ridge is blunted (Fig. 2K), and the wire bundle

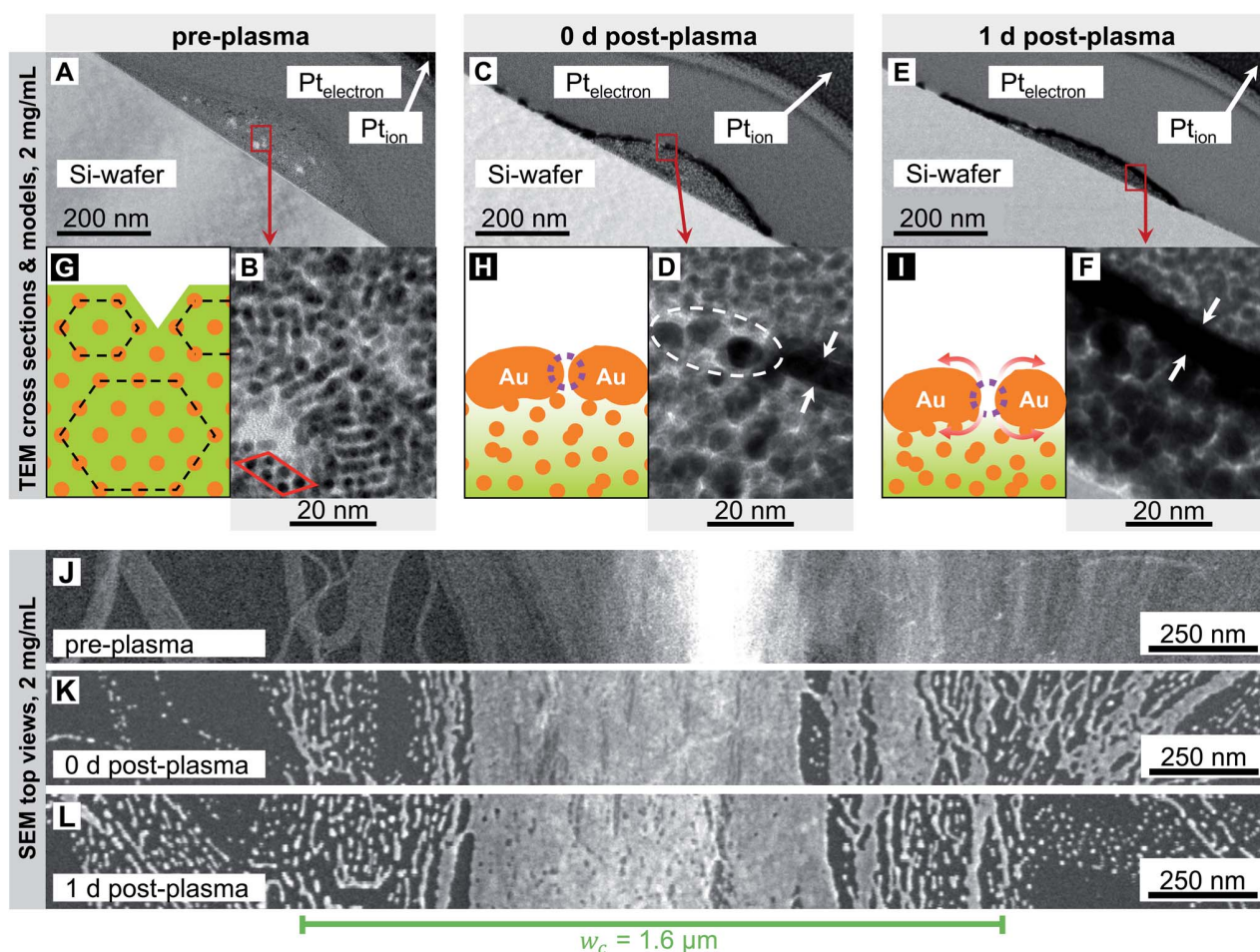


Fig. 2 Cross-sections and surfaces of lines imprinted at 2 mg mL^{-1} before (A, B and J), immediately after (C, D and K), and one day after (E, F and L) plasma sintering. They show the core-shell structure after plasma sintering (C and D), the densifying (A, C and E) and coarsening (B, D and F) core, and the coarse surface morphology with small pores in the shell (from K to L). The illustrations in panels (G–I) illustrate the overall structure. Orange depicts gold wires or shells, green indicates oleylamine ligand molecules and their fragments (residual organics). The wires are arranged in hexagonal bundles (dotted black lines) in (G). They form porous shells in (H), and the bundles loose their order. The pores in (I) have gently grown by surface diffusion and the densifying core causing the shell to collapse.

structure is lost (Fig. 2D). The shell was porous and has holes indicated in Fig. 2D. Shell porosity likely results from the bundle-induced roughness. Wires may partially fragment before they sinter.¹⁸ Thin layers of sparse AuNW adjacent to the main line fragmented, probably due to the Rayleigh–Plateau instability.^{17–19} They formed finger-like structures that indicate solid-state de-wetting.¹⁶

The morphology of the core (Fig. 2B) visibly coarsened during sintering (Fig. 2D) through its entire thickness (Fig. S3 in the ESI†) of up to $h_{\text{max}} = 68 \pm 14 \text{ nm}$.¹⁵ A relevant fraction of OAm has apparently been removed. This likely turns the core partially porous, too. The initial OAm content was $\approx 87 \text{ vol}\%$ ¹⁰ (see Section 2.2 in the ESI†). The plasma's kinetic ions remove the ligands and enhance the Au surface mobility,^{33–37} which renders the wires highly susceptible to the Rayleigh–Plateau instability.²⁶ There probably exists a gradient in the residual organic concentration from the shell (Fig. 2H, very light green)

towards the substrate (Fig. 2H, darker green), as the plasma sintering attacks from the outside.³⁸

We stored the samples for 24 h and analyzed morphological changes. The core appeared denser (Fig. 2C–F), probably because the cores' pores began to close, and the maximum line height h_{max} decreased (compare Fig. 2C and E). Small pores appeared on the surface. They are clearly visible in the SEM top view (Fig. 2L) but not in the cross-sectional TEM (Fig. 2E and F) that show lamellae with a thickness on the order of $\approx 200 \text{ nm}$. The pores probably form by solid-state de-wetting and the shrinkage of the core that compensates for the loss of OAm. Solid-state de-wetting starts at pre-existing holes (visible in Fig. 2D) in the thin shell. De-wetting requires diffusion and is faster for decreasing shell thicknesses.¹⁶ A continuous, $\approx 6 \text{ nm}$ thick Au film does not de-wet at room temperature during 24 h.¹⁶ It is thus likely that the compacting core is more important for the ageing of the line. This is consistent with the unchanged microstructures on both sides of the printed lines

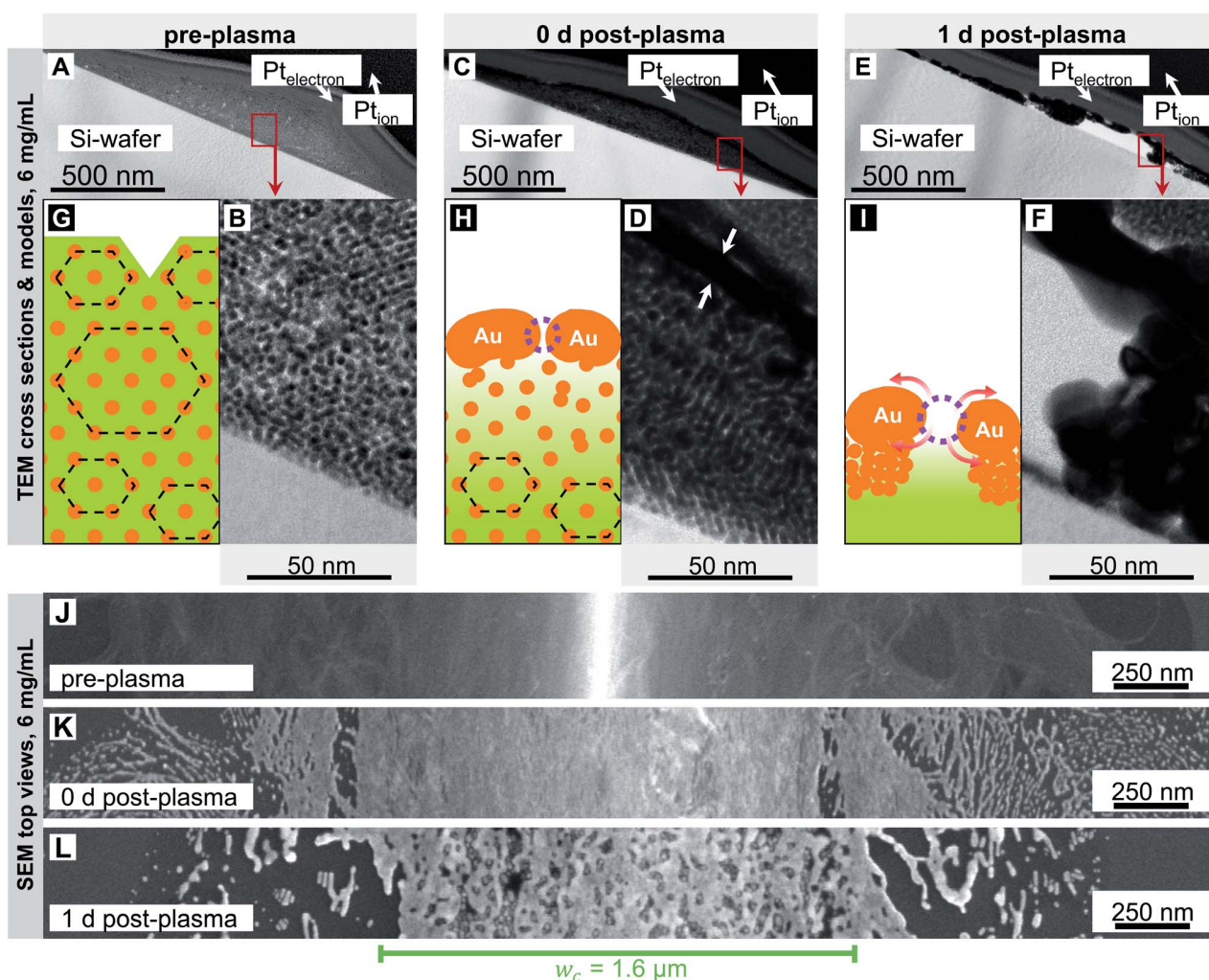


Fig. 3 Cross-sections and surfaces of lines imprinted at 6 mg mL^{-1} before (A, B and J), immediately after (C, D and K), and one day after (E, F and L) plasma sintering. They show the core-shell structure after plasma sintering (C and E), the densifying (A, C and E) and coarsening (B, D and F) core, and the coarse surface morphology with growing pores (from K to L). The illustrations in panels (G–I) illustrate the overall structure. Orange depicts gold wires or shells, green indicates oleylamine ligand molecules and fragments. The wires are arranged in hexagonal bundles (dotted black lines) in (G). They form porous shells in (H), and the bundles loose their order. The pores in (I) have grown prominently by surface diffusion and by the both de-mixing and densifying core causing the shell to collapse.

(Fig. 2L *versus* Fig. 2K) that did not de-wet. The increase in shell porosity increased R_{sh} by only 7.3% within 24 h. Apparently, the pores were small in size, and relaxation effects after plasma sintering that release stress and lattice distortions³⁹ in the shell counteracted a larger increase in R_{sh} . Compared with Fig. 2H and I shows an illustration with a slightly thicker shell, an increased pore size and due to the shrinking core a lower height. As the core has densified, the residual organics are now distributed within a smaller volume (represented by a slightly darker shade of green in Fig. 2I).

We now consider the lines printed at high particle concentration in more detail (Fig. 3). Before plasma-sintering, SAXS confirmed the same 2D hexagonal arrangement of the AuNW as observed at low concentrations (Fig. S2 in the ESI[†]). The morphology seen in TEM cross-sections appears unchanged, too (Fig. 3A and B). SEM top-views show wider lines with $w > w_c$

(Fig. 3J), but the surface morphology appears similar to that seen at 2 mg mL^{-1} (Fig. 2J). The most relevant change in line morphology before plasma sintering seems to be the increased height (compare Fig. 3A and 2A).

Plasma sintering yielded the same core-shell structure as described above. The pores in the shell are not visible in the TEM images (Fig. 3C and D) but have been identified in our previous work.¹⁵ A pronounced gradient in core density that decreased towards the substrate was visible in the cross-sections (compare Fig. 3B with D). We did not observe such strong gradients at lower concentrations, probably because those lines were thinner. The gradient likely results from partial removal of OAM that is more efficient close to the shell. The overall morphology of the sintered lines did not change with ink concentration and remained as shown in Fig. 2H, but with adjusted height and structural gradient (Fig. 3H).

Ageing for 24 h caused the shell to become increasingly porous (Fig. 3E). The density of pores was similar to that at 2 mg mL^{-1} , but the pores were larger (compare top view SEM images in Fig. 3L *versus* Fig. 2L). Some of the pores joined into large cracks that revealed the fragmented wires of the core. The hybrid core appeared heterogeneously densified and de-mixed (Fig. 3E and F); metallic gold accumulated on the fragmented shell. The metal-rich volumes appear to contain larger spheres, possibly formed by wires undergoing Rayleigh–Plateau fragmentation,^{17–19} and possibly growing by Ostwald ripening.⁴⁰ Fig. 3I shows an illustration of the de-mixing core–shell structure.

These results suggest that the same mechanisms are responsible for the ageing of sintered lines printed at 2 mg mL^{-1} and 6 mg mL^{-1} , but that they operate at larger rates for the higher concentration. The reason likely is the increased fraction of residual organic molecules in the cores of sintered lines printed at high concentration. Inks with high c_{Au} form thicker lines that are not fully penetrated by the plasma and thus remain richer in OAm and its fragments. The low binding energy of Au–NH₂,^{41,42} the partial fragmentation of OAm, and the low viscosity⁸ of OAm at room temperature increase the mobility of the core components^{43–45} and accelerate ageing. This effect apparently saturates at high fractions of residual organics reached at 6 mg mL^{-1} .

We conclude that some of the advantages that AuNWs have for the nanoimprinting of conductive structures limit the stability of the resulting structures. The wires' mechanical flexibility and high aspect ratio promote percolation but lead to coarse surface microstructures of the unsintered lines (see Fig. 2J and 3J), causing pores in the conductive shell which foster solid-state de-wetting after plasma sintering. The wires' small diameters make them susceptible to the Rayleigh–Plateau instability,^{17–19} which renders only partially sintered line cores unstable; the weakly bound OAm shell^{41,42} that occupies approximately $\approx 87 \text{ vol}\%$ ¹⁰ of the pre-plasma solid turns the sintered parts of the line core porous, and its residues accelerate de-mixing.^{43–45}

Lines printed at low ink concentrations are comparatively thin, and the OAm is largely removed from them during plasma sintering. This slows solid-state de-wetting of the shell and makes the electrodes comparatively stable. Lines printed at high concentrations are thicker, remain rich in OAm and its fragments after sintering. They age faster so that electrodes fail in less than 24 h. The transition from comparatively stable to highly unstable electrodes coincides with the concentration at which the line width w reaches the channel width w_c of the imprinting stamp (4 mg mL^{-1}). Above this concentration, the maximum line height h_{max} increases faster than the line width.¹⁵

How can we stabilize AuNW electrodes? Full sintering of the printed lines would reduce mobility and thus obviate several ageing mechanisms identified above. Plasma sintering of AuNW grids is self-limiting,³⁸ however, and excludes full sintering of the thick lines imprinted at high c_{Au} that have the best performance.¹⁵ The shell shields the core from the plasma and contains the (partially fragmented) OAm. We are not aware of

any other existing sintering technique that could retain the structure of the printed lines but remove all organic content.

An alternative approach is to stabilize the conductive shell. Metal thin films can be stabilized using adsorbates that prevent or slow the diffusive processes underlying solid-state de-wetting.¹⁶ A promising material for that purpose is PEDOT:PSS, a mixture of the positively charged poly(3,4-ethylenedioxythiophene) and the negatively charged polystyrene sulfonate. There is evidence that polythiophenes bind covalently to Au *via* sulphur.^{46,47} Their molecular configuration depends on the crystallographic orientation and the curvature of the Au surface.⁴⁸

We used the commercial PEDOT:PSS aqueous dispersion Clevios™ P that contains swollen, gel-like PEDOT:PSS particles of diameter $d_{50} = 80 \text{ nm}$ at a PEDOT : PSS weight ratio of 1 : 2.5 and a pH of 1.9 without any additives.^{49,50} While its acidity is harmful for AgNWs,²⁴ it does not etch AuNWs. Dried films of Clevios™ P exhibit conductivities of 5 S cm^{-1} ,⁵⁰ five orders of magnitude below that of the Au shells.¹⁵ We used dip-coating to prepare electrodes with adsorbate layers of PEDOT:PSS. Excess PEDOT:PSS was removed by washing in water to retain only the adsorbed film; some samples were not washed to retain a thicker capping layer after drying. Note that rough and porous Au surfaces improve the bonding of PEDOT:PSS.⁵¹ The samples were then stored under ambient conditions ($T \approx 22 \text{ }^\circ\text{C}$, $\text{rH} \approx 55\%$) in the dark and we analyzed their ageing.

Fig. 4 shows the relative change in sheet resistance of electrodes imprinted at 6 mg mL^{-1} for different coatings (A–C) and the reconstructed morphology illustrations (D–F). Bare electrodes deteriorated fast (five-fold increase of R_{sh} in roughly 7 h) and became insulating in less than 1 day. Their relative change in R_{sh} increased exponentially (Fig. 4A). The resistance of electrodes with a PEDOT:PSS adsorbate layer initially decreased by up to $\approx 16\%$ and then slowly increased with an almost linear trend, so that R_{sh} quintupled after 62 days (Fig. 4B). It is likely that the adsorbed PEDOT:PSS layer prevents a fast rupture of the shell but cannot entirely suppress diffusion at the shell's Au–air and neither at the core's Au–OAm residue interfaces. It cannot fully stabilize the shell mechanically when the hybrid core shrinks.

A thick PEDOT:PSS capping layer caused an initial increase in R_{sh} of about $+14\%$ within ≈ 7 days and a subsequent slow, almost linear decrease by 20 percentage points down to $\approx 94\%$ of the initial R_{sh} before saturating after 100 days (Fig. 4C). We think that the initial increase in R_{sh} is due to residual water at the Au–PEDOT:PSS interface which evaporates only slowly and drives de-wetting. At the same time, the thick capping layer prevents the shell from collapse and apparently slows de-mixing, probably by restricting material displacements through the shell. The decrease in R_{sh} by 20 percentage points suggests that it may even be possible to direct the remaining mobility such that the conductive cross-section of the shell grows with time.

In summary, we find that PEDOT:PSS adsorbate layers can slow electrode degradation noticeably, but cannot fully prevent it. A defect-free metal shell proves to be a key element of stable electrodes. PEDOT:PSS capping layers permanently patch the

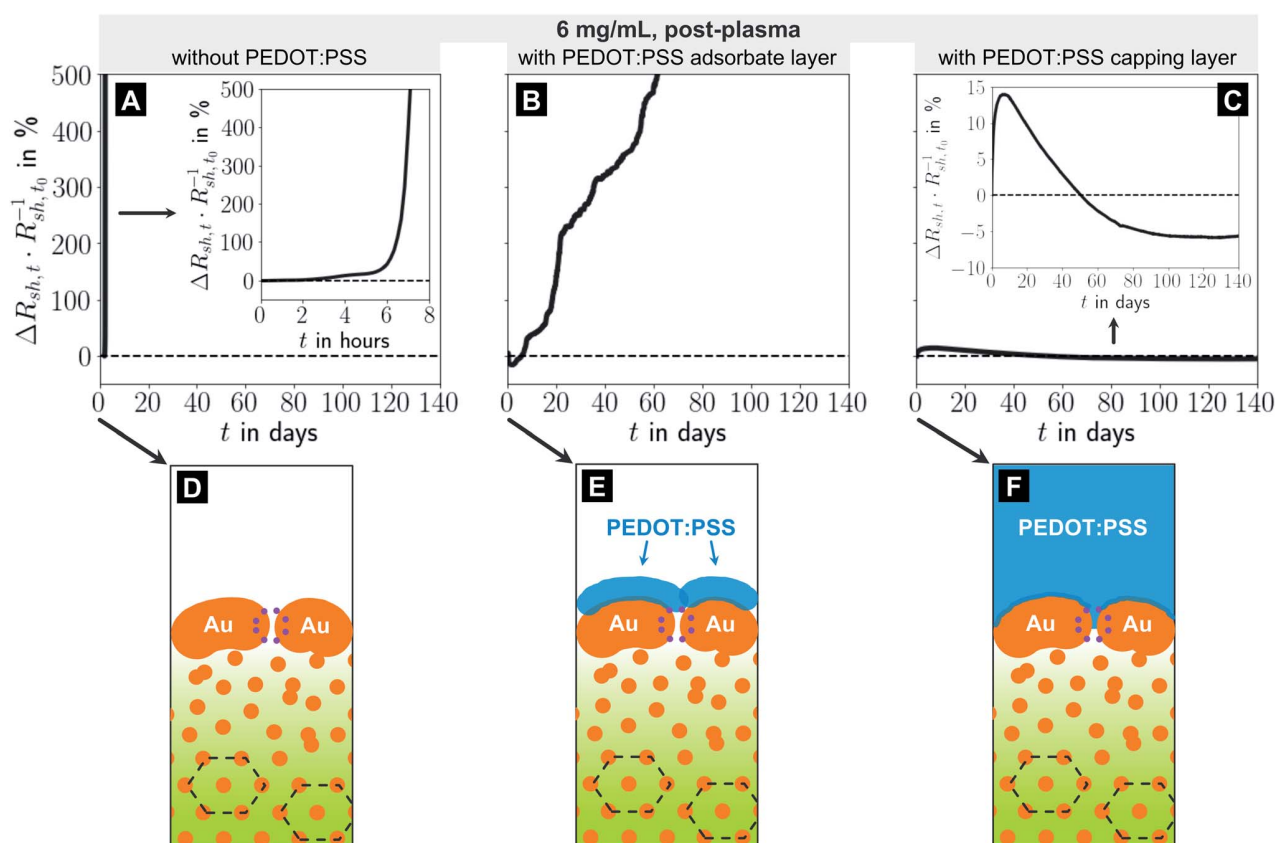


Fig. 4 (A–C): Relative change in sheet resistance $(R_{sh,t} - R_{sh,t_0})R_{sh,t_0}^{-1} = \Delta R_{sh,t}R_{sh,t_0}^{-1}$ after time t for electrodes imprinted at 6 mg mL^{-1} with different coating finishes. (D–F): illustrations of the apparent microstructures.

porous shells and prevent degradation. The patched shell directs the demixing of the core such that a larger fraction of the imprinted Au reduces the electrodes' R_{sh} .

4 Conclusions

Flexible transparent electrodes were imprinted from OAm-coated AuNW at different wire concentrations and plasma sintered, partially removing the OAm ligands. We found strong correlations between the c_{Au} used for imprinting, the resulting morphology of the FTEs after plasma sintering, and their ageing during storage under ambient conditions in the dark. The sheet resistances of all FTEs increased at rates that strongly depended on the ink concentration c_{Au} . Electrodes printed at low c_{Au} of 2 to 3 mg mL^{-1} increased their R_{sh} by $\approx 30\%$ within 14 days, whereas electrodes printed at high $c_{Au} \geq 5 \text{ mg mL}^{-1}$ lost all measurable conductivity within less than 1 day.

We demonstrated that the degradation is due to the microstructure of the printed lines after sintering. Plasma sintering yielded a porous, conductive Au shell around a core that contained a hybrid, nanostructured mixture of Au and OAm residues. We identified three ageing mechanisms: solid-state de-wetting of the shell, de-mixing inside the core, and partial collapse of the shell. The rates of solid-state de-wetting and de-mixing strongly depended on the fraction of residual organics

in the core that changed the overall microscale mobility. At low c_{Au} , most of the OAm was removed from the core, which slowed de-mixing and degradation. At high c_{Au} , thicker lines formed that were not fully penetrated during plasma sintering and retained a larger fraction of OAm and its fragments, resulting in less stable electrodes.

Degradation could be slowed and even inhibited by coating the conductive lines with PEDOT:PSS. Thin, adsorbed layers of PEDOT:PSS reduced the degradation rate by slowing de-wetting and hindering a fast rupture of the shell. Thicker layers prevented conductivity losses up to at least 120 days and led to a decrease in R_{sh} of 6% after 100 days. The layer changed the degradation mechanism, activating paths towards a slow growth of the conductive shell. This hints at a possible “ageing design” through coatings that direct the transport of the metal, similar to known self-healing concepts.⁵²

The importance of microstructure for degradation that we observed here suggests that the geometry of the colloid used for imprinting will affect ageing mechanisms, too. Spheres, for example, have been shown to yield lines with a smoother surface morphology than wires that form a thinner, porous shell after plasma sintering.¹⁵ Larger spheres reduce the fraction of OAm that affects the mobility of the core. The effect of another particle geometry is currently under investigation and will be the topic of a forthcoming manuscript.

Author contributions

L. F. Engel designed the experiments, performed the experiments himself or supervised them, implemented Python code for data analysis and visualization, analysed and visualized all acquired data, and wrote the original draft. T. Kraus and L. González-García devised the research strategy, acquired funding, administered, and supervised the project. They reviewed, edited, and commented the manuscript drafts.

Conflicts of interest

There are no conflicts to declare.

Acknowledgements

The authors thank Birgit Nothdurft for recording TEM images of the line cross-sections after preparation *via* FIB and for additional SEM microscopy, Marcus Koch for recording TEM images of the line cross-sections, Bart-Jan Niebuur for SAXS measurements, and Eduard Arzt for his continuing support of the project.

Notes and references

- 1 E. S. A. Nouh, E. A. Baquero, L.-M. Lacroix, F. Delpéch, R. Poteau and G. Viau, *Langmuir*, 2017, **33**, 5456–5463.
- 2 X. Lu, M. S. Yavuz, H.-Y. Tuan, B. A. Korgel and Y. Xia, *J. Am. Chem. Soc.*, 2008, **130**, 8900–8901.
- 3 M. Saitoh, Y. Kashiwagi and M. Chigane, *Soft matter*, 2017, **13**, 3927–3935.
- 4 J. H. M. Maurer, L. González-García, B. Reiser, I. Kanelidis and T. Kraus, *Nano Lett.*, 2016, **16**, 2921–2925.
- 5 J. H. M. Maurer, L. González-García, I. K. Backes, B. Reiser, S. M. Schlossberg and T. Kraus, *Adv. Mater. Technol.*, 2017, **2**, 1700034.
- 6 H. Feng, Y. Yang, Y. You, G. Li, J. Guo, T. Yu, Z. Shen, T. Wu and B. Xing, *Chem. Commun.*, 2009, 1984–1986.
- 7 Y. Zhang, W. Chu, A. D. Foroushani, H. Wang, D. Li, J. Liu, C. J. Barrow, X. Wang and W. Yang, *Materials*, 2014, **7**, 5169–5201.
- 8 *CRC Handbook of Chemistry and Physics: A Ready-Reference Book of Chemical and Physical Data*, ed. W. M. Haynes, CRC Press, Boca Raton and London and New York, 97th edn, 2017.
- 9 S. K. Kumar and R. Krishnamoorti, *Annu. Rev. Chem. Biomol. Eng.*, 2010, **1**, 37–58.
- 10 S. Bettscheider, B. Kuttich, L. F. Engel, L. González-García and T. Kraus, *J. Phys. Chem. C*, 2021, **125**, 3590–3598.
- 11 D. S. Ginley, *Handbook of Transparent Conductors*, Springer, New York, Heidelberg, 2010.
- 12 W. Cao, J. Li, H. Chen and J. Xue, *J. Photonics Energy*, 2014, **4**, 040990.
- 13 J. J. Patil, W. H. Chae, A. Trebach, K.-J. Carter, E. Lee, T. Sannicola and J. C. Grossman, *Adv. Mater.*, 2021, **33**, e2004356.
- 14 L. Lian, H. Wang, D. Dong and G. He, *J. Mater. Chem. C*, 2018, **6**, 9158–9165.
- 15 L. F. Engel, L. González-García and T. Kraus, *Nanoscale Adv.*, 2022, **4**, 3370–3380.
- 16 C. V. Thompson, *Annu. Rev. Mater. Res.*, 2012, **42**, 399–434.
- 17 S. Bettscheider, T. Kraus and N. A. Fleck, *J. Mech. Phys. Solids*, 2019, **123**, 3–19.
- 18 S. Bettscheider, T. Kraus and N. A. Fleck, *Acta Mater.*, 2022, **231**, 117799.
- 19 L. Rayleigh, *Proceedings of the London Mathematical Society*, 1878, vol. s1–10, pp. 4–13.
- 20 G. Deignan and I. A. Goldthorpe, *RSC Adv.*, 2017, **7**, 35590–35597.
- 21 J. Jiu, J. Wang, T. Sugahara, S. Nagao, M. Nogi, H. Koga, K. Sugauma, M. Hara, E. Nakazawa and H. Uchida, *RSC Adv.*, 2015, **5**, 27657–27664.
- 22 H. H. Khaligh and I. A. Goldthorpe, *Nanoscale Res. Lett.*, 2013, **8**, 235.
- 23 A. Madeira, M. Plissonneau, L. Servant, I. A. Goldthorpe and M. Tréguer-Delapierre, *Nanomaterials*, 2019, **9**, 899.
- 24 C. Mayousse, C. Celle, A. Fraczkiewicz and J.-P. Simonato, *Nanoscale*, 2015, **7**, 2107–2115.
- 25 T.-B. Song, Y. S. Rim, F. Liu, B. Bob, S. Ye, Y.-T. Hsieh and Y. Yang, *ACS Appl. Mater. Interfaces*, 2015, **7**, 24601–24607.
- 26 J. H. M. Maurer, L. González-García, B. Reiser, I. Kanelidis and T. Kraus, *ACS Appl. Mater. Interfaces*, 2015, **7**, 7838–7842.
- 27 J. H. M. Maurer, L. González-García, B. Reiser, I. Kanelidis and T. Kraus, *Phys. Status Solidi A*, 2016, **213**, 2336–2340.
- 28 U. Schubert, N. Hüsing and R. M. Laine, *Materials Syntheses: A Practical Guide*, Springer, Wien, 2008.
- 29 Y. Chen, Y. Wang, J. Peng, Q. Xu, J. Weng and J. Xu, *ACS Nano*, 2017, **11**, 2756–2763.
- 30 S. Gong, Y. Zhao, L. W. Yap, Q. Shi, Y. Wang, J. A. P. B. Bay, D. T. H. Lai, H. Uddin and W. Cheng, *Adv. Electron. Mater.*, 2016, **2**, 1600121.
- 31 B. Reiser, D. Gerstner, L. González-García, J. H. M. Maurer, I. Kanelidis and T. Kraus, *Phys. Chem. Chem. Phys.*, 2016, **18**, 27165–27169.
- 32 S. Mourdikoudis and L. M. Liz-Marzán, *Chem. Mater.*, 2013, **25**, 1465–1476.
- 33 J. E. Gerbi, P. M. Voyles, M. M. J. Treacy, J. M. Gibson and J. R. Abelson, *Appl. Phys. Lett.*, 2003, **82**, 3665–3667.
- 34 D. K. Goswami and B. N. Dev, *Phys. Rev. B: Condens. Matter Mater. Phys.*, 2003, **68**, 033401.
- 35 W. M. Greene, W. G. Oldham and D. W. Hess, *Appl. Phys. Lett.*, 1988, **52**, 1133–1135.
- 36 J. L. Hodgkinson and D. W. Sheel, *Surf. Coat. Technol.*, 2013, **230**, 73–76.
- 37 M. Marinov, *Thin Solid Films*, 1977, **46**, 267–274.
- 38 I. Reinhold, C. E. Hendriks, R. Eckardt, J. M. Kranenburg, J. Perelaer, R. R. Baumann and U. S. Schubert, *J. Mater. Chem.*, 2009, **19**, 3384.
- 39 S. M. Rossnagel and J. J. Cuomo, *Thin Solid Films*, 1989, **171**, 143–156.
- 40 W. Ostwald, *Z. Phys. Chem.*, 1897, **22U**, 289–330.
- 41 Q. Tang and D.-e. Jiang, *Chem. Mater.*, 2017, **29**, 6908–6915.

- 42 H. Shen, J. Niu, X. Li, H. Wang, M. Xing, X. Chen and L. S. Li, *Nanoscale*, 2012, **4**, 2741–2747.
- 43 W. D. Luedtke and U. Landman, *J. Phys. Chem.*, 1996, **100**, 13323–13329.
- 44 G. Tian, T. Zhao, J. Niu, H. Shen and L. S. Li, *RSC Adv.*, 2014, **4**, 39547.
- 45 Y. Zhang, P. Yu, Y. Qi, F. Chen, Y. Li and Y. Zhang, *Mater. Lett.*, 2017, **193**, 93–96.
- 46 J. Noh, E. Ito, K. Nakajima, J. Kim, H. Lee and M. Hara, *J. Phys. Chem. B*, 2002, **106**, 7139–7141.
- 47 R. Samba, *Open Surf. Sci. J.*, 2013, **5**, 17–20.
- 48 I. K. Backes, L. González-García, A. Holtsch, F. Müller, K. Jacobs and T. Kraus, *J. Phys. Chem. Lett.*, 2020, **11**, 10538–10547.
- 49 A. Elschner, *PEDOT: Principles and Applications of an Intrinsically Conductive Polymer*, CRC Press, Boca Raton FL, 2011.
- 50 W. Lövenich, *Polym. Sci., Ser. C*, 2014, **56**, 135–143.
- 51 A. S. Pranti, A. Schander, A. Bödecker and W. Lang, *Sens. Actuators, B*, 2018, **275**, 382–393.
- 52 M. D. Hager, P. Greil, C. Leyens, S. van der Zwaag and U. S. Schubert, *Adv. Mater.*, 2010, **22**, 5424–5430.

3.4 Publication 4




Reproduced from

L. F. Engel, L. González-García, and T. Kraus: “Consolidation and Performance Gains in Plasma-Sintered Printed Nanoelectrodes”. *Nanoscale Adv.*, 2023, **5**, 4124-4132. DOI: 10.1039/D3NA00293D.

with permission from the Royal Society of Chemistry.



Consolidation and performance gains in plasma-sintered printed nanoelectrodes†

Lukas F. Engel, ^a Lola González-García ^{*ab} and Tobias Kraus ^{*ac}

We report on the unusual, advantageous ageing of flexible transparent electrodes (FTEs) that were self-assembled from oleylamine-capped gold nanospheres (AuNPs) by direct nanoimprinting of inks with different particle concentrations ($c_{\text{Au}} = 3 \text{ mg mL}^{-1}$ to 30 mg mL^{-1}). The resulting lines were less than $2.5 \mu\text{m}$ wide and consisted of disordered particle assemblies. Small-Angle X-ray Scattering confirmed that particle packing did not change with ink concentration. Plasma sintering converted the printed structures into lines with a thin, electrically conductive metal shell and a less conductive hybrid core. We studied the opto-electronic performance directly after plasma sintering and after fourteen days of storage at $22 \text{ }^\circ\text{C}$ and $55\% \text{ rH}$ in the dark. The mean optical transmittance $\bar{T}_{400-800}$ in the range from 400 nm to 800 nm increased by up to $\approx 3\%$, while the sheet resistance R_{sh} strongly decreased by up to $\approx 82\%$ at all concentrations. We correlated the changes with morphological changes visible in scanning and transmission electron microscopy and identified two sequential ageing stages: (I) post-plasma relaxation effects in and consolidation of the shell, and (II) particle re-organization, de-mixing, coarsening, and densification of the core with plating of Au from the core onto the shell, followed by solid-state de-wetting (ink concentrations $c_{\text{Au}} < 15 \text{ mg mL}^{-1}$) or stability ($c_{\text{Au}} \geq 15 \text{ mg mL}^{-1}$). The plating of Au from the hybrid core improved the FTEs' Figure of Merit $\text{FOM} = \bar{T}_{400-800} \cdot R_{\text{sh}}^{-1}$ by up to ≈ 5.8 times and explains the stable value of $\approx 3.3\% \cdot \Omega_{\text{sq}}^{-1}$ reached after 7 days of ageing at $c_{\text{Au}} = 30 \text{ mg mL}^{-1}$.

Cite this: *Nanoscale Adv.*, 2023, 5, 4124Received 2nd May 2023
Accepted 2nd July 2023

DOI: 10.1039/d3na00293d

rsc.li/nanoscale-advances

1. Introduction

Flexible and transparent electrodes (FTEs) are indispensable components of modern opto-electronics such as foldable smartphones or wearables.¹ Metal grids with (sub-)micron line widths allow to combine mechanical flexibility and optical transparency with electrical conductance.² Micron-scale conductive metal lines are sufficiently conductive for many applications at areal fractions that let most light pass through. A useful figure of merit of such an electrode is the ratio between optical transmittance and sheet resistance.³ It can be tailored to the application by varying the grid pattern, line dimensions, or metal type, for example.⁴

Direct nanoimprinting of colloidal metal inks is an established route to metal grid FTEs.⁵ Printing is feasible in a single, roll-to-roll-compatible step under ambient conditions.⁶ It is possible to print at the sub-micron resolution required for ultra-

high definition displays.⁷ Advanced printing processes use a patterned polydimethylsiloxane (PDMS) elastomer stamp that patterns a colloidal metal ink when it meets the substrate. The stamp absorbs the solvent and/or its vapors, the colloids concentrate and self-assemble inside the stamp's cavities, and percolating networks form that follow the stamp's features.⁸

Ko *et al.*⁹ and Park *et al.*¹⁰ used such a process and nano-imprinted Au nanospheres with a core diameter of $d_c \approx 1 \text{ nm}$ to 3 nm and strongly bound hexanethiol ligands, dispersed in α -terpineol. Kister *et al.*⁷ employed Au nanospheres with $d_c \approx 3.2 \text{ nm}$ and weakly bound dodecylamine (C12) ligands, dispersed in cyclohexane. Maurer *et al.*⁸ imprinted ultra-thin Au nanowires with $d_c \approx 1.6 \text{ nm}$, lengths above $1.6 \mu\text{m}$, and a weakly bound oleylamine (OAm, C18) ligand shell, dispersed in cyclohexane. Park *et al.*¹¹ worked with Ag nanospheres with a core diameter of $d_c \approx 3 \text{ nm}$ to 7 nm and dodecylamine (C12) ligands, dispersed in a mixture of toluene and α -terpineol. Agrawal and Garnett¹² used Ag nanocubes with a core edge length of $\approx 75 \text{ nm}$ and a polyvinylpyrrolidone (PVP) ligand shell, dispersed in ethanol, to form monocrystalline structures.¹³

Nanoimprinting is usually followed by a densification step. For example, colloidal metal typically contains electrically insulating ligands that have to be removed after imprinting.¹⁴ Thermal, photonic, or plasma-based processes are commonly used for ligand removal and sintering.¹⁵ Nanoscale colloids can be plasma-sintered at temperatures far below the melting point

^aINM – Leibniz Institute for New Materials, Campus D2 2, 66123 Saarbrücken, Germany. E-mail: lola.gonzalez-garcia@leibniz-inm.de; Tel: +49 (0)681-9300-269

^bDepartment of Materials Science and Engineering, Saarland University, Campus D2 2, 66123 Saarbrücken, Germany

^cColloid and Interface Chemistry, Saarland University, Campus D2 2, 66123 Saarbrücken, Germany. E-mail: tobias.kraus@leibniz-inm.de; Tel: +49 (0)681-9300-389

† Electronic supplementary information (ESI) available. See DOI: <https://doi.org/10.1039/d3na00293d>

of the bulk metal.¹⁶ Plasma sintering avoids softening of the polymer substrate, *e.g.* polyethylene terephthalate (PET) with $T_g \approx 75$ °C.¹⁷ Oxygen-containing plasma removes organic ligands primarily through oxidation, while inert plasma acts by sputtering.¹⁸ Both accelerate surface diffusion on metals and cause sintering.¹⁹ Shaw *et al.*²⁰ showed that low-pressure O₂ plasma penetrates 440 nm thick layers of ceramic nanospheres (ZrO₂, core diameter $d_c \approx 3.7$ nm, trioctylphosphine oxide ligand shell) and removes virtually all organics while retaining the individual nanospheres. Reinhold *et al.*²¹ and Ma *et al.*²² provided evidence for the formation of a conductive Ag shell around an insulating core in a low-pressure Ar plasma for films of printed and drop-casted Ag nanospheres (*e.g.*, $d_c \approx 23$ nm with a gum arabicum ligand shell). Engel *et al.*²³ reported the formation of a conductive gold shell on top of an oleylamine-gold core for nanoimprinted lines of ultra-thin Au nanowires (AuNWs, $d_c \approx 1.7$ nm) or of Au nanospheres (AuNPs, $d_c \approx 3.7$ nm) in a low-pressure H₂/Ar plasma.

The last three reports find a strongly improved conductance immediately after plasma treatment. Few authors report on the stability of this improvement or on the efficiency of metal use. It is known that thermally annealed random networks of Ag nanowires degrade as a function of temperature, humidity, light, and electric current.^{24–29} Such electrodes may fragment into spheres upon heating due to the Rayleigh–Plateau instability³⁰ and are prone to failure due to electromigration. They are susceptible to UV light and chemical corrosion (sulfides, oxygen, and acids), which can be prevented by protective coatings that reduce surface diffusivity and the Rayleigh–Plateau instability. Maurer *et al.*^{31,32} reported that dip-coated layers (up to 10 nm thick) of AuNWs on glass substrate degraded within hours at room temperature, unless they were coarsened by a H₂/Ar plasma. Annealing resulted in de-wetting, which accelerated with growing temperature and decreasing film thickness. Engel *et al.*³³ examined the stability of grid-like FTEs (up to ≈ 275 nm thick) imprinted from AuNWs at different Au concentrations c_{Au} on PET foil and identified ageing by solid-state de-wetting of the shell, de-mixing of the hybrid core, and collapse of the shell. All reports indicated a degradation with time that has to be prevented *via* additional coatings or other stabilizing measures.

Here, we show that the degradation of plasma-treated metal grid FTEs is connected to the porosity of the conductive shell and the residual organics inside their hybrid core. We printed FTEs using gold nanospheres (AuNPs) at different concentrations to obtain parallel lines. Their structures were analyzed *via* Small-Angle X-ray Scattering (SAXS) and the lines were sintered in a H₂/Ar plasma. Electron microscopy (SEM/TEM) before and after sintering indicated the formation of increasingly smooth lines with growing gold concentration. The mean optical transmittances ($\bar{T}_{400-800}$) increased by up to $\approx 3.17\%$ within 14 days after sintering, while the electrical resistance R_{sh} strongly decreased by up to $\approx 82.2\%$, depending on the particle concentration. Detailed analyses of the morphological changes indicated that compact, stable shells formed during plasma sintering. They covered hybrid cores that de-mixed after sintering such that additional metal was plated onto the shell, increasing conductance.

2. Materials and methods

2.1. Synthesis of Au nanospheres

2.1.1. Chemicals. Tetrachloroauric(III) acid trihydrate (HAuCl₄·3H₂O) was synthesized according to Schubert *et al.*,³⁴ oleylamine (Acros Organics, C18 content of about 80–90%) was purchased from Thermo Fisher Scientific GmbH (Schwerte, Germany) and filtered with a 0.45 μm Rotilabo-PTFE syringe filter from Carl Roth GmbH + Co. KG (Karlsruhe, Germany) prior to each usage to remove any oxidized residues, pentane (Sigma Aldrich, for HPLC, $\geq 99\%$) and borane *tert*-butylamine complex (Sigma Aldrich, 97%) were obtained from Merck KGaA (Darmstadt, Germany), cyclohexane (ROTISOLV $\geq 99.9\%$, GC Ultra Grade) was bought from Carl Roth GmbH + Co. KG (Karlsruhe, Germany), and absolute ethanol ($\geq 99.8\%$, analytical reagent grade) was procured from Fisher Scientific GmbH (Schwerte, Germany). All chemicals were used without further purification unless explicitly mentioned.

2.1.2. Synthesis. Nanospheres (AuNPs) having a gold (Au) core and an oleylamine (OAm) ligand shell were synthesised at ambient conditions according to Kister *et al.*⁷ using an adapted protocol from Wu *et al.*³⁵ In a typical synthesis, 80 mg of *tert*-butylamine borane were dissolved in a mixture of 4 mL pentane and 4 mL OAm to obtain a solution A. Then, 200 mg of HAuCl₄·3H₂O were given into a disposable 100 mL glass snap-on vial from Carl Roth GmbH + Co. KG (Karlsruhe, Germany). 16 mL of pentane and 16 mL of OAm were added and the resulting mixture stirred at 500 rad min⁻¹ for 45 min to obtain a solution B. Precisely at the end of the 45 min (the waiting time determines the sphere radius), solution A was added into solution B (the color turned immediately dark brown). Then the mixture was stirred for further 60 min.

2.1.3. Purification, dilution and storage. After synthesis, the AuNPs were precipitated by adding twice the reaction volume of absolute ethanol and gently shaking the snap-on vial. Sedimentation was forced in a Rotanta 460 RS centrifuge from Andreas Hettich GmbH & Co. KG (Tuttlingen, Germany) with a swing-out rotor at 3435 rcf for 5 min. The supernatant was removed and the spheres were re-dispersed in *n*-hexane, in the amount which corresponded to the original reaction volume. The precipitation procedure was repeated once, followed by forced sedimentation, but this time for 60 min at 3435 rcf, before the spheres were re-dispersed in cyclohexane to obtain a stock dispersion of $c_{Au} \approx 30$ mg mL⁻¹ (estimated based on HAuCl₄·3H₂O weighed in and 100% yield). By diluting the stock dispersion, the other concentrations c_{Au} of the AuNP inks were prepared. After synthesis and dilution, all dispersions were stored for 16 h at room temperature before use.

2.2. Small-angle X-ray scattering (SAXS)

The AuNP core size d_{sp} and the colloidal state of order in the dispersions were determined *via* SAXS. The respective dispersion was filled into a glass mark-tube from Hilgenberg GmbH (Malfeld, Germany) with an inner diameter of 1.5 mm. The tube was sealed with a fast-curing two-component epoxy from R&G Faserverbundwerkstoffe GmbH (Waldenbuch, Germany) to

exclude solvent evaporation. Each sample was measured for a total of 30 min. The solvent's background was accounted for by measuring its scattering curve separately and subtracting it from the sample curves. To determine d_{sp} , fitting was performed using the software SASfit from the Laboratory for Neutron Scattering at Paul Scherrer Institute (Villigen, Switzerland).

The spheres' structural arrangement within the pre-plasma lines was studied in transmission right after imprinting on PET. Measurements were performed at room temperature on ambient air to prevent any influence from drawing vacuum. Each sample was measured for 120 min in total.

The scattering setup consisted of a Xeuss 2.0 HR SAXS/WAXS instrument from Xenocs SAS (Grenoble, France) with a Cu K α source and a detector PILATUS3 R 1 M from DECTRIS AG (Baden, Switzerland) which was placed at a distance of about 550 mm from the samples. Precise calibration of this distance was ensured using a standard of Ag behenate before each measurement. Through azimuthal integration, the scattering curves were obtained from the two-dimensional scattering images using the software Foxtrot from Synchrotron SOLEIL (Saint-Aubin, France).

2.3. Thermogravimetric analysis (TGA)

The sample for TGA was prepared by drying 0.360 mL of a 20 mg mL⁻¹ AuNP dispersion in a crucible made from aluminum oxide. To remove any solvent and moisture, the sample was dried in a drying oven for 16 h at 30 °C and 50 mbar before being placed in an analyzer of type STA 449 F3 Jupiter from NETZSCH-Gerätebau GmbH (Selb, Germany). The sample was heated from room temperature to 1200 °C at a rate of 10 °C min⁻¹ in synthetic dry air while the mass was continuously recorded from 50 °C onward.

2.4. Nanoimprinting

2.4.1. Substrate cleaning. PET foil of type Melinex 401 CW from DuPont Teijin Films UK Ltd. (Redcar, United Kingdom) with a thickness of 75 μ m was employed as imprinting substrate. This type of foil has one pure PET side and one which has been treated to slip more easily. We imprinted onto the pure PET side. Prior to use, the PET foil was cleaned in an ultrasonic bath in a custom-made cleaning rack, applying the following sequence of solvents: 5 min acetone, 5 min ethanol, and 5 min Milli-Q ultrapure water. The cleaned substrate was dried for 30 min at 60 °C, just below its glass transition temperature of 70–80 °C. Acetone removed greasy residues, ethanol and ultrapure water removed acetone (thereby increasing polarity); the ultrapure water dried without any trace.

2.4.2. Polydimethylsiloxane (PDMS) imprinting stamp fabrication. PDMS imprinting stamps were fabricated in a two-step moulding process. In the first step, a lithographically produced silicon master from AMO GmbH (Aachen, Germany), carrying the desired pattern of the final imprinting stamp (parallel line channels, patterned area $A \approx 7$ cm \times 7 cm, pitch $p \approx 19.5$ μ m, channel width $w_c \approx 1.6$ μ m and channel depth $d_c \approx 4.2$ μ m), was used as a mould for a first PDMS replicate. This

replicate was then used in a second step as the master mould for the actual imprinting stamp.

Both masters had to be silanized prior to the moulding procedure. Silanization of the silicon master was carried out without pre-treatment, while silanization of the PDMS master was performed after its plasma activation for 1.5 min using an oxygen plasma at 0.3 mbar in a low pressure plasma reactor of type Pico from Diener electronic GmbH & Co. KG (Ebhausen, Germany). Each silanization was performed inside a conventional glass desiccator with a snap-on vial cap containing 30 μ L of (tridecafluoro-1,1,2,2-tetrahydrooctyl)trichlorosilane from abcr GmbH (Karlsruhe, Germany). The snap-on vial cap was shielded from the respective master to achieve uniform silanization. Firstly, the desiccator was flushed with Ar (the silane is sensitive to humidity), evacuated to 3 mbar, and disconnected from the vacuum pump. After 30 min at room temperature, the desiccator was slowly ventilated with air.

The pre-polymer and the cross-linker of a PDMS kit, Sylgard 184 from Dow Inc. (Midland, USA), were mixed in a 10 : 1 (w/w) ratio prior to degassing in a Speedmixer DAC 600.2 VAC-P from Hauschild GmbH & Co. KG (Hamm, Germany) at 2350 rpm and 1 mbar for 3 min. The resulting mixture was poured onto the respective master which carried a Teflon ring (2 mm thick) as spacer, sealed at the edges with add-i-gum light N from DE Healthcare Products (Gillingham, UK), and a glass plate as top sealing to ensure uniform thickness. The PDMS was cured for 3 h at 80 °C before carefully peeling off the replica along the stamp channels.

The replica of the PDMS master was cut into two equal halves, each being an imprinting stamp with an area of 3.5 cm \times 8 cm of which 3.5 cm \times 7 cm were patterned and 3.5 cm \times 0.5 cm at either end were not. The latter served as run-in and run-out areas during imprinting. Larger areas can be printed using the complete replicate.⁸

2.4.3. Nanoimprinting. For nanoimprinting, a patterned PDMS stamp was attached to a custom-made cylindrical steel roller (3 kg, 8 cm in diameter and height) with a double-sided tape from tesa SE (Norderstedt, Germany). The weight of the roller provides the pressure needed for imprinting. We mounted the steel roller onto a modified TQC Sheen automatic film applicator from Industrial Physics Inks & Coatings GmbH (Hilden, Germany) which served as carrier. Right before imprinting, 60 μ L of ink were injected directly in-between the attached PDMS stamp and the PET substrate using a pipette (continuous processing is possible *e.g.* with a syringe pump for the ink). During imprinting, the linear movement of the carrier (4 mm s⁻¹) in direction of the stamp's parallel line-like channels is translated into a rolling motion of the steel roller over the substrate. A detailed description of the imprinting process is given in Maurer *et al.*⁸ and Kister *et al.*⁷ Before its reuse, ink residues adhering to the PDMS stamp after imprinting were removed using Scotch Magic Tape from 3M Deutschland GmbH (Kleinstheim, Germany). There was no degradation of the stamps apparent from the geometry of the prints after using the same stamp 60 times. To avoid capillary condensation during imprinting, it has to be executed well above the dew point. Typically, we imprinted at 22 °C and 55% *rH* (dew point of 12.5 °

C) and stored the electrodes under the same conditions in the dark.

2.5. Plasma sintering

Plasma sintering was performed within a low pressure 13.56 MHz RF plasma reactor of type Pico from Diener electronic GmbH & Co. KG (Ebhausen, Germany) right after nano-imprinting. A mixture of 5% H₂ in 95% Ar (H₂/Ar) served as process gas. Plasma sintering was carried out at room temperature for 20 min at ≈ 0.3 mbar with 100 W RF power.

2.6. Sheet resistance measurements

The electrodes' sheet resistances R_{sh} were determined in 2-point-probe configuration with a multi-channel multi-meter (DAQ6510 data acquisition logging multi-meter system) which was equipped with multiplexer cards (7702 40-channel differential multiplexer module with screw terminals) from Keithley Instruments GmbH (Germering, Germany). A fast drying Ag paste ACHESON Ag DAG 1415 from Plano GmbH (Wetzlar, Germany) and AGF 1 miniature crocodile clamps from SKS Kontakttechnik GmbH (Niederdorf, Germany) were used for contacting. The Ag paste was deposited as two parallel lines, each 1.5 cm long and spaced 1.5 cm apart, forming a square measurement field. The measured resistances corresponded directly to the desired sheet resistances. Measurements were automatically recorded every 10 min during storage under ambient conditions ($T \approx 22$ °C, $rH \approx 55\%$) in the dark to avoid *e.g.* radiation heating.

2.7. UV-vis spectroscopy

The electrodes' optical transmittances were determined using a Cary 5000 UV-vis-NIR spectrophotometer from Agilent Technologies Deutschland GmbH (Waldbronn, Germany) having a tungsten halogen light source for the visible and a deuterium arc light source for the UV range. The respective electrode on PET was mounted behind a blackened metal mask with circular aperture (5 mm in diameter). Measurements were carried out in the range 400 nm to 800 nm in double-beam mode against air at scan rates of 600 nm min⁻¹. A PET substrate with the imprinted electrode on top was placed such that the blank side was in contact with the mask to prevent any damage to the electrode on the other side. Baselines of the bare PET substrates were recorded, too, as references.

2.8. Cross-sectioning *via* focused ion beam (FIB)

Cross-sections of printed and of sintered lines were prepared with a FEI Versa 3D DualBeam from Thermo Fisher Scientific GmbH (Schwerte, Germany). The surfaces of the lines were protected by layers of Pt which were first deposited using the electron beam, and then with an ion beam.

2.9. Transmission electron microscopy (TEM)

All FIB cuts were characterized at an acceleration voltage of 200 kV in a JEM 2010 from JEOL GmbH (Freising, Germany).

2.10. Scanning electron microscopy (SEM)

For SEM imaging, either a FEI Quanta 400 ESEM or a FEI Versa 3D DualBeam from Thermo Fisher Scientific GmbH (Schwerte, Germany) with secondary electron detectors was used. Instead of PET, polished p-type silicon wafers from Siegert Wafer GmbH (Aachen, Germany) were used as substrate for better imaging.

3. Results and discussion

Fig. 1 illustrates the performance of freshly prepared (purple) and aged (orange) metal-grid FTEs printed using inks with different gold concentrations c_{Au} (denoted in the figure with the color gradient, where the intensity of the color indicates higher concentrations). We printed grids from oleylamine-capped gold nanospheres (AuNPs), plasma-sintered them, and compared their mean transmittances $\bar{T}_{400-800}$ in the visible range to their sheet resistances R_{sh} immediately after plasma sintering and two weeks later. Sheet resistances R_{sh} and optical transmittances $\bar{T}_{400-800}$ consistently decreased with increasing concentration c_{Au} in the range of 3–30 mg mL⁻¹. Lower concentrations were insufficient to form percolating, conductive lines; higher concentrations led to optical transmittances of below 85%. The figure of merit according to Fraser and Cook,³

$$\text{FOM} = \bar{T}_{400-800} \cdot R_{\text{sh}}^{-1}, \quad (1)$$

compares the ratio of $\bar{T}_{400-800}$ and R_{sh} at different concentrations c_{Au} ; it increased with c_{Au} .

Resistances were more sensitive to c_{Au} than transmittances, and the FOM of aged electrodes was more sensitive to c_{Au} than that of freshly sintered ones. During 14 days of ageing, $\bar{T}_{400-800}$ (Fig. S3 and S4 in the ESI† show the averaged optical transmittance spectra for all concentrations immediately after plasma sintering and 14 days later) always increased (by up to $\approx 3.17\%$) while R_{sh} always dropped (by up to $\approx 82.2\%$), which increased the FOM up to ≈ 5.8 times. This is in stark contrast to the situation for metal grid FTEs printed with oleylamine-capped ultra-thin gold nanowires (AuNWs). Their sheet resistances increased by $\approx 30\%$ in 14 days for concentrations up to 3 mg mL⁻¹, and they became non-conductive within 8 h for $c_{\text{Au}} \geq 5$ mg mL⁻¹.³³

We studied the ageing mechanisms to optimize the stability and performance of the affected FTEs. In the following, we give an overview of the resistances' temporal evolution, compare it to structural analyses, and develop mechanistic hypotheses.

The relative change in sheet resistance $(R_{\text{sh},t} - R_{\text{sh},t_0}) \cdot R_{\text{sh},t_0}^{-1} = \Delta R_{\text{sh},t} \cdot R_{\text{sh},t_0}^{-1}$ at time t progressed in two sequential stages. Their exact progressions depended on c_{Au} , but the qualitative features were similar for all concentrations. Differences between the stages were particularly distinct for $c_{\text{Au}} = 30$ mg mL⁻¹, the case shown in Fig. 2. An initial exponential decay (stage I) was followed by a reversed S-curve (stage II). We analyzed the morphological evolution of the lines and correlated it with the change in their resistance (Fig. 3).

The printed structure initially consisted of randomly and densely packed nanospheres. Small-angle X-ray scattering (SAXS, Fig. S6 of the ESI†) confirmed that the printed particles

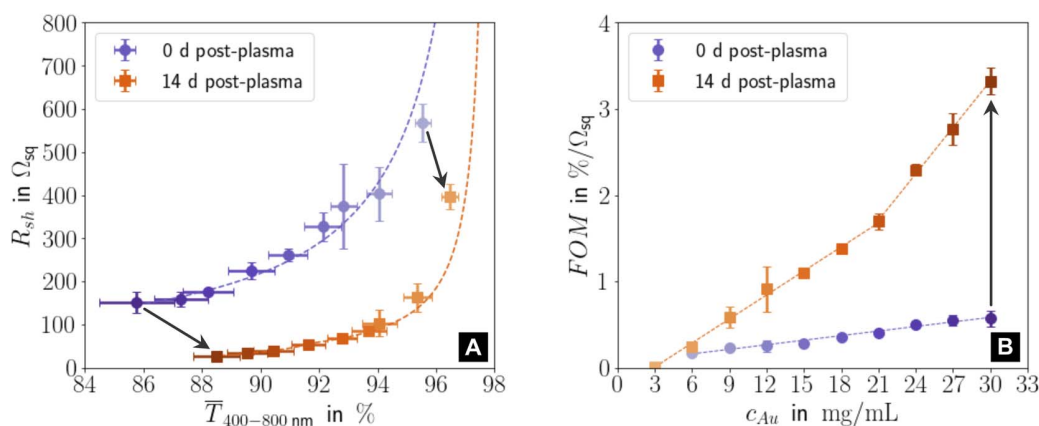


Fig. 1 (A) Sheet resistances R_{sh} and mean optical transmittances $\bar{T}_{400-800}$ for electrodes directly after plasma sintering and fourteen days later. (B) Change of the figure of merit $FOM = \bar{T}_{400-800} \cdot R_{sh}^{-1}$ with gold concentration c_{Au} for new and aged samples. All graphs show averages and standard deviations from three samples, and the corresponding fits (dashed lines). Fig. S1 in the ESI† has the complete data set and the fitting details for (A). Light colours represent lower c_{Au} .

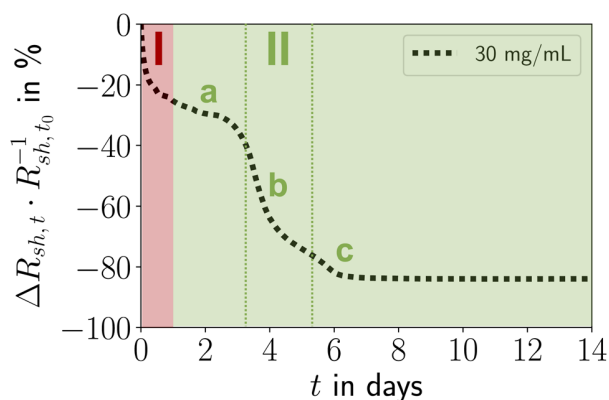


Fig. 2 Stages I and II of electrode ageing: (I) post-plasma relaxation effects in and consolidation of the shell, (II) particle re-organization, de-mixing, coarsening, and densification of the core with Au plating onto the shell, followed by stabilization or (for $c_{Au} < 15 \text{ mg mL}^{-1}$) solid-state de-wetting. Stage II can be split into an initial phase a, an intermediate phase b, and a final phase c.

with a core diameter of $d_{sp} = 3.7 \pm 0.37 \text{ nm}$ packed with a center-to-center distance of $a_{c-c} = 5.61 \pm 0.07 \text{ nm}$ (Sections 3.1 and 3.2 in the ESI†). The surface-to-surface distance of the Au cores of $a_{s-s} \approx 1.91 \text{ nm}$ was about the length of an oleylamine (OAm) molecule ($l_{OAm} \approx 2.05 \text{ nm}$ (ref. 36)), probably due to interdigitation of the OAm shells.³⁷

The printed lines were slightly narrower than the stamp feature $w_c = 1.6 \mu\text{m}$ and had triangular cross-sections with a central ridge that appears as a bright center (Fig. 3A). Limited bleeding formed a sub-mono AuNP layer barely visible in the cross-section of Fig. 3E.

Plasma sintering blunted the ridge (Fig. 3B), reduced its height, and formed a conductive line with a Gaussian profile (Fig. 3F). Gold and OAm were moved or removed during plasma sintering. The outermost particles were sintered and formed a thin Au shell with a thickness of $t_{shell} = 8.07 \pm 1.36 \text{ nm}$.²³ This

shell was slightly thicker than that reported for plasma-sintered AuNW lines.²³

Ageing stage I (Fig. 2) was not accompanied by visible morphological changes (Fig. 3M–O). The resistance in Fig. 2 indicates that ageing started immediately after plasma sintering, but there were no changes visible in electron microscopy (EM) that would explain the initial drop in R_{sh} during stage I. The unchanged microstructure and the time scale suggest that stage I is dominated by stress relaxation that reduces atomic lattice distortions in the metal shell.³⁸ Slow consolidation processes likely close small pores in the shell, and metal grain sizes increase. The overall process can be likened to the final stage of ceramic solid-phase sintering.³⁹ It is interesting to compare it to the ageing of AuNW grids at high c_{Au} . These rapidly age and degrade after plasma sintering by fast de-mixing and compaction of the hybrid core, processes that damage the conductive shell and are clearly visible in EM.³³ We find that plasma-sintered spherical nanoparticles form a thicker,²³ less porous shell that shields the hybrid core from the plasma. This limits the removal of OAm and fragments thereof from the core that dominates the ageing of AuNW-derived structures.³³

Ageing stage II was characterized by a reversed S-curve course that can be divided (Fig. 2) into an initial, an intermediate, and a final phase. The decrease of R_{sh} started slowly, accelerated, and finally stabilized. This may be compared to powder sintering with a liquid phase due to a low-melting secondary powder component, where most of the densification occurs quickly in the intermediate phase, too.³⁹ A similar liquid phase may form in the hybrid core due to "melting" of the ligand shells that are partially degraded by plasma sintering.

The decrease of resistance in stage II suggests coordinated particle movement inside the core rather than the motion of single particles that fill gaps. This is consistent with the average particle spacing from SAXS a_{s-s} that is $\approx 48\%$ below the particle diameter d_{sp} and would not allow single particles to move inside packing. Instead, collective particle motion caused morphological changes that were clearly visible in electron microscopy

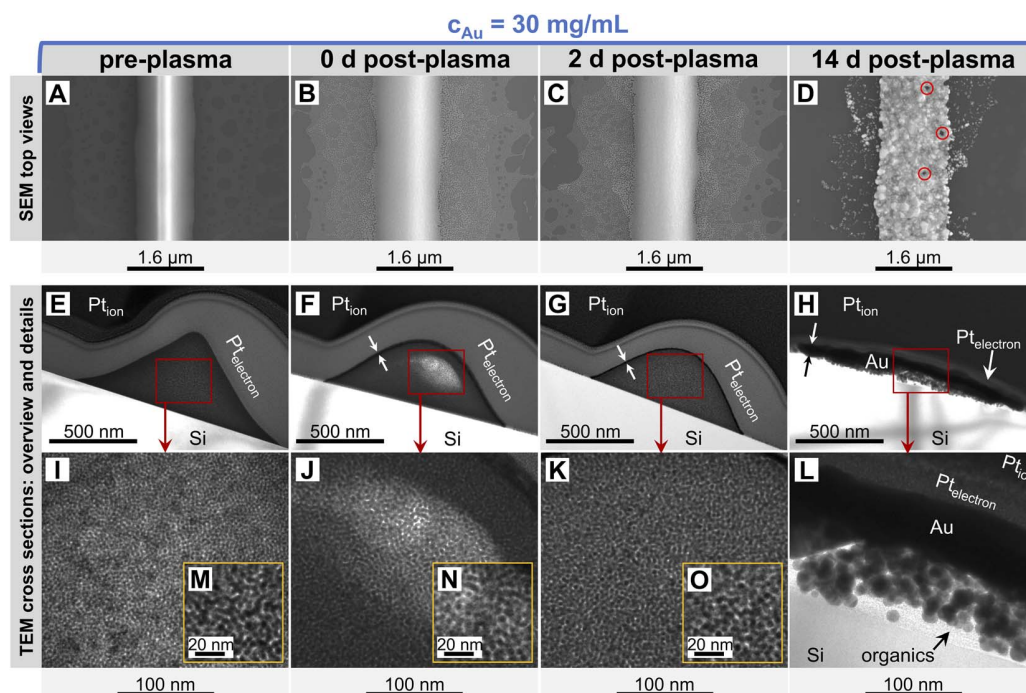


Fig. 3 Surfaces and cross-sections of lines imprinted at 30 mg mL^{-1} before (A, E, I, M), immediately after (B, F, J, N), two days after (C, G, K, O), and fourteen days after (D, H, L) plasma sintering. They show the smooth line surface flanked by a thin layer of bled spheres (A) and the amorphous sphere arrangement in triangular shape (E, I and M) before, the now Gaussian-shaped core-shell structure (F, J and N) right after and (G, K and O) two days after as well as the densified core (H and L), the coarsened surface with occasional pores (red circles) and the coalesced bled spheres (D) fourteen days after plasma sintering. Note that each TEM image was taken from an individual TEM lamella. We prepared lamellae from different locations of the same FTE sample.

Fig. 3D, H and L. The hybrid core had densified significantly, confirming the removal of a relevant fraction of OAM during plasma sintering. The surface of the lines had visibly coarsened after 14 days and pores were visible (indicated by red circles). We found that these pores appeared in lines printed at the same ink concentrations at similar densities, with spacings of at least $1 \mu\text{m}$. This may indicate a “depletion” volume that forms below the pores. Metallic Au apparently migrated to the shell and increased its thickness from $t_{\text{shell}} = 8.07 \pm 1.36 \text{ nm}$ (ref. 23) up to $\approx 100 \text{ nm}$ (Fig. 3H and L). This migration probably decreased R_{sh} and stabilized the aged lines against solid-state dewetting.⁴⁰ The shell thickness was surprisingly uniform across the entire width, indicating uniform plating from the core onto the inside of the shell. The aged lines appeared slightly wider than before, probably because the core partially collapsed in height with an intact shell. This reduced optical transmittance, an effect overcompensated by coalescence of the spheres in the thin layers surrounding the lines (Fig. 3D). This coalescence reduced optical scattering and probably explains the 3.17% increase in optical transmittance. Larger Au spheres formed in the core, probably by Ostwald ripening.⁴¹

The ageing of lines printed at lower c_{Au} was qualitatively similar (Fig. 4A–C). At $c_{\text{Au}} = 6 \text{ mg mL}^{-1}$ to 12 mg mL^{-1} (Fig. 4A), stage I was unchanged, but the intermediate phase of stage II started earlier than at $c_{\text{Au}} = 30 \text{ mg mL}^{-1}$ and caused a smaller relative decrease in R_{sh} .

Previous studies reported that lines printed at low c_{Au} were up to $\approx 41\%$ wider, lower in height, more porous, and had disconnected gold parts that did not contribute to conductance.²³ Lines printed at higher c_{Au} had smoother surfaces and were higher and narrower (minimum width at $c_{\text{Au}} = 12 \text{ mg mL}^{-1}$, Fig. 4B). Our recent results suggest that porous, flat, wide lines age unfavorably. The conductance decrease in stage II at $c_{\text{Au}} = 6 \text{ mg mL}^{-1}$ strongly reminds of the ageing of wire-based electrodes³³ imprinted at low concentrations that have a rough, porous surface and slowly degrade due to solid-state de-wetting.⁴⁰

Lines printed at $c_{\text{Au}} = 12 \text{ mg mL}^{-1}$ to 24 mg mL^{-1} (Fig. 4B) aged in similar ways. Stage II lasted longer with increasing c_{Au} . The (stable) resistance in its final phase consistently decreased with increasing c_{Au} , while its relative change increased due to the growing Au fraction in the hybrid core. The initial steep drop in relative R_{sh} remained unchanged, consistent with a relaxation mechanism. It is conceivable that the thin and wide lines that form at $c_{\text{Au}} \leq 9 \text{ mg mL}^{-1}$ (ref. 23) promote the rearrangement of particles in the hybrid core, obscuring the initial phase of stage II. A higher fraction of fragmented ligands may reduce viscosity and increase mobility.

Lines printed at $c_{\text{Au}} = 24 \text{ mg mL}^{-1}$ to 30 mg mL^{-1} (Fig. 4C) had similar stages I and II, but the length of the initial phase of stage II decreased with c_{Au} . It appears likely that the residual organics inside the hybrid core reach a critical concentration as

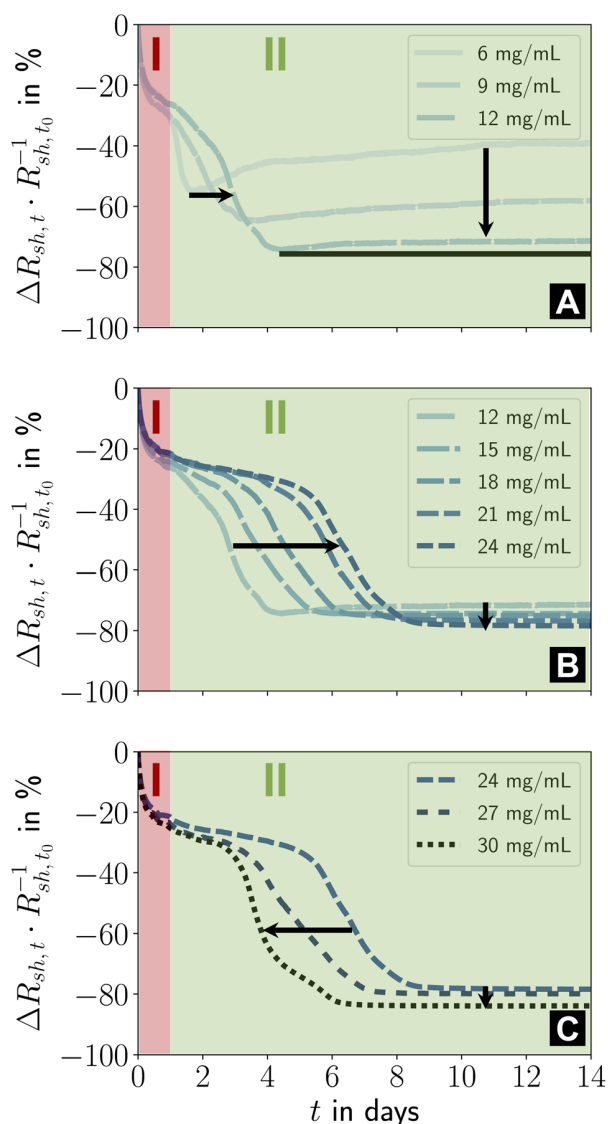


Fig. 4 (A–C) Effect of ink concentration c_{Au} on the two ageing stages I and II. Relative changes in sheet resistance during fourteen days of storage under ambient conditions in the dark are shown. The different concentrations were distributed over three plots for improved readability. Figure S2 in the ESI† illustrates the repeatability and the result for $c_{Au} = 3 \text{ mg mL}^{-1}$.

the line height grows linearly with c_{Au} , while the plasma penetration depth is limited. The low binding energy of Au-NH_2 ,^{42,43} the partial fragmentation of OAm during plasma sintering, and the low viscosity⁴⁴ of OAm at room temperature increase the mobility of the core components^{45–47} such that particle re-orientation accelerates. This is consistent with FTEs imprinted from AuNWs, where the fraction in residual organics inside the hybrid core controlled the ageing rate.³³

The ageing mechanisms discussed above explain the evolution of the FOM with c_{Au} after 14 days shown in Fig. 1B. The increase in the gold fraction of the compact shell with c_{Au} increased the overall conductance. The change in the slope

$\delta\text{FOM}/\delta c_{Au}$ at 21 mg mL^{-1} (“kink”) indicates that a larger fraction of the AuNPs within the core migrated to the conductive shell for $c_{Au} > 21 \text{ mg mL}^{-1}$ than for $c_{Au} \leq 21 \text{ mg mL}^{-1}$, probably due to their larger residual organic content that facilitates de-mixing. The kink in Fig. 1B coincides with the decreasing duration of the initial phase of stage II at approximately 21 mg mL^{-1} .

The effect of the residual organic concentration inside the hybrid core plausibly explains why ageing in stage II consistently accelerates, too. Any Au plated from the core onto the shell increases the fraction of residual organics in the core. Mobile gold in hybrid phases that enables low-temperature annealing has been previously reported, including the mobility-increasing effect of plasmas.^{48–50}

4. Conclusions

Flexible transparent electrodes were imprinted from AuNPs at different particle concentrations and plasma sintered, partially removing the OAm ligands. We found strong correlations between the ink concentration, the electrodes’ ageing, and the resulting opto-electronic performance.

Plasma sintering formed conductive lines with an outer Au shell that covered a hybrid core. Organic residues in the core caused it to re-organize, de-mix, coarsen, and compact. The shell thickened as metallic gold from the hybrid core deposited on it. Residual organics facilitated de-mixing and enabled further densification of the core.

The change in resistance during ageing was characterized by two sequential stages at all ink concentrations. Stage I comprised post-plasma relaxation in and consolidation of the shell. Stage II comprised the re-organization, de-mixing, coarsening, and densification of the core as well as Au plating from the core onto the shell. It ended with a stable resistance at $c_{Au} \geq 15 \text{ mg mL}^{-1}$ or solid-state de-wetting that degraded lines printed at lower concentrations.

Ageing in stage I was largely concentration independent, while stage II was clearly dependent on c_{Au} but always followed an inverted “S” shape. The largest relative decrease in R_{sh} within its intermediate phase of 40% to 50% within 2 to 3 days occurred at $c_{Au} > 12 \text{ mg mL}^{-1}$. The evolution is consistent with a liquid-like organic phase in the hybrid core not unlike the liquid phase in powder sintering after the liquefaction of a low-melting secondary powder component.³⁹ The organic phase promoted plating of metallic Au onto the shell. This thickened the shell up to 100 nm and caused the FOM in the aged state to increase rapidly: $\delta\text{FOM}/\delta c_{Au}$ increased, reaching the highest FOM $\approx 3.32\% \cdot \Omega_{sq}^{-1}$ at $c_{Au} = 30 \text{ mg mL}^{-1}$. Ink concentrations of 6 mg mL^{-1} to 24 mg mL^{-1} yielded thicker lines. This decreased the fraction of low-viscosity ligand fragments, increasing the duration of stage II.

The results confirm the importance of a robust shell during ageing. The concentration of residual organics and the ratio between particle spacing and core diameter set the kinetics of gold plating on the shell. Future studies could assess whether temperature can be used to control the ageing kinetics, and whether an optimal ratio of particle diameter to spacing exists.

Author contributions

L. F. Engel designed the experiments, performed the experiments himself or supervised them, implemented Python code for data analysis and visualization, analysed and visualized all acquired data and wrote the original draft. T. Kraus and L. González-García devised the research strategy, acquired funding, administered, and supervised the project. They reviewed, edited, and commented the manuscript drafts.

Conflicts of interest

There are no conflicts to declare.

Acknowledgements

The authors thank Birgit Nothdurft for recording TEM images of the line cross-sections after preparation *via* FIB and for additional SEM microscopy, Marcus Koch for recording TEM images of the line cross-sections, Bart-Jan Niebuur for SAXS measurements, and Robert Drumm for TGA measurements.

References

- 1 G. H. Kim, H. Woo, S. Kim, T. An and G. Lim, *RSC Adv.*, 2020, **10**, 9940–9948.
- 2 G. Xu and Y. Li, *Nano Select*, 2020, **1**, 169–182.
- 3 D. B. Fraser and H. D. Cook, *J. Electrochem. Soc.*, 1972, **119**, 1368.
- 4 X. Lu, Y. Zhang and Z. Zheng, *Adv. Electron. Mater.*, 2021, **7**, 2001121.
- 5 J. H. M. Maurer, L. González-García, B. Reiser, I. Kanelidis and T. Kraus, *Nano Lett.*, 2016, **16**, 2921–2925.
- 6 J. Woerle and H. Rost, *MRS Bull.*, 2011, **36**, 789–793.
- 7 T. Kister, J. H. M. Maurer, L. González-García and T. Kraus, *ACS Appl. Mater. Interfaces*, 2018, **10**, 6079–6083.
- 8 J. H. M. Maurer, L. González-García, I. K. Backes, B. Reiser, S. M. Schlossberg and T. Kraus, *Adv. Mater. Technol.*, 2017, **2**, 1700034.
- 9 S. H. Ko, I. Park, H. Pan, C. P. Grigoropoulos, A. P. Pisano, C. K. Luscombe and J. M. J. Fréchet, *Nano Lett.*, 2007, **7**, 1869–1877.
- 10 I. Park, S. H. Ko, H. Pan, C. P. Grigoropoulos, A. P. Pisano, J. M. J. Fréchet, E.-S. Lee and J.-H. Jeong, *Adv. Mater.*, 2008, **20**, 489–496.
- 11 I. Park, S. H. Ko, H. Pan, A. P. Pisano and C. P. Grigoropoulos, *Proceedings of IMECE2007*, 2007, 307–314.
- 12 H. Agrawal and E. C. Garnett, *ACS Nano*, 2020, **14**, 11009–11016.
- 13 B. Sciacca, A. Berkhout, B. J. M. Brenny, S. Z. Oener, M. A. van Huis, A. Polman and E. C. Garnett, *Adv. Mater.*, 2017, **29**, 1701064.
- 14 B. Reiser, L. González-García, I. Kanelidis, J. H. M. Maurer and T. Kraus, *Chem. Sci.*, 2016, **7**, 4190–4196.
- 15 J. Niittynen, R. Abbel, M. Mäntysalo, J. Perelaer, U. S. Schubert and D. Lupo, *Thin Solid Films*, 2014, **556**, 452–459.
- 16 W. H. Qi and M. P. Wang, *Mater. Chem. Phys.*, 2004, **88**, 280–284.
- 17 Y. Zhang, J. Zhang, Y. Lu, Y. Duan, S. Yan and D. Shen, *Macromolecules*, 2004, **37**, 2532–2537.
- 18 J. A. Poulis, J. C. Cool and E. Logtenberg, *Int. J. Adhes. Adhes.*, 1993, **13**, 89–96.
- 19 W. M. Greene, W. G. Oldham and D. W. Hess, *Appl. Phys. Lett.*, 1988, **52**, 1133–1135.
- 20 S. Shaw, B. Yuan, X. Tian, K. J. Miller, B. M. Cote, J. L. Colaux, A. Migliori, M. G. Panthani and L. Cademartiri, *Adv. Mater.*, 2016, **28**, 8892–8899.
- 21 I. Reinhold, C. E. Hendriks, R. Eckardt, J. M. Kranenburg, J. Perelaer, R. R. Baumann and U. S. Schubert, *J. Mater. Chem.*, 2009, **19**, 3384.
- 22 S. Ma, V. Bromberg, L. Liu, F. D. Egitto, P. R. Chiarot and T. J. Singler, *Appl. Surf. Sci.*, 2014, **293**, 207–215.
- 23 L. F. Engel, L. González-García and T. Kraus, *Nanoscale Adv.*, 2022, **4**, 3370–3380.
- 24 G. Deignan and I. A. Goldthorpe, *RSC Adv.*, 2017, **7**, 35590–35597.
- 25 J. Jiu, J. Wang, T. Sugahara, S. Nagao, M. Nogi, H. Koga, K. Suganuma, M. Hara, E. Nakazawa and H. Uchida, *RSC Adv.*, 2015, **5**, 27657–27664.
- 26 H. H. Khaligh and I. A. Goldthorpe, *Nanoscale Res. Lett.*, 2013, **8**, 235.
- 27 A. Madeira, M. Plissonneau, L. Servant, I. A. Goldthorpe and M. Tréguer-Delapierre, *Nanomaterials*, 2019, **9**, 899.
- 28 C. Mayousse, C. Celle, A. Fraczkiewicz and J.-P. Simonato, *Nanoscale*, 2015, **7**, 2107–2115.
- 29 T.-B. Song, Y. S. Rim, F. Liu, B. Bob, S. Ye, Y.-T. Hsieh and Y. Yang, *ACS Appl. Mater. Interfaces*, 2015, **7**, 24601–24607.
- 30 L. Rayleigh, *Proc. London Math. Soc.*, 1878, **s1-10(1)**, 4–13.
- 31 J. H. M. Maurer, L. González-García, B. Reiser, I. Kanelidis and T. Kraus, *ACS Appl. Mater. Interfaces*, 2015, **7**, 7838–7842.
- 32 J. H. M. Maurer, L. González-García, B. Reiser, I. Kanelidis and T. Kraus, *Phys. Status Solidi A*, 2016, **213**, 2336–2340.
- 33 L. F. Engel, L. González-García and T. Kraus, *Nanoscale Adv.*, 2022, **4**, 3940–3949.
- 34 U. Schubert, N. Hüsing and R. M. Laine, *Materials Syntheses: A Practical Guide*, Springer, Wien, 2008.
- 35 B.-H. Wu, H.-Y. Yang, H.-Q. Huang, G.-X. Chen and N.-F. Zheng, *Chin. Chem. Lett.*, 2013, **24**, 457–462.
- 36 S. Mourdikoudis and L. M. Liz-Marzán, *Chem. Mater.*, 2013, **25**, 1465–1476.
- 37 B. Reiser, D. Gerstner, L. González-García, J. H. M. Maurer, I. Kanelidis and T. Kraus, *Phys. Chem. Chem. Phys.*, 2016, **18**, 27165–27169.
- 38 S. M. Rossmagel and J. J. Cuomo, *Thin Solid Films*, 1989, **171**, 143–156.
- 39 H. Salmang, H. Scholze and R. Telle, *Keramik*, Springer, Dordrecht, 7th edn, 2007.
- 40 C. V. Thompson, *Annu. Rev. Mater. Res.*, 2012, **42**, 399–434.
- 41 W. Ostwald, *Z. Phys. Chem.*, 1897, **22**, 289–330.
- 42 Q. Tang and D.-e. Jiang, *Chem. Mater.*, 2017, **29**, 6908–6915.

- 43 H. Shen, J. Niu, X. Li, H. Wang, M. Xing, X. Chen and L. S. Li, *Nanoscale*, 2012, **4**, 2741–2747.
- 44 *CRC Handbook of chemistry and physics: A ready-reference book of chemical and physical data*, ed. W. M. Haynes, CRC Press, Boca Raton and London and New York, 97th edn, 2017.
- 45 W. D. Luedtke and U. Landman, *J. Phys. Chem.*, 1996, **100**, 13323–13329.
- 46 G. Tian, T. Zhao, J. Niu, H. Shen and L. S. Li, *RSC Adv.*, 2014, **4**, 39547.
- 47 Y. Zhang, P. Yu, Y. Qi, F. Chen, Y. Li and Y. Zhang, *Mater. Lett.*, 2017, **193**, 93–96.
- 48 B. Ingham, T. H. Lim, C. J. Dotzler, A. Henning, M. F. Toney and R. D. Tilley, *Chem. Mater.*, 2011, **23**, 3312–3317.
- 49 S. K. Volkman, S. Yin, T. Bakhishev, K. Puntambekar, V. Subramanian and M. F. Toney, *Chem. Mater.*, 2011, **23**, 4634–4640.
- 50 S. Wünscher, S. Stumpf, J. Perelaer and U. S. Schubert, *J. Mater. Chem. C*, 2014, **2**, 1642.

Chapter 4

Discussion

This dissertation investigates

- the bundling mechanism of OAm covered AuNWs in their colloidal solution in cyclohexane,
- the structure-property relationship of FTEs produced by direct nanoimprinting of OAm-stabilized gold nanoparticles, and
- the stability of such FTEs and their stabilization.

Direct nanoimprinting of colloidal solutions of ligand ligated metal nanoparticles creates material features during drying within the channels defined by the stamp pattern. If the particles in the colloidal solution already self-organized into assemblies, these are the building blocks. Understanding the AuNW bundling in cyclohexane allows for a better control of the building blocks and of the FTE morphology after imprinting. [Publication 1](#) studied the mechanism of bundle formation for colloidal solutions of AuNWs in cyclohexane with different gold and OAm concentrations and at varying temperatures, mainly using SAXS and TGA.

The microstructures of conductive FTEs develop during low pressure plasma sintering from the FTEs' morphology as printed and determine the electrodes' opto-electronic performance. [Publication 2](#) investigated the pre- and post-plasma microstructures and the performance of electrodes right after their manufacture. They were printed from colloidal inks containing AuNPs/AuNWs at different gold concentrations c_{Au} in cyclohexane and treated with H₂/Ar plasma to remove the OAm ligands and merge the self-assembled Au cores. The imprinted Au grids consisted

of straight parallel lines. The measurement quantities and methods used were R_{sh} and $\bar{T}_{400-800}$ (for the performance) and SAXS, SEM, TEM, and CLSM (for the morphology).

The opto-electronic performance of instable FTEs changes during storage. [Publication 3](#) and [Publication 4](#) studied post-plasma performance and morphology during ageing. Stabilization via slowing surface atom self-diffusion was investigated.

4.1 Bundling mechanism of OAm-stabilized AuNWs in cyclohexane

AuNWs with a monolayer of oleylamine (OAm) ligands tethered to their surface can self-assemble into elongated, close-packed hexagonal bundles (e.g., in n-hexane) or remain stable as individual, fully dispersed nanowires (e.g., in cyclohexane).^[118] Computer simulations indicate^[236] that bundling in n-hexane is entropy-driven. The line contact between OAm ligand shells of parallel wires allows linear n-hexane molecules to simultaneously solvate two adjacent ligand shells. Compared to freely dispersed wires, the entropy gains of solvent molecules imply a reduced Gibbs free energy of the system that bears the formation of bundles. Cyclohexane cannot form such bridges. This explains the fully dispersed AuNWs in cyclohexane.^[118,236] [Publication 1](#) investigated why and when such bundles can nonetheless form in cyclohexane after diluting such a fully dispersed solution.

Insight 1: In cyclohexane, unbound OAm ligands bridge adjacent OAm ligand shells within AuNW bundles.

Bundles in cyclohexane formed upon dilution to $c_{\text{Au}} \approx 4 \text{ mg/mL}$ or less and had an interwire distance d_i of 4.2 nm. Diluting at steadily increasing temperatures resulted in a significantly increased bundle fraction, as shown by the continuously growing SAXS structure peaks. Slight bundling was achieved at 25 °C, and a 45 % bundling fraction at 65 °C, while d_i increased from 4.2 to 4.4 nm. This suggests that adjacent ligand shells in the bundles did not touch (the OAm length in its fully stretched conformation is $\approx 2.05 \text{ nm}$ ^[227,237]), and that solvent was always present between

neighboring ligand shells. Based on^[187] $\Delta G_{\text{SA}} = \Delta H_{\text{SA}} - T \cdot \Delta S_{\text{SA}}$ (see section 2.3 herein), these findings indicate an entropic rather than an enthalpic bundling mechanism.

Unbound OAm and OAm bound to the wire surfaces are in a dynamic equilibrium.^[327,328] Dilution should shift the adsorption equilibrium towards fewer adsorbed ligands and an increased number of unbound ligands. Unbound OAm molecules can intercalate into adjacent ligand shells within the hexagonal wire bundles, analogous to the bridging by linear n-hexane molecules. Dilution releases previously adsorbed OAm ligands, turning them into free OAm molecules. The associated entropy gain bears the bundling. A similar interplay between ligand shells and unbound ligands, in the context of self-assembling colloidal nanocrystals, is suggested in the literature for a system of PbS nanocrystals, toluene solvent, and oleic acid ligand.^[329]

Insight 2: Entropy drives bundling only for sufficiently sparse ligand shells.

Many authors prepare AuNW dispersions following a protocol of Nough et al.^[206] that is based on a protocol of Feng et al.^[184] (see section 2.3.3 herein). It uses n-hexane as solvent and OAm as auxiliary agent. An individual purification cycle to remove excess OAm involves the precipitation of the AuNWs by addition of ethanol, sedimentation of the precipitate by gravity^[118] or centrifugation^[238], removal of the supernatant, and re-dispersion of the wires in the desired solvent at the desired concentration c_{Au} . The amount of OAm in the resulting colloidal cyclohexane solution could be tuned at a constant c_{Au} (8 mg/mL) by varying the purification protocol. The dense ligand shells in the sample with the highest OAm content prevented agglomeration even at maximum dilution. The sample with a lower OAm content agglomerated from a medium dilution onwards, and the sample with the least OAm coverage of its wires exhibited wire bundling at all concentrations across the entire dilution range (8 to 1 mg/mL). After its dilution to 2 mg/mL, the degree of bundling declined when adding OAm.

In summary, a dense ligand shell appears to prevent unbound ligands from intercalating it, thus preventing the entropic mechanism and hence

the wire bundling. Bundling in the inks to be imprinted not only favors the percolation of the printed lines, but also the lines' plasma sintering as bundles serve as self-templates^[228] that keep^[228,287] AuNWs from fragmentation during sintering.

Bundling in n-hexane also required a sparse ligand shell. Apparently, however, the intercalation of linear n-hexane molecules into the ligand shell started at higher OAm surface densities than the intercalation of unbound ligand in cyclohexane. Re-dispersion in n-hexane initially resulted in a fully dispersed solution, with bundling over a period of two to three hours^[118,222].

A corresponding entropy-driven agglomeration of OAm coated AuNPs in n-hexane/cyclohexane is geometrically excluded since the sphere-sphere contact area is three orders of magnitude smaller than for AuNWs.^[239] Consequently, the agglomeration with such AuNPs in cyclohexane only occurs at very high particle concentrations, favorable^[43] for the percolation of lines nanoimprinted with such inks.

4.2 Morphology and opto-electronic performance of printed metal grid electrodes

FTEs based on highly conductive metals cannot be produced by direct nanoimprinting of the metals' high-temperature melts due to the low thermal budget of flexible transparent substrates. Direct nanoimprinting of colloidal metal inks overcomes this dilemma at the price of sintering to remove the insulating ligands which stabilized the ink. The optical transmittances of the resulting metal grid electrodes meet expectations, their electrical properties do not.^[35,42,43] Sintering apparently does not convert the printed lines into a perfect gold grid.

To better understand the structure-property relations of the sintered lines, [Publication 2](#) studied the effects of particle shape and superstructure formation on the interplay between morphology and opto-electronic performance of metal grid electrodes imprinted from colloidal inks specified in [Insight 2](#) herein and based on OAm, cyclohexane, and either AuNPs or AuNWs which exhibit a very contrasting geometry.

In solution, the AuNPs were coated with shells of OAm with a thick-

ness of about 2 nm,^[227,237] which likely had irregular gaps^[205]. The AuNWs were coated with a sparse OAm monolayer. Within the whole c_{Au} range studied, the AuNPs were fully dispersed whereas at least 70 % of the AuNWs were part of dispersed bundles. The necessity of percolation and the demand for functional transmittances limited the feasible c_{Au} ranges.

PET foil was used as substrate. Plasma sintering applied a low pressure H_2/Ar plasma. The pattern of the PDMS imprinting stamp consisted of parallel, line-like channels. Quantitative details are specified in [Publication 2](#). The performance of the resulting FTEs was quantified using a figure of merit and compared to the FTE morphologies before and after sintering.

Insight 3: Plasma sintering is self-limiting and forms core-shell structures.

The printed FTE lines contained AuNWs in tight, hexagonally packed bundles and AuNPs as randomly densely packed assemblies. The wire surface-to-surface spacing was smaller ($d_i \approx 2.52$ nm) than in the ink ($d_i \approx 4.2$ nm). The d_i of the AuNPs, which showed only short-range order in the printed lines, was about the length (2.05 nm) of an OAm molecule. TEM images of cross-sections of the plasma sintered FTE lines revealed that plasma only sintered the outermost part of the printed lines for both AuNWs and AuNPs. Apparently, plasma sintering was self-limiting, proceeding from the outside to the inside, so that the plasma could not fully penetrate the deposited material. For both particle types, the cross-sections exhibited a thin, conductive metal shell that covered a thicker hybrid and probably significantly less conductive core. The shell's average thickness t_{shell} was practically independent of c_{Au} and well below λ_{Au}^e (≈ 38 nm^[16]). Both particle types yielded lines with a Gaussian cross-section. This core/shell structure explains the high, but still practically useful sheet resistances reported^[35,42,43] for nanoimprinted gold electrodes. Such FTEs exhibit competitive opto-electronic properties, e.g. for transparent sensors where high transmittance has priority over low R_{sh} ^[42].

Insight 4: Defects in the printed line dominate the conductivity.

The shells' mean conductivities σ_{shell} increased with c_{Au} , but remained below one third of the bulk gold value ($\sigma_{\text{Au}} = 4.52 \times 10^7 \text{ S/m}^{[330]}$). The most conductive Au shells had a σ_{shell} of $1.39 \times 10^7 \text{ S/m}$ (AuNW-based) and $1.02 \times 10^7 \text{ S/m}$ (AuNP-based), in the range reported^[331] for ultra-thin polycrystalline Au films with thicknesses of 5.5 to 8 nm. However, at the same c_{Au} , the thicker AuNP-based shells always exhibited the lower σ_{shell} . This appears contradictory as the resistivity of metal films decreases with thickness.^[92] Tapered or clogged stamp channels as well as stamp or substrate irregularities cause defects in the printed lines. Although rare, these defects interrupt the lines not just locally, but across their entire width and thus render them entirely non-conductive such that they cannot contribute to σ_{shell} . Lines imprinted from fully dispersed spheres are more susceptible to these defects as they percolate less easy than the pre-bundled, μm -long, flexible AuNWs.

Consistent with this view, percolation occurred already at $c_{\text{Au}} \approx 1 \text{ mg/mL}$ in case of the wires and only at $\approx 3 \text{ mg/mL}$ in case of the spheres. With rising c_{Au} , i.e., increasingly distant from the respective percolation threshold, the probability grows that irregularities may be bridged. This is the main cause for the improvement of σ_{shell} with c_{Au} . Before sintering, the imprinted μm -long single crystalline AuNWs are likely largely aligned in imprinting direction. Compared to the AuNPs, this may implicate a lower grain boundary density in the shell after sintering^[233] and some conduction in the hybrid core (see section 2.1.3 herein). Both contribute to $\delta\sigma_{\text{shell}}/\delta c_{\text{Au}}$. Above 5 mg/mL, this slope turns negative in case of the wires, likely due to crack-like defects that formed at the edges of the sintered lines.

Insight 5: AuNWs percolate easier than AuNPs and yield FTEs with the better FOM.

The figure of merit $FOM = \bar{T}_{400-800}/R_{\text{sh}}$, developed by Fraser and Cook^[317,326], compares the mean optical transmittance to the sheet resistance of FTEs. The plasma sintered printed lines of the FTEs reduce $\bar{T}_{400-800}$ mainly by the opacity of their metal shells. Accordingly, the av-

erage transmittance was dominated by the mean width w of the sintered lines and decreased in case of both nanoparticle types with c_{Au} . At the same c_{Au} , wire-based electrodes had the lower $\overline{T}_{400-800}$.

R_{sh} was roughly inversely proportional to $w \cdot \sigma_{\text{shell}}$, where σ_{shell} is the mean conductivity of the plasma sintered gold shells of the imprinted lines (see [Insight 4](#) herein). With increasing c_{Au} , σ_{shell} increased more than twenty-fold for both particle types. At the same c_{Au} , the wire-based lines exhibited the higher σ_{shell} and at higher concentrations also the higher w . Accordingly, the R_{sh} decreased with c_{Au} for both particle types, and the wire-based R_{sh} was always lower.

Overall, the concentration dependence of the FOM was dominated by the increase of σ_{shell} with c_{Au} . The wire-based FTEs outperformed the sphere-based FTEs at FOMs of up to $\approx 0.9\%/\Omega_{\text{sq}}$ while spheres only reached $\approx 0.55\%/\Omega_{\text{sq}}$. The ability of the mechanically flexible, high aspect ratio (> 1000) wires to self-assemble into percolating, flexible superstructures of its in solution pre-built bundles that could withstand stamp and substrate irregularities better than the sphere-based lines, is the basis for their superior σ_{shell} and hence their superior FOM .

4.3 Morphology and stability of metal grid electrodes

Post-plasma, the AuNW-based FTEs had conductive lines with thicknesses in the range of ≈ 60 to 275 nm and thin (≈ 5.7 nm), rough, porous, and conductive Au shells around an insulating hybrid core. The cores likely contained AuNWs from which the OAm was partially removed. The OAm removal rendered the core porous, likely with a gradient from the shell to the substrate. Ultra-thin, porous Au shells tend to de-wet even at moderate temperatures (see section 2.5.2 herein). Ultra-thin AuNWs, especially those with a partially degraded ligand shell, are susceptible to the Plateau-Rayleigh instability even at RT (see section 2.5.1 herein).

[Publication 3](#) reports on the relative change in sheet resistance and the morphology of the AuNW-based FTEs over time when stored under ambient conditions ($T \approx 22^\circ\text{C}$, $rH \approx 55\%$) in the dark. It introduces measures to stabilize morphology and performance.

FTEs imprinted from AuNPs in cyclohexane had post-plasma lines with thicknesses of ≈ 100 to 240 nm. The conductive gold shells were ≈ 8.1 nm thick, $\approx 40\%$ above that of AuNW-based FTEs. The sphere-based Au shells were smoother and less porous than the wire-based ones, and, with increasing c_{Au} , porosity even decreased. Such thicker and less porous shells were less susceptible to solid-state de-wetting (see section 2.5.2 herein), and better shielded the hybrid cores underneath the shells from the plasma and its low pressure compared to the wire-based situation. During sintering, this did not only limit the OAm removal from the cores more effectively, but also of its low-boiling fragments in comparison to the wires. The AuNPs in the hybrid cores were more stable than the Plateau-Rayleigh instable AuNWs (see section 2.5.1 herein). TEM images of post-plasma cross-sections of sphere-based cores neither showed coarsening nor relevant loss in height. [Publication 4](#) studied possible implications on FTE stability. It reports on the morphology and opto-electronic performance of the FTEs imprinted from the colloidal AuNP inks during a 14 d period of storage after plasma sintering.

Insight 6: De-wetting shells cause FTE ageing.

The R_{sh} of all AuNW-derived FTEs increased with the duration of storage. The rates $\delta R_{\text{sh}}/\delta t$ were strongly dependent on the ink concentration c_{Au} used for imprinting: the R_{sh} of FTEs printed at $c_{\text{Au}} = 2$ to 3 mg/mL increased within 14 d by about 30% whereas FTEs printed at $c_{\text{Au}} \geq 5$ mg/mL became insulators within less than 24 h. Pre-plasma SAXS patterns and electron micrographs taken of the surfaces and cross-sections before, immediately after, and 24 h (1 d) after plasma sintering revealed solid-state de-wetting of the thin, porous Au shell, fragmentation and spheroidization of AuNWs within the core due to the Plateau-Rayleigh instability, followed by Ostwald ripening^[303,304] and finally de-mixing, leading to a coarsening and densification of the core, compensating for the OAm removed by the plasma, along a loss of line height (thickness), and, at high c_{Au} , the rupture of the conductive shell within less than one day.

Insight 7: Stable shells and ageing of the hybrid core lead to performance gains of AuNP-based electrodes.

The AuNP-derived FTEs exhibited an unusual, because advantageous, ageing: a rapid exponential decrease of R_{sh} was followed by a decrease that always started slowly, accelerated, and finally either stabilized for high c_{Au} or re-increased for low c_{Au} . The stabilized R_{sh} consistently decreased with c_{Au} and the associated change in R_{sh} increased with c_{Au} by up to 82%.

The initial exponential decay is likely due to consolidation mechanisms that proceed in the shell: rapid stress relaxation^[332] and the closure of pores and grain growth. Similar consolidations occur in the final stage of ceramic solid-phase sintering.^[333]

The decrease in R_{sh} , following the exponential decay, was associated with the re-organization of the particles in the hybrid core, detectable in electron micrographs of cross-sections of conducting lines. It involved demixing, coarsening, and densification of the core, as well as deposition of Au from the core to the underside of the shell. The Au deposition likely caused the decrease of R_{sh} with increasing duration t of ageing. Au migration from the core to the shell increases the organics concentration in the core. Apparently, such increase favored the ageing kinetics in the core and accelerated the decrease of R_{sh} with t .

The Au plating increased t_{shell} with c_{Au} up to ≈ 100 nm. The thicker shell and the at higher c_{Au} lower shell porosity stabilized the shell against solid-state de-wetting. Compared to FTEs from AuNWs, the core and the surrounding shell shrank in height without rupture of the shell. From $c_{\text{Au}} > 9$ mg/mL onward, the stable shell caused R_{sh} to stabilize in the final ageing phase at a consistently decreasing value with increasing c_{Au} , reflecting the increasing t_{shell} .

The shrinkage of the conducting lines in height widened the lines slightly, yet the optical transmittance increased by up to 3.17%. AuNPs which bled beyond the lines during imprinting coalesced and reduced optical scattering during ageing. This overcompensated the effect of the widening.

At $c_{\text{Au}} \leq 9$ mg/mL, the conductance decreased in the final ageing phase due to solid-state de-wetting. Towards the percolation threshold,

the aged Au shells are increasingly thinner, rougher, and more porous than the ones at $c_{\text{Au}} > 9 \text{ mg/mL}$. This is similar to the post-plasma situation of AuNW-based FTEs at low c_{Au} . They also had a thin, rough, and porous shell and slowly degraded due to solid-state de-wetting.

Insight 8: Bundles of AuNWs form thin, porous, unstable shells.

Pre-bundling of the ultra-high aspect ratio AuNWs in their colloidal inks is beneficial for achieving a low R_{sh} after plasma: the superstructures built from the bundles favor percolation. However, I found that it is a serious handicap in terms of ageing. The same superstructures account for the porosity of the plasma sintered shells which contributes significantly to the shells' solid-state de-wetting (see section 2.5.2 herein) and the final collapse of the shells during storage of high c_{Au} FTEs.

Plasma sintering of the thin top layer of the AuNW network superstructures likely follows the mechanism outlined by Maurer et al.^[228] for the plasma sintering of comparatively thin, dip-coated layers of similar superstructures, also built from bundles of OAm-capped AuNWs (see section 2.5 herein). Gold wire strands that are thinner than the bundles and thicker than the ultra-thin wires form.^[228] Remarkably, the wire-based t_{shell} is approximately equal to the diameter of an individual, hexagonally arranged bundle of seven bare ultra-thin gold nanowires. The plasma induced OAm removal leads to pore formation. A porous gold shell is also a prominent feature of the plasma sintered microfibres produced by Reiser et al.^[239] from precipitates of OAm covered AuNWs through spinning.

Insight 9: AuNPs form thicker, less porous, stable shells.

OAm-stabilized AuNPs in cyclohexane form continuous lines of disordered particles. Their percolation is prone to nanoimprinting defects caused by tapered or clogged stamp channels as well as stamp or substrate irregularities (see Insight 4 herein). On the other hand, the disordered arrangement of AuNPs results in a smooth surface. Plasma sintering preserves the shell's smoothness with little porosity. The larger sphere diameter led to a greater thickness of the sintered shell as noted earlier by Ma et al.^[277]. A greater thickness and fewer pores make a gold layer more resilient against solid-state de-wetting (see section 2.5.2 herein).

Insight 10: Coating electrodes with PEDOT:PSS stabilizes them.

Coating AuNW-derived, sintered high c_{Au} lines with PEDOT:PSS slowed their ageing. The conductance initially improved during storage, probably from fast relaxation effects within the stabilized shell. The stabilization is likely due to a slowing self-diffusion of Au surface atoms as polythiophenes can bind covalently to Au via sulfur.^[334,335] It prevents rough and porous surfaces that favor the binding of PEDOT:PSS layers.^[336] Compared to thin, adsorbed layers, thicker layers prevented conductance losses up to at least 120 d and even led to a decline of 6% in R_{sh} after 100 d, possibly due to a mechanical hindrance of material displacements, similar to the effect of SiO_2 overlayers reported in literature^[307]. The capping layers also restrict the migration of residual organics from the core through the pores of the shell. The decline in R_{sh} after 100 d may indicate the migration of Au from the core to the bottom side of the shell.

Insight 11: Larger organic fractions accelerate ageing in the cores and the de-wetting of porous shells.

FTEs based on AuNWs at $c_{\text{Au}} > 2 \text{ mg/mL}$ or on AuNPs at $c_{\text{Au}} > 9 \text{ mg/mL}$ have line thicknesses (heights) that increase with increasing c_{Au} . Both the penetration depth of the accelerated plasma ions and the time for the formation of the thin metal shell are, however, limited. Thus, the hybrid core of a thicker line is less affected by the plasma, and the total post-plasma fraction of residual organics in the core increases with c_{Au} , too.

Once formed, the shells shield the hybrid core from the plasma. The thinner, porous wire-based shells shield the core from plasma particles, but not from the plasma's low pressure, whereas the thicker and largely non-porous AuNP-based shells shield from both. This limits the removal of OAm and its fragments from the sphere-based core. The organics fraction in AuNP-based cores should thus be lower-boiling, lower-viscosity, and lower molar mass than in the AuNW-based cores. With increasing c_{Au} , the proportion of organics in the cores increases. For the wires, it always consists mainly of OAm, whereas for the spheres, its fraction of

OAm fragments decreases with c_{Au} , reducing its fluidity.

The less porous shells of AuNP-based FTEs imprinted at $c_{\text{Au}} > 9$ mg/mL largely resist de-wetting during the 14-day storage period and retain their integrity. It is conceivable that the effect of c_{Au} on the composition of the organics in their hybrid cores affects ageing kinetics. This possibly dominates the pronounced c_{Au} dependence of the inverted “S” sections in the ageing curves of sphere-based electrodes, plotted as the relative change in $R_{\text{sh},t}$, normalized to R_{sh,t_0} over the storage time t (where t_0 corresponds to $t = 0$ d): $\Delta R_{\text{sh},t}/R_{\text{sh},t_0}$ (see Fig. 4 on page 4130 of [Publication 4](#)).

The largest relative decrease in R_{sh} occurred consistently in the intermediate section of the inverted “S”. At $c_{\text{Au}} \geq 12$ mg/mL, it amounted to 40 to 50 % within 2 to 3 d. This resembles the densification curves in powder sintering with a liquid phase, where most of the densification also occurs within a short time in the intermediate phase.^[333] The ligand shells that were partially degraded and fragmented during sintering may detach from the AuNP surfaces at ambient temperature and form a comparable liquid which promotes the microscale mobility in the core.^[254,255,264] At RT, OAm is a low viscosity liquid.^[330]

As the line height increases, a decreasing fraction of low molar mass fragments in the post-plasma ligand shells of the core conceivably decelerates the organic shells’ detachment and increases the lubricant’s viscosity. Consistent with that, the total ageing time t (until a stable $R_{\text{sh},t}$) increased from ≈ 4 to 9 d when the sphere concentration c_{Au} increased from 12 to 24 mg/mL. In the lines imprinted at $c_{\text{Au}} = 24$ to 30 mg/mL, the ageing time t to reach a stable $R_{\text{sh},t}$ decreased again from ≈ 9 to 7 d.

The high average rate $\delta(\Delta R_{\text{sh},t}/R_{\text{sh},t_0})/\delta t$ in the intermediate section of the reversed “S” curve likely results from coordinated particle movements in the core. At a surface-to-surface spacing between AuNPs which is ≈ 48 % less than the AuNP size, such movements are more plausible than movements of individual particles to fill free space.

At $c_{\text{Au}} \leq 9$ mg/mL, thin and wide lines formed and facilitated the re-arrangement of the particles in the hybrid core, supported by a higher proportion of the low-viscosity OAm fragments. Therefore, the initial decrease of $R_{\text{sh},t}$ after its exponential decay accelerates with decreasing c_{Au} . With increasing duration of the ageing process, $R_{\text{sh},t}$ increases be-

cause the porosity and the density of defects in the shell increases. They facilitate the de-wetting of the shell which develops into the dominant mechanism as ageing proceeds.

With increasing c_{Au} , AuNW-based FTEs become thicker. They have thinner, more porous shells with more defects than AuNP-based FTEs. Crack-like defects formed at the edge of the sintered lines with growing density as c_{Au} increased and the line width exceeded the width of the stamp channels. Due to the pores in their shells, the low pressure plasma during and after the shell formation does not only remove of the comparatively high boiling OAm,^[228] but also of its low boiling fragments produced by the plasma. With increasing c_{Au} , the faster line height growth, when compared to the spheres, also results in a faster growth of the concentration in residual organics c_{org} (mainly OAm) within the sintered cores.

SEM and TEM images of surfaces and cross-sections of AuNW-based sintered lines imprinted at different c_{Au} , taken at different storage times, suggest that always the same mechanisms caused the FTEs ageing seen in $\Delta R_{\text{sh},t}/R_{\text{sh},t_0}$, but that these operated at higher rates for higher c_{Au} . This acceleration is likely due to three reasons. First, the higher c_{org} of post-plasma FTEs printed at the higher c_{Au} accelerates the kinetics of the de-mixing in the core. Second, as c_{Au} increases, the growing defectiveness of the thin, porous Au shell and an increasing migration of organics from the core through the pores onto the shell accelerate solid-state de-wetting of the shell. Third, as c_{org} increases, the core's compaction, which compensates for the core's loss in organics during plasma treatment and which links the de-wetting shell with the de-mixing core, accelerates, too. Hence, both the core and the surrounding shell shrink in height and, as the shrinkage exceeds a critical level, the degraded shell ruptures (fragments) and the wire-based FTEs loose measurable conductivity. Metallic Au accumulates on the ruptured shell. The growth of the shrinkage rate approaches saturation as c_{Au} exceeds 5 mg/mL. The loss of conductivity then occurred as of that concentration onward within less than 1 d of storage time. At wire concentrations of 2 to 3 mg/mL, the moderate increase in $\Delta R_{\text{sh},t}/R_{\text{sh},t_0}$ is mainly due to solid-state de-wetting of the shell and post-plasma relaxation effects which release stress and Au-lattice distur-

tions in the shell, thus counteracting a larger rate $\delta(\Delta R_{\text{sh},t}/R_{\text{sh},t_0})/\delta t$.

Insight 12: AuNP-based FTEs stored at ambient conditions surpass AuNW-based FTEs in FOM.

After fabrication, the R_{sh} of an FTE is strongly influenced by the density of defects in the sintered lines that render individual lines discontinuous. These defects result from stamp and substrate irregularities during imprinting. The AuNWs and their bundles self-assemble into superstructures during nanoimprinting and bridge the irregularities better than the amorphous self-assemblies of the AuNPs. For both nanostructures, bridging improves with c_{Au} . Wire-based electrodes thus outperform the sphere-based ones in the ratio of mean optical transmittance to sheet resistance with up to $\approx 0.9\%/\Omega_{\text{sq}}$ (with increasing c_{Au}), while spheres only achieved $\approx 0.55\%/\Omega_{\text{sq}}$.

During 14 d of storage under ambient conditions in the dark, the R_{sh} of all AuNW-based FTEs increased significantly. The underlying ageing mechanisms accelerated with c_{Au} due to the growing defectiveness of the shell and the increasing proportion of organic residues in the core of the increasingly thicker lines. At $c_{\text{Au}} \geq 5 \text{ mg/mL}$, the wire-based FTEs lost all measurable conductance within less than 1 d of ageing and the associated *FOM* dropped to $0\%/\Omega_{\text{sq}}$.

FTEs built from AuNPs have more stable conductive Au shells and stability improves with c_{Au} . The thick, stable shells divert the migration of Au from the core onto themselves during aging. This likely reduced R_{sh} and further improves the stability of the shell; to a larger extent for higher concentrations, as the residual amount of Au in the hybrid core grows with rising c_{Au} . The associated *FOM* in the aged state increased rapidly with c_{Au} , reaching the highest value of $\approx 3.32\%/\Omega_{\text{sq}}$ at $c_{\text{Au}} = 30 \text{ mg/mL}$. After 14 d of ageing at ambient conditions in the dark, all AuNP-based FTEs imprinted in the concentration range of 12 to 24 mg/mL achieved the minimum requirements published^[22] in literature for industrial/commercial viability: $\bar{T}_{400-800} > 90\%$; $R_{\text{sh}} < 100 \Omega_{\text{sq}}$; and $FOM > 0.9\%/\Omega_{\text{sq}}$.

Chapter 5

Conclusion and Outlook

In this dissertation, flexible and transparent regular gold grid electrodes (FTEs) were prepared. The fabrication method was direct nanoimprint lithography of self-assembling colloidal Au nanoparticles dissolved in cyclohexane, combined with low-pressure H₂/Ar plasma sintering for oleylamine (OAm) ligand removal. Two distinctly contrasting Au nanostructures were imprinted using the same stamp to investigate the interplay between microstructure and performance of the FTEs and their ageing. Spheres of 3.7 ± 0.37 nm (core) diameter (AuNPs) and wires of uniform 1.6 to 1.7 nm diameter at lengths around 2 to 6 μm (AuNWs) were compared. The study was carried out at different particle concentrations c_{Au} (mg/mL), which enabled printed lines of varying thickness (height) and width.

The nanostructures had different agglomeration states within the inks that were retained during printing: crystalline, hexagonally bundled superstructures for the AuNWs and amorphous arrangements for the AuNPs. When imprinted, the OAm ligand shells interdigitated and caused a denser packing than in the ink. The volume fractions of OAm in the lines were similar: ≈ 87 vol% for the wires, and ≈ 81 vol% for the spheres. At the same c_{Au} , the wire-based lines had the larger volume. For the wires the surface-to-surface distance d_i of adjacent particles (≈ 2.52 nm) was noticeably (about a third) larger than for the spheres (≈ 1.91 nm). However, for AuNWs d_i was significantly larger than the wire diameter (≈ 1.6 nm), while for AuNPs it was the other way around (≈ 3.7 nm diameter). The line widths were in the range from 1 to 3 μm .

The heights ranged from ≈ 60 to 275 nm.

The experiments confirmed that OAm can be completely removed from the particle surfaces through plasma treatment. However, in contrast to published hypotheses, the relatively compact imprinted lines did not sinter through. For both nanostructures, sintering progressed top-down in a self-limiting manner. Thin conductive Au shells were on top of insulating hybrid cores. In both cases, the average shell thickness t_{shell} was virtually independent of c_{Au} and smaller than the mean free path of electrons in bulk gold ($\lambda_{\text{Au}}^e \approx 38$ nm, $t_{\text{shell}} = 5.7 \pm 1.1$ nm for the wires and 8.1 ± 1.4 nm for AuNPs).

These findings suggest a sintering mechanism as suggested by Maurer et al.^[228] (see sections 2.4.4 and 2.5 herein) for the plasma sintering of dip-coated layers of OAm-stabilized AuNWs. In a first step, the plasma removes OAm from a top layer of the printed nanoparticles. In case of the crystallized AuNWs, it likely has the thickness of the crystals' unit cell. The remaining bare gold cores merge quickly^[233] into a fabric-like superstructure with a thickness that roughly equals the thickness of the hexagonal arrangement of seven bare wires: 3×1.7 nm = 5.1 nm $\approx t_{\text{shell}} = 5.7 \pm 1.1$ nm.

In case of the amorphous sphere assembly, the relevant layer after OAm removal likely has the thickness of two layers of bare spheres on top of each other. The lower layer closes gaps between adjacent spheres of the layer above for the plasma. Compared to the AuNWs, adjacent AuNPs fuse slower^[282] and into a Au skin. Its thickness roughly equals two sphere diameters: 2×3.7 nm = 7.4 nm $\approx t_{\text{shell}} = 8.1 \pm 1.4$ nm.

The gold shells formed from the pre-bundled AuNWs resulted in porous shells with a rough surface. They originated from a "randomly" self-assembled wire bundle network layer (see section 2.1.3 herein). At $c_{\text{Au}} > 5$ mg/mL, the widths of the wire-based lines exceeded the width of the imprinting stamp channels. This caused small cracks in the shells at the line edges. Their density increased with c_{Au} . Less porous shells with smooth surfaces formed from the AuNPs and the density of pores decreased in these shells with c_{Au} .

Localized defects had a minor impact and impaired the mean conductivity σ_{shell} only moderately. Less common, severe defects are likely to be

extrinsic in nature and caused by tapered or clogged stamp channels or irregularities in the substrate or stamp. They turn the respective line into an insulator not contributing to σ_{shell} . Apparently, AuNP assemblies are more susceptible to these severe defects. This would explain why at any c_{Au} , contrary to expectations, the more porous, rougher, and thinner AuNW-based shells exhibited the greater σ_{shell} .

With increasing c_{Au} , the likelihood of severe defects decreases, since higher concentrated inks are better in bridging irregularities. Thus, σ_{shell} increased for both particle types with c_{Au} . Above 5 mg/mL, the peripheral crack-like defects reversed this trend in case of the wires. Both the defectiveness and thinness of the shells prevented σ_{shell} from reaching bulk Au conductivity. However, consistent with the assumption of a non-conductive core as basis for the determination of σ_{shell} , the mean conductivities of the best conducting shells were in the range of the conductivity values reported for ultra-thin polycrystalline Au films with similar thickness as the shells.

The mean width w and the average maximum height h_{max} of the FTEs' lines generally increased with c_{Au} for both nanostructures. In case of both w and h_{max} , wires had the larger value at the same c_{Au} and the difference in height increased significantly with increasing c_{Au} . Together with the shell conductivities, this explains why R_{sh} decreased with c_{Au} for both particle types, and why R_{sh} was always lower in case of the wires at a given c_{Au} .

The opacity of the sintered lines and their contact area with the polyethylene terephthalate (PET) substrate reduced the mean optical transmittance $\bar{T}_{400-800}$ of the FTE. $\delta\bar{T}_{400-800}/\delta c_{\text{Au}}$ was always negative for both wires and spheres. At the same c_{Au} , wire-based electrodes exhibited the lower optical transmittance.

In case of both nanoparticles, c_{Au} affected $\bar{T}_{400-800}$ much less than R_{sh} . Consequently, the figure of merit (FOM) increased for both FTE types with c_{Au} . At the same Au concentration, the wire-based FTEs outperformed the sphere-based FTEs by at least 3.4 times in terms of the ratio $\bar{T}_{400-800}/R_{\text{sh}}$. The highest post-plasma FOM of all FTEs prepared in the scope of this dissertation amounted to $\approx 0.9\%/\Omega_{\text{sq}}$ for AuNWs at $c_{\text{Au}} = 10$ mg/mL, while AuNPs only achieved $0.55\%/\Omega_{\text{sq}}$ at 30 mg/mL.

The electrodes derived from AuNWs were not stable post-plasma. Their performance deteriorated during storage at ambient conditions in the dark. The dependence of the aged FOM on c_{Au} was pronounced for both imprinted nanostructures, the FOM ranking of the two FTE types reversed.

While the FOM of wire-based FTEs imprinted at $c_{Au} > 5$ mg/mL dropped to $0\%/\Omega_{sq}$ within less than 24 h, each AuNP-derived FTE improved its post-plasma FOM during the storage period (14 d) to a higher, largely stable value when imprinted at $c_{Au} > 9$ mg/mL. The best FOM achieved was $\approx 3.32\%/\Omega_{sq}$ for $c_{Au} = 30$ mg/mL. All aged AuNP-based FTEs imprinted at 12 mg/mL $\leq c_{Au} \leq 24$ mg/mL had transmittances $> 90\%$ and a $FOM > 0.9\%/\Omega_{sq}$, the minimum values required^[22] for practical use.

As with the freshly prepared FTEs, c_{Au} influenced mainly the electrodes' aged electrical performance. The different sign of this influence for spheres and wires correlated well with the different post-plasma microstructures of the conductor shells and the resulting difference in evolution during storage, including the difference in interplay with the ageing cores.

Three ageing mechanisms dominated the development of $R_{sh,t}$ during a storage time t for both FTE types. These mechanisms were a) solid-state de-wetting of the shell, b) de-mixing in the hybrid core, and c) shrinkage of the core and the shell in height due to compaction of the core during de-mixing. Solid-state de-wetting preferably starts at pre-existing voids (holes) and is faster for the thinner shell as it requires surface atom self-diffusion. De-mixing is largely triggered by partial sintering. It is favored by a high fraction of organic residues in the post-plasma core. The densification of the core compensates for losses of organics during plasma sintering which rendered the core porous. Such loss is high in case of a porous shell, which, even when formed quickly, cannot shield the core well from the plasma.

With increasing c_{Au} , the AuNW-based FTEs aged faster. They formed $\approx 40\%$ thinner, pronounced porous, and otherwise increasingly defective shells. At $c_{Au} = 10$ mg/mL (≈ 275 nm), the height of their conductive line was greater than that in case of the spheres at $c_{Au} = 30$ mg/mL

(≈ 240 nm). At $c_{\text{Au}} = 10$ mg/mL, the wire-based height exceeded that of the spheres by more than 100 %. The porous shell implied a greater loss of organics during sintering. At the same time, the significantly greater height likely ensured a larger post-plasma organic residue fraction in the core. The AuNW's being prone to the Rayleigh-Plateau instability and a surface spacing d_i of adjacent wires in the core that was greater than their ultra-thin diameter, additionally favored de-mixing of the core. Migration of organics from the core through the voids in the shell possibly promoted de-wetting, too.

The decisive mechanism that linked de-wetting of the shell and de-mixing of the core was the densification of the core. Compaction of the core was more extensive in the FTEs with the porous shell due to the higher loss in organics during sintering. Here, it additionally met with the greater conductor height. For the AuNW-based FTEs, this entailed a pronounced shrinkage in the height of the core and of the thin shell which, at the same time, degraded substantially through de-wetting. From $c_{\text{Au}} > 5$ mg/mL onwards, it jointly led to a loss of conductivity within less than 1 d due to a rupture of the sagging shell and rendered any determination of the optical transmittance obsolete.

In the AuNP-based FTEs with the almost pore-free, less defective, and thicker shells, the shrinkage in height of core and shell as well as the degradation of the shell by de-wetting, were less pronounced. The shell extended slightly in width during height shrinkage, but remained intact. Au migrated from the core to the lower side of the shell. This thickened the shell up to 100 nm depending on c_{Au} , further fostering its resistivity to de-wetting, and increasing its conductance. From $c_{\text{Au}} > 12$ mg/mL onwards, the 14 d storage ended with a lowered and stable R_{sh} which decreased by up to 82 % due to the growing Au reservoir in the core with increasing c_{Au} .

The effect of the slight extension in width of the sphere based shells on the transmittances of the FTEs was overcompensated by reduced optical scattering in bleeding areas of the printed lines so that $\bar{T}_{400-800}$ slightly increased with c_{Au} by up to 3.17 %.

The highly instable FTEs imprinted at high c_{Au} from AuNWs could be stabilized by PEDOT:PSS layers, which slowed or largely prevented the

processes underlying solid-state de-wetting. PEDOT:PSS adsorbate layers did not entirely prevent the relevant diffusion processes, but hindered the rapid rupture of the shell. This was revealed by a slight decrease of $R_{\text{sh,t}}$ at the beginning of the storage. It was attributed to relaxation effects within the shell which released stress and lattice distortions after plasma sintering and which improved the mean shell conductivity σ_{shell} . Thicker capping layers of the same material prevented the shell from collapsing. A such stabilized shell has likely successfully caught gold from the core on its bottom side, leading to a visible reduction in R_{sh} .

The differences in FTE performance and ageing are based on the same origin: the ultra-high ratio of length to diameter for the ultra-thin wires versus the minimal ratio for the spheres. It enables a deeper OAm-OAm interdigitation for adjacent AuNPs in printed lines and the huge contact area of aligned AuNWs which, despite the stronger particle curvature, is three orders of magnitude larger than the AuNP-AuNP contact area.^[240] This lends the OAm-capped ultra-thin wires a tendency to self-assemble into hexagonal bundles even in the good solvent cyclohexane, and to build well-percolating network-like superstructures during imprinting. These, on the one hand, protect the conductor lines during imprinting from severe defects which are likely extrinsic in nature. On the other hand, they are the cause of the formation of conducting shells as ultra-thin, distinctly porous, and in other ways defective layers covering the thicker, non-conductive hybrid cores comprising intact, yet instable wires. The fragmentation of such shells, already during ambient storage, and thus the failure of the FTE, is inherent. In contrast, the thicker, robust, and isotropic gold spheres, and their disordered assembly in both cyclohexane and the imprinted lines even at high c_{Au} , entail a shell-core design of the sintered electrode that inheres a self-healing concept. After production, it diverts Au from the core to the shell, at RT, to “repair” the self-limitation of the plasma sintering.

Prior to this dissertation, it was generally accepted knowledge that AuNWs, coated by a single layer of oleylamine (OAm) ligands, agglomerate into elongated hexagonal bundles after dispersion in n-hexane, but remain freely dispersed in cyclohexane. In the scope of this dissertation, it was observed that such AuNWs can also self-assemble into elongated

hexagonal bundles in cyclohexane: dilution with the solvent shifts the equilibrium to the side of the bundles. This was surprising since Au nanospheres typically remain dispersed at smaller and only agglomerate at higher concentrations. In the case of Au nanospheres with a diameter of 3.2 nm and coated with long-chain alkylamines, the agglomeration threshold is even particularly high in cyclohexane.

The divergent findings could be reconciled by the observation that the bundling of the OAm-stabilized AuNWs requires in both n-hexane and cyclohexane sparse ligand shells, the required degree of depletion being higher in cyclohexane. The respective sparsity of the ligand shell had been implicitly set during the post-synthesis purification of the AuNWs which removed unbound OAm.

A depleted shell in the solvent n-hexane appears to cause solvent molecules, and in the solvent cyclohexane unbound ligands to align with the OAm ligand shell. By assembling into hexagonal bundles, a n-hexane or an unbound OAm molecule can simultaneously align with two ligand shells of adjacent AuNWs by bridging them. This limits the loss of entropy resulting from the alignment and drives the bundling.

For the purpose of this dissertation, the colloidal solutions of sparsely OAm-coated AuNWs in cyclohexane combined both the advantages of bundled AuNWs in n-hexane and of fully dispersed AuNWs in cyclohexane, and at the same time avoided the disadvantages of these colloidal solutions:

- at least 70% of the AuNWs contained in an imprinted ink were pre-bundled;
- the imprinted inks involved a lowered OAm content;
- unlike n-hexane, cyclohexane was also well suited for direct nanoimprinting of OAm coated AuNPs; and
- cyclohexane swelled PDMS stamps less than n-hexane^[221].

This enabled nanoimprinting of FTEs from colloidal gold inks which differed basically only in the geometry of the dissolved nanoparticles. That provided an ideal basis for the comparative study of the interplay between morphology, performance, and stability of FTEs imprinted from different colloidal Au particles carried out in this dissertation.

As the most important result, this dissertation shows that the combination of direct nanoimprinting of metal nanoparticle inks with core diameters well below λ_{metal}^e into lines with thicknesses well above λ_{metal}^e and low-pressure H₂/Ar plasma sintering, does not use the invested metal efficiently for the resulting FTE's electrical performance. After plasma sintering, the conductance is significantly improved. However, the electric performance of the fabricated FTEs remains well below the potential of the amount of metal processed, since the plasma only sinters outer nanoparticle layers of a printed line to a thin, electrically conducting metal shell. The remaining thicker hybrid core underneath the shell remains largely non-conductive. Imprinting defects within the metal shell, inherent to the combination of the process and the selected nanoparticle or extrinsic in nature, further limit conductivity.

The material (Au) efficiency can be considerably improved by annealing the fabricated FTE. The remaining ligands/fragments then de-couple from the surface of the metal nanoparticles and the hybrid cores de-mix, depositing additional metal from the cores onto the shells such that R_{sh} de- and the stability of the shells further increases.

If the inherent stability of the shell is insufficient, it can be reinforced prior to annealing with a coating (e.g., PEDOT:PSS) that bonds to the metal.

A low binding energy between the ligands' terminal functional group and the metal particles as well as partial fragmentation of the ligands by the plasma, aid in lowering the required annealing temperature. In case of the OAm-stabilized AuNWs and AuNPs imprinted for this dissertation, room temperature was sufficient. Similar mobilization of metal in hybrid phases by low temperature annealing, including the supportive plasma effect, has previously been noticed.^[254,255,264,276]

The results of this dissertation suggest that the following approach leads not only to practically useful^[22] FTEs with transmittances $> 90\%$ and a stable $FOM > 0.9\%/\Omega_{\text{sq}}$, but also to an increased material (Au) efficiency:

- FTE production as described in Publication 2, but
- imprinting the lines with a thickness in the range of 60 to 150 nm only,

-
- use of a semi-crystalline PET^[276] or of a PEN^[264] substrate with T_g up to 120 °C,
 - use of monodisperse Au nanospheres with a core diameter in the range of 5 to 10 nm (preferably thicker spheres and imprinted into the thinner lines), and
 - applying the plasma sintering jointly with (preferred) or prior to a moderate thermal annealing at $30\text{ °C} < T < T_g - 10\text{ °C}$.

As the sphere size increases, it may be necessary to lengthen the tail group of the alkylamine ligand to counteract premature agglomeration during imprinting for percolation reasons.^[43,248] The use of substrates and imprinting stamps that are and remain poor in irregularities and tapered/clogged stamp channels, would further improve the FTEs' *FOM*.

Bibliography

- [1] Liz Allen, Alison O’Connell, and Veronique Kiermer. How can we ensure visibility and diversity in research contributions? How the Contributor Role Taxonomy (CRediT) is helping the shift from authorship to contributorship. *Learned Publishing*, 32(1):71–74, 2019. ISSN 0953-1513. doi:10.1002/leap.1210.
- [2] Amy Brand, Liz Allen, Micah Altman, Marjorie Hlava, and Jo Scott. Beyond authorship: attribution, contribution, collaboration, and credit. *Learned Publishing*, 28(2):151–155, 2015. ISSN 0953-1513. doi:10.1087/20150211.
- [3] Liz Allen, Jo Scott, Amy Brand, Marjorie Hlava, and Micah Altman. Publishing: Credit where credit is due. *Nature*, 508(7496): 312–313, 2014. doi:10.1038/508312a.
- [4] Liangbing Hu, Hui Wu, and Yi Cui. Metal nanogrids, nanowires, and nanofibers for transparent electrodes. *MRS Bulletin*, 36(10): 760–765, 2011. ISSN 0883-7694. doi:10.1557/mrs.2011.234.
- [5] Lukas Kinner, Felix Hermerschmidt, Theodoros Dimopoulos, and Emil J. W. List-Kratochvil. Implementation of Flexible Embedded Nanowire Electrodes in Organic Light-Emitting Diodes. *physica status solidi (RRL) – Rapid Research Letters*, 14(11):2000305, 2020. ISSN 1862-6254. doi:10.1002/pssr.202000305.
- [6] Anna Isabel Hofmann, Eric Cloutet, and Georges Hadziioannou. Materials for Transparent Electrodes: From Metal Oxides to Organic Alternatives. *Advanced Electronic Materials*, 4(10):1700412, 2018. ISSN 2199-160X. doi:10.1002/aelm.201700412.

- [7] Minghui Luo, Yanhua Liu, Wenbin Huang, Wen Qiao, Yun Zhou, Yan Ye, and Lin-Sen Chen. Towards Flexible Transparent Electrodes Based on Carbon and Metallic Materials. *Micromachines*, 8(1):12, 2017. doi:10.3390/mi8010012.
- [8] Lukas Kinner, Theodoros Dimopoulos, Giovanni Ligorio, Emil J. W. List-Kratochvil, and Felix Hermerschmidt. High performance organic light-emitting diodes employing ITO-free and flexible $TiO_x/Ag/Al:ZnO$ electrodes. *RSC advances*, 11(28):17324–17331, 2021. doi:10.1039/d1ra02214h.
- [9] Michael Layani, Alexander Kamyshny, and Shlomo Magdassi. Transparent conductors composed of nanomaterials. *Nanoscale*, 6(11):5581–5591, 2014. doi:10.1039/c4nr00102h.
- [10] Darran R. Cairns, Richard P. Witte, Daniel K. Sparacin, Suzanne M. Sachsman, David C. Paine, Gregory P. Crawford, and R. R. Newton. Strain-dependent electrical resistance of tin-doped indium oxide on polymer substrates. *Applied Physics Letters*, 76(11):1425–1427, 2000. ISSN 0003-6951. doi:10.1063/1.126052.
- [11] Kirill Zilberberg and Thomas Riedl. Metal-nanostructures – a modern and powerful platform to create transparent electrodes for thin-film photovoltaics. *Journal of Materials Chemistry A*, 4(38):14481–14508, 2016. ISSN 2050-7488. doi:10.1039/C6TA05286J.
- [12] Monica Morales-Masis, Stefaan de Wolf, Rachel Woods-Robinson, Joel W. Ager, and Christophe Ballif. Transparent Electrodes for Efficient Optoelectronics. *Advanced Electronic Materials*, 3(5):1600529, 2017. ISSN 2199-160X. doi:10.1002/aelm.201600529.
- [13] Yuanchao Zhang, Wendy Chu, Alireza Dibaji Foroushani, Hongbin Wang, Da Li, Jingquan Liu, Colin J. Barrow, Xin Wang, and Wenrong Yang. New Gold Nanostructures for Sensor Applications: A Review. *Materials*, 7(7):5169–5201, 2014. doi:10.3390/ma7075169.
- [14] J. Nutting and J. L. Nuttall. The malleability of gold. *Gold Bulletin*, 10(1):2–8, 1977. ISSN 2364-821X. doi:10.1007/BF03216517.

- [15] C. Guillén and J. Herrero. TCO/metal/TCO structures for energy and flexible electronics. *Thin Solid Films*, 520(1):1–17, 2011. ISSN 00406090. doi:10.1016/j.tsf.2011.06.091.
- [16] Cheng Zhang, Chengang Ji, Yong-Bum Park, and L. Jay Guo. Thin–Metal–Film–Based Transparent Conductors: Material Preparation, Optical Design, and Device Applications. *Advanced Optical Materials*, 9(3):2001298, 2021. ISSN 2195-1071. doi:10.1002/adom.202001298.
- [17] Dhriti Sundar Ghosh. *Ultrathin Metal Transparent Electrodes for the Optoelectronics Industry*. Springer International Publishing, Heidelberg, 2013. ISBN 978-3-319-00347-4. doi:10.1007/978-3-319-00348-1.
- [18] Chuan Fei Guo and Zhifeng Ren. Flexible transparent conductors based on metal nanowire networks. *Materials Today*, 18(3):143–154, 2015. ISSN 13697021. doi:10.1016/j.mattod.2014.08.018.
- [19] Chaewon Kim, Kunsik An, Mingu Kang, Phillip Won, Jung-Jae Park, Kwan Hyun Cho, Seung Hwan Ko, Byeong-Kwon Ju, and Kyung-Tae Kang. Facile fabrication of flexible metal grid transparent electrode using inkjet-printed dot array as sacrificial layer. *Scientific reports*, 12(1):1572, 2022. doi:10.1038/s41598-022-05312-w.
- [20] Yongrui Yang, Yang Wang, Yali Qiao, and Yanlin Song. Flexible transparent electrodes based on metallic micro–nano architectures for perovskite solar cells. *Journal of Materials Chemistry C*, 10(7):2349–2363, 2022. ISSN 2050-7526. doi:10.1039/D1TC04101K.
- [21] Xi Lu, Yaokang Zhang, and Zijian Zheng. Metal–Based Flexible Transparent Electrodes: Challenges and Recent Advances. *Advanced Electronic Materials*, 7(5):2001121, 2021. ISSN 2199-160X. doi:10.1002/aelm.202001121.
- [22] Hock Beng Lee, Won-Yong Jin, Manoj Mayaji Ovhal, Neetesh Kumar, and Jae-Wook Kang. Flexible transparent conducting electrodes based on metal meshes for organic optoelectronic device

- applications: a review. *Journal of Materials Chemistry C*, 7(5): 1087–1110, 2019. ISSN 2050-7526. doi:10.1039/C8TC04423F.
- [23] Sergey Gorelick, Vitaliy A. Guzenko, Joan Vila-Comamala, and Christian David. Direct e-beam writing of dense and high aspect ratio nanostructures in thick layers of PMMA for electroplating. *Nanotechnology*, 21(29):295303, 2010. doi:10.1088/0957-4484/21/29/295303.
- [24] H. H. Solak, C. David, J. Gobrecht, V. Golovkina, F. Cerrina, S. O. Kim, and P. F. Nealey. Sub-50 nm period patterns with EUV interference lithography. *Microelectronic Engineering*, 67-68:56–62, 2003. ISSN 01679317. doi:10.1016/S0167-9317(03)00059-5.
- [25] Sungmo Ahn, Sihan Kim, and Heonsu Jeon. Single-defect photonic crystal cavity laser fabricated by a combination of laser holography and focused ion beam lithography. *Applied Physics Letters*, 96(13): 131101, 2010. ISSN 0003-6951. doi:10.1063/1.3373527.
- [26] Chia-Ching Liang, Mei-Yi Liao, Wen-Yu Chen, Tsung-Chieh Cheng, Wen-Huei Chang, and Chun-Hung Lin. Plasmonic metallic nanostructures by direct nanoimprinting of gold nanoparticles. *Optics express*, 19(5):4768–4776, 2011. doi:10.1364/OE.19.004768.
- [27] Yonghee Jang, Jihoon Kim, and Doyoung Byun. Invisible metal-grid transparent electrode prepared by electrohydrodynamic (EHD) jet printing. *Journal of Physics D: Applied Physics*, 46(15):155103, 2013. ISSN 0022-3727. doi:10.1088/0022-3727/46/15/155103.
- [28] Xiaoyang Zhu, Mingyang Liu, Ximeng Qi, Hongke Li, Yuan-Fang Zhang, Zhenghao Li, Zilong Peng, Jianjun Yang, Lei Qian, Quan Xu, Nairui Gou, Jiankang He, Dichen Li, and Hongbo Lan. Templateless, Plating-Free Fabrication of Flexible Transparent Electrodes with Embedded Silver Mesh by Electric-Field-Driven Microscale 3D Printing and Hybrid Hot Embossing. *Advanced materials*, 33(21):e2007772, 2021. doi:10.1002/adma.202007772.
- [29] Yi-lun Wang, Bao-jia Li, Shuang-shuang Li, Li-jing Huang, Yongying Wang, and Nai-fei Ren. Fabrication of metal mesh flexible

- transparent electrodes and heaters by a cost-effective method based on ultrafast laser direct writing. *Optics & Laser Technology*, 138: 106867, 2021. ISSN 00303992. doi:10.1016/j.optlastec.2020.106867.
- [30] Le Zhao, Shihui Yu, Junjun Li, Muying Wu, Lingxia Li, and Xiuyu Wang. Highly reliable flexible transparent conductors prepared with Cu/Ni grid by vacuum-free solution process. *Optical Materials*, 120:111427, 2021. ISSN 09253467. doi:10.1016/j.optmat.2021.111427.
- [31] Lu Zhou, Xiaolian Chen, Wenming Su, Zheng Cui, and Wen-Yong Lai. In-Depth Investigation of Inkjet-Printed Silver Electrodes over Large-Area: Ink Recipe, Flow, and Solidification. *Advanced Materials Interfaces*, page 2102548, 2022. ISSN 2196-7350. doi:10.1002/admi.202102548.
- [32] Dongdong Li, Xing Liu, Xin Chen, Wen-Yong Lai, and Wei Huang. A Simple Strategy towards Highly Conductive Silver-Nanowire Inks for Screen-Printed Flexible Transparent Conductive Films and Wearable Energy-Storage Devices. *Advanced Materials Technologies*, 4(8):1900196, 2019. doi:10.1002/admt.201900196.
- [33] Lei Zhou, Heng-Yang Xiang, Su Shen, Yan-Qing Li, Jing-De Chen, Hao-Jun Xie, Irene A. Goldthorpe, Lin-Sen Chen, Shuit-Tong Lee, and Jian-Xin Tang. High-performance flexible organic light-emitting diodes using embedded silver network transparent electrodes. *ACS nano*, 8(12):12796–12805, 2014. doi:10.1021/nn506034g.
- [34] Namyong Kwon, Kyohyeok Kim, Sihyun Sung, Insook Yi, and IISub Chung. Highly conductive and transparent Ag honeycomb mesh fabricated using a monolayer of polystyrene spheres. *Nanotechnology*, 24(23):235205, 2013. doi:10.1088/0957-4484/24/23/235205.
- [35] Johannes H. M. Maurer, Lola González-García, Beate Reiser, Ioannis Kanelidis, and Tobias Kraus. Templated Self-Assembly of Ultrathin Gold Nanowires by Nanoimprinting for Transparent Flexible Electronics. *Nano letters*, 16(5):2921–2925, 2016. doi:10.1021/acs.nanolett.5b04319.

- [36] I. Park, S. H. Ko, H. Pan, C. P. Grigoropoulos, A. P. Pisano, J. M. J. Fréchet, E.-S. Lee, and J.-H. Jeong. Nanoscale Patterning and Electronics on Flexible Substrate by Direct Nanoimprinting of Metallic Nanoparticles. *Advanced Materials*, 20(3):489–496, 2008. ISSN 0935-9648. doi:10.1002/adma.200702326.
- [37] Fionnuala McGrath, Jing Qian, Kelsey Gwynne, Cindy Kumah, Dermot Daly, Calin Hrelescu, Xia Zhang, Deirdre M. O’Carroll, and A. Louise Bradley. Structural, optical, and electrical properties of silver gratings prepared by nanoimprint lithography of nanoparticle ink. *Applied Surface Science*, 537:147892, 2021. ISSN 01694332. doi:10.1016/j.apsusc.2020.147892.
- [38] Seung H. Ko, Inkyu Park, Heng Pan, Costas P. Grigoropoulos, Albert P. Pisano, Christine K. Luscombe, and Jean M. J. Fréchet. Direct nanoimprinting of metal nanoparticles for nanoscale electronics fabrication. *Nano letters*, 7(7):1869–1877, 2007. doi:10.1021/nl070333v.
- [39] Harshal Agrawal and Erik C. Garnett. Nanocube Imprint Lithography. *ACS nano*, 14(9):11009–11016, 2020. doi:10.1021/acsnano.0c04793.
- [40] Xi Yu, Jonathan T. Pham, Chandramouleeswaran Subramani, Brian Creran, Yi-Cheun Yeh, Kan Du, Debabrata Patra, Oscar R. Miranda, Alfred J. Crosby, and Vincent M. Rotello. Direct patterning of engineered ionic gold nanoparticles via nanoimprint lithography. *Advanced materials*, 24(47):6330–6334, 2012. doi:10.1002/adma.201202776.
- [41] YoungJa Kim, GeeHong Kim, and JaeJong Lee. Fabrication of a conductive nanoscale electrode for functional devices using nanoimprint lithography with printable metallic nanoink. *Microelectronic Engineering*, 87(5-8):839–842, 2010. ISSN 01679317. doi:10.1016/j.mee.2009.12.062.
- [42] Johannes H. M. Maurer, Lola González-García, Indra K. Backes, Beate Reiser, Sarah M. Schlossberg, and Tobias Kraus. Direct Nanoimprinting of a Colloidal Self-Organizing Nanowire Ink for

- Flexible, Transparent Electrodes. *Advanced Materials Technologies*, 2(6):1700034, 2017. doi:10.1002/admt.201700034.
- [43] Thomas Kister, Johannes H. M. Maurer, Lola González-García, and Tobias Kraus. Ligand-Dependent Nanoparticle Assembly and Its Impact on the Printing of Transparent Electrodes. *ACS applied materials & interfaces*, 10(7):6079–6083, 2018. doi:10.1021/acsami.7b18579.
- [44] Suresh K. Balasubramanian, Liming Yang, Lin-Yue L. Yung, Choon-Nam Ong, Wei-Yi Ong, and Liya E. Yu. Characterization, purification, and stability of gold nanoparticles. *Biomaterials*, 31(34):9023–9030, 2010. doi:10.1016/j.biomaterials.2010.08.012.
- [45] H.-G. Boyen, G. Kästle, F. Weigl, B. Koslowski, C. Dietrich, P. Ziemann, J. P. Spatz, S. Riethmüller, C. Hartmann, M. Möller, G. Schmid, M. G. Garnier, and P. Oelhafen. Oxidation-resistant gold-55 clusters. *Science (New York, N.Y.)*, 297(5586):1533–1536, 2002. doi:10.1126/science.1076248.
- [46] S. B. Lyon. Corrosion of Noble Metals. In Tony J. A. Richardson and L. L. Shreir, editors, *Shreir’s Corrosion*, volume 3, pages 2205–2223. Elsevier Science, 2010. ISBN 978-0-444-52787-5. doi:10.1016/B978-044452787-5.00109-8.
- [47] Shengyun Huang, Yannan Liu, Fan Yang, Yong Wang, Ting Yu, and Dongling Ma. Metal nanowires for transparent conductive electrodes in flexible chromatic devices: a review. *Environmental Chemistry Letters*, 20(5):3005–3037, 2022. ISSN 1610-3653. doi:10.1007/s10311-022-01471-4.
- [48] Taehwan Lim, Huanan Zhang, and Sohee Lee. Gold and silver nanocomposite-based biostable and biocompatible electronic textile for wearable electromyographic biosensors. *APL Materials*, 9(9):091113, 2021. doi:10.1063/5.0058617.
- [49] Minjae Ku, Jae Chul Hwang, Byungkook Oh, and Jang-Ung Park. Smart Sensing Systems Using Wearable Optoelectronics. *Advanced Intelligent Systems*, 2(3):1900144, 2020. ISSN 2640-4567. doi:10.1002/aisy.201900144.

- [50] Daniel Gall. Electron mean free path in elemental metals. *Journal of Applied Physics*, 119(8):085101, 2016. ISSN 0021-8979. doi:10.1063/1.4942216.
- [51] Jeffrey R. S. Brownson. *Solar Energy Conversion Systems*. Elsevier, Saint Louis, 2014. ISBN 978-0-12-397021-3. doi:10.1016/C2011-0-07039-4.
- [52] Norbert Koch. *Supramolecular Materials for Opto-Electronics*. The Royal Society of Chemistry, Cambridge, 1st edition, 2014. ISBN 978-1-84973-826-2. doi:10.1039/9781782626947.
- [53] Stephen J. Sweeney and Jayanta Mukherjee. Optoelectronic Devices and Materials. In Safa Kasap and Peter Capper, editors, *Springer Handbook of Electronic and Photonic Materials*, Springer Handbooks. Springer International Publishing, Cham, 2017. ISBN 978-3-319-48931-5. doi:10.1007/978-3-319-48933-9_35.
- [54] Sukanta De, Thomas M. Higgins, Philip E. Lyons, Evelyn M. Doherty, Peter N. Nirmalraj, Werner J. Blau, John J. Boland, and Jonathan N. Coleman. Silver Nanowire Networks as Flexible, Transparent, Conducting Films: Extremely High DC to Optical Conductivity Ratios. *ACS nano*, 3(7):1767–1774, 2009. doi:10.1021/nm900348c.
- [55] David S. Hecht and Richard B. Kaner. Solution-processed transparent electrodes. *MRS Bulletin*, 36(10):749–755, 2011. ISSN 0883-7694. doi:10.1557/mrs.2011.211.
- [56] A. E. Becquerel. Memoire sur les effets électroniques produits sous l’influence des rayons solaires. *Comptes Rendus de L’Academie des Sciences*, (9):561–567, 1839.
- [57] R. S. Ohl. Light-sensitive electric device, US 2402662A (patent), 1946.
- [58] D. M. Chapin, C. S. Fuller, and G. L. Pearson. A New Silicon p–n Junction Photocell for Converting Solar Radiation into Electrical Power. *Journal of Applied Physics*, 25(5):676–677, 1954. ISSN 0021-8979. doi:10.1063/1.1721711.

- [59] Bernard Kippelen and Jean-Luc Brédas. Organic photovoltaics. *Energy Environ. Sci.*, 2(3):251, 2009. ISSN 1754-5692. doi:10.1039/b812502n.
- [60] C. W. Tang. Two-layer organic photovoltaic cell. *Applied Physics Letters*, 48(2):183–185, 1986. ISSN 0003-6951. doi:10.1063/1.96937.
- [61] C. W. Tang and S. A. VanSlyke. Organic electroluminescent diodes. *Applied Physics Letters*, 51(12):913–915, 1987. ISSN 0003-6951. doi:10.1063/1.98799.
- [62] Weiran Cao, Jian Li, Hongzheng Chen, and Jianguo Xue. Transparent electrodes for organic optoelectronic devices: a review. *Journal of Photonics for Energy*, 4(1):040990, 2014. ISSN 1947-7988. doi:10.1117/1.JPE.4.040990.
- [63] Jan Meiss, Christian L. Uhrich, Karsten Fehse, Steffen Pfuetzner, Moritz K. Riede, and Karl Leo. Transparent electrode materials for solar cells. In Andreas Gombert, editor, *Photonics for Solar Energy Systems II*, SPIE Proceedings, page 700210. SPIE, 2008. doi:10.1117/12.781275.
- [64] Ankush Kumar. Predicting efficiency of solar cells based on transparent conducting electrodes. *Journal of Applied Physics*, 121(1):014502, 2017. ISSN 0021-8979. doi:10.1063/1.4973117.
- [65] Ana Sánchez-Iglesias, Beatriz Rivas-Murias, Marek Grzelczak, Jorge Pérez-Juste, Luis M. Liz-Marzán, Francisco Rivadulla, and Miguel A. Correa-Duarte. Highly transparent and conductive films of densely aligned ultrathin Au nanowire monolayers. *Nano letters*, 12(12):6066–6070, 2012. doi:10.1021/nl3021522.
- [66] Gregory J. Exarhos and Xiao-Dong Zhou. Discovery-based design of transparent conducting oxide films. *Thin Solid Films*, 515(18):7025–7052, 2007. ISSN 00406090. doi:10.1016/j.tsf.2007.03.014.
- [67] Charles Kittel. *Introduction to solid state physics*. Wiley, Hoboken, NJ, 8th edition, 2005. ISBN 0-471-41526-X.

- [68] Jörg Schube. *Metallization of silicon solar cells with passivating contacts*. Dissertation (Doktorarbeit), Albert-Ludwigs-Universität Freiburg, Freiburg im Breisgau, 2020.
- [69] S. M. Sze and Kwok K. Ng. *Physics of semiconductor devices*. Wiley-Interscience, Hoboken, NJ, 3rd edition, 2007. ISBN 978-0-471-14323-9. doi:10.1002/0470068329.
- [70] Neil W. Ashcroft and N. David Mermin. *Solid State Physics*. Saunders College Publishing, Philadelphia, college edition, 1976. ISBN 0-03-083993-9. doi:10.1002/piuz.19780090109.
- [71] Sharon Ann Holgate. *Understanding Solid State Physics*. CRC Press Taylor & Francis Group, Boca Raton, 2nd edition, 2021. ISBN 9780429288234.
- [72] J. Vossen. Method of Fabricating Transparent Conductors, US 3749658A (patent), 1973.
- [73] P. P. Edwards, A. Porch, M. O. Jones, D. V. Morgan, and R. M. Perks. Basic materials physics of transparent conducting oxides. *Dalton transactions*, (19):2995–3002, 2004. doi:10.1039/b408864f.
- [74] Radhouane Bel Hadj Tahar, Takayuki Ban, Yutaka Ohya, and Yasutaka Takahashi. Tin doped indium oxide thin films: Electrical properties. *Journal of Applied Physics*, 83(5):2631–2645, 1998. ISSN 0021-8979. doi:10.1063/1.367025.
- [75] H. Kim, J. S. Horwitz, G. Kushto, A. Piqué, Z. H. Kafafi, C. M. Gilmore, and D. B. Chrisey. Effect of film thickness on the properties of indium tin oxide thin films. *Journal of Applied Physics*, 88(10):6021–6025, 2000. ISSN 0021-8979. doi:10.1063/1.1318368.
- [76] I. Hamberg and C. G. Granqvist. Evaporated Sn-doped In_2O_3 films: Basic optical properties and applications to energy-efficient windows. *Journal of Applied Physics*, 60(11):R123–R160, 1986. ISSN 0021-8979. doi:10.1063/1.337534.
- [77] A. Gondorf, M. Geller, J. Weißbon, A. Lorke, M. Inhester, A. Prodi-Schwab, and D. Adam. Mobility and carrier density in nanoporous

- indium tin oxide films. *Physical Review B*, 83(21):212201, 2011. ISSN 1098-0121. doi:10.1103/PhysRevB.83.212201.
- [78] Lukas Kinner, Martin Bauch, Rachmat Adhi Wibowo, Giovanni Ligorio, Emil J.W. List-Kratochvil, and Theodoros Dimopoulos. Polymer interlayers on flexible PET substrates enabling ultra-high performance, ITO-free dielectric/metal/dielectric transparent electrode. *Materials & Design*, 168:107663, 2019. ISSN 02641275. doi:10.1016/j.matdes.2019.107663.
- [79] Yan-Gang Bi, Yue-Feng Liu, Xu-Lin Zhang, Da Yin, Wen-Quan Wang, Jing Feng, and Hong-Bo Sun. Ultrathin Metal Films as the Transparent Electrode in ITO-Free Organic Optoelectronic Devices. *Advanced Optical Materials*, 7(6):1800778, 2019. ISSN 2195-1071. doi:10.1002/adom.201800778.
- [80] Lukas Kinner, Emil J. W. List-Kratochvil, and Theodoros Dimopoulos. Gentle plasma process for embedded silver-nanowire flexible transparent electrodes on temperature-sensitive polymer substrates. *Nanotechnology*, 31(36):365303, 2020. doi:10.1088/1361-6528/ab97aa.
- [81] Akshay Kumar and Chongwu Zhou. The race to replace tin-doped indium oxide: which material will win? *ACS nano*, 4(1):11–14, 2010. doi:10.1021/nn901903b.
- [82] R. Kykyneshi, B. C. Nielsen, J. Tate, J. Li, and A. W. Sleight. Structural and transport properties of $\text{CuSc}_{1-x}\text{Mg}_x\text{O}_{2+y}$ delafossites. *Journal of Applied Physics*, 96(11):6188–6194, 2004. ISSN 0021-8979. doi:10.1063/1.1806256.
- [83] Z. Chen, B. Cotterell, W. Wang, E. Guenther, and S.-J. Chua. A mechanical assessment of flexible optoelectronic devices. *Thin Solid Films*, 394(1-2):201–205, 2001. ISSN 00406090. doi:10.1016/S0040-6090(01)01138-5.
- [84] Jungheum Yun. Ultrathin Metal films for Transparent Electrodes of Flexible Optoelectronic Devices. *Advanced Functional Materials*, 27(18):1606641, 2017. doi:10.1002/adfm.201606641.

- [85] Claes G. Granqvist. Transparent conductors as solar energy materials: A panoramic review. *Solar Energy Materials and Solar Cells*, 91(17):1529–1598, 2007. ISSN 09270248. doi:10.1016/j.solmat.2007.04.031.
- [86] U. Betz, M. Kharrazi Olsson, J. Marthy, M. F. Escolá, and F. Atamny. Thin films engineering of indium tin oxide: Large area flat panel displays application. *Surface and Coatings Technology*, 200(20-21):5751–5759, 2006. ISSN 02578972. doi:10.1016/j.surfcoat.2005.08.144.
- [87] Claes G. Granqvist. Electrochromics for smart windows: Oxide-based thin films and devices. *Thin Solid Films*, 564:1–38, 2014. ISSN 00406090. doi:10.1016/j.tsf.2014.02.002.
- [88] Sebastian Wilken, Thomas Hoffmann, Elizabeth von Hauff, Holger Borchert, and Jürgen Parisi. ITO-free inverted polymer/fullerene solar cells: Interface effects and comparison of different semi-transparent front contacts. *Solar Energy Materials and Solar Cells*, 96:141–147, 2012. ISSN 09270248. doi:10.1016/j.solmat.2011.09.044.
- [89] Robert Lemasters, Cheng Zhang, Manoj Manjare, Wenqi Zhu, Junyeob Song, Sergei Urazhdin, Henri J. Lezec, Amit Agrawal, and Hayk Harutyunyan. Ultrathin Wetting Layer-Free Plasmonic Gold Films. *ACS Photonics*, 6(11):2600–2606, 2019. ISSN 2330-4022. doi:10.1021/acsp Photonics.9b00907.
- [90] Pengpeng Xiong, Yunfei Liu, Tao Ding, Ping Chen, Haoran Wang, and Yu Duan. Transparent electrodes based on ultrathin/ultra smooth Cu films produced through atomic layer deposition as new ITO-free organic light-emitting devices. *Organic Electronics*, 58: 18–24, 2018. ISSN 15661199. doi:10.1016/j.orgel.2018.03.036.
- [91] Cheng Zhang, Dewei Zhao, Deen Gu, Hyunsoo Kim, Tao Ling, Yi-Kuei Ryan Wu, and L. Jay Guo. An ultrathin, smooth, and low-loss Al-doped Ag film and its application as a transparent electrode in organic photovoltaics. *Advanced materials*, 26(32):5696–5701, 2014. doi:10.1002/adma.201306091.

- [92] David S. Hecht, Liangbing Hu, and Glen Irvin. Emerging transparent electrodes based on thin films of carbon nanotubes, graphene, and metallic nanostructures. *Advanced materials*, 23(13):1482–1513, 2011. doi:10.1002/adma.201003188.
- [93] Brendan O’Connor, Chelsea Haughn, Kwang-Hyup An, Kevin P. Pipe, and Max Shtein. Transparent and conductive electrodes based on unpatterned, thin metal films. *Applied Physics Letters*, 93(22):223304, 2008. ISSN 0003-6951. doi:10.1063/1.3028046.
- [94] E. H. Sondheimer. The mean free path of electrons in metals. *Advances in Physics*, 1(1):1–42, 1952. ISSN 0001-8732. doi:10.1080/00018735200101151.
- [95] Thomas Sannicolo, Mélanie Lagrange, Anthony Cabos, Caroline Celle, Jean-Pierre Simonato, and Daniel Bellet. Metallic Nanowire-Based Transparent Electrodes for Next Generation Flexible Devices: a Review. *Small*, 12(44):6052–6075, 2016. doi:10.1002/sml.201602581.
- [96] Peiyun Yi, Yuwen Zhu, and Yujun Deng. Fabrication and Applications of Flexible Transparent Electrodes Based on Silver Nanowires. In Simas Rackauskas, editor, *Flexible Electronics*. IntechOpen, Erscheinungsort nicht ermittelbar, 2018. ISBN 978-1-78923-456-5. doi:10.5772/intechopen.77506.
- [97] Lihong Dong. One pod synthesis of single-crystal silver nanowires for selective detection of Pb(II). *Micro & Nano Letters*, 14(2):137–141, 2019. ISSN 1750-0443. doi:10.1049/mnl.2018.5110.
- [98] George Z. Voyiadjis and Mohammadreza Yaghoobi. *Size Effects in Plasticity: From macro to nano*. Academic Press, London and San Diego and Cambridge and Oxford, 2019. ISBN 9780128122365. doi:10.1016/B978-0-12-812236-5.00003-7.
- [99] Sunghwan Jin and Rodney S. Ruoff. Preparation and uses of large area single crystal metal foils. *APL Materials*, 7(10), 2019. doi:10.1063/1.5114861.

- [100] Mikita Marus, Aliaksandr Hubarevich, Reuben Jeremy Weixiong Lim, Hui Huang, Aliaksandr Smirnov, Hong Wang, Weijun Fan, and Xiao Wei Sun. Effect of silver nanowire length in a broad range on optical and electrical properties as a transparent conductive film. *Optical Materials Express*, 7(3):1105, 2017. doi:10.1364/OME.7.001105.
- [101] Shengrong Ye, Aaron R. Rathmell, Zuofeng Chen, Ian E. Stewart, and Benjamin J. Wiley. Metal nanowire networks: the next generation of transparent conductors. *Advanced materials*, 26(39):6670–6687, 2014. doi:10.1002/adma.201402710.
- [102] Vittorio Scardaci. Copper Nanowires for Transparent Electrodes: Properties, Challenges and Applications. *Applied Sciences*, 11(17):8035, 2021. doi:10.3390/app11178035.
- [103] Renyun Zhang, Magnus Engholm, Magnus Hummelgård, Henrik Andersson, Jonas Örtengren, and Håkan Olin. High-Performance Transparent and Flexible Electrodes Made by Flash-Light Sintering of Gold Nanoparticles. *ACS Applied Energy Materials*, 1(12):7191–7198, 2018. ISSN 2574-0962. doi:10.1021/acsaem.8b01649.
- [104] Phillip Lee, Jinhwan Lee, Hyungman Lee, Junyeob Yeo, Sukjoon Hong, Koo Hyun Nam, Dongjin Lee, Seung Seob Lee, and Seung Hwan Ko. Highly stretchable and highly conductive metal electrode by very long metal nanowire percolation network. *Advanced materials*, 24(25):3326–3332, 2012. doi:10.1002/adma.201200359.
- [105] M. Arefpour, M. Almasi Kashi, F. Khansari Barzoki, M. Noormohammadi, and A. Ramazani. Electrodeposited metal nanowires as transparent conductive electrodes: Their release conditions, electrical conductivity, optical transparency and chemical stability. *Materials & Design*, 157:326–336, 2018. ISSN 02641275. doi:10.1016/j.matdes.2018.07.048.
- [106] Jinpeng Yang, Fayin Yu, Anran Chen, Shuwen Zhao, Yao Zhou, Shusheng Zhang, Tao Sun, and Guangzhi Hu. Synthesis and application of silver and copper nanowires in high transparent solar cells.

- Advanced Powder Materials*, 1(4):100045, 2022. ISSN 2772834X. doi:10.1016/j.apmate.2022.100045.
- [107] Jung-Yong Lee, Stephen T. Connor, Yi Cui, and Peter Peumans. Solution-processed metal nanowire mesh transparent electrodes. *Nano letters*, 8(2):689–692, 2008. doi:10.1021/nl073296g.
- [108] Mingshang Jin, Guannan He, Hui Zhang, Jie Zeng, Zhaoxiong Xie, and Younan Xia. Shape-controlled synthesis of copper nanocrystals in an aqueous solution with glucose as a reducing agent and hexadecylamine as a capping agent. *Angewandte Chemie (International ed. in English)*, 50(45):10560–10564, 2011. doi:10.1002/anie.201105539.
- [109] Youngjae Seo, Heebo Ha, Paolo Matteini, and Byungil Hwang. A Review on the Deformation Behavior of Silver Nanowire Networks under Many Bending Cycles. *Applied Sciences*, 11(10):4515, 2021. doi:10.3390/app11104515.
- [110] Caroline Celle, Anthony Cabos, Thomas Fontecave, Bruno Laguitton, Anass Benayad, Laure Guettaz, Nathalie Pélissier, Viet Huong Nguyen, Daniel Bellet, David Muñoz-Rojas, and Jean-Pierre Simonato. Oxidation of copper nanowire based transparent electrodes in ambient conditions and their stabilization by encapsulation: application to transparent film heaters. *Nanotechnology*, 29(8):085701, 2018. doi:10.1088/1361-6528/aaa48e.
- [111] Céline Mayousse, Caroline Celle, Alexandre Carella, and Jean-Pierre Simonato. Synthesis and purification of long copper nanowires. Application to high performance flexible transparent electrodes with and without PEDOT:PSS. *Nano Research*, 7(3): 315–324, 2014. ISSN 1998-0124. doi:10.1007/s12274-013-0397-4.
- [112] Ahiud Morag, Vladimir Ezersky, Natalya Froumin, Dimitry Mogiliansky, and Raz Jelinek. Transparent, conductive gold nanowire networks assembled from soluble Au thiocyanate. *Chemical Communications*, 49(76):8552–8554, 2013. doi:10.1039/c3cc44397c.
- [113] Satoshi Takane, Yuki Noda, Naomi Toyoshima, Takafumi Uemura, Yuki Bando, and Tsuyoshi Sekitani. Gold nanowire electrodes for

-
- flexible organic thin-film transistors. *Applied Physics Express*, 15 (9):096501, 2022. ISSN 1882-0778. doi:10.35848/1882-0786/ac896a.
- [114] Nana Zhao, Yang Wei, Nijuan Sun, Qian Chen, Jingwei Bai, Longping Zhou, Yao Qin, Meixian Li, and Limin Qi. Controlled synthesis of gold nanobelts and nanocombs in aqueous mixed surfactant solutions. *Langmuir*, 24(3):991–998, 2008. doi:10.1021/la702848x.
- [115] Johannes H. M. Maurer, Lola González-García, Beate Reiser, Ioannis Kanelidis, and Tobias Kraus. Sintering of ultrathin gold nanowires for transparent electronics. *ACS applied materials & interfaces*, 7(15):7838–7842, 2015. doi:10.1021/acsami.5b02088.
- [116] Simon Bettscheider, Tobias Kraus, and Norman A. Fleck. On the geometric stability of an inorganic nanowire and an organic ligand shell. *Journal of the Mechanics and Physics of Solids*, 123:3–19, 2019. ISSN 00225096. doi:10.1016/j.jmps.2018.07.017.
- [117] Aveek Bid, Achyut Bora, and A. K. Raychaudhuri. Temperature dependence of the resistance of metallic nanowires of diameter ≥ 15 nm: Applicability of Bloch-Grüneisen theorem. *Physical Review B*, 74(3):035426, 2006. ISSN 1098-0121. doi:10.1103/PhysRevB.74.035426.
- [118] B. Reiser, D. Gerstner, L. González-García, J. H. M. Maurer, I. Kanelidis, and T. Kraus. Multivalent bonds in self-assembled bundles of ultrathin gold nanowires. *Physical Chemistry Chemical Physics*, 18(39):27165–27169, 2016. doi:10.1039/c6cp05181b.
- [119] Shouyi Xie, Zi Ouyang, Baohua Jia, and Min Gu. Large-size, high-uniformity, random silver nanowire networks as transparent electrodes for crystalline silicon wafer solar cells. *Optics express*, 21 S3: A355–A362, 2013. doi:10.1364/OE.21.00A355.
- [120] Ankush Kumar and G. U. Kulkarni. Evaluating conducting network based transparent electrodes from geometrical considerations. *Journal of Applied Physics*, 119(1):015102, 2016. ISSN 0021-8979. doi:10.1063/1.4939280.

- [121] Taegeon Kim, Ali Canlier, Changsoon Cho, Vepa Rozyyev, Jung-Yong Lee, and Seung Min Han. Highly transparent Au-coated Ag nanowire transparent electrode with reduction in haze. *ACS applied materials & interfaces*, 6(16):13527–13534, 2014. doi:10.1021/am502632t.
- [122] Colin Preston, Yunlu Xu, Xiaogang Han, Jeremy N. Munday, and Liangbing Hu. Optical haze of transparent and conductive silver nanowire films. *Nano Research*, 6(7):461–468, 2013. ISSN 1998-0124. doi:10.1007/s12274-013-0323-9.
- [123] Yaowen Li, Guiying Xu, Chaohua Cui, and Yongfang Li. Flexible and Semitransparent Organic Solar Cells. *Advanced Energy Materials*, 8(7):1701791, 2018. ISSN 16146832. doi:10.1002/aenm.201701791.
- [124] Sanggil Nam, Myungkwan Song, Dong-Ho Kim, Byungjin Cho, Hye Moon Lee, Jung-Dae Kwon, Sung-Gyu Park, Kee-Seok Nam, Yongsoo Jeong, Se-Hun Kwon, Yun Chang Park, Sung-Ho Jin, Jae-Wook Kang, Sungjin Jo, and Chang Su Kim. Ultrasoother, extremely deformable and shape recoverable Ag nanowire embedded transparent electrode. *Scientific reports*, 4:4788, 2014. doi:10.1038/srep04788.
- [125] Youngwoo Lee, Won-Yong Jin, Kuk Young Cho, Jae-Wook Kang, and Jihoon Kim. Thermal pressing of a metal-grid transparent electrode into a plastic substrate for flexible electronic devices. *Journal of Materials Chemistry C*, 4(32):7577–7583, 2016. ISSN 2050-7526. doi:10.1039/C6TC01234E.
- [126] Jatin J. Patil, Woo Hyun Chae, Adam Trebach, Ki-Jana Carter, Eric Lee, Thomas Sannicolo, and Jeffrey C. Grossman. Failing Forward: Stability of Transparent Electrodes Based on Metal Nanowire Networks. *Advanced materials*, 33(5):2004356, 2021. doi:10.1002/adma.202004356.
- [127] D. P. Langley, M. Lagrange, G. Giusti, C. Jiménez, Y. Bréchet, N. D. Nguyen, and D. Bellet. Metallic nanowire networks: effects of

- thermal annealing on electrical resistance. *Nanoscale*, 6(22):13535–13543, 2014. doi:10.1039/c4nr04151h.
- [128] Cemal Basaran and Minghui Lin. Damage mechanics of electromigration induced failure. *Mechanics of Materials*, 40(1-2):66–79, 2008. ISSN 01676636. doi:10.1016/j.mechmat.2007.06.006.
- [129] Zeping Li, Geng Wang, Zhongming Li, Zhengze Cheng, Guopeng Zhou, and Shan Li. Flexible Transparent Electrodes Based on Gold Nanomeshes. *Nanoscale research letters*, 14(1):132, 2019. ISSN 1931-7573. doi:10.1186/s11671-019-2973-3.
- [130] Chiao-Chi Lin, Dong-Xuan Lin, and Shih-He Lin. Degradation problem in silver nanowire transparent electrodes caused by ultraviolet exposure. *Nanotechnology*, 31(21):215705, 2020. doi:10.1088/1361-6528/ab724f.
- [131] Liang Xu, Yuan Yang, Zeng-Wen Hu, and Shu-Hong Yu. Comparison Study on the Stability of Copper Nanowires and Their Oxidation Kinetics in Gas and Liquid. *ACS nano*, 10(3):3823–3834, 2016. doi:10.1021/acsnano.6b00704.
- [132] Vicki J. Keast. Corrosion processes of silver nanoparticles. *Applied Nanoscience*, 12(6):1859–1868, 2022. ISSN 2190-5509. doi:10.1007/s13204-022-02462-1.
- [133] Michael B. McNeil and Brenda J. Little. Corrosion Mechanisms for Copper and Silver Objects in Near-Surface Environments. *Journal of the American Institute for Conservation*, 31(3):355, 1992. ISSN 01971360. doi:10.2307/3179729.
- [134] Michel Dubus, Milan Kouril, Thi-Phuong Nguyen, Tomas Prosek, Mandana Saheb, and Jim Tate. Monitoring Copper and Silver Corrosion in Different Museum Environments by Electrical Resistance Measurement. *Studies in Conservation*, 55(2):121–133, 2010. ISSN 0039-3630. doi:10.1179/sic.2010.55.2.121.
- [135] Vicki J. Keast. Atmospheric Corrosion of Silver and Silver Nanoparticles. *Corrosion and Materials Degradation*, 3(2):221–234, 2022. doi:10.3390/cmd3020013.

- [136] Jinting Jiu, Jun Wang, Tohru Sugahara, Shijio Nagao, Masaya Nogi, Hirotaka Koga, Katsuaki Sukanuma, Masanao Hara, Eri Nakazawa, and Hiroshi Uchida. The effect of light and humidity on the stability of silver nanowire transparent electrodes. *RSC Advances*, 5(35):27657–27664, 2015. doi:10.1039/C5RA02722E.
- [137] Helmut Goesmann and Claus Feldmann. Nanoparticulate functional materials. *Angewandte Chemie (International ed. in English)*, 49(8):1362–1395, 2010. doi:10.1002/anie.200903053.
- [138] Ph. Buffat and J-P. Borel. Size effect on the melting temperature of gold particles. *Physical Review A*, 13(6):2287–2298, 1976. ISSN 0556-2791. doi:10.1103/PhysRevA.13.2287.
- [139] Jose Luis Elechiguerra, Leticia Larios-Lopez, Cui Liu, Domingo Garcia-Gutierrez, Alejandra Camacho-Bragado, and Miguel Jose Yacaman. Corrosion at the Nanoscale: The Case of Silver Nanowires and Nanoparticles. *Chemistry of Materials*, 17(24):6042–6052, 2005. ISSN 0897-4756. doi:10.1021/cm051532n.
- [140] M. Reid, J. Punch, C. Ryan, J. Franey, G. E. Derkits, W. D. Reents, and L. F. Garfias. The Corrosion of Electronic Resistors. *IEEE Transactions on Components and Packaging Technologies*, 30(4):666–672, 2007. ISSN 1521-3331. doi:10.1109/TCAPT.2007.901749.
- [141] Céline Mayousse, Caroline Celle, Alexandra Fraczkiewicz, and Jean-Pierre Simonato. Stability of silver nanowire based electrodes under environmental and electrical stresses. *Nanoscale*, 7(5):2107–2115, 2015. doi:10.1039/c4nr06783e.
- [142] Bruno F. E. Matarèse, Paul L. C. Feyen, Aniello Falco, Fabio Benfenati, Paolo Lugli, and John C. deMello. Use of SU8 as a stable and biocompatible adhesion layer for gold bioelectrodes. *Scientific reports*, 8(1):5560, 2018. doi:10.1038/s41598-018-21755-6.
- [143] M.-G. Kang and L. J. Guo. Nanoimprinted Semitransparent Metal Electrodes and Their Application in Organic Light-Emitting Diodes. *Advanced Materials*, 19(10):1391–1396, 2007. ISSN 0935-9648. doi:10.1002/adma.200700134.

- [144] Myung-Gyu Kang, Myung-Su Kim, Jinsang Kim, and L. Jay Guo. Organic Solar Cells Using Nanoimprinted Transparent Metal Electrodes. *Advanced Materials*, 20(23):4408–4413, 2008. ISSN 0935-9648. doi:10.1002/adma.200800750.
- [145] N. D. Lang and W. Kohn. Theory of Metal Surfaces: Work Function. *Physical Review B*, 3(4):1215–1223, 1971. ISSN 1098-0121. doi:10.1103/PhysRevB.3.1215.
- [146] Kristiaan Neyts, Alfonso Real, Matthias Marescaux, Saso Mladenovski, and Jeroen Beeckman. Conductor grid optimization for luminance loss reduction in organic light emitting diodes. *Journal of Applied Physics*, 103(9):093113, 2008. ISSN 0021-8979. doi:10.1063/1.2907960.
- [147] Jorik van de Groep, Pierpaolo Spinelli, and Albert Polman. Transparent conducting silver nanowire networks. *Nano letters*, 12(6):3138–3144, 2012. doi:10.1021/nl301045a.
- [148] Ping Kuang, Joong-Mok Park, Wai Leung, Rakesh C. Mahadevaram, Kanwar S. Nalwa, Tae-Geun Kim, Sumit Chaudhary, Kai-Ming Ho, and Kristen Constant. A new architecture for transparent electrodes: relieving the trade-off between electrical conductivity and optical transmittance. *Advanced materials*, 23(21):2469–2473, 2011. doi:10.1002/adma.201100419.
- [149] Sungwoo Jang, Woo-Bin Jung, Cheolgyu Kim, Phillip Won, Sang-Gil Lee, Kyeong Min Cho, Ming Liang Jin, Cheng Jin An, Hwan-Jin Jeon, Seung Hwan Ko, Taek-Soo Kim, and Hee-Tae Jung. A three-dimensional metal grid mesh as a practical alternative to ITO. *Nanoscale*, 8(29):14257–14263, 2016. doi:10.1039/c6nr03060b.
- [150] Salman A. Abbasi, Zhimin Chai, and Ahmed Busnaina. Scalable Printing of High-Resolution Flexible Transparent Grid Electrodes Using Directed Assembly of Silver Nanoparticles. *Advanced Materials Interfaces*, 6(21):1900898, 2019. ISSN 2196-7350. doi:10.1002/admi.201900898.
- [151] Gregory Burwell, Nicholas Burrridge, Eloise Bond, Wei Li, Paul Meredith, and Ardalan Armin. Parameterization of Metallic Grids

- on Transparent Conductive Electrodes for the Scaling of Organic Solar Cells. *Advanced Electronic Materials*, 7(6):2100192, 2021. ISSN 2199-160X. doi:10.1002/aelm.202100192.
- [152] Stephen Y. Chou, Peter R. Krauss, and Preston J. Renstrom. Imprint of sub-25 nm vias and trenches in polymers. *Applied Physics Letters*, 67(21):3114–3116, 1995. ISSN 0003-6951. doi:10.1063/1.114851.
- [153] Stephen Y. Chou, Peter R. Krauss, and Preston J. Renstrom. Imprint Lithography with 25-Nanometer Resolution. *Science*, 272(5258):85–87, 1996. ISSN 0036-8075. doi:10.1126/science.272.5258.85.
- [154] Stephen Y. Chou. Nanoimprint lithography. *Journal of Vacuum Science & Technology B: Microelectronics and Nanometer Structures*, 14(6):4129, 1996. ISSN 0734211X. doi:10.1116/1.588605.
- [155] Helmut Schiff. Nanoimprint lithography: An old story in modern times? A review. *Journal of Vacuum Science & Technology B: Microelectronics and Nanometer Structures*, 26(2):458, 2008. ISSN 0734211X. doi:10.1116/1.2890972.
- [156] Dongxu Wu, Nitul S. Rajput, and Xichun Luo. Nanoimprint Lithography - the Past, the Present and the Future. *Current Nanoscience*, 12(6):712–724, 2016. ISSN 15734137. doi:10.2174/1573413712666160530120432.
- [157] Clivia M. Sotomayor Torres, editor. *Alternative Lithography: Unleashing the Potentials of Nanotechnology*. Nanostructure Science and Technology. Springer, New York, 2003. ISBN 978-1-4613-4836-8. doi:10.1007/978-1-4419-9204-8.
- [158] L. J. Guo. Nanoimprint Lithography: Methods and Material Requirements. *Advanced Materials*, 19(4):495–513, 2007. ISSN 0935-9648. doi:10.1002/adma.200600882.
- [159] L. Jay Guo. Recent progress in nanoimprint technology and its applications. *Journal of Physics D: Applied Physics*, 37(11):R123–R141, 2004. ISSN 0022-3727. doi:10.1088/0022-3727/37/11/R01.

- [160] Bharat Bhushan, editor. *Springer Handbook of Nanotechnology*. Springer Handbooks. Springer, Berlin, 4th edition, 2017. ISBN 978-3-662-54355-9. doi:10.1007/978-3-662-54357-3.
- [161] Linfa Peng, Yujun Deng, Peiyun Yi, and Xinmin Lai. Micro hot embossing of thermoplastic polymers: a review. *Journal of Micromechanics and Microengineering*, 24(1):013001, 2014. ISSN 0960-1317. doi:10.1088/0960-1317/24/1/013001.
- [162] Se Hyun Ahn and L. Jay Guo. Large-area roll-to-roll and roll-to-plate nanoimprint lithography: a step toward high-throughput application of continuous nanoimprinting. *ACS nano*, 3(8):2304–2310, 2009. doi:10.1021/nn9003633.
- [163] Se Hyun Ahn and L. Jay Guo. High-Speed Roll-to-Roll Nanoimprint Lithography on Flexible Plastic Substrates. *Advanced Materials*, 20(11):2044–2049, 2008. ISSN 0935-9648. doi:10.1002/adma.200702650.
- [164] Elizabeth A. Costner, Michael W. Lin, Wei-Lun Jen, and C. Grant Willson. Nanoimprint Lithography Materials Development for Semiconductor Device Fabrication. *Annual Review of Materials Research*, 39(1):155–180, 2009. ISSN 1531-7331. doi:10.1146/annurev-matsci-082908-145336.
- [165] John A. Rogers and Hong H. Lee. *Unconventional Nanopatterning Techniques and Applications*. Wiley, Hoboken, N.J, 2008. ISBN 9780470099575. doi:10.1002/9780470405789.
- [166] Weimin Zhou. *Nanoimprint lithography: An enabling process for nanofabrication*. Springer, Berlin and Heidelberg, 2013. ISBN 978-3-642-34427-5. doi:10.1007/978-3-642-34428-2.
- [167] Huseyin Yildirim and Haydar Arslan. Size and composition effect on structural properties and melting behaviors of Cu–Ag–Au ternary nanoalloys. *International Journal of Modern Physics C*, 31(06):2050078, 2020. ISSN 0129-1831. doi:10.1142/S0129183120500783.
- [168] Ying Zhang, Jianming Zhang, Yonglai Lu, Yongxin Duan, Shouke Yan, and Deyan Shen. Glass Transition Temperature De-

- termination of Poly(ethylene terephthalate) Thin Films Using Reflection–Absorption FTIR. *Macromolecules*, 37(7):2532–2537, 2004. ISSN 0024-9297. doi:10.1021/ma035709f.
- [169] Adones Sales, Lorena de Oliveira Felipe, and Juliano Lemos Bicas. Production, Properties, and Applications of α -Terpineol. *Food and Bioprocess Technology*, 13(8):1261–1279, 2020. ISSN 1935-5130. doi:10.1007/s11947-020-02461-6.
- [170] Paul E. Gagnon, Jean L. Boivin, and Donald C. Watson. Thermal Decomposition of 1-Hexanethiol. *Canadian Journal of Chemistry*, 37(11):1846–1850, 1959. ISSN 0008-4042. doi:10.1139/v59-271.
- [171] Younan Xia and George M. Whitesides. Soft Lithography. *Annual Review of Materials Science*, 28(1):153–184, 1998. ISSN 0084-6600. doi:10.1146/annurev.matsci.28.1.153.
- [172] Pei Bian, Yan Wang, and Thomas J. McCarthy. Rediscovering Silicones: The Anomalous Water Permeability of "Hydrophobic" PDMS Suggests Nanostructure and Applications in Water Purification and Anti-Icing. *Macromolecular rapid communications*, 42(5):2000682, 2021. doi:10.1002/marc.202000682.
- [173] Greg C. Randall and Patrick S. Doyle. Permeation-driven flow in poly(dimethylsiloxane) microfluidic devices. *Proceedings of the National Academy of Sciences of the United States of America*, 102(31):10813–10818, 2005. ISSN 0027-8424. doi:10.1073/pnas.0503287102.
- [174] Jessamine Ng Lee, Cheolmin Park, and George M. Whitesides. Solvent compatibility of poly(dimethylsiloxane)-based microfluidic devices. *Analytical chemistry*, 75(23):6544–6554, 2003. ISSN 0003-2700. doi:10.1021/ac0346712.
- [175] A. Lamberti, S. L. Marasso, and M. Cocuzza. PDMS membranes with tunable gas permeability for microfluidic applications. *RSC Adv*, 4(106):61415–61419, 2014. doi:10.1039/C4RA12934B.
- [176] Enoch King, Younan Xia, Xiao-Mei Zhao, and George M. Whitesides. Solvent-assisted microcontact molding: A convenient

- method for fabricating three-dimensional structures on surfaces of polymers. *Advanced Materials*, 9(8):651–654, 1997. ISSN 0935-9648. doi:10.1002/adma.19970090814.
- [177] Inkyu Park, Seung H. Ko, Heng Pan, Albert P. Pisano, and Costas P. Grigoropoulos. Micro/Nanoscale Structure Fabrication by Direct Nanoimprinting of Metallic and Semiconducting Nanoparticles. In ASME, editor, *Micro and Nano Systems, Parts A and B*, volume 11 of *Proceedings of the ASME International Mechanical Engineering Congress and Exposition - 2007*, pages 307–314, New York, NY, 2008. ASME. ISBN 0-7918-4305-X. doi:10.1115/IMECE2007-43878.
- [178] Seung H. Ko, Yeonho Choi, David J. Hwang, Costas P. Grigoropoulos, Jaewon Chung, and Dimos Poulikakos. Nanosecond laser ablation of gold nanoparticle films. *Applied Physics Letters*, 89(14):141126, 2006. ISSN 0003-6951. doi:10.1063/1.2360241.
- [179] T. E. Vittal Prasad, B. Reddi Prasad Naidu, D. Madhukiran, and D. H. L. Prasad. Boiling Temperature Measurements on the Binary Mixtures of Cyclohexane with Some Alcohols and Chlorohydrocarbons. *Journal of Chemical & Engineering Data*, 46(2):414–416, 2001. ISSN 0021-9568. doi:10.1021/je000139p.
- [180] U. Tariq, A. R. B. Jusoh, N. Riesco, and V. Vesovic. Reference Correlation of the Viscosity of Cyclohexane from the Triple Point to 700 K and up to 110 MPa. *Journal of Physical and Chemical Reference Data*, 43(3):033101, 2014. ISSN 0047-2689. doi:10.1063/1.4891103.
- [181] Bénédicte Lepoittevin and Philippe Roger. Poly(ethylene terephthalate). In Sabu Thomas and Visakh P.M., editors, *Handbook of Engineering and Speciality Thermoplastics*, volume 3, pages 97–126. Wiley and Scrivener, Hoboken, N.J and Salem, Mass, 2011. ISBN 9780470639269. doi:10.1002/9781118104729.ch4.
- [182] Susanna Andreasi Bassi, Davide Tonini, Hans Saveyn, and Thomas Fruergaard Astrup. Environmental and Socioeconomic Impacts of Poly(ethylene terephthalate) (PET) Packaging Manage-

- ment Strategies in the EU. *Environmental science & technology*, 56(1):501–511, 2022. doi:10.1021/acs.est.1c00761.
- [183] Utkarsh S. Chaudhari, Yingqian Lin, Vicki S. Thompson, Robert M. Handler, Joshua M. Pearce, Gerard Caneba, Prapti Muhuri, David Watkins, and David R. Shonnard. Systems Analysis Approach to Polyethylene Terephthalate and Olefin Plastics Supply Chains in the Circular Economy: A Review of Data Sets and Models. *ACS Sustainable Chemistry & Engineering*, 9(22):7403–7421, 2021. ISSN 2168-0485. doi:10.1021/acssuschemeng.0c08622.
- [184] Huajun Feng, Yanmei Yang, Yumeng You, Gongping Li, Jun Guo, Ting Yu, Zexiang Shen, Tom Wu, and Bengang Xing. Simple and rapid synthesis of ultrathin gold nanowires, their self-assembly and application in surface-enhanced Raman scattering. *Chemical Communications*, (15):1984–1986, 2009. doi:10.1039/b822507a.
- [185] George M. Whitesides and Bartosz Grzybowski. Self-assembly at all scales. *Science*, 295(5564):2418–2421, 2002. ISSN 0036-8075. doi:10.1126/science.1070821.
- [186] Michael A. Boles, Michael Engel, and Dmitri V. Talapin. Self-Assembly of Colloidal Nanocrystals: From Intricate Structures to Functional Materials. *Chemical reviews*, 116(18):11220–11289, 2016. doi:10.1021/acs.chemrev.6b00196.
- [187] Juan Carlos Moreno-Piraján, editor. *Thermodynamics: Systems in Equilibrium and Non-Equilibrium*. IntechOpen, 2011. ISBN 9789533072838.
- [188] Samer Bayda, Muhammad Adeel, Tiziano Tuccinardi, Marco Cordani, and Flavio Rizzolio. The History of Nanoscience and Nanotechnology: From Chemical-Physical Applications to Nanomedicine. *Molecules*, 25(1):112, 2020. doi:10.3390/molecules25010112.
- [189] Hoa T. Phan and Amanda J. Haes. What Does Nanoparticle Stability Mean? *The Journal of Physical Chemistry C*, 123(27):16495–16507, 2019. ISSN 1932-7447. doi:10.1021/acs.jpcc.9b00913.

- [190] Jitendra N. Tiwari, Rajanish N. Tiwari, and Kwang S. Kim. Zero-dimensional, one-dimensional, two-dimensional and three-dimensional nanostructured materials for advanced electrochemical energy devices. *Progress in Materials Science*, 57(4):724–803, 2012. ISSN 00796425. doi:10.1016/j.pmatsci.2011.08.003.
- [191] Sundus Jabeen Amina and Bin Guo. A Review on the Synthesis and Functionalization of Gold Nanoparticles as a Drug Delivery Vehicle. *International journal of nanomedicine*, 15:9823–9857, 2020. doi:10.2147/IJN.S279094.
- [192] Pengxiang Zhao, Na Li, and Didier Astruc. State of the art in gold nanoparticle synthesis. *Coordination Chemistry Reviews*, 257(3-4): 638–665, 2013. ISSN 00108545. doi:10.1016/j.ccr.2012.09.002.
- [193] R. Nagarajan. Nanoparticles: Building Blocks for Nanotechnology. In R. Nagarajan and T. Alan Hatton, editors, *Nanoparticles: Synthesis, Stabilization, Passivation, and Functionalization*, volume 996 of *ACS Symposium Series*, pages 2–14, Washington, DC, 2008. American Chemical Soc. ISBN 9780841269699. doi:10.1021/bk-2008-0996.ch001.
- [194] Mohammed Ali Dheyab, Azlan Abdul Aziz, Pegah Moradi Khaniabadi, Mahmood S. Jameel, Nazila Oladzadabbasabadi, Selwan Abduljabbar Mohammed, Raja Saleh Abdullah, and Baharak Mehrdel. Monodisperse Gold Nanoparticles: A Review on Synthesis and Their Application in Modern Medicine. *International journal of molecular sciences*, 23(13):7400, 2022. doi:10.3390/ijms23137400.
- [195] Dmitri V. Talapin and Elena V. Shevchenko. Introduction: Nanoparticle Chemistry. *Chemical reviews*, 116(18):10343–10345, 2016. doi:10.1021/acs.chemrev.6b00566.
- [196] Xi Chen, Dongyun Zhao, Yingli An, Yan Zhang, Jing Cheng, Beilei Wang, and Linqi Shi. Formation and catalytic activity of spherical composites with surfaces coated with gold nanoparticles. *Journal of colloid and interface science*, 322(2):414–420, 2008. doi:10.1016/j.jcis.2008.03.029.

- [197] Carla Daruich De Souza, Beatriz Ribeiro Nogueira, and Maria Elisa C.M. Rostelato. Review of the methodologies used in the synthesis gold nanoparticles by chemical reduction. *Journal of Alloys and Compounds*, 798:714–740, 2019. ISSN 09258388. doi:10.1016/j.jallcom.2019.05.153.
- [198] Prerna Sharma. Self-Assembly of Colloidal Particles. *Resonance*, 23(3):263–275, 2018. ISSN 0971-8044. doi:10.1007/s12045-018-0616-0.
- [199] Sakineh Alizadeh and Zahra Nazari. A Review on Gold Nanoparticles Aggregation and Its Applications. *Journal of Chemical Reviews*, pages 228–242, 2020. doi:10.22034/jcr.2020.108561.
- [200] Luis M. Liz-Marzán. Nanometals: formation and color. *Materials Today*, 7(2):26–31, 2004. ISSN 13697021. doi:10.1016/S1369-7021(04)00080-X.
- [201] M. P. Neupane, S. J. Lee, I. S. Park, M. H. Lee, T. S. Bae, Y. Kuboki, M. Uo, and F. Watari. Synthesis of gelatin-capped gold nanoparticles with variable gelatin concentration. *Journal of Nanoparticle Research*, 13(2):491–498, 2011. ISSN 1388-0764. doi:10.1007/s11051-010-9971-9.
- [202] M. Aslam, Lei Fu, Ming Su, K. Vijayamohanan, and Vinayak P. Dravid. Novel one-step synthesis of amine-stabilized aqueous colloidal gold nanoparticles. *Journal of Materials Chemistry*, 14(12):1795, 2004. ISSN 0959-9428. doi:10.1039/b402823f.
- [203] P. Forrer, F. Schlottig, H. Siegenthaler, and M. Textor. Electrochemical preparation and surface properties of gold nanowire arrays formed by the template technique. *Journal of Applied Electrochemistry*, 30(5):533–541, 2000. ISSN 0021891X. doi:10.1023/A:1003941129560.
- [204] Kangze Liu, Zhonglei He, James F. Curtin, Hugh J. Byrne, and Furong Tian. A novel, rapid, seedless, in situ synthesis method of shape and size controllable gold nanoparticles using phosphates. *Scientific reports*, 9(1):7421, 2019. doi:10.1038/s41598-019-43921-0.

- [205] Bing-Hui Wu, Hua-Yan Yang, Hua-Qi Huang, Guang-Xu Chen, and Nan-Feng Zheng. Solvent effect on the synthesis of monodisperse amine-capped Au nanoparticles. *Chinese Chemical Letters*, 24(6): 457–462, 2013. ISSN 10018417. doi:10.1016/j.cclet.2013.03.054.
- [206] El Said A. Nouh, Edwin A. Baquero, Lise-Marie Lacroix, Fabien Delpech, Romuald Poteau, and Guillaume Viau. Surface-Engineering of Ultrathin Gold Nanowires: Tailored Self-Assembly and Enhanced Stability. *Langmuir*, 33(22):5456–5463, 2017. doi:10.1021/acs.langmuir.7b00477.
- [207] Lihua Pei, Koichi Mori, and Motonari Adachi. Formation process of two-dimensional networked gold nanowires by citrate reduction of AuCl₄⁻ and the shape stabilization. *Langmuir*, 20(18):7837–7843, 2004. doi:10.1021/la049262v.
- [208] Xiaogang Liu, Nianqiang Wu, Benjamin H. Wunsch, Robert J. Barsotti, and Francesco Stellacci. Shape-controlled growth of micrometer-sized gold crystals by a slow reduction method. *Small*, 2(8-9):1046–1050, 2006. doi:10.1002/smll.200600219.
- [209] Franklin Kim, Kwonnam Sohn, Jinsong Wu, and Jiaying Huang. Chemical synthesis of gold nanowires in acidic solutions. *Journal of the American Chemical Society*, 130(44):14442–14443, 2008. ISSN 0002-7863. doi:10.1021/ja806759v.
- [210] Li Wang, Yonghai Song, Lanlan Sun, Cunlan Guo, Yujing Sun, and Zhuang Li. Controllable synthesis of gold nanowires. *Materials Letters*, 62(25):4124–4126, 2008. ISSN 0167577X. doi:10.1016/j.matlet.2008.06.014.
- [211] Chao Wang, Yongjie Hu, Charles M. Lieber, and Shouheng Sun. Ultrathin Au nanowires and their transport properties. *Journal of the American Chemical Society*, 130(28):8902–8903, 2008. ISSN 0002-7863. doi:10.1021/ja803408f.
- [212] Chao Wang and Shouheng Sun. Facile synthesis of ultrathin and single-crystalline Au nanowires. *Chemistry, an Asian journal*, 4(7): 1028–1034, 2009. doi:10.1002/asia.200900002.

- [213] Hanying Bai, Ke Xu, Yujia Xu, and Hiroshi Matsui. Fabrication of Au nanowires of uniform length and diameter using a monodisperse and rigid biomolecular template: collagen-like triple helix. *Angewandte Chemie (International ed. in English)*, 46(18):3319–3322, 2007. doi:10.1002/anie.200605213.
- [214] Zhaoxuan Wu, Yong-Wei Zhang, Mark H. Jhon, Huajian Gao, and David J. Srolovitz. Nanowire failure: long = brittle and short = ductile. *Nano letters*, 12(2):910–914, 2012. doi:10.1021/nl203980u.
- [215] Chaolun Ni, Qi Zhu, and Jiangwei Wang. Mechanical property of metallic nanowires: the shorter is stronger and ductile. *Materials Science and Engineering: A*, 733:164–169, 2018. ISSN 09215093. doi:10.1016/j.msea.2018.07.054.
- [216] Johannes H. M. Maurer. *Ultrathin gold nanowires for transparent electronics*. Dissertation (Doktorarbeit), Universität des Saarlandes, Saarbrücken, 2017.
- [217] Xianmao Lu, Mustafa S. Yavuz, Hsing-Yu Tuan, Brian A. Korgel, and Younan Xia. Ultrathin gold nanowires can be obtained by reducing polymeric strands of oleylamine-AuCl complexes formed via aurophilic interaction. *Journal of the American Chemical Society*, 130(28):8900–8901, 2008. ISSN 0002-7863. doi:10.1021/ja803343m.
- [218] A. Halder and N. Ravishankar. Ultrafine Single-Crystalline Gold Nanowire Arrays by Oriented Attachment. *Advanced Materials*, 19(14):1854–1858, 2007. ISSN 0935-9648. doi:10.1002/adma.200602325.
- [219] Nicolás Pazos-Pérez, Dmitry Baranov, Stephan Irsen, Michael Hildendorff, Luis M. Liz-Marzán, and Michael Giersig. Synthesis of flexible, ultrathin gold nanowires in organic media. *Langmuir*, 24(17):9855–9860, 2008. doi:10.1021/la801675d.
- [220] Ziyang Huo, Chia-Kuang Tsung, Wenyu Huang, Xiaofeng Zhang, and Peidong Yang. Sub-two nanometer single crystal Au nanowires. *Nano letters*, 8(7):2041–2044, 2008. doi:10.1021/nl8013549.

- [221] Indra Backes. *Large-area nanoimprint of ultrathin gold nanowires: ink-stamp interplay*. Master thesis, Universität des Saarlandes, Saarbrücken, 2016.
- [222] Anaïs Loubat, Marianne Impéror-Clerc, Brigitte Pansu, Florian Meneau, Bertrand Raquet, Guillaume Viau, and Lise-Marie Lacroix. Growth and self-assembly of ultrathin Au nanowires into expanded hexagonal superlattice studied by in situ SAXS. *Langmuir*, 30(14):4005–4012, 2014. doi:10.1021/la500549z.
- [223] Fernando Pschunder, Julieta Puig, Lisandro J. Giovanetti, Cristián Huck-Iriart, Félix G. Requejo, David Buceta, Cristina E. Hoppe, and José M. Ramallo-López. New Insights into the Growth Mechanism of Ultrathin Au Nanowires from Combined in Situ EXAFS and SAXS Studies. *The Journal of Physical Chemistry C*, 122(50):29051–29061, 2018. ISSN 1932-7447. doi:10.1021/acs.jpcc.8b10449.
- [224] Yi Yu, Fan Cui, Jianwei Sun, and Peidong Yang. Atomic Structure of Ultrathin Gold Nanowires. *Nano letters*, 16(5):3078–3084, 2016. doi:10.1021/acs.nanolett.6b00233.
- [225] Anaïs Loubat, Lise-Marie Lacroix, Antoine Robert, Marianne Impéror-Clerc, Romuald Poteau, Laurent Maron, Raul Arenal, Brigitte Pansu, and Guillaume Viau. Ultrathin Gold Nanowires: Soft-Templating versus Liquid Phase Synthesis, a Quantitative Study. *The Journal of Physical Chemistry C*, 119(8):4422–4430, 2015. ISSN 1932-7447. doi:10.1021/acs.jpcc.5b00242.
- [226] Ryo Takahata and Tatsuya Tsukuda. Ultrathin Gold Nanowires and Nanorods. *Chemistry Letters*, 48(8):906–915, 2019. ISSN 0366-7022. doi:10.1246/cl.190313.
- [227] Stefanos Mourdikoudis and Luis M. Liz-Marzán. Oleylamine in Nanoparticle Synthesis. *Chemistry of Materials*, 25(9):1465–1476, 2013. ISSN 0897-4756. doi:10.1021/cm4000476.
- [228] Johannes H. M. Maurer, Lola Gonzalez-Garcia, Beate Reiser, Ioannis Kanelidis, and Tobias Kraus. Ultrathin gold nanowires for transparent electronics: Soft sintering and temperature stability: Soft

- sintering and temperature stability. *Phys. Status Solidi A*, 213(9): 2336–2340, 2016. doi:10.1002/pssa.201532874.
- [229] Yi Chen, Zi Ouyang, Min Gu, and Wenlong Cheng. Mechanically strong, optically transparent, giant metal superlattice nanomembranes from ultrathin gold nanowires. *Advanced materials*, 25(1): 80–85, 2013. doi:10.1002/adma.201202241.
- [230] Ahin Roy, Tribhuvan Pandey, N. Ravishankar, and Abhishek K. Singh. Single crystalline ultrathin gold nanowires: Promising nanoscale interconnects. *AIP Advances*, 3(3):032131, 2013. doi:10.1063/1.4796188.
- [231] Rose M. Mutiso, Michelle C. Sherrott, Aaron R. Rathmell, Benjamin J. Wiley, and Karen I. Winey. Integrating simulations and experiments to predict sheet resistance and optical transmittance in nanowire films for transparent conductors. *ACS nano*, 7(9): 7654–7663, 2013. doi:10.1021/nm403324t.
- [232] Kevin Critchley, Bishnu P. Khanal, Marcin Ł. Górzny, Leonid Vighderman, Stephen D. Evans, Eugene R. Zubarev, and Nicholas A. Kotov. Near-bulk conductivity of gold nanowires as nanoscale interconnects and the role of atomically smooth interface. *Advanced materials*, 22(21):2338–2342, 2010. doi:10.1002/adma.201000236.
- [233] Yang Lu, Jian Yu Huang, Chao Wang, Shouheng Sun, and Jun Lou. Cold welding of ultrathin gold nanowires. *Nature nanotechnology*, 5(3):218–224, 2010. doi:10.1038/nnano.2010.4.
- [234] Bin Wu, Andreas Heidelberg, and John J. Boland. Mechanical properties of ultrahigh-strength gold nanowires. *Nature materials*, 4(7):525–529, 2005. ISSN 1476-1122. doi:10.1038/nmat1403.
- [235] My Duyen Ho, Yunzhi Ling, Lim Wei Yap, Yan Wang, Dashen Dong, Yunmeng Zhao, and Wenlong Cheng. Percolating Network of Ultrathin Gold Nanowires and Silver Nanowires toward “Invisible” Wearable Sensors for Detecting Emotional Expression and Apexcardiogram. *Advanced Functional Materials*, 27(25):1700845, 2017. doi:10.1002/adfm.201700845.

-
- [236] Hongyu Gao, Simon Bettscheider, Tobias Kraus, and Martin H. Müser. Entropy Can Bundle Nanowires in Good Solvents. *Nano letters*, 19(10):6993–6999, 2019. doi:10.1021/acs.nanolett.9b02379.
- [237] João Borges, José A. Ribeiro, Elisa M. Pereira, Cátia A. Carreira, Carlos M. Pereira, and Fernando Silva. Preparation and characterization of DNA films using oleylamine modified Au surfaces. *Journal of colloid and interface science*, 358(2):626–634, 2011. doi:10.1016/j.jcis.2011.03.039.
- [238] Pierre Moutet, Lise-Marie Lacroix, Antoine Robert, Marianne Impéror-Clerc, Guillaume Viau, and Laurence Ressler. Directed assembly of single colloidal gold nanowires by AFM nanoxerography. *Langmuir*, 31(14):4106–4112, 2015. doi:10.1021/acs.langmuir.5b00299.
- [239] Beate Reiser, Dominik Gerstner, Lola González-García, Johannes H. M. Maurer, Ioannis Kanelidis, and Tobias Kraus. Spinning Hierarchical Gold Nanowire Microfibers by Shear Alignment and Intermolecular Self-Assembly. *ACS nano*, 11(5):4934–4942, 2017. doi:10.1021/acsnano.7b01551.
- [240] Beate Reiser. *Tailored ligands for hybrid materials from colloidal inks*. Dissertation (Doktorarbeit), Universität des Saarlandes, Saarbrücken, 2018.
- [241] Brian A. Korgel and Donald Fitzmaurice. Condensation of Ordered Nanocrystal Thin Films. *Physical Review Letters*, 80(16):3531–3534, 1998. ISSN 0031-9007. doi:10.1103/PhysRevLett.80.3531.
- [242] Debora Monego, Thomas Kister, Nicholas Kirkwood, David Dolbas, Paul Mulvaney, Tobias Kraus, and Asaph Widmer-Cooper. When Like Destabilizes Like: Inverted Solvent Effects in Apolar Nanoparticle Dispersions. *ACS nano*, 14(5):5278–5287, 2020. doi:10.1021/acsnano.9b03552.
- [243] Ana Sánchez-Iglesias, Marek Grzelczak, Jorge Pérez-Juste, and Luis M. Liz-Marzán. Binary self-assembly of gold nanowires with nanospheres and nanorods. *Angewandte Chemie (International ed. in English)*, 49(51):9985–9989, 2010. doi:10.1002/anie.201005891.

- [244] Nanfeng Zheng, Jie Fan, and Galen D. Stucky. One-step one-phase synthesis of monodisperse noble-metallic nanoparticles and their colloidal crystals. *Journal of the American Chemical Society*, 128(20):6550–6551, 2006. ISSN 0002-7863. doi:10.1021/ja0604717.
- [245] Derk P. Kooi and Paola Gori-Giorgi. A Variational Approach to London Dispersion Interactions without Density Distortion. *The journal of physical chemistry letters*, 10(7):1537–1541, 2019. doi:10.1021/acs.jpcclett.9b00469.
- [246] J. H. Adair, E. Suvaci, and J. Sindel. Surface and Colloid Chemistry. In Kurt H. J. Buschow, editor, *Encyclopedia of materials: science and technology*, pages 8996–9006. Elsevier, Amsterdam, 2001. ISBN 0-08-0431526. doi:10.1016/B0-08-043152-6/01622-3.
- [247] David Doblás, Thomas Kister, Marina Cano-Bonilla, Lola González-García, and Tobias Kraus. Colloidal Solubility and Agglomeration of Apolar Nanoparticles in Different Solvents. *Nano letters*, 19(8):5246–5252, 2019. doi:10.1021/acs.nanolett.9b01688.
- [248] Debora Monego, Thomas Kister, Nicholas Kirkwood, Paul Mulvaney, Asaph Widmer-Cooper, and Tobias Kraus. Colloidal Stability of Apolar Nanoparticles: Role of Ligand Length. *Langmuir*, 34(43):12982–12989, 2018. doi:10.1021/acs.langmuir.8b02883.
- [249] Thomas Kister, Debora Monego, Paul Mulvaney, Asaph Widmer-Cooper, and Tobias Kraus. Colloidal Stability of Apolar Nanoparticles: The Role of Particle Size and Ligand Shell Structure. *ACS nano*, 12(6):5969–5977, 2018. doi:10.1021/acs.nano.8b02202.
- [250] Brandon C. Lohman, Jeffrey A. Powell, Sreeram Cingarapu, Christer B. Aakeroy, Amit Chakrabarti, Kenneth J. Klabunde, Bruce M. Law, and Christopher M. Sorensen. Solubility of gold nanoparticles as a function of ligand shell and alkane solvent. *Physical Chemistry Chemical Physics*, 14(18):6509–6513, 2012. doi:10.1039/c2cp40645d.
- [251] Sebastian Wünscher, Robert Abbel, Jolke Perelaer, and Ulrich S. Schubert. Progress of alternative sintering approaches of inkjet-

- printed metal inks and their application for manufacturing of flexible electronic devices. *J. Mater. Chem. C*, 2(48):10232–10261, 2014. ISSN 2050-7526. doi:10.1039/C4TC01820F.
- [252] Jolke Perelaer, Patrick J. Smith, Dario Mager, Daniel Soltman, Steven K. Volkman, Vivek Subramanian, Jan G. Korvink, and Ulrich S. Schubert. Printed electronics: the challenges involved in printing devices, interconnects, and contacts based on inorganic materials. *Journal of Materials Chemistry*, 20(39):8446, 2010. ISSN 0959-9428. doi:10.1039/c0jm00264j.
- [253] O. Kravchuk, R. Lesyuk, Ya. Bobitski, and M. Reichenberger. Sintering Methods of Inkjet-Printed Silver Nanoparticle Layers. In Olena Fesenko and Leonid Yatsenko, editors, *Nanooptics, Nanophotonics, Nanostructures, and Their Applications*, volume 210 of *Springer Proceedings in Physics*, pages 317–339, Cham, 2018. Springer International Publishing. ISBN 978-3-319-91082-6. doi:10.1007/978-3-319-91083-3_23.
- [254] Bridget Ingham, Teck H. Lim, Christian J. Dotzler, Anna Henning, Michael F. Toney, and Richard D. Tilley. How Nanoparticles Coalesce: An in Situ Study of Au Nanoparticle Aggregation and Grain Growth. *Chemistry of Materials*, 23(14):3312–3317, 2011. ISSN 0897-4756. doi:10.1021/cm200354d.
- [255] Steven K. Volkman, Shong Yin, Teymur Bakhishev, Kanan Puntambekar, Vivek Subramanian, and Michael F. Toney. Mechanistic Studies on Sintering of Silver Nanoparticles. *Chemistry of Materials*, 23(20):4634–4640, 2011. ISSN 0897-4756. doi:10.1021/cm202561u.
- [256] P. Pawlow. Über die Abhängigkeit des Schmelzpunktes von der Oberflächenenergie eines festen Körpers. *Zeitschrift für Physikalische Chemie*, 65U(1):1–35, 1909. ISSN 0942-9352. doi:10.1515/zpch-1909-6502.
- [257] C. L. Cleveland, W. D. Luedtke, and Uzi Landman. Melting of gold clusters. *Physical Review B*, 60(7):5065–5077, 1999. ISSN 1098-0121. doi:10.1103/physrevb.60.5065.

- [258] Daisuke Wakuda, Mariko Hatamura, and Katsuaki Suganuma. Novel method for room temperature sintering of Ag nanoparticle paste in air. *Chemical Physics Letters*, 441(4-6):305–308, 2007. ISSN 00092614. doi:10.1016/j.cplett.2007.05.033.
- [259] Aaron T. Fafarman, Sung-Hoon Hong, Humeyra Caglayan, Xingchen Ye, Benjamin T. Diroll, Taejong Paik, Nader Engheta, Christopher B. Murray, and Cherie R. Kagan. Chemically tailored dielectric-to-metal transition for the design of metamaterials from nanoimprinted colloidal nanocrystals. *Nano letters*, 13(2):350–357, 2013. doi:10.1021/nl303161d.
- [260] Aaron T. Fafarman, Weon-kyu Koh, Benjamin T. Diroll, David K. Kim, Dong-Kyun Ko, Soong Ju Oh, Xingchen Ye, Vicky Doan-Nguyen, Michael R. Crump, Danielle C. Reifsnyder, Christopher B. Murray, and Cherie R. Kagan. Thiocyanate-capped nanocrystal colloids: vibrational reporter of surface chemistry and solution-based route to enhanced coupling in nanocrystal solids. *Journal of the American Chemical Society*, 133(39):15753–15761, 2011. ISSN 0002-7863. doi:10.1021/ja206303g.
- [261] Ximin Cui, Qifeng Ruan, Xiaolu Zhuo, Xinyue Xia, Jingtian Hu, Runfang Fu, Yang Li, Jianfang Wang, and Hongxing Xu. Photothermal Nanomaterials: A Powerful Light-to-Heat Converter. *Chemical reviews*, 123(11):6891–6952, 2023. doi:10.1021/acs.chemrev.3c00159.
- [262] Simone Neermann, Michael Steindl, Joerg Franke, Edgar Mayer, and Michael Schmidt. Qualification of NIR, UV and Laser Irradiation as Alternative Photonic Sintering Methods for Printed Electronics. In *2020 Pan Pacific Microelectronics Symposium (Pan Pacific)*, pages 1–8. IEEE, 2020. ISBN 978-1-944543-14-3. doi:10.23919/PanPacific48324.2020.9059353.
- [263] Luca Bonatti, Gabriel Gil, Tommaso Giovannini, Stefano Corni, and Chiara Cappelli. Plasmonic Resonances of Metal Nanoparticles: Atomistic vs. Continuum Approaches. *Frontiers in chemistry*, 8:340, 2020. ISSN 2296-2646. doi:10.3389/fchem.2020.00340.

- [264] Sebastian Wünscher, Steffi Stumpf, Jolke Perelaer, and Ulrich S. Schubert. Towards single-pass plasma sintering: temperature influence of atmospheric pressure plasma sintering of silver nanoparticle ink. *Journal of Materials Chemistry C*, 2(9):1642, 2014. ISSN 2050-7526. doi:10.1039/c3tc32120g.
- [265] E. Wagenaars. *Plasma breakdown of low-pressure gas discharges*. Dissertation (Proefschrift), Eindhoven University of Technology, Eindhoven, 2006.
- [266] I. Langmuir. Oscillations in Ionized Gases. *Proceedings of the National Academy of Sciences of the United States of America*, 14(8):627–637, 1928. ISSN 0027-8424. doi:10.1073/pnas.14.8.627.
- [267] Daphne Pappas. Status and potential of atmospheric plasma processing of materials. *Journal of Vacuum Science & Technology A: Vacuum, Surfaces, and Films*, 29(2):020801, 2011. ISSN 0734-2101. doi:10.1116/1.3559547.
- [268] Fabiano A. N. Fernandes and Sueli Rodrigues. Cold Plasma Processing on Fruits and Fruit Juices: A Review on the Effects of Plasma on Nutritional Quality. *Processes*, 9(12):2098, 2021. doi:10.3390/pr9122098.
- [269] N. Korner, E. Beck, A. Dommann, N. Onda, and J. Ramm. Hydrogen plasma chemical cleaning of metallic substrates and silicon wafers. *Surface and Coatings Technology*, 76-77:731–737, 1995. ISSN 02578972. doi:10.1016/0257-8972(95)02503-0.
- [270] Sebastian Wünscher, Steffi Stumpf, Anke Teichler, Oliver Pabst, Jolke Perelaer, Erik Beckert, and Ulrich S. Schubert. Localized atmospheric plasma sintering of inkjet printed silver nanoparticles. *Journal of Materials Chemistry*, 22(47):24569, 2012. ISSN 0959-9428. doi:10.1039/c2jm35586h.
- [271] Friedrich Paschen. Ueber die zum Funkenübergang in Luft, Wasserstoff und Kohlensäure bei verschiedenen Drucken erforderliche Potentialdifferenz. *Annalen der Physik*, 273(5):69–96, 1889. ISSN 00033804. doi:10.1002/andp.18892730505.

- [272] Delphine Merche, Nicolas Vandencastele, and François Reniers. Atmospheric plasmas for thin film deposition: A critical review. *Thin Solid Films*, 520(13):4219–4236, 2012. ISSN 00406090. doi:10.1016/j.tsf.2012.01.026.
- [273] P. Fuchs. Low-pressure plasma cleaning of Au and PtIr noble metal surfaces. *Applied Surface Science*, 256(5):1382–1390, 2009. ISSN 01694332. doi:10.1016/j.apsusc.2009.08.093.
- [274] Michael R. Winchester and Richard Payling. Radio-frequency glow discharge spectrometry. *Spectrochimica Acta Part B: Atomic Spectroscopy*, 59(5):607–666, 2004. ISSN 05848547. doi:10.1016/j.sab.2004.02.013.
- [275] Dirk Hegemann, Herwig Brunner, and Christian Oehr. Plasma treatment of polymers for surface and adhesion improvement. *Nuclear Instruments and Methods in Physics Research Section B: Beam Interactions with Materials and Atoms*, 208:281–286, 2003. ISSN 0168583X. doi:10.1016/S0168-583X(03)00644-X.
- [276] Ingo Reinhold, Chris E. Hendriks, Rebecca Eckardt, Johannes M. Kranenburg, Jolke Perelaer, Reinhard R. Baumann, and Ulrich S. Schubert. Argon plasma sintering of inkjet printed silver tracks on polymer substrates. *Journal of Materials Chemistry*, 19(21):3384, 2009. ISSN 0959-9428. doi:10.1039/b823329b.
- [277] Siyuan Ma, Vadim Bromberg, Liang Liu, Frank D. Egitto, Paul R. Chiarot, and Timothy J. Singler. Low temperature plasma sintering of silver nanoparticles. *Applied Surface Science*, 293(9):207–215, 2014. ISSN 01694332. doi:10.1016/j.apsusc.2013.12.135.
- [278] Lola Gonzalez-Garcia, Johannes H.M. Maurer, Beate Reiser, Ioannis Kanelidis, and Tobias Kraus. Ultrathin Gold Nanowires for Transparent Electronics: Breaking Barriers. *Procedia Engineering*, 141:152–156, 2016. ISSN 18777058. doi:10.1016/j.proeng.2015.08.1120.
- [279] Bok Yeop Ahn, David J. Lorang, and Jennifer A. Lewis. Transparent conductive grids via direct writing of silver nanoparticle inks. *Nanoscale*, 3(7):2700–2702, 2011. doi:10.1039/c1nr10048c.

- [280] Sukjoon Hong, Junyeob Yeo, Gunho Kim, Dongkyu Kim, Habeom Lee, Jinhyeong Kwon, Hyungman Lee, Phillip Lee, and Seung Hwan Ko. Nonvacuum, maskless fabrication of a flexible metal grid transparent conductor by low-temperature selective laser sintering of nanoparticle ink. *ACS nano*, 7(6):5024–5031, 2013. doi:10.1021/nm400432z.
- [281] Daeho Lee, Dongwoo Paeng, Hee K. Park, and Costas P. Grigoriopoulos. Vacuum-free, maskless patterning of Ni electrodes by laser reductive sintering of NiO nanoparticle ink and its application to transparent conductors. *ACS nano*, 8(10):9807–9814, 2014. doi:10.1021/nm503383z.
- [282] F. A. Nichols. Surface-(interface-) and volume-diffusion contributions to morphological changes driven by capillarity. *Trans. Aime*, 233:1840–1848, 1965.
- [283] Hadi Hosseinzadeh Khaligh and Irene A. Goldthorpe. Failure of silver nanowire transparent electrodes under current flow. *Nanoscale research letters*, 8(1):235, 2013. ISSN 1931-7573. doi:10.1186/1556-276X-8-235.
- [284] Geoffrey Deignan and Irene A. Goldthorpe. The dependence of silver nanowire stability on network composition and processing parameters. *RSC Advances*, 7(57):35590–35597, 2017. doi:10.1039/C7RA06524H.
- [285] Alexandra Madeira, Marie Plissonneau, Laurent Servant, Irene A. Goldthorpe, and Mona Tréguer-Delapierre. Increasing Silver Nanowire Network Stability through Small Molecule Passivation. *Nanomaterials*, 9(6):899, 2019. doi:10.3390/nano9060899.
- [286] Tze-Bin Song, You Seung Rim, Fengmin Liu, Brion Bob, Shenglin Ye, Yao-Tsung Hsieh, and Yang Yang. Highly Robust Silver Nanowire Network for Transparent Electrode. *ACS applied materials & interfaces*, 7(44):24601–24607, 2015. doi:10.1021/acsami.5b06540.
- [287] Simon Bettscheider, Tobias Kraus, and Norman A. Fleck. Stabilization of ultrathin nanowires by self-assembly into

- bundles. *Acta Materialia*, 231:117799, 2022. ISSN 13596454. doi:10.1016/j.actamat.2022.117799.
- [288] Chen Xuan and John Biggins. Plateau-Rayleigh instability in solids is a simple phase separation. *Physical review. E*, 95(5-1):053106, 2017. doi:10.1103/PhysRevE.95.053106.
- [289] S. I. Tamim and J. B. Bostwick. Plateau-Rayleigh instability in a soft viscoelastic material. *Soft matter*, 17(15):4170–4179, 2021. doi:10.1039/d1sm00019e.
- [290] C.-H. Zhang, F. Kassubek, and C. A. Stafford. Surface fluctuations and the stability of metal nanowires. *Physical Review B*, 68(16):165414, 2003. ISSN 1098-0121. doi:10.1103/PhysRevB.68.165414.
- [291] Aveek Bid, Achyut Bora, and Arup K. Raychaudhuri. Experimental study of Rayleigh instability in metallic nanowires using resistance fluctuations measurements from 77K to 375K. *Proc. SPIE 5843, Fluctuations and Noise in Materials II*, page 147, 2005. doi:10.1117/12.609419.
- [292] Jay Prakash Naik. *Nanowires Fabricated by Focused Ion Beam*. Dissertation (PhD Thesis), University of Birmingham, Birmingham, 2013.
- [293] Peifeng Li, Weibing Liao, Lijie Yue, Zhanxi Fan, and Feng Rao. Key factors affecting Rayleigh instability of ultrathin 4H hexagonal gold nanoribbons. *Nanoscale Advances*, 2(7):3027–3032, 2020. doi:10.1039/d0na00186d.
- [294] Pierre-Gilles de Gennes, Françoise Brochard-Wyart, and David Quéré. *Capillarity and wetting phenomena: Drops, bubbles, pearls, waves*. Springer, New York, 2004. ISBN 978-0-387-00592-8.
- [295] Harvey E. White. *Modern college physics*. Van Nostrand, New York, 6th edition, 1972. ISBN 978-0-442-29401-4.
- [296] Nan Wang and Alain Karma. Fragmentation of faceted crystalline wires. *Physical Review Materials*, 6(10):106002, 2022. doi:10.1103/PhysRevMaterials.6.106002.

- [297] S. Karim, M. E. Toimil-Molares, A. G. Balogh, W. Ensinger, T. W. Cornelius, E. U. Khan, and R. Neumann. Morphological evolution of Au nanowires controlled by Rayleigh instability. *Nanotechnology*, 17(24):5954–5959, 2006. doi:10.1088/0957-4484/17/24/009.
- [298] F. A. Nichols and W. W. Mullins. Morphological Changes of a Surface of Revolution due to Capillarity-Induced Surface Diffusion. *Journal of Applied Physics*, 36(6):1826–1835, 1965. ISSN 0021-8979. doi:10.1063/1.1714360.
- [299] Carl V. Thompson. Solid-State Dewetting of Thin Films. *Annual Review of Materials Research*, 42(1):399–434, 2012. ISSN 1531-7331. doi:10.1146/annurev-matsci-070511-155048.
- [300] M. E. Toimil Molares, A. G. Balogh, T. W. Cornelius, R. Neumann, and C. Trautmann. Fragmentation of nanowires driven by Rayleigh instability. *Applied Physics Letters*, 85(22):5337–5339, 2004. ISSN 0003-6951. doi:10.1063/1.1826237.
- [301] Yugang Sun, Brian Mayers, and Younan Xia. Transformation of Silver Nanospheres into Nanobelts and Triangular Nanoplates through a Thermal Process. *Nano Letters*, 3(5):675–679, 2003. ISSN 1530-6984. doi:10.1021/nl034140t.
- [302] Shang Xu, Peifeng Li, and Yang Lu. In situ atomic-scale analysis of Rayleigh instability in ultrathin gold nanowires. *Nano Research*, 11(2):625–632, 2018. ISSN 1998-0124. doi:10.1007/s12274-017-1667-3.
- [303] Victor Gold, editor. *The IUPAC Compendium of Chemical Terminology*. International Union of Pure and Applied Chemistry (IUPAC), Research Triangle Park, NC, 2019. doi:10.1351/goldbook.
- [304] Stuart T. Gentry, Shane F. Kendra, and Mark W. Bezpalko. Ostwald Ripening in Metallic Nanoparticles: Stochastic Kinetics. *The Journal of Physical Chemistry C*, 115(26):12736–12741, 2011. ISSN 1932-7447. doi:10.1021/jp2009786.

- [305] E. Jiran and C. V. Thompson. Capillary instabilities in thin films. *Journal of Electronic Materials*, 19(11):1153–1160, 1990. ISSN 0361-5235. doi:10.1007/BF02673327.
- [306] E. Jiran and C. V. Thompson. Capillary instabilities in thin, continuous films. *Thin Solid Films*, 208(1):23–28, 1992. ISSN 00406090. doi:10.1016/0040-6090(92)90941-4.
- [307] P. R. Gadkari, A. P. Warren, R. M. Todi, R. V. Petrova, and K. R. Coffey. Comparison of the agglomeration behavior of thin metallic films on SiO₂. *Journal of Vacuum Science & Technology A: Vacuum, Surfaces, and Films*, 23(4):1152–1161, 2005. ISSN 0734-2101. doi:10.1116/1.1861943.
- [308] Anna Kosinova, Oleg Kovalenko, Leonid Klinger, and Eugen Rabkin. Mechanisms of solid-state dewetting of thin Au films in different annealing atmospheres. *Acta Materialia*, 83:91–101, 2015. ISSN 13596454. doi:10.1016/j.actamat.2014.09.049.
- [309] Nimrod Gazit, Leonid Klinger, and Eugen Rabkin. Chemically-induced solid-state dewetting of thin Au films. *Acta Materialia*, 129:300–311, 2017. ISSN 13596454. doi:10.1016/j.actamat.2017.02.054.
- [310] Jang-Yeon Kwon, Tae-Sik Yoon, Ki-Bum Kim, and Seok-Hong Min. Comparison of the agglomeration behavior of Au and Cu films sputter deposited on silicon dioxide. *Journal of Applied Physics*, 93(6):3270–3278, 2003. ISSN 0021-8979. doi:10.1063/1.1556178.
- [311] Florian Niekief, Peter Schweizer, Simon M. Kraschewski, Benjamin Butz, and Erdmann Spiecker. The process of solid-state dewetting of Au thin films studied by in situ scanning transmission electron microscopy. *Acta Materialia*, 90:118–132, 2015. ISSN 13596454. doi:10.1016/j.actamat.2015.01.072.
- [312] Anna Kosinova, Leonid Klinger, Oleg Kovalenko, and Eugen Rabkin. The role of grain boundary sliding in solid-state dewetting of thin polycrystalline films. *Scripta Materialia*, 82:33–36, 2014. ISSN 13596462. doi:10.1016/j.scriptamat.2014.03.015.

- [313] William W. Mullins. Flattening of a Nearly Plane Solid Surface due to Capillarity. *Journal of Applied Physics*, 30(1):77–83, 1959. ISSN 0021-8979. doi:10.1063/1.1734979.
- [314] M. Magnozzi, F. Bisio, and M. Canepa. Solid-state dewetting of thin Au films studied with real-time, in situ spectroscopic ellipsometry. *Applied Surface Science*, 421, Part B:651–655, 2017. ISSN 01694332. doi:10.1016/j.apsusc.2016.09.115.
- [315] Sergio B. Sepulveda-Mora and Sylvain G. Cloutier. Figures of Merit for High-Performance Transparent Electrodes Using Dip-Coated Silver Nanowire Networks. *Journal of Nanomaterials*, 2012:1–7, 2012. ISSN 1687-4110. doi:10.1155/2012/286104.
- [316] Dieter K. Schroder. *Semiconductor Material and Device Characterization*. Wiley Interscience, New York, 3rd edition, 2006. ISBN 978-0-471-73906-5. doi:10.1002/0471749095.
- [317] Aman Anand, Md Moidul Islam, Rico Meitzner, Ulrich S. Schubert, and Harald Hoppe. Introduction of a Novel Figure of Merit for the Assessment of Transparent Conductive Electrodes in Photovoltaics: Exact and Approximate Form. *Advanced Energy Materials*, 11(26): 2100875, 2021. ISSN 1614-6832. doi:10.1002/aenm.202100875.
- [318] Mohammad Matboo Ghorbani and Reza Taherian. Methods of Measuring Electrical Properties of Material. In Reza Taherian and Ayesha Kausar, editors, *Electrical Conductivity in Polymer-Based Composites*, *Plastics Design Library*, pages 365–394. William Andrew, San Diego, 2018. ISBN 978-0-12-812541-0. doi:10.1016/B978-0-12-812541-0.00012-4.
- [319] Heinrich Gobrecht, Hans-Joachim Eichler, Ludwig Bergmann, and Clemens Schaefer, editors. *Optik*, volume 3 of *Lehrbuch der Experimentalphysik*. De Gruyter, Berlin, 7th edition, 1978. ISBN 3-11-007457-5.
- [320] Thomas A. Germer, Joanne C. Zwinkels, and Benjamin K. Tsai, editors. *Spectrophotometry: Accurate Measurement of Optical Properties of Materials*, volume 46 of *Experimental Methods in*

- the Physical Sciences*. Elsevier Science, Burlington, 2014. ISBN 9780123860224.
- [321] Klaus Hentschel. Das Brechungsgesetz in der Fassung von Snellius. *Archive for History of Exact Sciences*, 55(4):297–344, 2001. ISSN 0003-9519. doi:10.1007/s004070000026.
- [322] Felix Hermerschmidt, Michael Hengge, Vincent R. Schröder, Paul Hänsch, Konstantin Livanov, Natalia Zamoshchik, and Emil J. W. List-Kratochvil. A guide to qualitative haze measurements demonstrated on inkjet-printed silver electrodes for flexible OLEDs. In Chihaya Adachi, Tae-Woo Lee, and Franky So, editors, *Organic and Hybrid Light Emitting Materials and Devices XXV*, volume 11808 of *Proceedings of SPIE*, pages 11808 0B 1–11, Bellingham, Washington, USA, 2021. SPIE. ISBN 9781510644540. doi:10.1117/12.2594486.
- [323] Viet Huong Nguyen, Dorina T. Papanastasiou, Joao Resende, Laetitia Bardet, Thomas Sannicolo, Carmen Jiménez, David Muñoz-Rojas, Ngoc Duy Nguyen, and Daniel Bellet. Advances in Flexible Metallic Transparent Electrodes. *Small*, 18(19):2106006, 2022. doi:10.1002/sml.202106006.
- [324] Yasuo Chiba, Ashraful Islam, Ryoichi Komiya, Naoki Koide, and Liyuan Han. Conversion efficiency of 10.8% by a dye-sensitized solar cell using a TiO_2 electrode with high haze. *Applied Physics Letters*, 88(22):223505, 2006. ISSN 0003-6951. doi:10.1063/1.2208920.
- [325] H.-J. Hoffmann. Optical Glasses. In *Reference Module in Materials Science and Materials Engineering*, volume 13, pages 1–18. doi:10.1016/B978-0-12-803581-8.02344-4.
- [326] D. B. Fraser and H. D. Cook. Highly Conductive, Transparent Films of Sputtered $In[2-x]Sn[x]O[3-y]$. *Journal of The Electrochemical Society*, 119(10):1368, 1972. ISSN 00134651. doi:10.1149/1.2403999.
- [327] Irving Langmuir. The Adsorption of Gases On Plane Surfaces of Glass, Mica and Platinum. *Journal of the Amer-*

-
- ican Chemical Society*, 40(9):1361–1403, 1918. ISSN 0002-7863. doi:10.1021/ja02242a004.
- [328] Herbert Freundlich. Über die Adsorption in Lösungen. *Zeitschrift für Physikalische Chemie*, 57U(1):385–470, 1907. ISSN 0942-9352. doi:10.1515/zpch-1907-5723.
- [329] Samuel W. Winslow, James W. Swan, and William A. Tisdale. The Importance of Unbound Ligand in Nanocrystal Superlattice Formation. *Journal of the American Chemical Society*, 142(21):9675–9685, 2020. ISSN 0002-7863. doi:10.1021/jacs.0c01809.
- [330] William M. Haynes, editor. *CRC Handbook of Chemistry and Physics: A ready-reference book of chemical and physical data*. CRC Press, Boca Raton and London and New York, 97th edition, 2017. ISBN 978-1-4987-5429-3.
- [331] M. C. Salvadori, A. R. Vaz, R. J. C. Farias, and M. Cattani. Electrical resistivity of nanostructured platinum and gold thin films. *Surface Review and Letters*, 11(02):223–227, 2004. ISSN 0218-625X. doi:10.1142/S0218625X04006086.
- [332] S. M. Rossnagel and J. J. Cuomo. Film modification by low energy ion bombardment during deposition. *Thin Solid Films*, 171(1):143–156, 1989. ISSN 00406090. doi:10.1016/0040-6090(89)90040-0.
- [333] Rainer Telle, Hermann Salmang, and Horst Scholze, editors. *Keramik*. Springer, Berlin and Heidelberg, 7th edition, 2007. ISBN 3-540-63273-5.
- [334] Jaegeun Noh, Eisuke Ito, Ken Nakajima, Jinyeol Kim, Haiwon Lee, and Masahiko Hara. High-Resolution STM and XPS Studies of Thiophene Self-Assembled Monolayers on Au(111). *The Journal of Physical Chemistry B*, 106(29):7139–7141, 2002. ISSN 1520-6106. doi:10.1021/jp020482w.
- [335] Ramona Samba, Thomas Chassé, and Martin Stelzle. Is the Enhanced Adhesion of PEDOT Thin Films on Electrodes Due to Sulfur - Gold Interaction? - An XPS Study. *The Open*

BIBLIOGRAPHY

Surface Science Journal, 5(1):17–20, 2013. ISSN 18765319.
doi:10.2174/1876531901305010017.

- [336] Anmona S. Pranti, Andreas Schander, André Bödecker, and Walter Lang. PEDOT: PSS coating on gold microelectrodes with excellent stability and high charge injection capacity for chronic neural interfaces. *Sensors and Actuators B: Chemical*, 275:382–393, 2018. ISSN 09254005. doi:10.1016/j.snb.2018.08.007.

Supporting Information (SI) to Publications 1-4

SI to Publication 1

Reprinted with permission from

S. Bettscheider, B. Kuttich, [L. F. Engel](#), L. González-García, and T. Kraus: “Bundling of Nanowires Induced by Unbound Ligand”.
J. Phys. Chem. C, 2021, 125, 6, 3590–3598.
DOI: [10.1021/acs.jpcc.0c10919](https://doi.org/10.1021/acs.jpcc.0c10919).

Copyright 2021 American Chemical Society.

SUPPORTING INFORMATION TO: Bundling of Nanowires Induced by Unbound Ligand

Simon Bettscheider,^{†,‡} Björn Kuttich,^{†,‡} Lukas F. Engel,^{†,‡} Lola
González-García,^{†,‡} and Tobias Kraus^{*,†,‡}

[†]*INM — Leibniz Institute for New Materials, Campus D2 2, 66123 Saarbrücken, Germany*

[‡]*Colloid and Interface Chemistry, Saarland University, Campus D2 2, 66123 Saarbrücken,
Germany*

E-mail: tobias.kraus@leibniz-inm.de

1 Ligand grafting density and the free energy of adsorption

In order to determine the grafting density of a monolayer ligand shell, we purified a dispersion of AuNWs several times (see main text). The results are shown in Fig. S1.

Besides the grafting density, we intend to approximately quantify the adsorption equilibrium between a gold surface and oleylammonium chloride. To this end, we estimate the order of magnitude of the free energy of adsorption based on data from the literature and use this value to calculate a Langmuir adsorption isotherm. Following classic adsorption isotherms,^{1,2} we expect some ligands to desorb when the amount of ligand is reduced from 28 mmol/L to 0.9 mmol/L. We further know from the experiments discussed in the main text

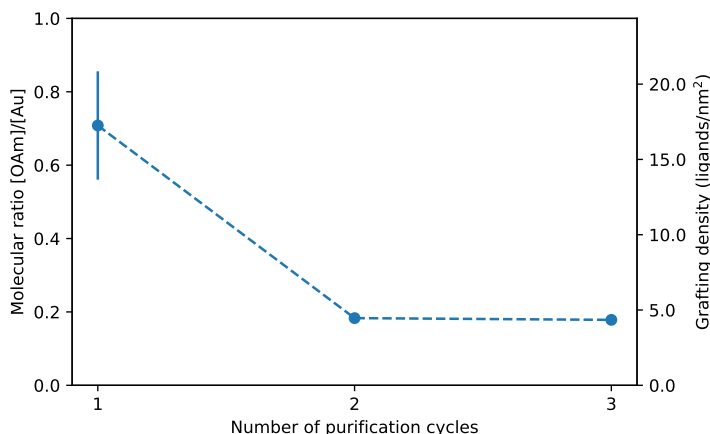


Figure S1: Amount of ligand in the system and nominal grafting density for an increasing number of purification cycles as obtained by TGA. The error bars display \pm the standard deviation of measuring three independent batches of AuNWs. For 2 and 3 purification cycles, the error bars are within the size of the marker. The dashed line is only a guide to the eye.

that the transition from dispersed to bundled AuNWs occurs at a ligand concentration of ca. 4.4 mmol/L. Above this threshold, the AuNWs are dispersed. Below, they are bundled.

We start by assessing a better-known system: the adsorption of alkanethiols onto gold. From experimental data by Karpovich and Blanchard and by Schessler *et al.*, we know that the free energy of adsorption for octadecanethiol onto gold at room temperature is $\Delta G_{\text{ads}} = -5.5$ kcal/mol, the enthalpy is $\Delta H_{\text{ads}} = -20$ kcal/mol, and the entropy is $\Delta S_{\text{ads}} = -48$ cal/(mol K).

We now estimate the free energy of adsorption for oleylammonium chloride adsorbing onto a gold surface. For the enthalpic part of the free energy, we know from DFT calculations⁵ that the enthalpy of adsorption for an amine is -23.4 kcal/mol and for an ammonium chloride end group -40.1 kcal/mol. It is difficult to directly compare these values to experimental data but we can compare to DFT values of alkanethiols. There, the reported adsorption enthalpies are on the order of -50 kcal/mol.⁶⁻¹⁰ This means that the adsorption enthalpy of the ammonium chloride group is 20% smaller than the one of a thiol group.

For the entropic part of the free energy, we make the very crude assumption that the change in entropy due to adsorption for oleylammonium chloride is the same as for 1-

octadecanethiol.^{3,4} Both molecules possess the same chain length of 18 carbon atoms. They differ in their functional group, which will not influence the entropy fundamentally, and in the double bond at the center of oleylamine. This latter difference most likely influences the entropy of adsorption since it will influence the packing of a monolayer. For the present order-of-magnitude estimation, we ignore this difference.

Given these estimates for the enthalpy and entropy of adsorption of oleylammonium chloride, we obtain the adsorption isotherm depicted in Fig. S2B with a free energy of adsorption of $\Delta G_{\text{ads}} = -1.9 \text{ kcal/mol} = -8.1 \text{ kJ/mol}$. This should be interpreted as an estimate and not as an accurate account of the adsorption isotherm of oleylammonium chloride onto a gold surface.

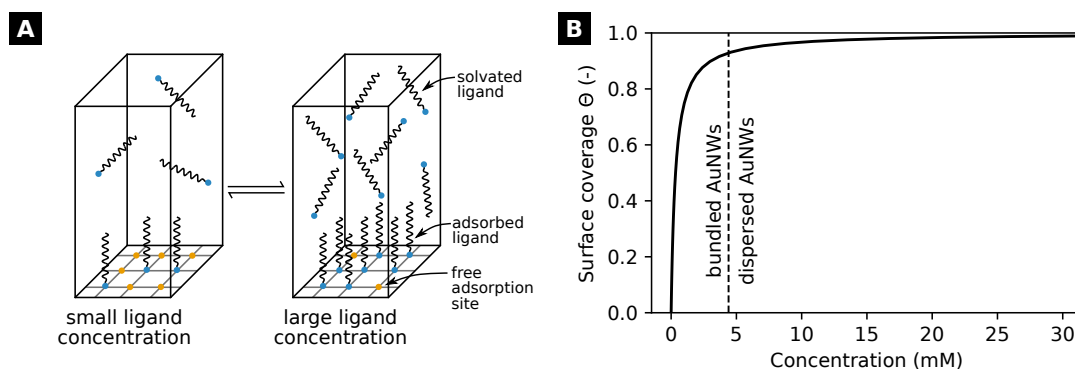


Figure S2: **A** Schematic of the adsorption equilibrium between free and adsorbed ligands and the influence of diluting a dispersion. **B** Estimated adsorption isotherm with an free energy of adsorption

2 Addition of oleylamine to dispersed AuNWs

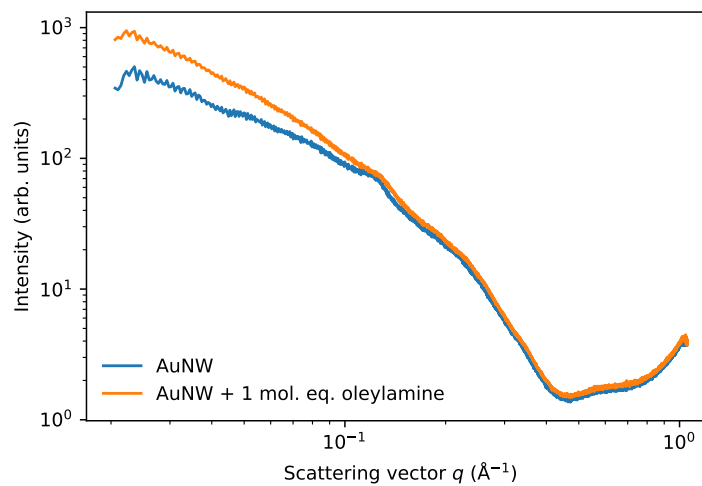


Figure S3: SAXS curve of AuNWs dispersed in cyclohexane at 6 mg/mL (blue) and the same sample with 1 mol of the ligand oleylamine added per mole of gold (orange).

3 Bundling in dependence of amount of ligand in linear alkanes

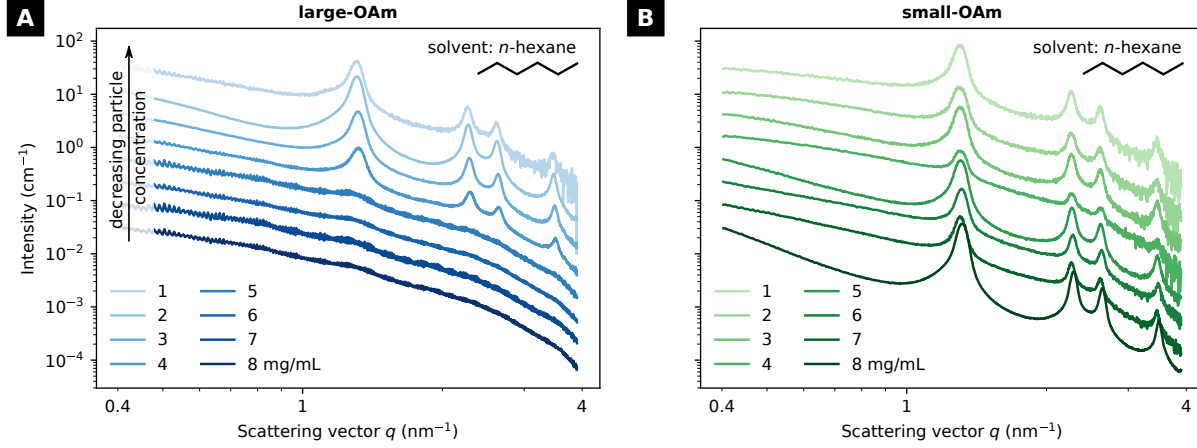


Figure S4: SAXS scattering curves of AuNWs in *n*-hexane with different amounts ligand (see Table 1 in the main text for ligand quantities) and at different nanowire concentrations. **A** In the sample centrifuged once with the larger amount of ligand, distinct scattering peaks are present in the curves with smaller nanowire concentrations of 1 to 3 mg/mL, indicating AuNWs assembled in elongated bundles. For larger concentrations, no scattering peaks can be found indicating that the AuNWs are completely dispersed. **B** In the sample centrifuged twice with the smaller amount of ligand, distinct scattering peaks indicative of bundles are present at all concentrations.

4 The van der Waals interaction between two gold cylinders

In the following, the vdW interaction is approximated by pairwise summation with the Hamaker-Lifshitz theory neglecting for retardation screening. The equations are summarized in¹¹ and¹² The interaction energy G is given by

$$G = -\frac{2A}{3z} \sum_{i,j=1}^{\infty} \frac{\Gamma^2(i+j+\frac{1}{2})}{i!j!(i-1)!(j-1)!} \left(\frac{R_1}{z}\right)^{2i} \left(\frac{R_2}{z}\right)^{2j}, \quad (\text{S1})$$

where A is the Hamaker constant, Γ is the Gamma function, R_1 and R_2 are the radii of the cylinders, and z is the distance between the centers of the cylinders. In our case, $R_1 = R_2 = R$ so that

$$G = -\frac{2A}{3z} \sum_{i,j=1}^{\infty} \frac{\Gamma^2(i+j+\frac{1}{2})}{i!j!(i-1)!(j-1)!} \left(\frac{R}{z}\right)^{2(i+j)}. \quad (\text{S2})$$

The Hamaker constant for a body of material 1 interacting through medium 3 with a body of material 2 can be approximated by

$$A_{123} = (\sqrt{A_1} - \sqrt{A_3})(\sqrt{A_2} - \sqrt{A_3}), \quad (\text{S3})$$

which simplifies to

$$A_{121} = (\sqrt{A_1} - \sqrt{A_2})^2 \quad (\text{S4})$$

in our case where a cylinder of material 1 interacts with another cylinder of the same material through medium 2. The resulting vdW interaction energy, with Hamaker constants of 1.96×10^{-19} J for gold and 4.69×10^{-20} J for the hydrocarbons from Ref. 11 p. 64, is plotted in Fig. S5. At an interwire distance of 5.9 nm as measured in the AuNWs bundled in cyclohexane, the interaction energy due to van der Waals forces is $1.245 \times 10^{-3} k_B T/\text{nm}$.

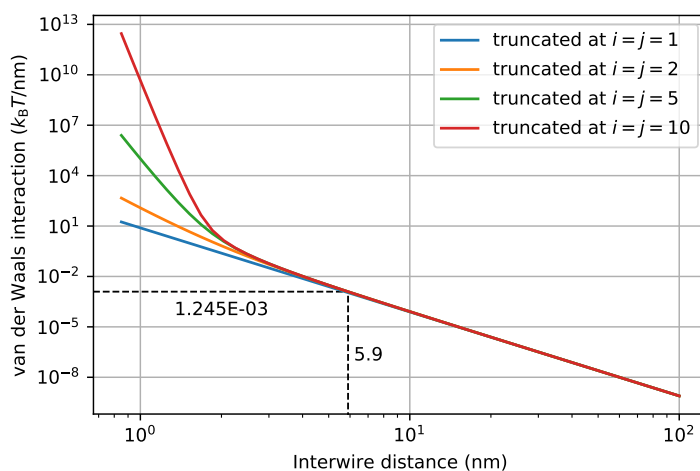


Figure S5: The van der Waals interaction between two parallel cylinders of diameter of 1.7 nm made from gold across alkanes. The marked distance of 5.9 nm is the one found in bundled AuNWs in cyclohexane. To calculate the interaction energy, Hamaker constants of 1.96×10^{-19} J for gold and 4.69×10^{-20} J for hydrocarbon from Ref. 11 p. 64 were used.

References

1. Langmuir, I. The Adsorption of Gases on Plane Surfaces of Glass, Mica and Platinum. *Journal of the American Chemical Society* **1918**, *40*, 1361–1403, DOI: 10.1021/ja02242a004.
2. Adamson, A. W.; Gast, A. P. *Physical Chemistry of Surfaces*; Wiley: New York, 1997.
3. Karpovich, D. S.; Blanchard, G. J. Direct Measurement of the Adsorption Kinetics of Alkanethiolate Self-Assembled Monolayers on a Microcrystalline Gold Surface. *Langmuir* **1994**, *10*, 3315–3322, DOI: 10.1021/1a00021a066.
4. Schessler, H. M.; Karpovich, D. S.; Blanchard, G. J. Quantitating the Balance between Enthalpic and Entropic Forces in Alkanethiol/Gold Monolayer Self Assembly. *Journal of the American Chemical Society* **1996**, *118*, 9645–9651, DOI: 10.1021/ja961565r.
5. Nouh, E. S. A.; Baquero, E. A.; Lacroix, L.-M.; Delpech, F.; Poteau, R.; Viau, G. Surface-Engineering of Ultrathin Gold Nanowires: Tailored Self-Assembly and Enhanced Stability. *Langmuir* **2017**, *33*, 5456–5463, DOI: 10.1021/acs.langmuir.7b00477.

6. Vericat, C.; Vela, M. E.; Benitez, G.; Carro, P.; Salvarezza, R. C. Self-Assembled Monolayers of Thiols and Dithiols on Gold: New Challenges for a Well-Known System. *Chemical Society Reviews* **2010**, *39*, 1805, DOI: 10.1039/b907301a.
7. Peiretti, L. F.; Quaino, P.; Tielens, F. Competition between Two High-Density Assemblies of Poly(phenyl)thiols on Au(111). *The Journal of Physical Chemistry C* **2016**, *120*, 25462–25472, DOI: 10.1021/acs.jpcc.6b08977.
8. Grönbeck, H.; Curioni, A.; Andreoni, W. Thiols and Disulfides on the Au(111) Surface: The Headgroup-Gold Interaction. *Journal of the American Chemical Society* **2000**, *122*, 3839–3842, DOI: 10.1021/ja993622x.
9. Fajín, J. L. C.; Teixeira, F.; Gomes, J. R. B.; Cordeiro, M. N. D. S. Effect of van der Waals Interactions in the DFT Description of Self-Assembled Monolayers of Thiols on Gold. *Theoretical Chemistry Accounts* **2015**, *134*, 67, DOI: 10.1007/s00214-015-1666-y.
10. Mete, E.; Yortanlı, M.; Danişman, M. F. A van der Waals DFT Study of Chain Length Dependence of Alkanethiol Adsorption on Au(111): Physisorption vs. Chemisorption. *Physical Chemistry Chemical Physics* **2017**, *19*, 13756–13766, DOI: 10.1039/C7CP01653K.
11. Parsegian, V. A. *Van der Waals Forces*; Cambridge University Press: Cambridge, 2006; DOI: 10.2277/0521839068.
12. Langbein, D. Van der Waals Attraction Between Cylinders, Rods or Fibers. *Physik der Kondensierten Materie* **1972**, *15*, 61–86, DOI: 10.1007/BF02422580.

SI to Publication 2

Reproduced from

L. F. Engel, L. González-García, and T. Kraus: “Flexible and Transparent Electrodes Imprinted from Metal Nanostructures: Morphology and Opto-Electronic Performance”. *Nanoscale Adv.*, 2022, **4**, 3370-3380. DOI: 10.1039/D2NA00259K.

with permission from the Royal Society of Chemistry.

SUPPORTING INFORMATION TO:
Flexible and transparent electrodes
imprinted from metal nanostructures:
morphology and opto-electronic performance

Lukas F. Engel,[†] Lola González-García,^{*,†} and Tobias Kraus^{*,†,‡}

[†]*INM — Leibniz Institute for New Materials, Campus D2 2, 66123 Saarbrücken, Germany*

[‡]*Colloid and Interface Chemistry, Saarland University, Campus D2 2, 66123 Saarbrücken,
Germany*

E-mail: lola.gonzalez-garcia@leibniz-inm.de, tobias.kraus@leibniz-inm.de

1 Nanoimprinting method

The nano-objects were assembled into the desired structure using direct nanoimprinting. We illustrate the method using the example of AuNW and a hexagonally patterned stamp because spherical particles and other stamp patterns do not change the procedure. A patterned PDMS stamp (1) was attached to a steel cylinder and rolled over a substrate that carried a sessile droplet of the AuNW ink (2). The ink is confined by the stamp's cavities, the solvent permeates the PDMS, particle concentration slowly increases, the AuNW self-assemble into larger bundles (3) and finally percolate. The resulting structures (4) closely follow the stamp features.^[1]

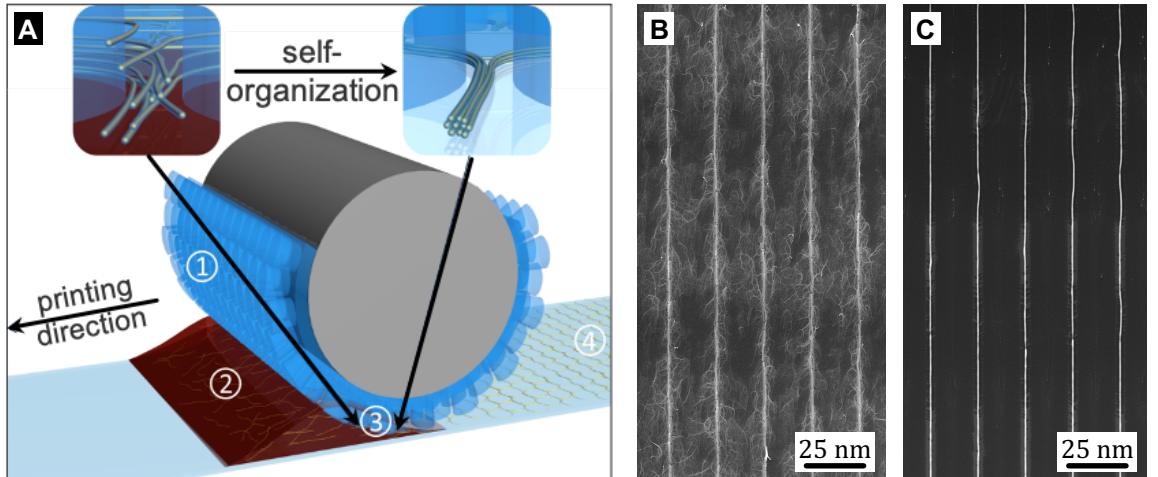


Figure S1: **A**: Nanoimprinting with (1) a hexagonally patterned PDMS stamp attached to a steel cylinder, (2) the AuNW-based ink confined between PET substrate and stamp, (3) AuNW self-assembly upon solvent permeation through the stamp, and (4) the resulting Au grid. Figure adapted from [Maurer et al.](#)^[1] **B**: SEM micrograph of a AuNW-based line grid electrode imprinted at 6 mg/mL on Si, after plasma sintering. **C**: SEM micrograph of a AuNP-based line grid electrode imprinted at 30 mg/mL on Si, after plasma sintering.

The imprinting stamps had an area of 3.5 cm x 8 cm, of which 3.5 cm x 7 cm were patterned. The flat 3.5 cm x 0.5 cm at either end of the stamp served as run-in and run-out areas during imprinting. The stamp pattern consisted of parallel, line-like channels with a pitch $p \approx 19.5 \mu\text{m}$, a channel width $w_c \approx 1.6 \mu\text{m}$ and a channel depth $d_c \approx 4.2 \mu\text{m}$.

2 Fitting the opto-electronic trade-off

Sheet resistance R_{sh} was determined as the resistance R of a square electrode section of edge length $l = 15\,000\ \mu\text{m}$, contacted with Ag paste and miniature crocodile clamps in two-point-probe configuration. Such a sub-area comprised 750 conductive lines and had an anisotropic sheet resistance of

$$R_{sh}^{-1} = R^{-1} = G = \sigma_{shell} \cdot \frac{750 \cdot A_{shell}}{l}, \quad (\text{S1})$$

measured parallel to the lines, where G is the overall conductance of 750 parallel lines.

To reduce the weight of the R_{sh} data points at the lowest concentration c_{Au} (which were off-the-charts) during fitting of the trade-off between sheet resistance and optical transmittance, we thus used the relation above to fit $R_{sh}^{-1} = G$ vs. $\bar{T}_{400-800\text{nm}}$ rather than R_{sh} vs. $\bar{T}_{400-800\text{nm}}$. The fits in Fig. S2B are therefore the inverse of the linear fits in Fig. S2A.

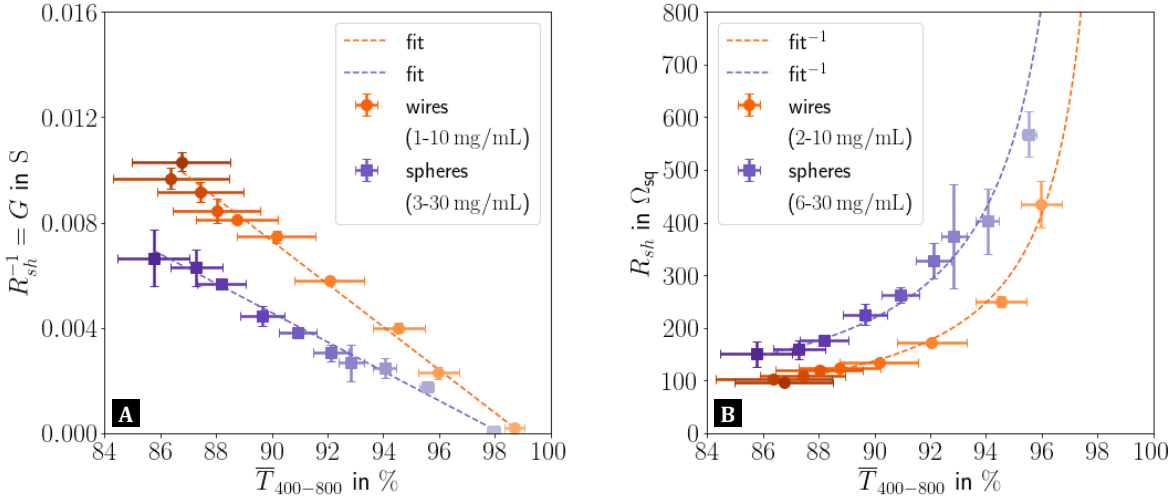


Figure S2: Trade-off between (A) conductance $G = R_{sh}^{-1}$ and optical transmittance $\bar{T}_{400-800}$ as well as (B) between sheet resistance R_{sh} and optical transmittance $\bar{T}_{400-800}$ for both AuNW and AuNP based electrodes directly after plasma sintering. Data points for $c_{Au}^{wires} = 1\ \text{mg/mL}$ and $c_{Au}^{spheres} = 3\ \text{mg/mL}$ have been omitted in B due to off-the-chart high R_{sh} (up to two orders of magnitude higher). | All graphs show average values from three measurements each and the belonging standard deviation. The colour gradient reflects the concentration gradient, with light colours representing the lowest and dark colours the highest concentration.

3 Spherical gold nanoparticle dispersion

SAXS measurements were carried out to determine the average AuNP diameter d_{sp} and to study the AuNP agglomeration state over the entire concentration range used for imprinting.

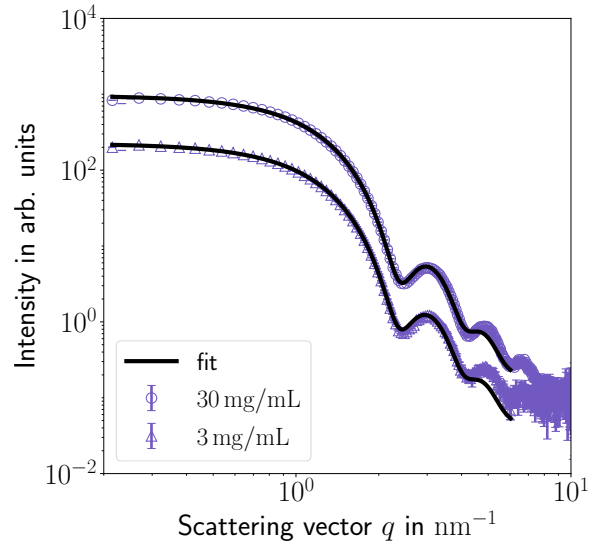


Figure S3: Radially integrated and fitted SAXS curves of the AuNP used for nanoimprinting at both the lowest (3 mg/mL) and the highest concentration (30 mg/mL). No agglomeration peaks are visible. The core size is $d_{sp} = 3.7 \text{ nm} \pm 10\%$.

4 Morphology of plasma-sintered electrodes

4.1 Electrode topography

CLSM was used to characterize the electrode topography and to derive the conductor geometry thereof. Each topography map consisted of 1240 equidistant height traces across eight parallel conductor segments.

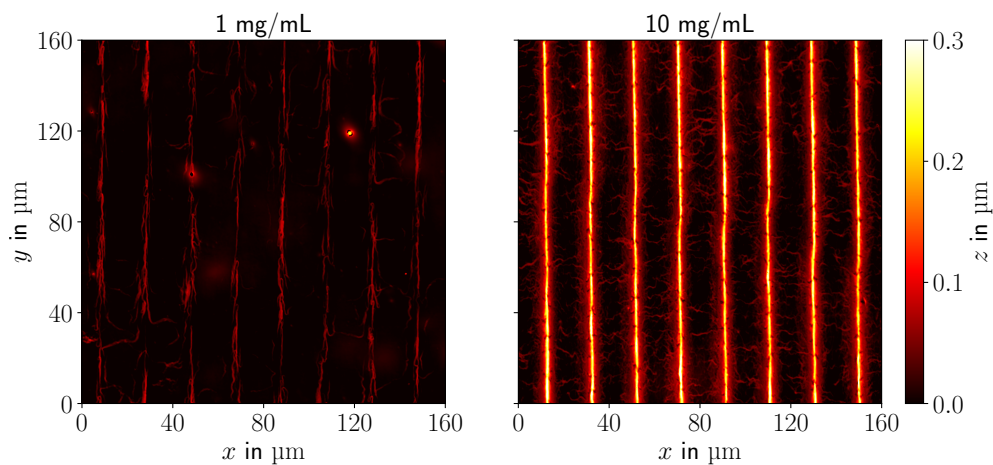


Figure S4: Exemplary CLSM topography maps of AuNW-based electrode sections after plasma sintering for the lowest (1 mg/mL) and the highest (10 mg/mL) concentration c_{Au} .

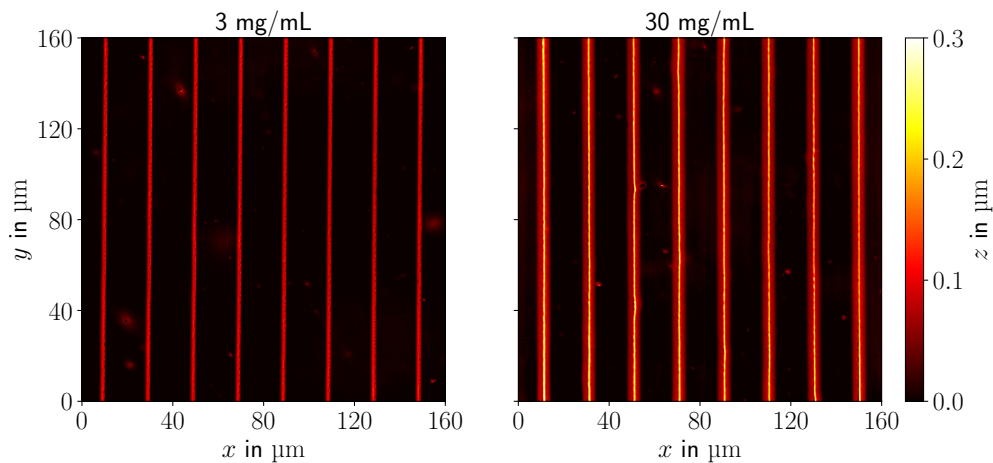


Figure S5: Exemplary CLSM topography maps of AuNP-based electrode sections after plasma sintering for the lowest (3 mg/mL) and the highest (30 mg/mL) concentration c_{Au} .

4.2 Determining the average conductor shell thickness

To determine the average conductor shell thickness t_{shell} , TEM images were taken after plasma-sintering from FIB cross-sections which had been thinned out strongly to reveal the true shell thickness (Fig. S6). In particular the such revealed shell morphology of the AuNW-based electrodes was compared with SEM surface images to rule out the possibility that the observed holes (blue arrows) were due to the FIB milling. The shell thicknesses (in nm) were measured in ten approximately equidistant locations each and were then averaged.

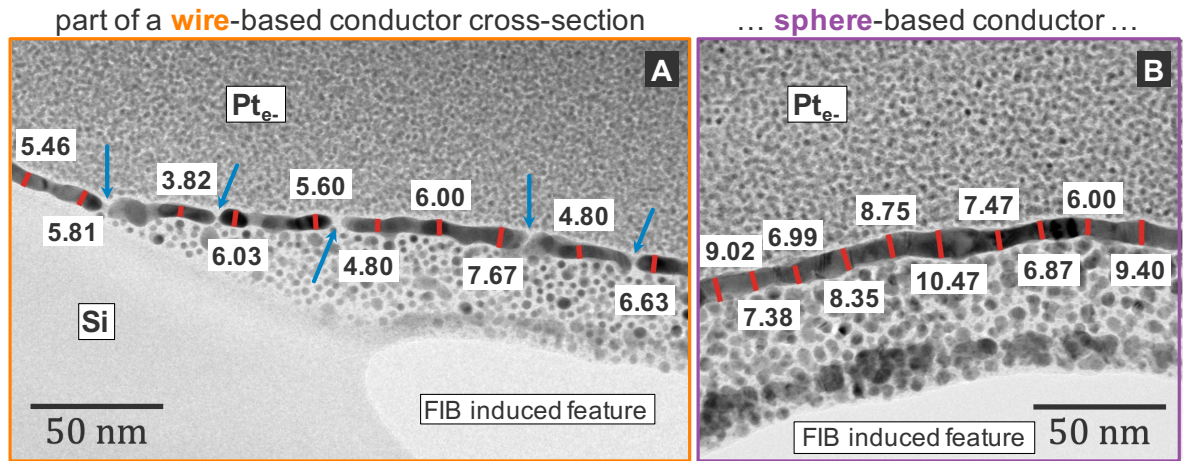


Figure S6: (A) shows a part of a AuNW-based conductor cross-section (6 mg/mL) with $t_{shell} = 5.66 \pm 1.06$ nm and (B) depicts a part of a AuNP-based conductor cross-section (30 mg/mL) with $t_{shell} = 8.07 \pm 1.36$ nm. So both shell thicknesses were well below the electron mean free path of bulk Au which amounts to $\lambda_{Au} \approx 37.7$ nm at room temperature.²

4.3 Defects in sphere-based conductors after plasma sintering

Subtle defects occurring at concentrations close to the percolation threshold could be revealed with SEM (Fig. S7).

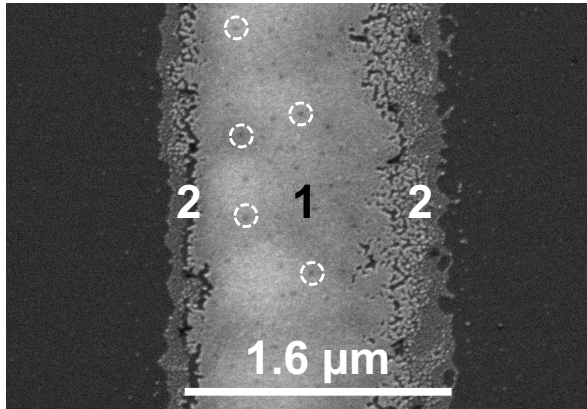


Figure S7: Exemplary post-plasma electrode conductor surface morphology (high-magnification SEM top view) on Si substrate at the lowest concentration c_{Au} (3 mg/mL) used for nanoimprinting with AuNP. (1) designates the conducting part and (2) the non-conducting edges. The dashed circles indicate pores exemplary. | Note that the scale bar has the width w_c of the stamp's channel.

Severe defects could be detected with CLSM. They were less common and thus harder to find, but were present even at high c_{Au} (Fig. S8).

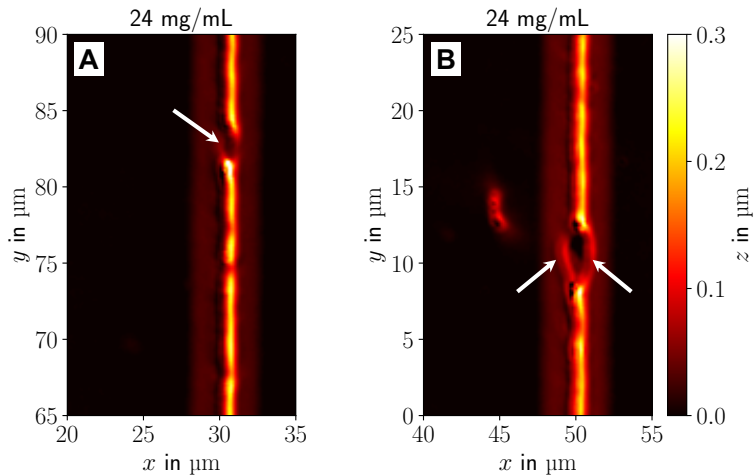


Figure S8: **A:** Fully interrupted conductor (white arrow). **B:** Interrupted conductor with bypasses on either side (white arrows) effectively resulting in a line tapering.

4.4 Post-plasma conductor aspect ratios

The conductor aspect ratios illustrate how conductor width w and maximum conductor height h_{max} develop in relation to each other with increasing concentration c_{Au} (Fig. S9).

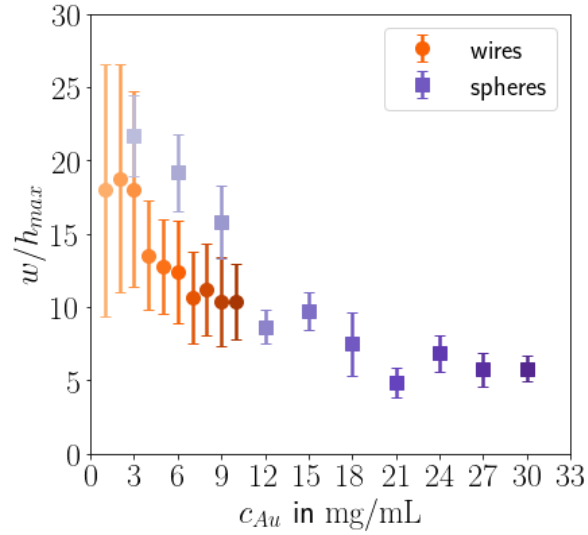


Figure S9: Evolution of the conductor aspect ratios with concentration. The graph shows average values and the belonging standard deviation. The colour gradient reflects the concentration gradient, with light colours representing the lowest and dark colours the highest concentration.

5 Electrode model unit cell: optical transmittance

An electrode unit cell was used to model the electrodes' optical transmittance under the assumption of completely opaque conductors (Fig. S10).

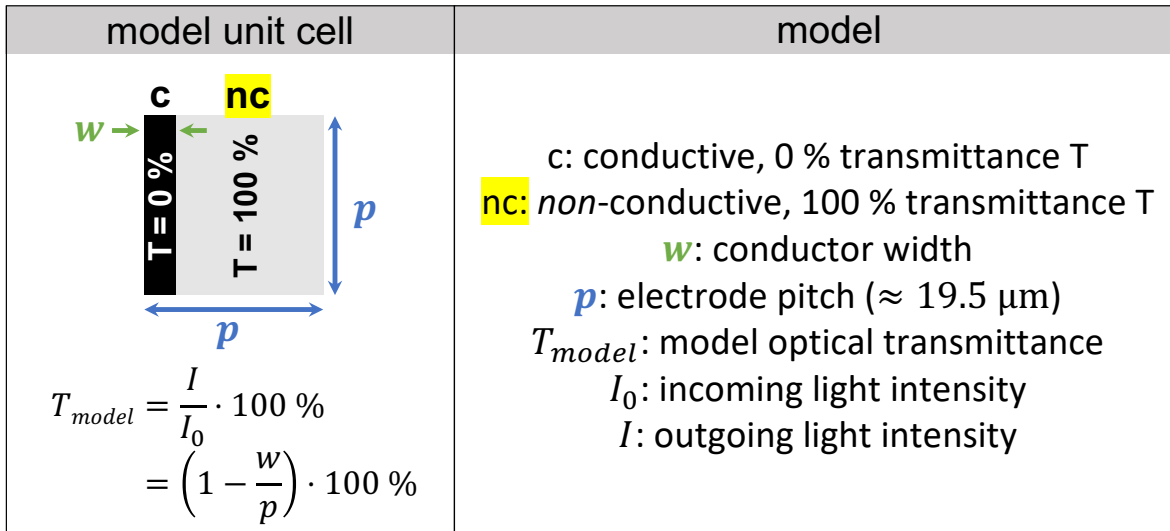


Figure S10: Scheme of the electrode model unit cell.

References

- (1) Maurer, J. H. M.; González-García, L.; Backes, I. K.; Reiser, B.; Schlossberg, S. M.; Kraus, T. Direct Nanoimprinting of a Colloidal Self-Organizing Nanowire Ink for Flexible, Transparent Electrodes. *Advanced Materials Technologies* **2017**, *2*, 1700034.
- (2) Gall, D. Electron mean free path in elemental metals. *Journal of Applied Physics* **2016**, *119*, 085101.

SI to Publication 3

Reproduced from

L. F. Engel, L. González-García, and T. Kraus: “Flexible and Transparent Electrodes Imprinted from Au Nanowires: Stability and Ageing”. *Nanoscale Adv.*, 2022, 4, 3940-3949.
DOI: 10.1039/D2NA00352J.

with permission from the Royal Society of Chemistry.

SUPPORTING INFORMATION TO:
Flexible and transparent electrodes
imprinted from Au nanowires:
stability and ageing

Lukas F. Engel,[†] Lola González-García,^{*,‡} and Tobias Kraus^{*,‡,†}

[†]*Colloid and Interface Chemistry, Saarland University, Campus D2 2, 66123 Saarbrücken,
Germany*

[‡]*INM — Leibniz Institute for New Materials, Campus D2 2, 66123 Saarbrücken, Germany*

E-mail: lola.garcia@leibniz-inm.de; tobias.kraus@leibniz-inm.de

1 Ageing of AuNW electrodes

We monitored the sheet resistance of AuNW electrodes imprinted using ink concentrations between 1 mg/mL and 10 mg/mL on PET foil to study their ageing behaviour. Note that imprinting at 1 mg/mL led to structures that were close to the percolation threshold so that their initial sheet resistance was too high for FTEs.

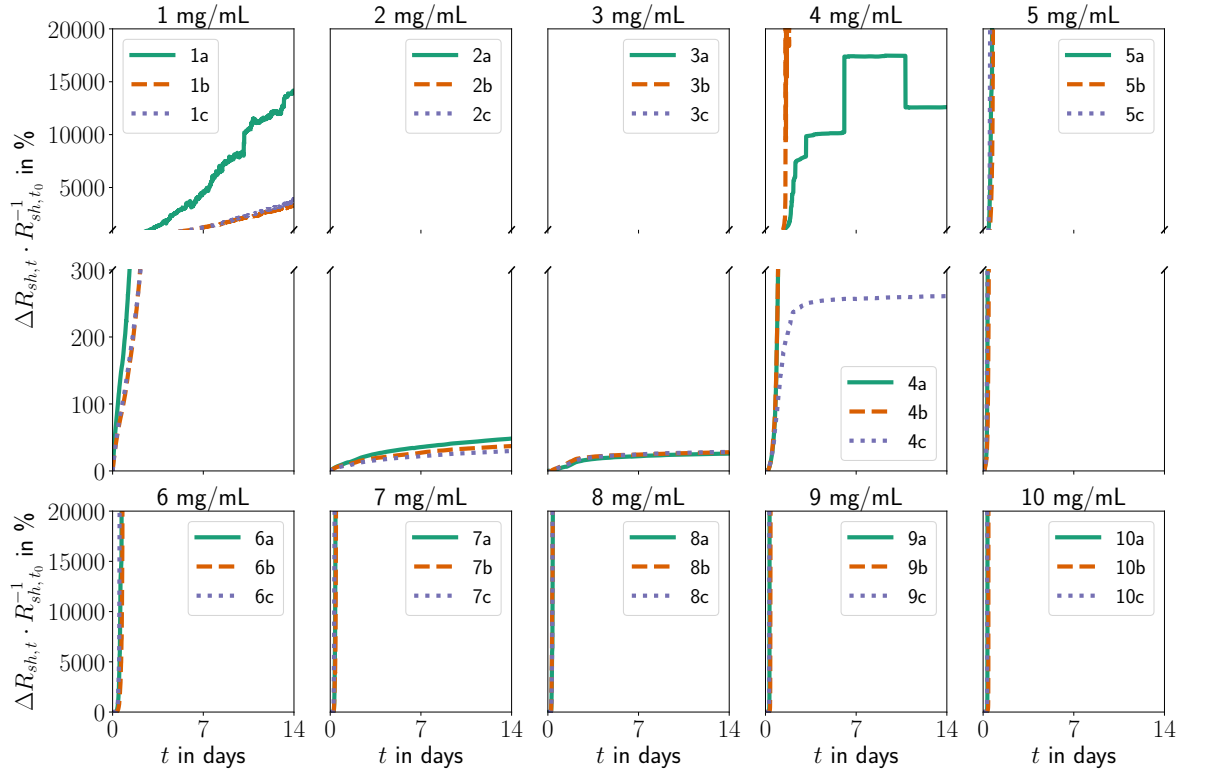


Figure S1: Relative change in sheet resistance $(R_{sh,t} - R_{sh,t_0}) \cdot R_{sh,t_0}^{-1} = \Delta R_{sh,t} \cdot R_{sh,t_0}^{-1}$ after time t for three electrodes each, imprinted at the respective same concentration c_{Au} .

2 AuNW properties

2.1 Wire arrangement and inter-wire distance within printed lines

SAXS measurements were carried out to determine the wires' arrangement within lines imprinted at $c_{Au} = 2 \text{ mg/mL}$ and 6 mg/mL . The peak positions $q_{(1,0)}$ and $q_{(1,1)} \approx \sqrt{3} \cdot q_{(1,0)}$ indicate the same 2D hexagonal wire arrangement with a core center-to-center distance of $a_{c-c} = 4.22 \pm 0.04 \text{ nm}$ for both concentrations, according to Förster et al.^[1]

$$a_{c-c} = \frac{4\pi}{\sqrt{3}} \cdot q_{(1,0)}^{-1} = 4\pi \cdot q_{(1,1)}^{-1} = 4.22 \pm 0.04 \text{ nm} \quad (\text{S1})$$

a_{c-c} in TEM appears smaller because a) the wires do not always run straight, but overlap and intertwine, and b) a TEM lamella has a finite thickness and multiple wires overlap.

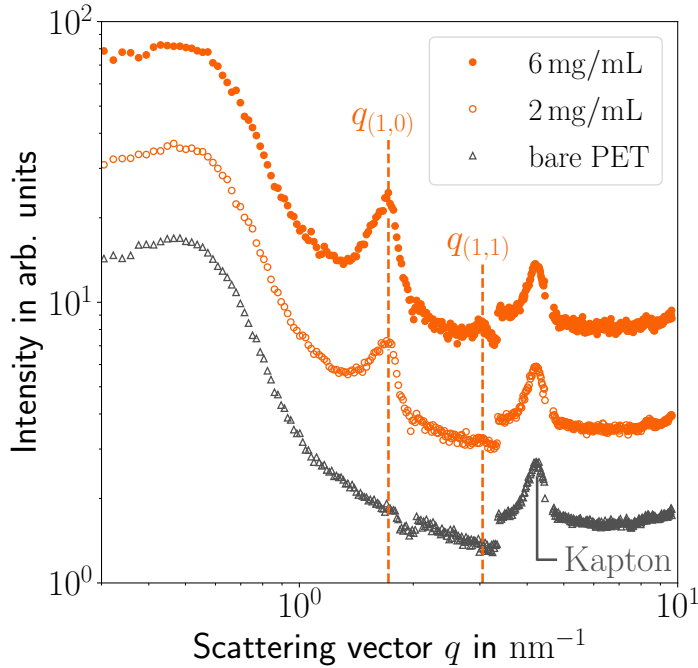


Figure S2: Integrated SAXS scattering of grids imprinted at 2 mg/mL (relatively stable electrode) and 6 mg/mL (highly instable electrode) on PET as well as of bare PET as reference (the Kapton[®] peak stems from the Kapton[®] window used to separate the sample from the evacuated scattering path | scattering curves have been shifted for better visibility).

2.2 Organic content: volumetric fraction

The volumetric fraction of OAm in printed lines was estimated from the organic content of AuNW that had been purified twice and analyzed via thermogravimetric analysis (TGA) in a previous publication:

$$f_{V,OAm} = \frac{f_{w,OAm} \cdot (\rho_{OAm})^{-1}}{f_{w,OAm} \cdot (\rho_{OAm})^{-1} + f_{w,Au} \cdot (\rho_{Au})^{-1}} \cdot 100 \% \approx 87.05 \text{ vol\%} \quad (\text{S2})$$

with $f_{V,OAm}$ the volume fraction of OAm, $f_{w,OAm} \approx 22 \text{ wt\%}$ the mass fraction of OAm (determined via TGA by Bettscheider et al.^[2]), $f_{w,Au} \approx 78 \text{ wt\%}$ the mass fraction of Au, $\rho_{OAm} = 0.81 \text{ g/cm}^3$ the density of OAm^[3] and $\rho_{Au} = 19.3 \text{ g/cm}^3$ the density of Au,^[4] both at room temperature.

3 Sintered line morphology in cross section at 2 mg/mL

Transmission electron microscopy (TEM) was used to test the effect of plasma sintering on the inner morphology of the printed lines. For grids imprinted at 2 mg/mL, plasma sintering visibly coarsened the inner morphology down to the substrate.

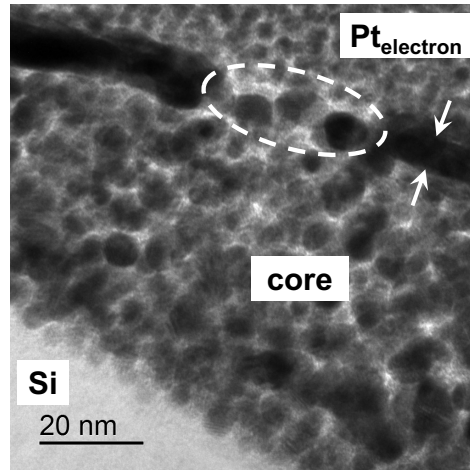


Figure S3: TEM close-up of the inner line morphology directly after plasma sintering for grids imprinted at 2 mg/mL on a Si wafer. White arrows indicate the sintered shell. The white dashed oval marks a porous part of the shell.

References

- (1) Förster, S.; Timmann, A.; Konrad, M.; Schellbach, C.; Meyer, A.; Funari, S. S.; Mulvaney, P.; Knott, R. Scattering curves of ordered mesoscopic materials. *The journal of physical chemistry. B* **2005**, *109*, 1347–1360.
- (2) Bettscheider, S.; Kuttich, B.; Engel, L. F.; González-García, L.; Kraus, T. Bundling of Nanowires Induced by Unbound Ligand. *The Journal of Physical Chemistry C* **2021**, *125*, 3590–3598.
- (3) Oleylamine, approximate C18-content 80-90%: SDS. 2009; <https://www.fishersci.de/store/msds?partNumber=10400380&productDescription=100ML+Oleylamine%2C+approximate+C18-content+80-90%25&countryCode=DE&language=de>.
- (4) Haynes, W. M., Ed. *CRC Handbook of chemistry and physics: A ready-reference book of chemical and physical data*, 97th ed.; CRC Press: Boca Raton and London and New York, 2017.

SI to Publication 4

Reproduced from

L. F. Engel, L. González-García, and T. Kraus: “Consolidation and Performance Gains in Plasma-Sintered Printed Nanoelectrodes”. *Nanoscale Adv.*, 2023, **5**, 4124-4132. DOI: 10.1039/D3NA00293D.

with permission from the Royal Society of Chemistry.

SUPPORTING INFORMATION TO: Consolidation and performance gains in plasma-sintered printed nanoelectrodes

Lukas F. Engel,[†] Lola González-García,^{*,†,‡} and Tobias Kraus^{*,†,¶}

[†]*INM — Leibniz Institute for New Materials, Campus D2 2, 66123 Saarbrücken, Germany*

[‡]*Department of Materials Science and Engineering, Saarland University, Campus D2 2,
66123 Saarbrücken, Germany*

[¶]*Colloid and Interface Chemistry, Saarland University, Campus D2 2, 66123 Saarbrücken,
Germany*

E-mail: lola.gonzalez-garcia@leibniz-inm.de, tobias.kraus@leibniz-inm.de

1 Comparing optical transmittance and electric conductance of different grids

We determined the sheet resistance R_{sh} as resistance R of a quadratic electrode section with edge length $l = 15\,000\ \mu\text{m}$, used Ag paste for contacting and miniature crocodile clamps for two-point probe measurements. The square area contained 750 conducting lines. Its anisotropic sheet resistance was

$$R_{sh}^{-1} = R^{-1} = G = \sigma_{shell} \cdot \frac{750 \cdot A_{shell}}{l}, \quad (\text{S1})$$

measured parallel to the lines, with G being the conductance of the 750 lines in parallel.

To restrict the influence of R_{sh} data points at the lowest concentration c_{Au} (they were off-the-charts) when fitting the trade-off between sheet resistance and optical transmittance, the relation above was used for fitting $R_{sh}^{-1} = G$ vs. $\bar{T}_{400-800\text{ nm}}$ instead of R_{sh} vs. $\bar{T}_{400-800\text{ nm}}$. Thus, the fits in Fig. S1B correspond to the inverse of the linear fits in Fig. S1A.

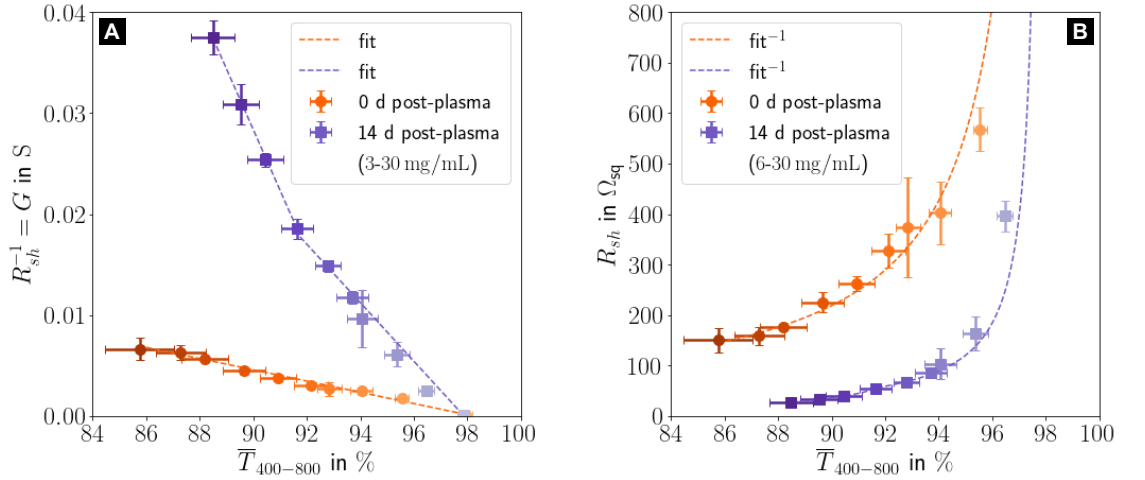


Figure S1: Trade-off between **(A)** conductance $G = R_{sh}^{-1}$ and optical transmittance $\bar{T}_{400-800}$ as well as **(B)** between sheet resistance R_{sh} and optical transmittance $\bar{T}_{400-800}$ for electrodes right after plasma sintering (initial state) and fourteen days later (aged state). The data points for $c_{Au} = 3\text{ mg/mL}$ have been omitted in B due to off-the-charts high R_{sh} . | The graphs show averaged values from three measurements each, the corresponding standard deviation as well as a fit (dashed lines). Light colours indicate lower c_{Au} .

2 Quantification of electrode ageing

We tracked the sheet resistance of AuNP electrodes imprinted at ink concentrations ranging from 3 mg/mL to 30 mg/mL on PET foil over time to investigate their ageing behaviour. Nanoimprinting at 3 mg/mL resulted in structures near the percolation threshold, exhibiting initial sheet resistances which were too high for FTEs.

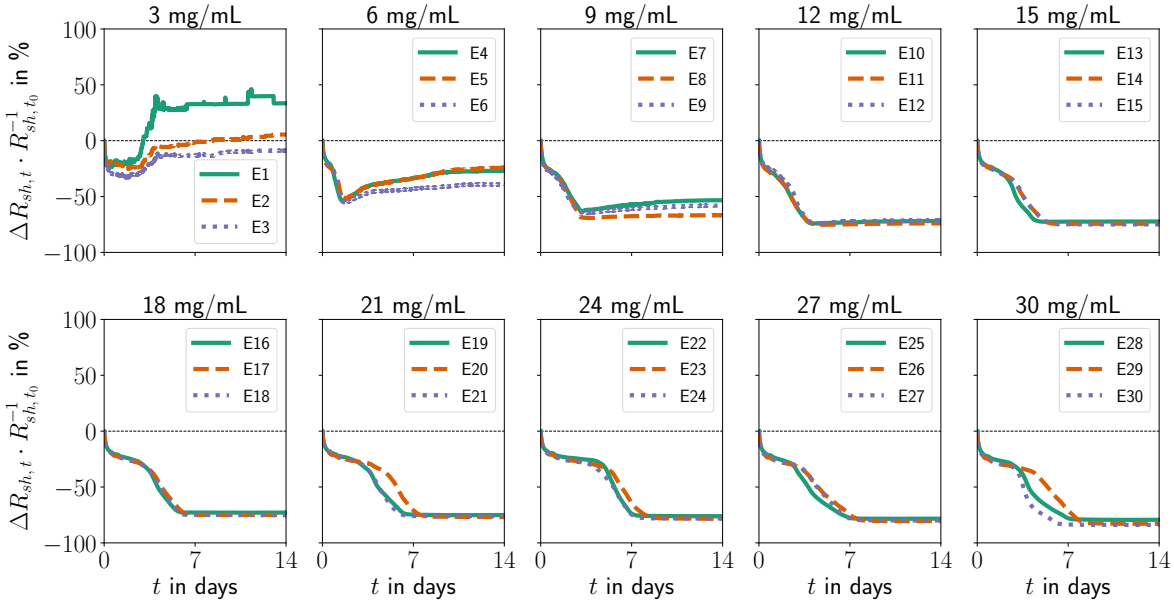


Figure S2: Relative change in sheet resistance $(R_{sh,t} - R_{sh,t_0}) \cdot R_{sh,t_0}^{-1} = \Delta R_{sh,t} \cdot R_{sh,t_0}^{-1}$ with time t for three electrodes each, nanoimprinted at the respectively same concentration c_{Au} .

In addition, we measured the optical transmittance spectra of the FTEs immediately after plasma sintering and 14 days later for all concentrations.

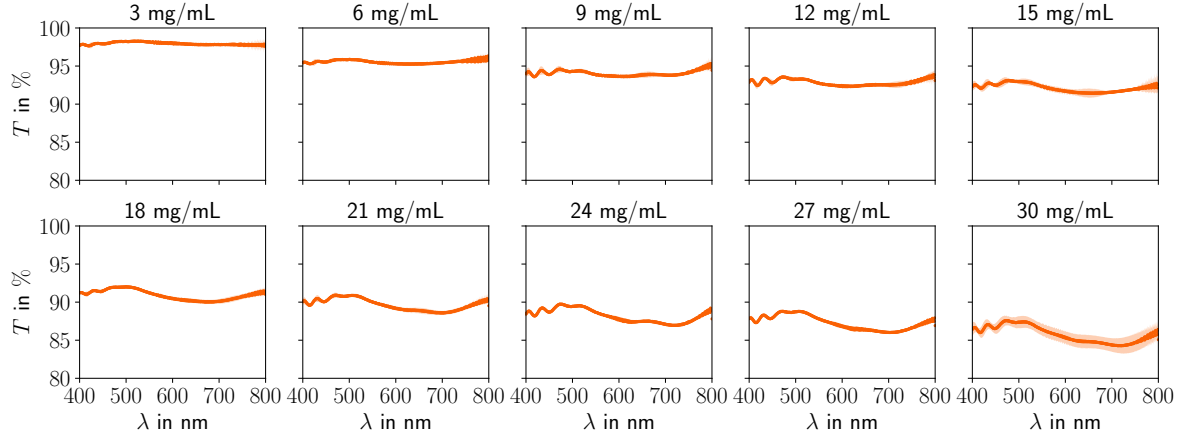


Figure S3: Optical transmittance spectra of the FTEs immediately after plasma sintering. Each graph shows the average from measurements on three FTEs imprinted at the same concentration c_{Au} as well as the standard deviation.

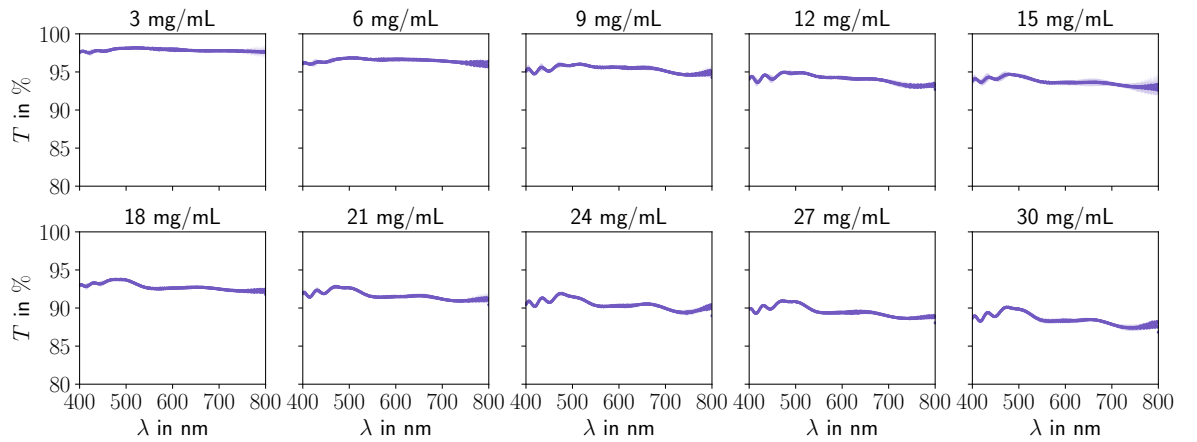


Figure S4: Optical transmittance spectra of the FTEs 14 days after plasma sintering. Each graph shows the average from measurements on three FTEs imprinted at the same concentration c_{Au} as well as the standard deviation.

3 Sphere properties

3.1 Core sizes and dispersion states

SAXS was employed to study the AuNP dispersion state within the whole concentration range used for nanoimprinting and to determine the average AuNP core diameter d_{sp} .

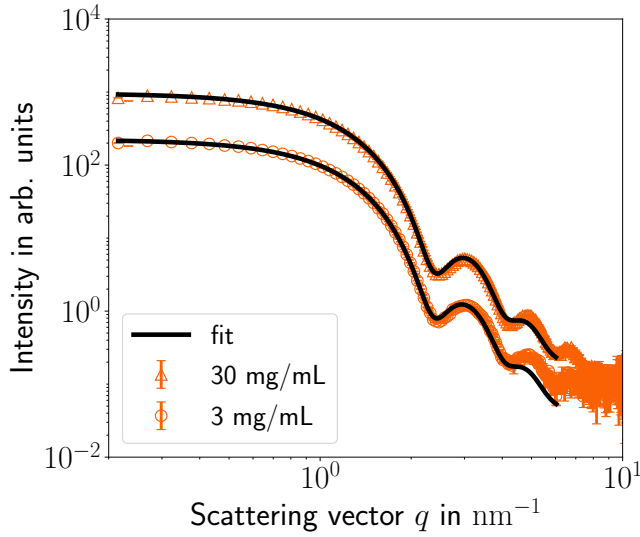


Figure S5: Radially integrated, fitted SAXS curves of the AuNPs used for nanoimprinting at both the highest (30 mg/mL) and the lowest concentration (3 mg/mL). The fits yield a core size of $d_{sp} = 3.7 \text{ nm} \pm 10\%$. Agglomeration peaks are not present.

3.2 Core center-to-centre distance and sphere arrangement after imprinting

Small-Angle X-ray Scattering (SAXS) was employed to study the spheres' structural arrangement within lines nanoimprinted at $c_{Au} = 3 \text{ mg/mL}$ and 30 mg/mL . The single peak position q^* suggests an amorphous sphere arrangement. Based on the Ehrenfest relation,^[12] the core center-to-center distance for spheres with a short range order (amorphous arrangement) corresponds to:

$$a_{c-c}^{amorph} = \frac{2\pi}{q^*} \cdot 1.23 = 5.61 \pm 0.07 \text{ nm} \quad (\text{S2})$$

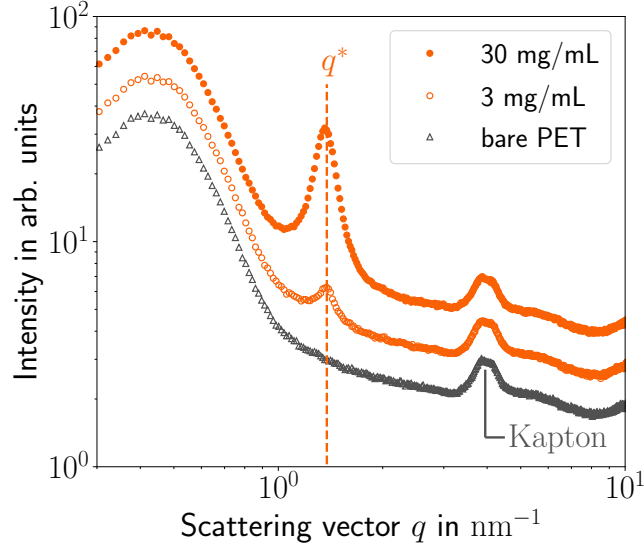


Figure S6: Radially integrated SAXS curves of electrodes nanoimprinted at 30 mg/mL (highest concentration) and 3 mg/mL (lowest concentration) on PET as well as of the bare PET as reference (the Kapton[®] peak is due to the Kapton[®] window separating sample and evacuated scattering path | scattering curves are shifted for improved visibility).

3.3 Organic content

The organic content of the synthesized and twice-purified Au nanospheres was determined with Thermogravimetric Analysis (TGA) and amounted to 16.98 wt% (see Fig. S7). This corresponds to a volume fraction of:

$$f_{V,OAm} = \frac{f_{w,OAm} \cdot (\rho_{OAm})^{-1}}{f_{w,OAm} \cdot (\rho_{OAm})^{-1} + f_{w,Au} \cdot (\rho_{Au})^{-1}} \cdot 100 \% \approx 80.79 \text{ vol\%} \quad (\text{S3})$$

with $f_{V,OAm}$ the volume fraction of OAm, $f_{w,OAm} \approx 15 \text{ wt\%}$ the mass fraction of OAm, $f_{w,Au} \approx 85 \text{ wt\%}$ the mass fraction of Au, $\rho_{OAm} = 0.81 \text{ g/cm}^3$ the density of OAm³ and $\rho_{Au} = 19.3 \text{ g/cm}^3$ the density of Au,⁴ both at room temperature.

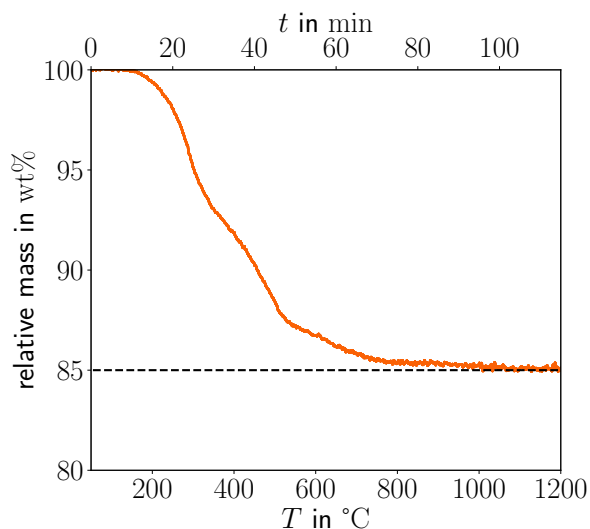


Figure S7: TGA of the synthesized and twice purified AuNPs.

References

1. Guinier, A.; Fournet, G. *Small-Angle Scattering of X-Rays*; John Wiley & Sons, Inc.: New York, 1955.
2. Feng, R.; Stachurski, Z. H.; Rodriguez, M. D.; Kluth, P.; Araujo, L. L.; Bulla, D.; Ridgway, M. C. X-ray scattering from amorphous solids. *Journal of Non-Crystalline Solids* **2014**, *383*, 21–27, DOI: 10.1016/j.jnoncrysol.2013.04.070.
3. Oleylamine, approximate C18-content 80-90%: SDS. 2009; <https://www.fishersci.de/store/msds?partNumber=10400380&productDescription=100ML+Oleylamine%2C+approximate+C18-content+80-90%25&countryCode=DE&language=de>.
4. Haynes, W. M., Ed. *CRC Handbook of chemistry and physics: A ready-reference book of chemical and physical data*, 97th ed.; CRC Press: Boca Raton and London and New York, 2017.